UNIVERSITY OF CRETE – ΠΑΝΕΠΙΣΤΗΜΙΟ ΚΡΗΤΗΣ

Conductometric gas sensors based on nanostructured metal oxide thin films

Master's Thesis by Tsichlis Christos Panagiotis - ph744

Supervisors: Prof. Binas Vassilios
Dr. Gagaoudakis Emmanouil

Committee: Prof. Binas Vassilios
Prof. Georgakilas Alexandros
Prof. Iliopoulos Eleftherios

Thesis submitted to the Department of Physics for partial fulfillment of the requirements for the award of the degree of Master of Science
"Photonics and Nanoelectronics"

June 2024

Abstract:

The aim of this master's thesis is to study the properties and the sensing efficiency of ZnAlO, $ZnAl_5O_x$ and $ZnAlSiO_x$ thin films to hydrogen and methane gases. In this work, all the sensing thin films were developed with the dc sputtering technique, and they were structurally, morphologically and optically studied with UV-Vis spectroscopy, X-Ray diffraction (XRD), Atomic Force Microscopy (AFM), Energy Dispersive Spectroscopy (EDS) and Scanning Electron Microscopy (SEM) techniques. All sensors were tested for low input voltage in a wide temperature range, from room temperature (RT) to T=400°C. In both the cases of hydrogen and methane gas sensing, the optimal results were retrieved from the upper range of temperatures.

Περίληψη:

Σκοπός της μεταπτυχιακής μου εργασίας ήταν η μελέτη των ιδιοτήτων και της δυνατότητας ανίχνευσης αερίων υδρογόνου και μεθανίου από τα λεπτά υμένια των υλικών ZnAlO, $ZnAl_5O_x$ και $ZnAlSiO_x$. Στην παρούσα εργασία, όλα τα αισθητήρια υμένια δημιουργήθηκαν με την τεχνική dc sputtering και στην συνέχεια μελετήθηκαν για τις δομικές, μορφολογικές και οπτικές τους ιδιότητες μέσω των τεχνικών χαρακτηρισμού της φασματοσκοπίας ορατού-υπερύθρου, της περίθλασης ακτίνων Χ, της φασματοσκοπίας ενεργειακής διασποράς και της ηλεκτρονικής μικροσκοπίας σάρωσης. Όλοι οι αισθητήρες δοκιμάστηκαν σε χαμηλές εφαρμοζόμενες τάσεις και για ένα ευρύ φάσμα θερμοκρασιών, ξεκινώντας από θερμοκρασία δωματίου, έως και τους 400°C. Η βέλτιστη απόδοση των αισθητήριων υλικών τόσο για το αέριο υδρογόνο, όσο και για το μεθάνιο, προέκυψε να είναι στο εύρος των υψηλών θερμοκρασιών.

Contents

Chapter I - Introduction

a) Gas sensors review:

In the twenty-first century, we have witnessed the revolutionary development in industrialization with the major purpose being the optimization of the quality of people's lives. However, the continuous strive of improving livelihood has led to the unrestrained usage of environmental resources, affecting both the environment with the enormous pollution and the human health. After long term observations, it is certain that the emission of polluting and hazardous gases, like ammonia (NH_3), carbon monoxide (CO), nitrogen oxides (NO_x), ozone (O_3), sulfur dioxide (SO_2), hydrogen sulfide (H_2S) and the volatile organic compounds (VOCs) like acetone, benzene, formaldehyde, toluene, and chloroform; to the environment affects all living beings and disrupts the ecological balance on Earth. According to the World Health Organization, air pollution is causing around 7 million deaths annually due to various diseases related to heart attack, respiratory infections and lung cancer [1]. For instance, the typical levels of ammonia in atmosphere are 1-5 ppb, while the exposure limit for humans is 25 ppm for 8 hours or 35 ppm for 10 minutes [2]; further interaction can cause skin irritation, eye damage and respiratory distress. Also, NO_2 is respiratory harmful gas and according to the European Chemical Agency, the occupational exposure limit for long term interaction is 0.5 ppm and 1 ppm for short term interaction [3]. Among other gases, flammable (CH_4), explosive (H_2) ones require high attention and sensing mechanisms in order to prevent leakages and human exposure.

For the reasons mentioned above, it is necessary to develop gas sensing devices commonly referred to as gas sensors. They are widely used to detect low concentrations of flammable, toxic, oxidizing, corrosive and dangerously reactive gases in several applicable areas including environmental monitoring, disease diagnosis, food packaging-industrial hygiene control, automotive industry and military security. A good sensor must have specific characteristics such as high sensitivity for specific gases, fast response and recovery time, good selectivity in a gas mixture, low energy consumption and low production cost.

Gas sensors can be categorized according to the material used as sensing element and the detection method that is applied. In this master thesis conductometric gas sensors were developed and used in the sensing process, which means that the electric properties (resistance) of the sensing material alter with the gas interaction. Other sensing methods include optic, acoustic, chromatographic and calorimetric techniques. The materials usually used for the gas sensing process are semiconductor metal oxides which are sensitive in specific gases and when interacting with the gas molecules, they donate or accept electrons resulting in changes of their electrical properties. Among others, 2D semiconductors, carbon nanotubes and conducting polymers can be used as sensing materials (Figure 1).

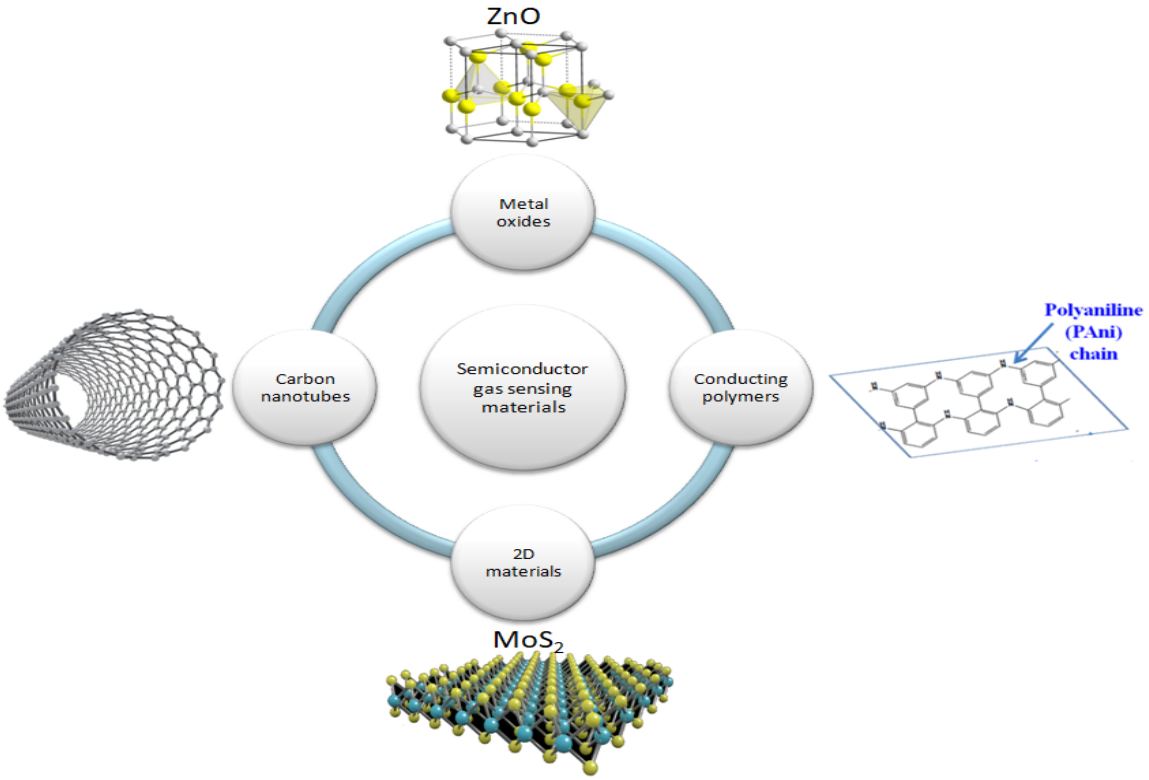

Figure 1: Categories of semiconducting gas sensing materials

A typical gas sensor device is formed upon a glass substrate structured with interdigitated electrodes (IDE's) or metallic contacts on its surface, in order to be able to measure conductivity alteration when voltage is applied and the gas molecules enter the experimental chamber.

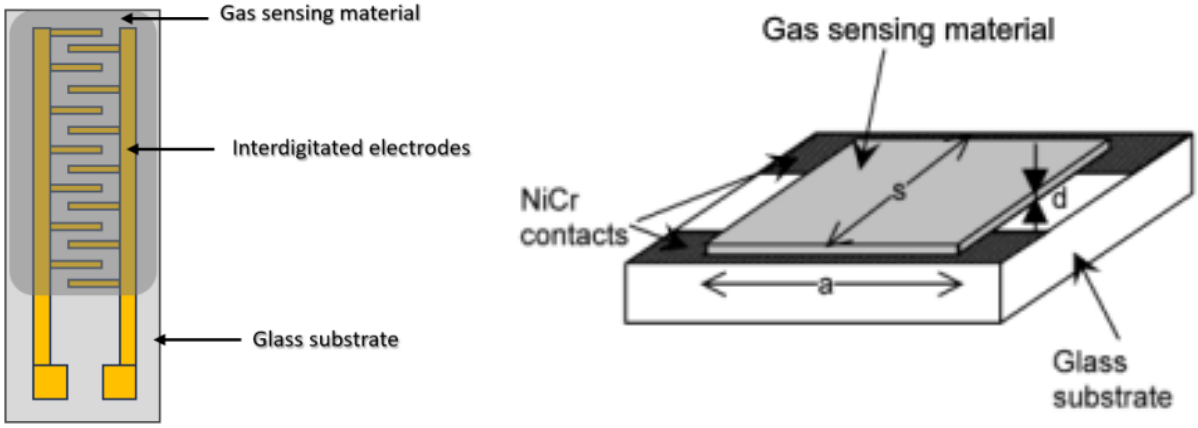

Figure 2: Typical gas sensor structured with IDE's (left) and typical gas sensor with metallic contacts

As far as the efficiency of a gas sensor is concerned, sensitivity is a key factor to rate the response of the sensor to a specific gas. The response (S) can be calculated by the following formulas:

$$S\,(\%) = \frac{R_{gas} - R_{air}}{R_{air}} * 100\% \;, or\; S\,(\%) = \frac{R_{gas}}{R_{air}} * 100\%\; if\; R_{gas} \gg R_{air} \qquad (1)$$

$$S\,(\%) = \frac{R_{air} - R_{gas}}{R_{gas}} * 100\%\,, or\; S\,(\%) = \frac{R_{air}}{R_{gas}} * 100\%\; if\; R_{gas} \ll R_{air} \qquad (2)$$

In the above equation, R_{gas} is the resistance value measured in the presence of the gas inserted in the experimental chamber, while R_{air} is the resistance value measured in the presence of synthetic air that simulates real atmospheric conditions. The response of the sensor can alternatively be calculated from the variance in the measured current in the presence of a specific gas or synthetic air. In direct analogy with equations (1), (2) we have that:

$$S\,(\%) = \frac{I_{gas} - I_{air}}{I_{air}} * 100\% \;, or\; S\,(\%) = \frac{I_{gas}}{I_{air}} * 100\%\; if\; I_{gas} \gg I_{air} \qquad (3)$$

$$S\,(\%) = \frac{I_{air} - I_{gas}}{I_{gas}} * 100\%\,, or\; S\,(\%) = \frac{I_{air}}{I_{gas}} * 100\%\; if\; I_{gas} \ll I_{air} \qquad (4)$$

Except from sensitivity, the sensor must exhibit selectivity to a target gas between gas mixtures. A highly selective gas sensor will provide more reliable data resulting in more accurate monitoring and analysis of the obtained results. Moreover, the sensor must exhibit stability in the sensing process, providing data – results without significant deviations.

In addition to the 3S (Sensitivity-Selectivity-Stability) key properties of a sensor, the response and recovery times are also important parameters of a high quality sensor. The response time can be defined as the period of time the sensor needs to interact with the sensing gas and reach 90% of the final electrical signal value. During the recovery period, synthetic air replaces the target gas. The recovery time is defined as the period of time the sensor needs to return to its initial state, reaching 10% of the initial electrical signal value.

b) Gas sensing mechanism

Conductometric gas sensors consist of metal oxide semiconductor (MOS) configurations, in which their electrical resistance is correspondingly changing with various types of gases, making these materials convenient for gas sensing. According to the different conductive behaviors, MOS's are classified into two main categories, the n-type and p-type. N-type MOS have electrons as major carriers, while p-type MOS have holes as major carriers. ZnO, SnO_2, TiO_2, Fe_2O_3, In_2O_3 exhibit n-type oxide conductivity features. In contrast, NiO, CuO, Co_3O_4, Cr_2O_3 exhibit p-type oxide conductivity features and they have been investigated less for gas sensing due to their lower response to target gases compared with the n-type MOS. Also, according to the bibliography, it is suggested that with identical morphological structures, the response on an n-type MOS based gas sensor is equal to the square of the equivalent response of the p-type MOS sensor [4]. Thus, this indicates that p-type gas sensors must receive further treating techniques to enhance their gas sensing response and to increase the gas sensing properties.

The n-type semiconductivity occurs due to the formation of anion (oxygen) vacancies or due to the substitution of the cations with higher valence ones which increase the number of free electrons. On the other hand, p-type semiconductivity can be attributed to the generated holes generated by the addition of interstitial anions or with lower valence cations [5].

Further categorization on the MOS can be done, based on their electronic structure:

1. Transition-metal oxides (Co_3O_4, NiO, TiO_2, WO_3, Fe_2O_3)
2. Non-transition-metal oxides, including the pre-transition metal oxide (Al_2O_3, MgO) and the post-transition metal oxides (ZnO, ZrO_2)

The gas sensitivity of metal oxides is highly correlated with their electronic structure. Pre-transition metal oxides are not extensively used because of their wide band gap and the difficulty to form both electrons and holes. In contrast, the other two categories of transition metal oxides and the post-transition metal oxides are highly recommended for gas sensing application due to their electronic configurations.

The working principle of a typical gas sensor is based on the electrical conductivity alteration of the sensing material. In bibliography, the most widespread and accepted gas sensing mechanism is the physical adsorption of the target gas molecules by the oxygen ions that have already been adsorbed at the metal oxide surface. That mechanism presupposes the existence of an enormous number of active sites in the sensing material. As the metal oxide sensing material gets exposure to atmospheric conditions, the oxygen molecules from air are adsorbed in the sensing surface according to equation (5).

The highly electronegative adsorbed oxygen molecules extract electrons from the conduction band of the sensing surface, resulting in the formation of negatively charged ionized oxygen (O^-, O_2^-, O^{-2}) according to the equations (6), (7), (8) depending on the applied temperature that the gas sensor is operating at [6].

$$O_{2(gas)} \leftrightarrow O_{2(ads)} \quad (5)$$

$$O_{2(ads)} + e^- \leftrightarrow O_{2(ads)}^- \ , when\ T < 100°C \quad (6)$$

$$O_{2(ads)}^- + e^- \leftrightarrow 2O_{(ads)}^- \ , when\ 100°C < T < 300°C \quad (7)$$

$$O_{(ads)}^- + e^- \leftrightarrow O_{(ads)}^{-2} \ , when\ T > 300°C \quad (8)$$

The adsorbed oxygen ions are crucial in the gas detection process because their interaction with the target gas induces resistance variations by forming a space charge region on the sensing material. For the n-type metal oxide semiconductor materials, the transfer of electrons to the oxygen gas induces an electron-depleted space area between the surface and the interior of the sensing material resulting in a reduced electron density region termed as the electron depletion layer. This results in an upward band bending as well as the formation of a potential barrier at the grain interface. That potential barrier obstructs the free flow of electrons across the sensing surface (current decreases), resulting in a resistance increase under ambient atmosphere compared to vacuum conditions.
The above mechanism for the n-type MOS can be represented schematically in figure 4:

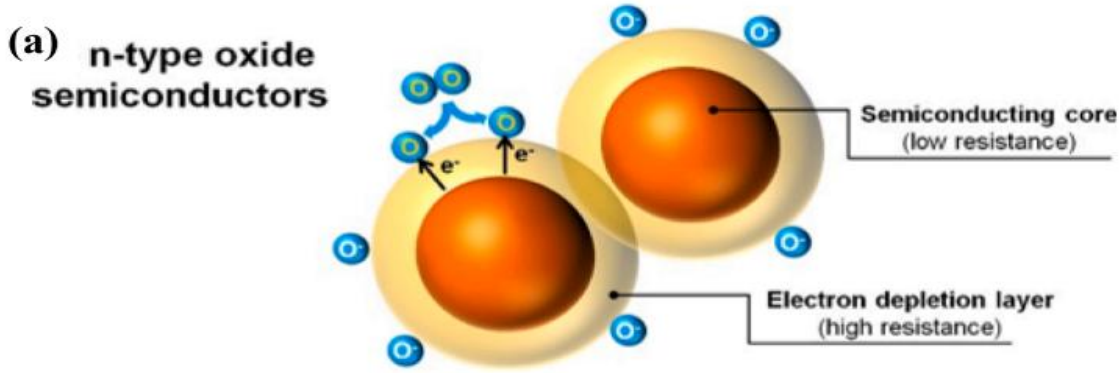

Figure 3: Schematic representation of the surface adsorbed oxygen ions mechanism and the formation of the electron depletion layer [7].

When an n-type sensing material gets exposure to reducing gases, the adsorbed oxygen ions interact with the gas molecules, releasing the trapped electrons to the sensing surface

and reversing the band bending. Thus, the downward band bending along with the decreased electron depletion layer thickness and reduced potential barrier, lead to a decline in the sensor's resistance.

In contrast, when an n-type sensing material gets exposed to an oxidizing gas, more electrons are extracted from the sensing material, increasing the electron depletion layer thickness and the height of the potential barrier. That leads to an upward band bending, resulting in the electrons overcoming the high potential barrier energy and increasing the sensor's resistance.

For instance, in the case of an n-type MOS and a reducing gas (CO), the release of trapped electrons to the sensing surface can be described by the following equations (9), (10).

$$CO_{(gas)} \leftrightarrow CO_{(ads)} \qquad (9)$$

$$CO_{(ads)} + O^-_{(ads)} \rightarrow CO_{2(gas)} + e^- \qquad (10)$$

On the other hand, in the case of an n-type MOS and an oxidizing gas (NO_2), the extraction of electrons from the sensing surface can be described by the following equations (11), (12).

$$NO_{2(gas)} \leftrightarrow NO_{2(ads)} \qquad (11)$$

$$NO_{2(ads)} + e^- \rightarrow NO^-_{2(ads)} \qquad (12)$$

The sensing mechanism that was analyzed above for an n-type MOS sensing material, exhibits a totally opposite trend for a p-type MOS sensing material toward a reducing or an oxidizing target gas. In p-type sensing materials, the adsorption of oxygen species increases the hole concentration (major carrier) through the extraction of electrons from the sensing surface. This forms a space charge region with accumulated holes, termed as the hole accumulation layer, simultaneously implying an upward band bending in the valence band. The accumulated holes possess lower resistance under ambient conditions in comparison to vacuum conditions, because of the increased availability of holes in the sensing material [9]. The above mechanism for p-type MOS can be represented schematically in the figure 5:

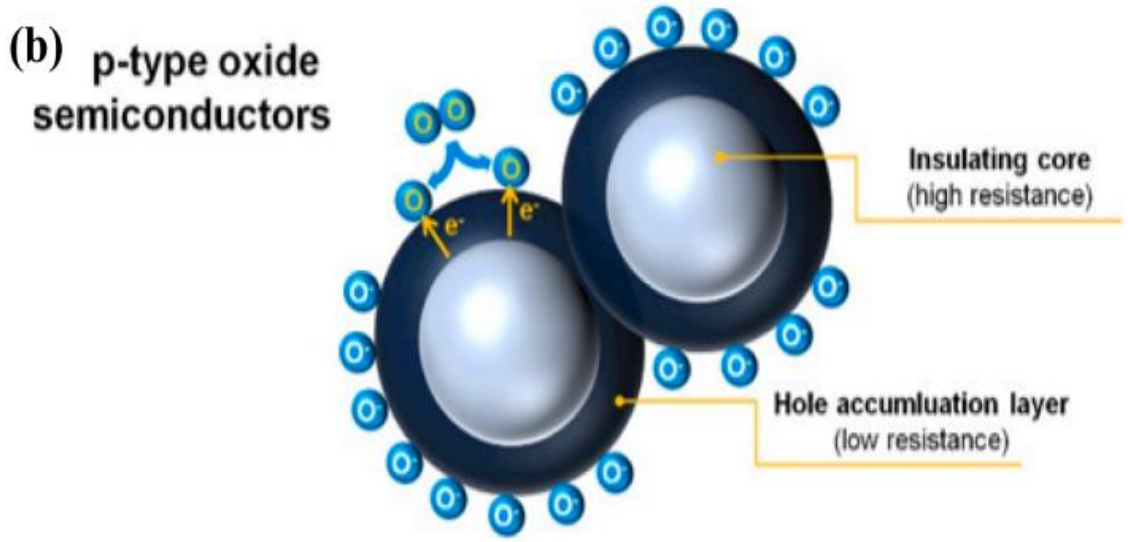

Figure 4: Schematic representation of the surface adsorbed oxygen ions mechanism and the formation of hole accumulation layer in p-type MOS [7].

When a p-type MOS sensing material gets exposure to a reducing gas, the thickness of the hole accumulation layer is reduced and the sensor's resistance increases. On the other hand, if the sensing material gets exposure to an oxidizing gas, the thickness of the hole accumulation layer increases and the sensor's resistance decreases [8].

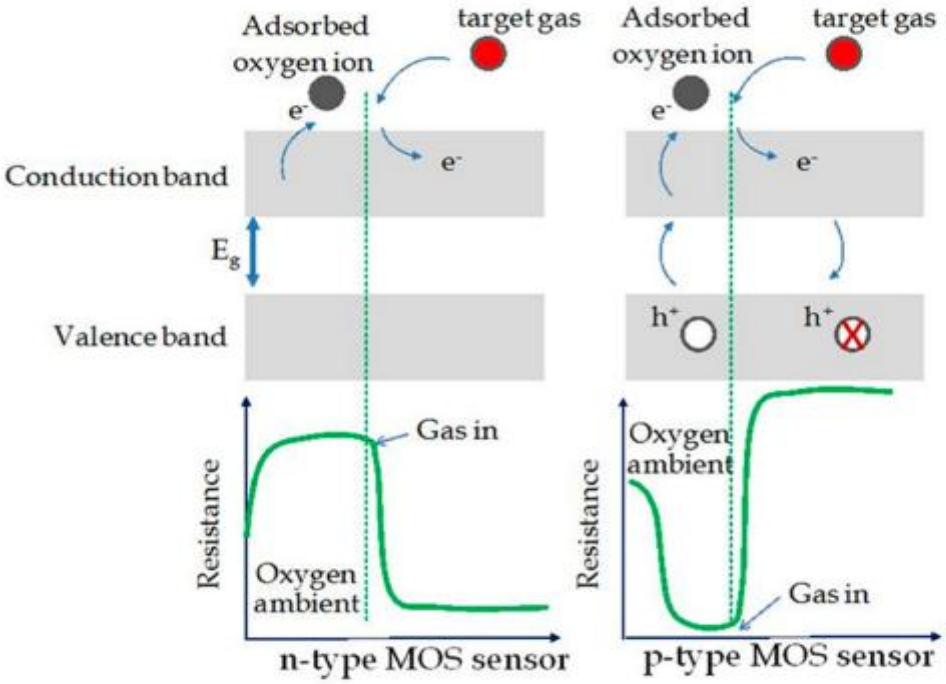

Figure 5: Schematic representation of the resistance change of the sensor when it gets exposed to a reducing gas, in the cases of n-type and p-type MOS sensing material [10].

Type and Examples of MOS	Major charge carrier	Reducing gases (H_2, CH_4, CO)	Oxidizing gases (O_2, O_3, NO_2, SO_2)	Sensor's response (S)
n-type (ZnO,SnO_2, TiO_2, WO_3, In_2O_3)	electrons	Decreasing the resistance	Increasing the resistance	○ $S_n = \frac{R_{gas} - R_{air}}{R_{air}}$, for oxidizing gases ○ $S_n = \frac{R_{air} - R_{gas}}{R_{gas}}$, for reducing gases
p-type (NiO, Co_3O_4, Cu_2O)	holes	Increasing the resistance	Decreasing the resistance	○ $S_p = \frac{R_{air} - R_{gas}}{R_{gas}}$, for oxidizing gases ○ $S_p = \frac{R_{gas} - R_{air}}{R_{air}}$, for reducing gases

Table 1: Summarizing the gas sensing performance of an n-type or p-type MOS towards reducing and oxidizing gases.

c) Hydrogen gas

Hydrogen gas (H_2) is an odorless, colorless, tasteless and flammable gas making it unperceived by human senses. It must be handled with caution as it can ignite at concentrations of 4% - 75% in the presence of air. In the past few years, hydrogen attracted global interest as a "green" and sustainable fuel source that could partially replace the burn of fossil fuels and thus would contribute to the reduction of environmental pollution. Some of the fields that hydrogen is widely utilized are power generators, automobile industry (cars) and aviation industries. Its small molecule size leads to the occurrence of leakage easily during the storage, transportation and utilization process. Therefore, there is great need of developing high performance hydrogen sensors that could detect it timely and accurately in the above application [12], [13].

d) Methane gas

Methane gas (CH_4) is a colorless and odorless gas that occurs abundantly in nature and as a product of human activities. It is flammable in concentrations between 5% - 15% in the presence of air, so it threatens human safety. Also, methane gas constitutes the second main factor (10% of the greenhouse gases) for the greenhouse effect that results in the increase of the global temperature. Thus, we need to develop gas sensors that would be able to detect methane gas at low concentrations both for human protection and environmental monitoring [14], [15].

e) ZnO characteristics

Zinc oxide (ZnO) is an inorganic compound which is present in the earth's crust as the mineral named zincite. However, most zinc oxide is produced synthetically [17]. ZnO is the most abundant and broadly studied metal oxide semiconductor because, due to its photo-physical properties, it can be used in a wide range of applications including electrochemical biosensors [18], gas sensors [19] [20], super capacitors [21], photodetectors [22], photocatalysts [23], energy storage devices [24], dye-sensitized solar cells [25], water splitting for H_2 production [26] etc.

The crystal structures of ZnO are the wurtzite, the zinc blende and the rocksalt. Among them the wurtzite structure is the only thermodynamically stable phase under ambient conditions. The wurtzite structure has a hexagonal unit cell with two lattice parameters a, c in the ratio of $c/a = \sqrt{8/3} = 1.633$ (in the ideal wurtzite structure). The structure is composed of two interpenetrating hexagonal close-packed (hcp) sublattices, each of which consists of one type of atom displaced with respect to each other along the threefold c-axis by the amount of 0.375 (in the ideal wurtzite structure). Each sublattice includes four atoms per unit cell and every atom of one kind (group II atom – Zn) is surrounded by four atoms of the other kind (group VI atom-O), or vice versa.

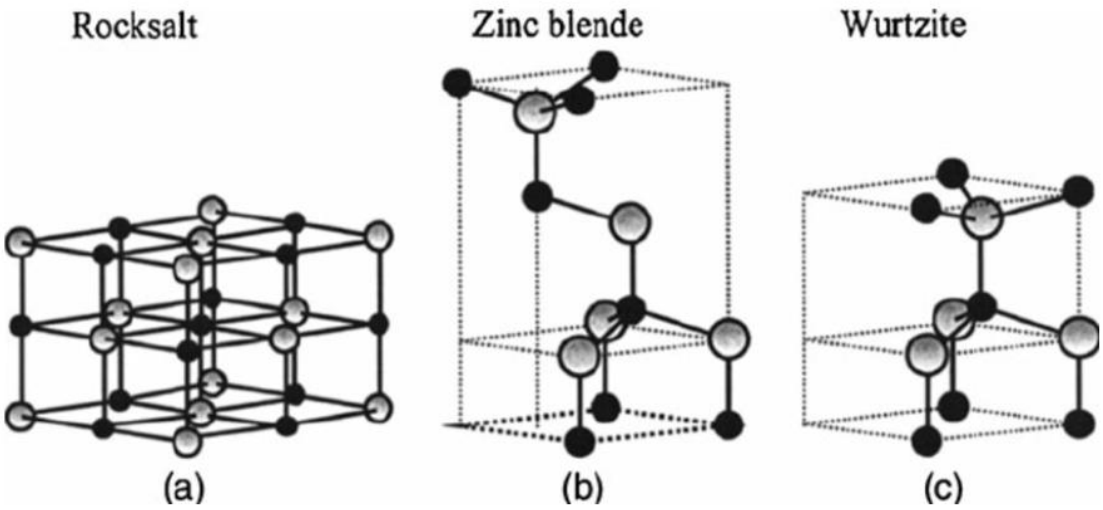

Figure 6: ZnO crystal structures: cubic rocksalt (a), cubic zinc blende (b) and hexagonal wurtzite (c). The grey and black spheres represent zinc and oxygen atoms [27].

Physical parameters	Values
Lattice parameters at T=300°K	a=3.2495nm, c=5.2069nm
Stable phase at T=300°K	Wurtzite
Melting point	1975°C
Energy gap at T=300°K	3.37 eV, direct
Exciton binding energy	60 meV
Electron effective mass	0.24
Electron Hall mobility at T=300°K	200 $cm^2/V*s$

Table 2: Physical parameters of ZnO

Generally, in semiconductor metal oxides the bandgap energies are determined from the Tauc plot formula in which $(ahv)^2$ is displayed as a function of the photon energy (hv). ZnO exhibits a direct large energy gap between 3.0 – 3.38 eV with a huge exciton binding energy of 60 meV [28], [29]. The E_g magnitude is influenced by several competing parameters, including morphology, defect type and concentration, in addition to crystallite size, as evidenced by the drop-in E_g values compared to the macro-sized E_g value (3.37ev) and the scarce indirect dependency with particle dimension [30]. Also, its large energy bandgap (3.37ev) makes ZnO thin films highly transparent to visible light (400-700 nm), while they exhibit strong broad absorption between 280-400 nm with maximum peak at around 380-90 nm in the UV/Visible region.

The electrical properties of nanomaterials are dependent on their crystal phase, shape and dopant ions in the host lattices. Thus, in order to increase the potential applications of ZnO in nanoelectronics, a fundamental revision of their electrical characteristics is required. In their pristine form, the ZnO nanoparticles illustrate n-type semiconducting properties with a donor concentration of the order of 10^{17} cm^{-3} [31]. An increased electron concentration of the order of 10^{21} cm^{-3}, induced by electron doping, results in an operative mass of 0.24 m_o and a Hall movement of 200 $cm^2V^{-1}s^{-1}$. In addition, ZnO's intrinsic n-type conductivity is caused by the Oxygen species or Zn^{+2} interstitials, either due to the impurity integration through the production of narrow contributors such as H_2 [32]. These inherent imperfections are important in the optical and electrical properties of ZnO, impacting the charge mobility, oxygen vacancies, decay time and optical performance.

In literature, when ZnO is doped with a Mg alloy its energy gap value is shifted to 3.3-4.63 eV, while being doped with a Cd alloy shifts the energy gap value to 2.51 eV [33]. Other studies reference that the E_g value of ZnO may be adjusted by adding 3d transition metal (2.1 – 3.5 eV) ions, including: Li^{+1} (3.17-3.26 eV), Cu^{+2} (3.1-3.2 eV) and Al^{+3} ions (3.15-3.20 eV) [34].

Aluminum is one of the most common doping in ZnO thin films and that's why it has been extensively studied due to its significant impact on the electrical, optical and structural properties of the material. When Aluminum substitutes Zn atoms in the ZnO lattice, there is

one extra electron that contributes to the conduction band of ZnO, resulting in the increase of electron concentration, enhancing its electrical conductivity. Also, Al doping on ZnO thin films slightly widens the energy bandgap, leading to increased transparency in the visible spectrum. Moreover, the Aluminum doped ZnO can lead to better crystalline quality, by reducing lattice defects and dislocations, as well as exhibit a preferred orientation along the c – axis (002), which is beneficial for many applications that transparent conducting oxides are required such as gas sensors, solar cells and UV light emitters.

The ZnO nanoparticles and thin films can be developed with a variety of chemical and physical deposition techniques such as DC/Magnetron Sputtering, spray pyrolysis, hydrothermal synthesis, sol-gel, atomic layer deposition, chemical vapor deposition, plant extract, etc.

A summarizing table with some of their advantages and disadvantages of each developing technique follows:

Method	Advantages	Disadvantages
DC/Magnetron Sputtering	Low substrate temperature, high deposition rate, good film adhesion, uniform film thickness, simple operation and low deposition cost	Low in target material utilization and plasma instability
Spray pyrolisis	Easy technique to control microstructure, high film-forming rate, easy doping, large area film formation	Only Newtonian fluids
Hydrothermal synthesis	Secures highly purity, control of the shape and size of the particles	Operating in higher temperature, insoluble in most aqueous media
Sol-gel	High uniformity and purity of products, low process temperature, easy to prepare various new materials	Harmful organic solvents, long production time and easily cracking
Chemical vapor deposition	Fast deposition speed, easy control of film composition, good adhesion, compactness and uniformity of the obtained film	Reduce the product quality
Plant extract	Eco-friendly, cost effective, non-toxic, ambient reaction condition and stable product. It does not require solvent or perilous chemicals	Uncontrollable shape and size
Pulsed laser deposition	Low operating temperatures, control coating density and coating purity, high deposition rate and works on complex shapes	High equipment cost, slow sedimentary speed

Table 3: The advantages and disadvantages of the different methods for the synthesis of ZnO, ZnO:Al films

Chapter II - Experimental

a) Sputtering process – film growth

All the sensing films were developed with the DC Magnetron Sputtering technique, on the top of corning glass substrates. Before their use, the corning glass substrates were cleaned following the laboratory protocol. In details, the substrates were passed through two cleaning steps: 1) soaking 5 minutes in acetone inside the sonication machine, 2) soaking 5 minutes in iso-propanol inside the sonication machine. Then the substrates were rinsed with deionized water and finally dried with nitrogen gas blowing. The dimensions of the substrate glass are 1 inch x 1 inch. Before the sputtering procedure, two wide conduction areas were formed by thermal evaporation of NiCr. This was done by placing the glass substrate on the upper base of the chamber of the thermal evaporator, while a metallic "boat" (ME3-Ao-Mo) filled with rhinestones of NiCr was placed on the bottom one. Then, we create vacuum conditions of the order of 10^{-6} mbar with the use of a mechanical and a diffusion pump. Supplying the boat with current, there is a high increase in temperature until the limit of the evaporation temperature of NiCr (~ I=60 A). Then NiCr is evaporated, developing a thin film of NiCr (nm) at the surface of the corning glass. The aim of NiCr evaporation is to create electrodes on either side of the area that will be deposited on each sensing film, thus making it possible to measure changes in electrical conductivity.

The next step is to cover the substrate with a photoresist material, except from a square area at the center of the substrate. This area will be deposited with the sensing film of the material and it will have specified dimensions (length and width). Then, the substrates are placed at the top base of the sputtering chamber, where the film growth deposition with DC Magnetron sputtering technique takes place. At the bottom base of the chamber, we placed the target material of each sensing film deposition we performed. As target materials, we used three different targets of Heraeus company. The first target material was ZnAlO (Heraeus-Metallic ZnAl2%), used for the development of #743 and #745 sensing films. The second target material was $ZnAl_5O_x$ (ZAO5 Heraeus), used for the development of #532, #533, #534 sensing films. The third target material was $ZnAlSiO_x$ (ZAO2D Heraeus), used for the development of #524, #525 and #530 sensing films. A mechanical and a diffusion pump are used to create vacuum ($5*10^{-7}$ mbar) inside the chamber. As soon as we achieve this vacuum value, the targets cleaning process starts (pre – sputtering). At this stage we use only O_2 gas in order to achieve homogeneous plasma creation. After that, the sputtering process begins, by setting the per cent ratio between Argon and Oxygen gas used to create the plasma that eventually hits the target material, resulting in the formation of each oxide material. Then, we open the cover between the created plasma and the substrates, resulting

in the oxide material in each case being deposited upon them. During the process of the film growth, we need to maintain a constant pressure of $8*10^{-3}$ mbar inside the chamber as well as a constant applied bias that achieves the plasma creation. The thickness of the deposited sensing film depends on the deposition duration time and the applied current voltage in the plasma creation.

It must be mentioned that all the deposited films were developed at room temperature and their thickness varied from 68nm to 1.050μm.

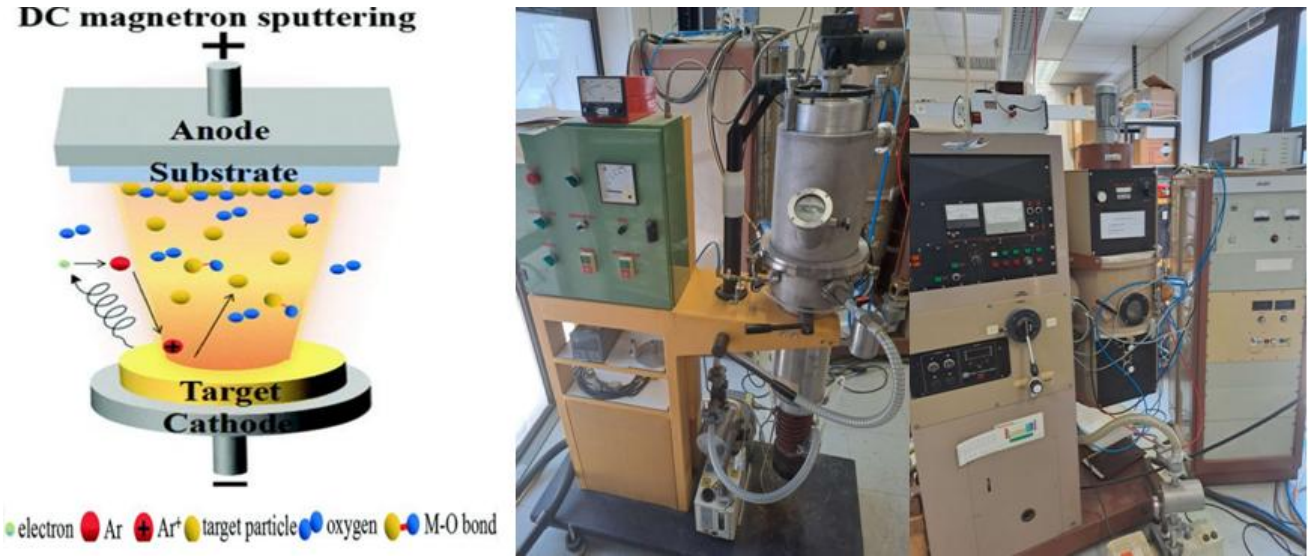

Figure 7: DC Magnetron sputtering film growth technique (left)[16], thermal evaporator (middle) and sputtering equipment (right)

To examine the effect of the supplied power in the plasma creation, for structural and electrical properties of the sensing materials, we changed the current from 0.25A to 0.45A. The supplied power change results in the deposition rate of the material upon the substrate because of the increased flow of ions in the plasma created. Thus, more target material is reconstructed and deposited faster upon the substrate. Finally, in the case of ZnAl2% target we tested two different ratios (20% - 80% and 40% - 60%) of Ar-O_2 gas mixture for the plasma creation.

#	Material	Thickness (d)	Deposition time	Ar	O_2	$I_{sputtering}$	$T_{Substrate}$
524	$ZnAlSiO_X$ (ZAO2D Heraeus)	202.8nm	5min, 50sec	100% (8sccm)	-	0.45A	RT
525	$ZnAlSiO_X$ (ZAO2D Heraeus)	503.6nm	12min, 10sec	100% (8sccm)	-	0.45A	RT
530	$ZnAlSiO_X$ (ZAO2D Heraeus)	101.5nm	6min	100% (8sccm)	-	0.25A	RT
532	$ZnAl_5O_x$ (ZAO5 Heraeus)	101.4nm	3min, 10sec	100% (8sccm)	-	0.45A	RT
533	$ZnAl_5O_x$ (ZAO5 Heraeus)	101.3nm	5min, 50sec	100% (8sccm)	-	0.25A	RT
534	$ZnAl_5O_x$ (ZAO5 Heraeus)	1.050μm	25min, 30sec	100% (8sccm)	-	0.45A	RT
743	ZnAlO (Metallic ZnAl2% Heraeus)	110nm	4min, 30sec	20% (3.2 sccm)	80% (12.8 sccm)	0.45A	RT
745	ZnAlO (Metallic ZnAl2% Heraeus)	68nm	3min	40% (6.4 sccm)	60% (9.6 sccm)	0.45A	RT

Table 4: Deposition parameters for the sensing film grown with DC sputtering technique.

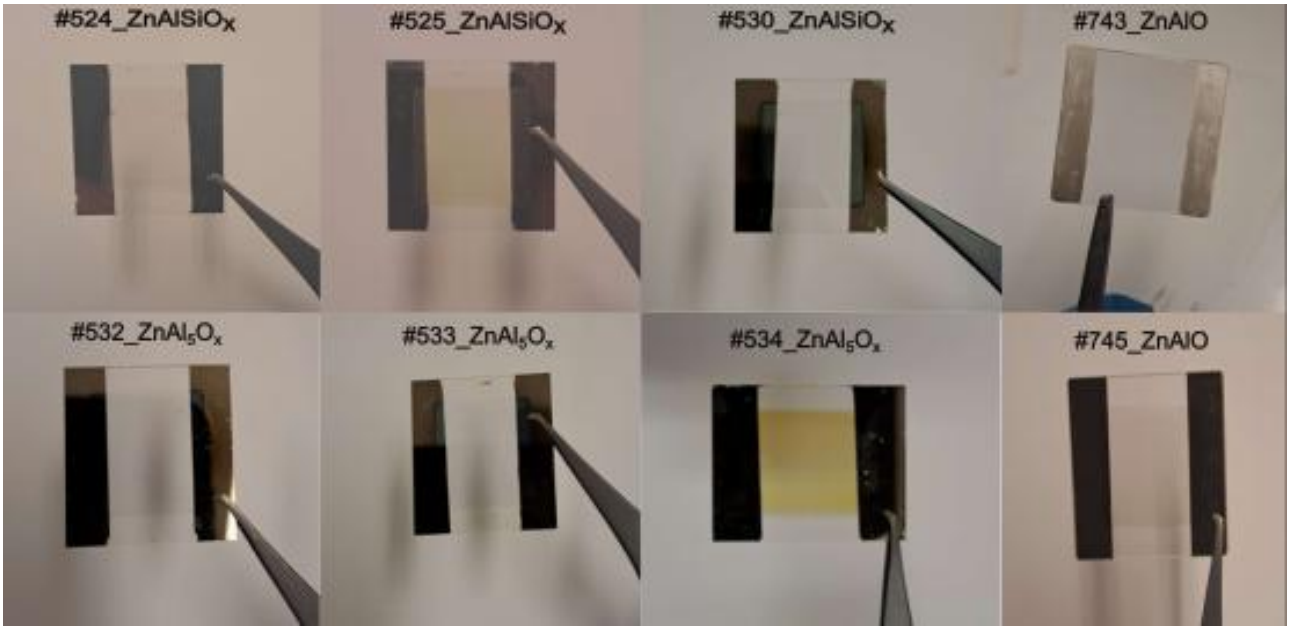

Figure 8: Indicative illustration of all the developed transparent sensing films

It must be mentioned that the #743_ZnAlO sensor broke while it was operating at high temperature in the presence of hydrogen. To replace this sensor, a conducting colloidal silver paint (Ted Pella) was spread upon the glass substrate to form the metallic contacts. The majority of the silver flake grain size (80%) is less than 1μm and the resistance value is 0.02 Ohm per square at 1mm thickness. Acetone was used to dilute the silver paint before usage.

b) Characterization techniques – Structural, morphological and optical properties

1. X-Ray Diffraction (XRD)

The structural analysis of the thin films was done with the help of the X-Ray Diffraction technique. This technique is based on the principles of constructive interference and Bragg's law, which describes the condition for diffraction of X-Rays by the crystalline lattice. When the X-Ray beam hits a crystalline material, the atoms within the crystal cause scatter to the X-Rays. If the wavelength of the X-Rays is similar to the distances between the planes in the crystal lattice, then constructive interference occurs for specific angles, leading to intense peaks in the diffraction pattern.

Bragg's law is expressed as: 2*d*sinθ = n*λ, where d is the spacing between the crystal planes, θ is the incident angle, n is the order of reflection and λ is the wavelength of the X-Ray beam. By analyzing the angles and the intensity of the diffracted beams we are able to obtain important information about the position of atoms within the crystal, the distance between the planes and the symmetry of the crystal structure.

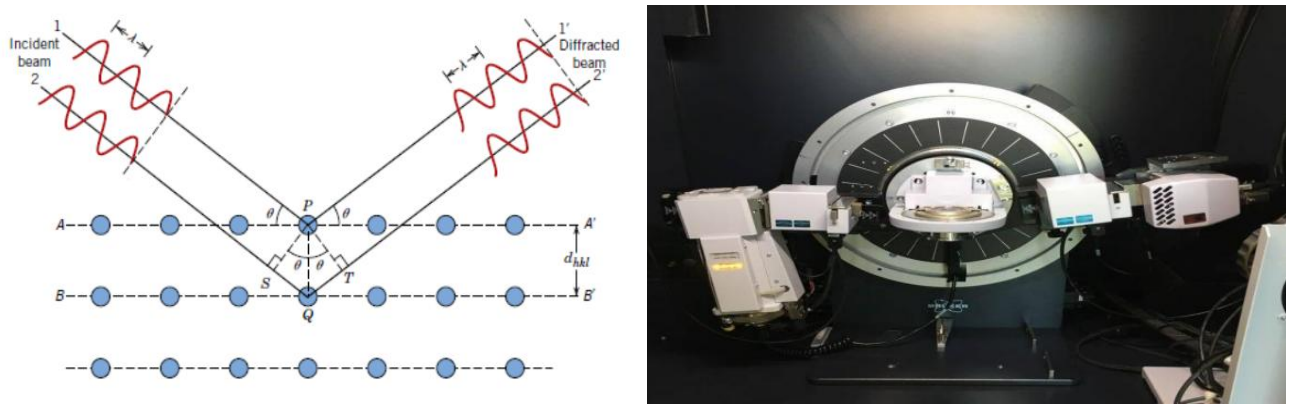

Figure 9: X-ray diffraction by the crystalline lattice (left) and the experimental setup (right)

In our case, the X-Ray diffraction patterns of the sensing films were obtained by a Bruker AXS D8 Advance copper anode diffractometer (Cu Ka radiation), equipped with a Nickel foil monochromator operated at 40kV and 40mA over the 2θ collection range of 5° - 90° with scanning step of 0.05 °/s. From the obtained data we were able to calculate the crystallite size (D) by using the Scherrer equation (13):

$$D\ (nm) = \frac{K * \lambda}{\beta * cos\theta} \qquad (13)$$

, where K = 0.9, λ = 0.15406 nm and β is the full width at half maximum (FWHM) of the main peak of the X-Ray diffraction pattern at an angle of 2θ.

Then, we can calculate the interplanar spacing distance (d_{hkl}) by using the Bragg equation (14):

$$d_{hkl}(\AA) = \frac{n * \lambda}{2 * sin\theta} \qquad (14)$$

, where (hkl) are the Miller indices of the crystal lattice.

The unit cell in the crystal of ZnO exhibits hexagonal wurtzite structure, with lattice parameters a,c describing the distance between Zn atoms in the basal plane (a) and the distance between Zn atoms in the basal direction (c). Thus, we can calculate the lattice parameters a,c by using the following equation (15):

$$\frac{1}{d^2_{(hkl)}} = \frac{4}{3} * \left(\frac{h^2 + h * k + k^2}{a^2}\right) + \frac{l^2}{c^2} \qquad (15)$$

Finally, we are able to calculate the lattice strain parameter (ε_w) caused by impurities or crystallite defects, by the following equation (16):

$$\varepsilon_w = \frac{\beta * cot\theta}{4} \qquad (16)$$

2. Scanning Electron Microscopy (SEM) and Energy Dispersive X-Ray spectroscopy (EDS)

Scanning Electron Microscopy is a common technique used to provide detailed images of the materials surface. This technique operates by scanning a focused electron beam across the sample and detecting the various signals that are produced from the electron – sample interactions. These interactions result in the emission of secondary electrons, backscattered electrons and characteristic X-Rays. In each of the above cases a different type of information is provided. For example, in the case of secondary electrons emission; images with high resolution and topographical contrast are produced. In the case of the backscattered electrons which possess more energy, information about compositional contrast and atomic number differences can be acquired. In the case of the generated X-Rays from the interaction with the sample, information for the elemental analysis and mapping through EDS spectroscopy can be obtained.

In SEM experiments, the samples require being conductive. Non – conductive samples are typically coated with a thin layer of conductive material such as gold. Also, a high vacuum environment in the SEM chamber is necessary to allow the electrons to travel without scattering.

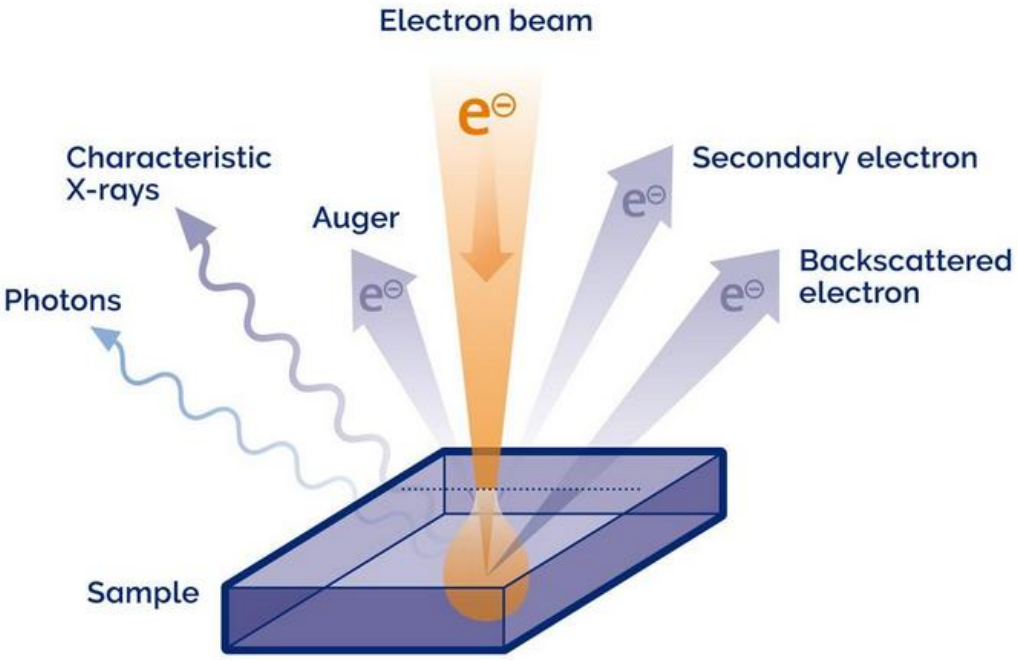

Figure 10: Schematic illustration of the interaction between the electron beam and the sample

Energy Dispersive X-Ray Spectroscopy (EDS) is an analytical technique used for elemental analysis or chemical characterization of a sample. As mentioned above, EDS technique operates on the principle that when a material is bombarded with a focused beam of high – energy electrons in Scanning Electron Microscopy, the X-Rays emitted from the sample are characteristic of the elements present in the sample. Each element has a unique atomic structure that emits X-Rays with specific energies. In EDS technique, a detector measures the energy and the intensity of these X-Rays, producing a spectrum that can be analyzed to determine the elemental composition of the sample.

3. Atomic Force Microscopy (AFM)

Atomic Force Microscopy (AFM) is a technique used to provide high resolution imaging at the nanoscale climax, by probing the surface of the sample with a sharp tip. The working principle of AFM stands in the interaction between the tip and the sample surface. A typical tip is made of silicon or silicon nitride and it is placed on a cantilever that bends in response to the forces between the tip and the sample. These forces include van der Waals forces, electrostatic, magnetic and mechanical contact forces. As the tip scans across the surface, the cantilever deflection is measured using a laser beam that reflects off the top of the cantilever into a photodetector. Then, the deflection data are processed to create a topographical map of the surface at nanometer resolution.

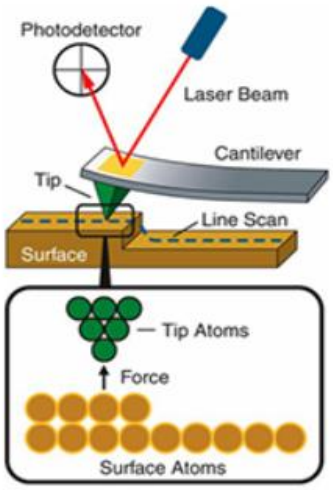

Figure 11: Schematic illustration of the AFM technique

AFM imaging was performed in our co-operating laboratory at the Department of Chemistry in Thessaloniki using a commercial NT-MDT SOLVER-PRO microscope at room temperature (~20◦C). The microscope was sitting on a vibration isolator. Samples were attached to polycrystalline slides using a double sided tape. The scans were performed in air

medium. The images were obtained in the dynamic contact mode with a fabricated silicon NT-MDT cantilever (NSG10 Series) (thickness = 1.5-2.5 μm, length = 90-100 μm, width = 25-35 μm, resonant frequency 140-390 kHz, spring constant = 3.1-37.6 N/m, tip radius of curvature < 10 nm). The scanning rate, to acquire 256 × 256 data points, was 0.5 Hz. Damping set point was 50%. Image data were flattened and noise filtering was used when needed, using NT-MDT 1.1.0.1912 image analysis software. Roughness analysis parameters were also acquired by the same software.

4. Ultraviolet – visible spectroscopy (UV-vis)

Ultraviolet – visible spectroscopy (UV-vis) is an analytical technique that measures the absorption of ultraviolet or visible light by a substance or a solution. The fundamental principle of UV-vis spectroscopy is based on the interaction of light with matter, specifically the absorption of light at different wavelengths by the electrons in the molecules of a sample. When a light beam passes through a sample, there is absorption of certain wavelengths by the electrons of the sample, causing them to transit from a lower energy level to higher energy levels. The amount of light absorbed at each wavelength is recorded, resulting in a final absorption spectrum that is characteristic of the sample. The characteristic peaks of the recorded spectrum are related to the electronic structure of the electrons in the sample.

The UV-vis transmittance spectra of the sensing films were measured on the CARY 50 Conc UV-visible spectrophotometer, receiving data for the wavelength starting from λ = 190 nm to λ = 1100 nm. We can calculate the absorption coefficient, by using the following equation (17):

$$T = T_0 * e^{-a*d} \Rightarrow a = -\frac{1}{d} * \ln\left(\frac{T}{T_0}\right) \qquad (17)$$

, where T is the measured transmittance of the sensing film, T_0 is the measured transmittance of the glass substrate, d is the thickness of the film and a is the absorption coefficient. Then, the energy gap (E_g) can be calculated by producing the Tauc plot following equation (18):

$$(a * h * v)^n = A * (h * v - E_g) \qquad (18)$$

, where h is the Planck constant, v is the frequency and n = 2 for direct electron transitions or n=1/2 for indirect electron transitions.

c) Experimental gas sensing setup

The experimental equipment used for the sensing measurements consists of a mechanical pump, a mass flow controller, an electrometer, a heater, a micro probe system and the gases cylinders. The gas sensing properties of the materials were studied in a micro probe system, equipped with eight probes. The sensors were placed in the center of the stainless – steel chamber, upon the thermal heater which increased the temperature inside the chamber. The mechanical pump was used to evacuate the chamber and for the pressure stabilization. The flow of the gases was controlled through a mass flow controller and its corresponding program on the computer (NEXTRON-TKMHV). With the same program it is possible to choose the operating temperature and the time duration of each gas flow. A KEITHLEY 6517A electrometer was used to apply voltage through a Labview program in the two probes applied upon the sensor in order to measure the electric current variations of the sensing material in the presence of the target gas.

It must be mentioned that for the I-V characteristics of the sensing films, the experimental setup used was the same.

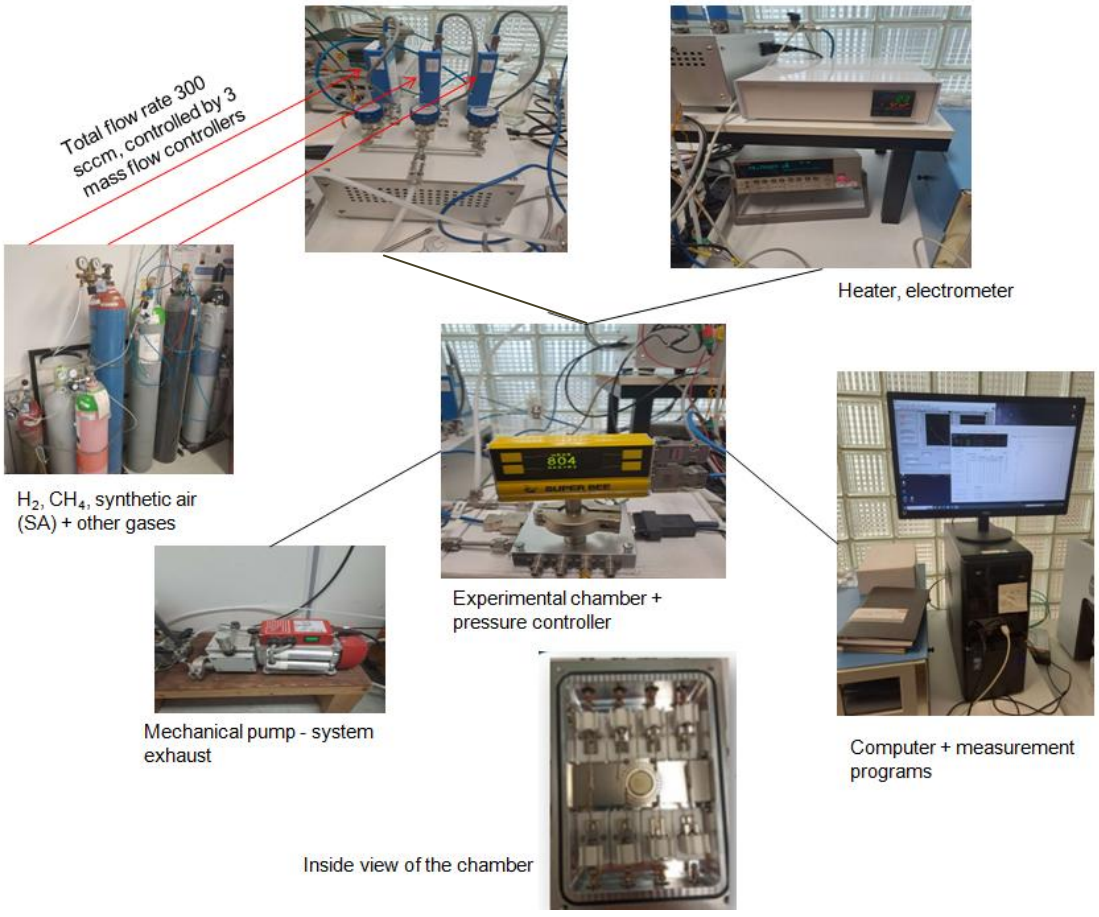

Figure 12: Experimental gas sensing setup

Chapter III – Experimental results

a) ZnAlO gas sensors results

1. Characterization of #743_ZnAlO – Structural, morphological and optical properties

In order to determine the structural, morphological and optical properties of the #743_ZnAlO sensing films, XRD, SEM, AFM, UV-vis spectroscopy techniques were utilized..

1.1 X-Ray Diffraction analysis

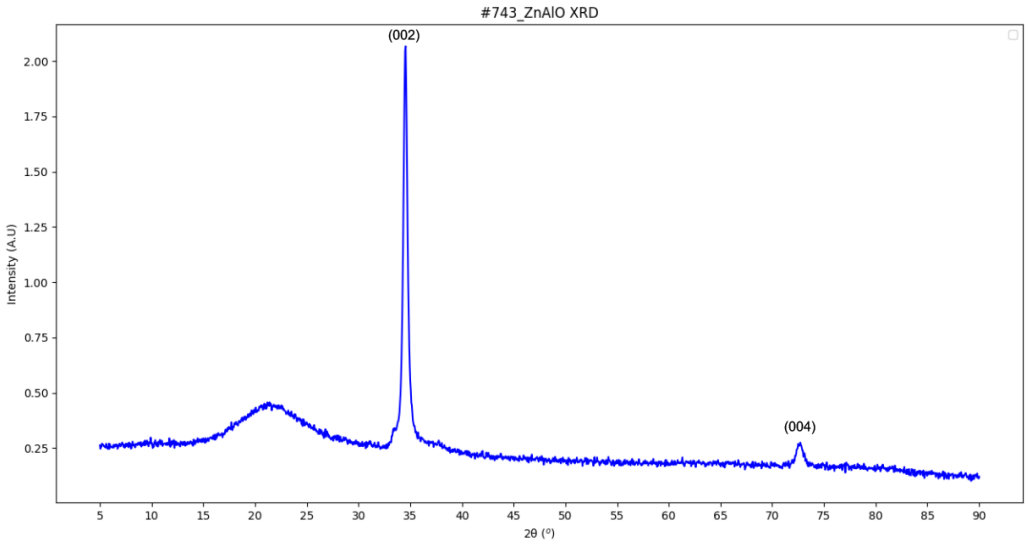

Figure 13: XRD pattern of #743_ZnAlO sensing film

The XRD spectra were measured in the range of 5° - 90°, exhibiting the main peak of ZnAlO at $2\theta_1 = 34.54°$ and a secondary peak at $2\theta_2 = 72.68°$.

According to bibliography, the main peak θ_1 corresponds to the crystal plane with Miller indices (hkl) = (002), while the secondary peak θ_2 corresponds to the crystal plane with Miller indices (hkl) = (004).

Applying Gaussian fitting around the main peak, we can obtain the full width at half maximum (FWHM) of the peak, which is $\beta = 8.869*10^{-3}$ rad.

Then, the crystallite size and the interplanar spacing of the sensing material can be calculated by using the equations (13) and (14):

$$(13):\ D\ (nm) = \frac{K * \lambda}{\beta * cos\theta} \Rightarrow D = 16.372\ nm$$

$$(14):\ d_{hkl}(\text{Å}) = \frac{n * \lambda}{2 * sin\theta} \Rightarrow d_{002} = 2.595\ \text{Å}$$

After calculating the interplanar spacing, the lattice parameters a,c for the hexagonal wurtzite ZnAlO structure can be calculated by using equation (15):

$$(15):\ \frac{1}{d^2_{(hkl)}} = \frac{4}{3} * \left(\frac{h^2 + h * k + k^2}{a^2}\right) + \frac{l^2}{c^2} \Rightarrow c^2 = 4 * d^2_{002} \Rightarrow c = 5.189\ \text{Å}$$

In the ideal wurtzite structure, the ratio $\frac{c}{a} = \sqrt{\frac{8}{3}}$ is constant [11], thus if we make the assumption that there is low local symmetry distortion for the aluminum doped film, then a close approach – calculation for the lattice parameter a can be made resulting in a = 3.178 Å

Finally, the lattice strain parameter ε_w is calculated through the equation (16):

$$(16):\ \varepsilon_w = \frac{\beta * cot\theta}{4} \Rightarrow \varepsilon_w = 7.13 * 10^{-3}$$

The same analysis was held for the secondary peak, with the results quoted in the following summarizing table:

Peak 2θ	Crystallite size D (nm)	Interplanar spacing d_{hkl} (Å)	Lattice parameter c (Å)	Lattice parameter a (Å)	Lattice strain ε_w
$2\theta_1$=34.54°	16.372	(hkl)=(002) 2.595	5.189	3.178	$7.13*10^{-3}$
$2\theta_2$=72.68°	12.122	(hkl)=(004) 1.299	5.199	3.184	$4.82*10^{-3}$

Table5: Structural parameters of #743_ZnAlO thin film

From the analysis above, we can observe that both peaks correspond to crystal planes regarding the c – axis. Especially the (002) –crystalline plane provokes the highest XRD peak intensity, indicating that in the sample #743_ZnAlO, the ZnAlO crystal has strong preference in c – axis orientation perpendicular to the substrate.

1.2 SEM

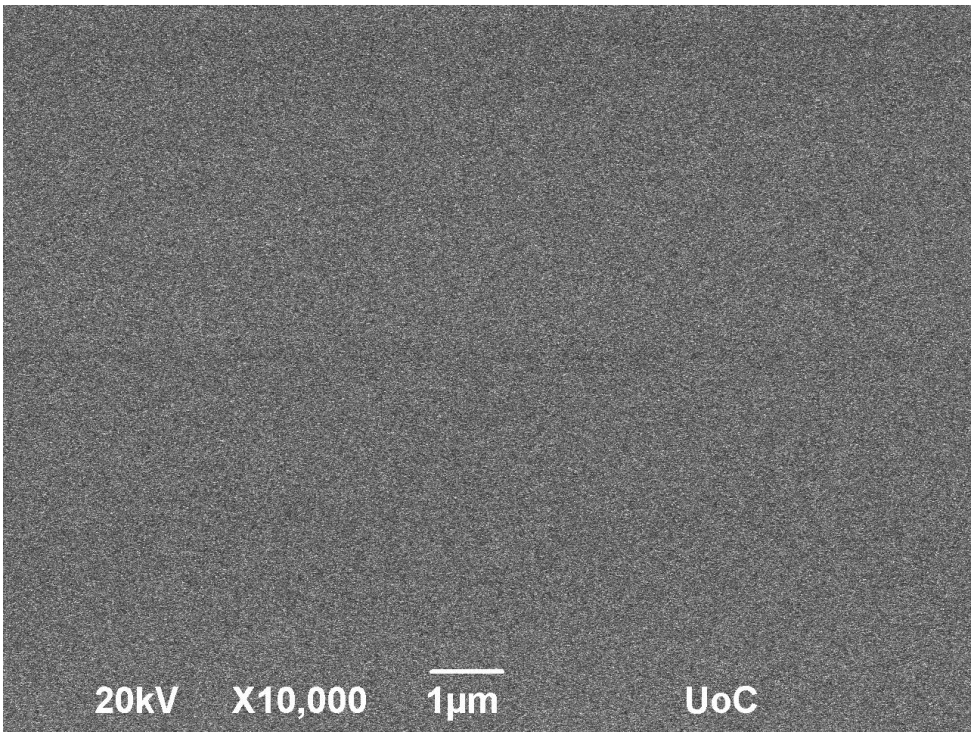

Figure 14: SEM micrograph of the #743_ZnAlO film

The film shows good uniformity and dense surface without visible holes or faulty zones on the film surface.

1.3 AFM

The roughness of the #743_ZnAlO sensing film was calculated through an AFM measurement. The average roughness value was found to be R_a=0.249nm, while the root mean square value was found to be R_s=0.365nm.

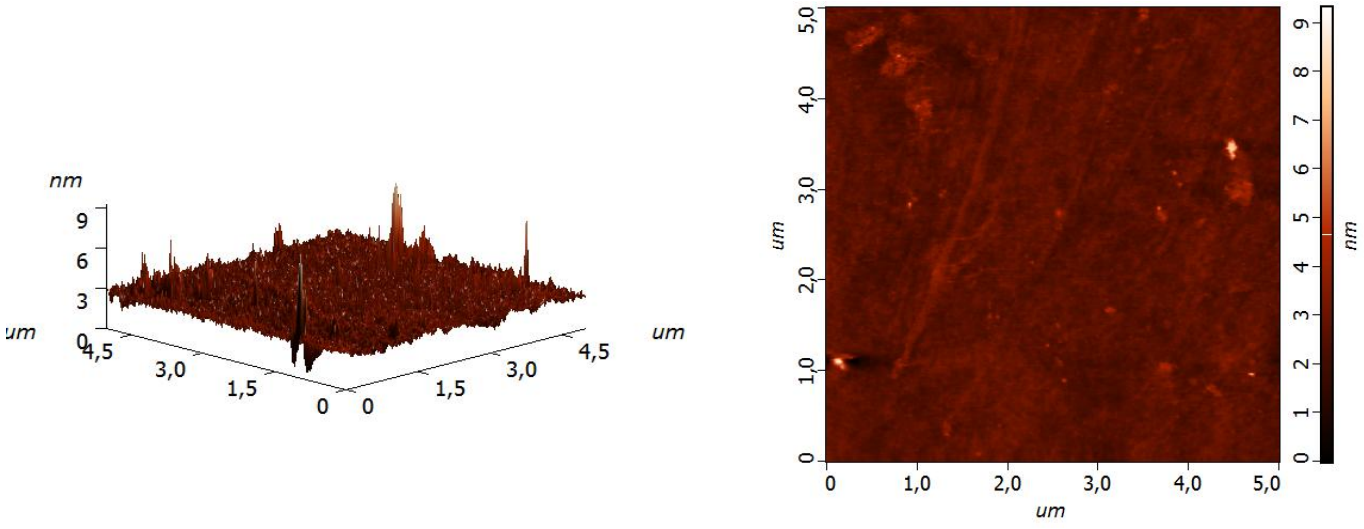

Figure 15: 3D and 2D AFM micrographs (4.5µm x 4.5µm) of the #743_ZnAlO film

1.4 UV-vis spectroscopy

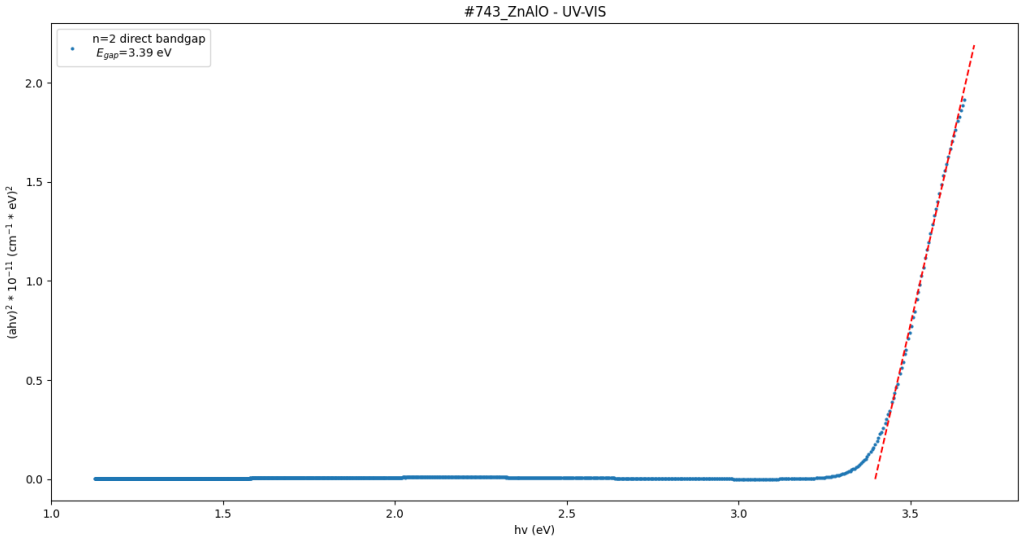

Figure 16: Tauc plot of #743_ZnAlO for the direct energy band gap case (n=2)

The energy gap was calculated via the Tauc plot to be E_g=3.39 eV for the direct case. This value is in the acceptable value range mentioned in the bibliography.

1.5 I-V characteristics

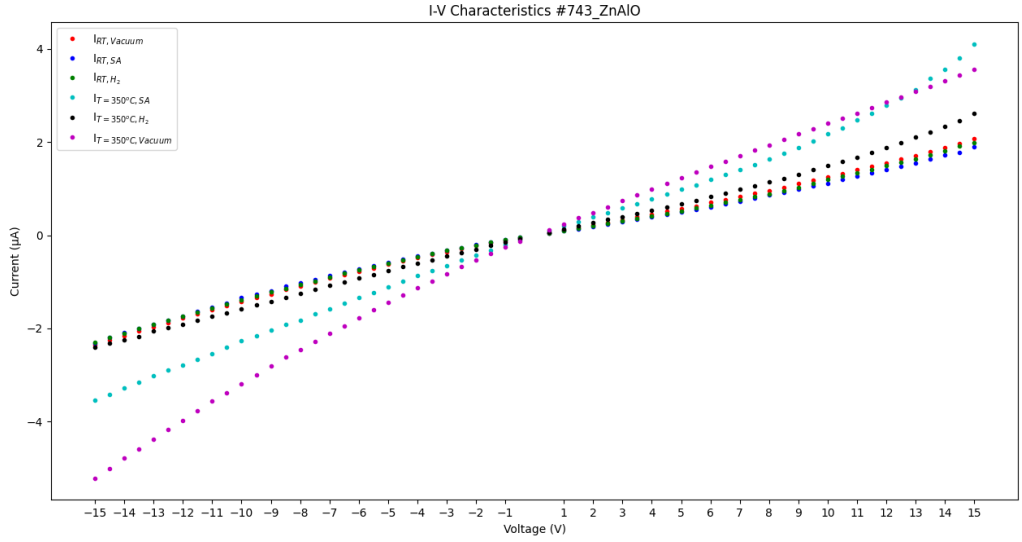

Figure 17: I-V measurements of #743_ZnAlO sensor operating in room temperature (RT) or at T=350°C under vacuum either in the presence of synthetic air or 1000ppm of hydrogen.

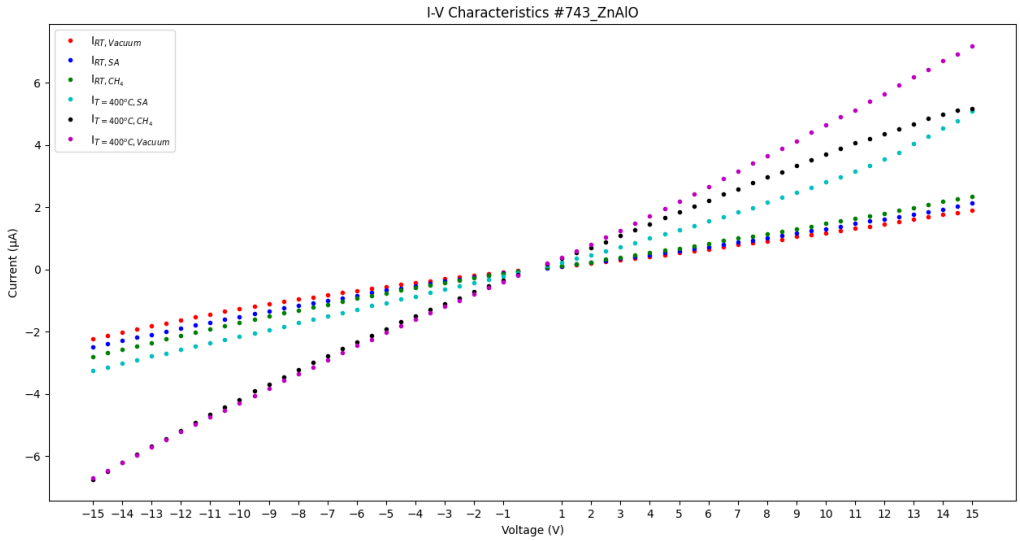

Figure 18: I-V measurements of #743_ZnAlO sensor operating in room temperature (RT) or at T=400°C under vacuum either in the presence of synthetic air or 100% methane.

For both hydrogen and methane gases, we observe linearity in the I-V characteristics around the applied bias of V=5Volts. That linearity indicates that we have an Ohmic junction.

2. #743_ZnAlO sensing results

#	Material	Thickness (d)	Sputtering deposition time	Ar	O_2	$I_{sputtering}$	$T_{substrate}$
743	ZnAlO (Heraeus-Metallic ZnAl2%)	110 nm	4 min, 30sec	20% (3.2 sccm)	80% (12.8 sccm)	0.45A	RT

Table 6: Sputtering parameters used for #743_ZnAlO sensor development

2.1 Hydrogen sensing

The developed sensor was tested against H_2 gas. The sensor was placed in the chamber under vacuum, applying a bias of 5 Volts. Synthetic air was inserted into the chamber with a constant flow of 300 sccm, for 20 minutes to create a constant current baseline and a standard pattern of conditions that were maintained for the following measurements as well. The pressure inside the chamber was stabilized at 800 mbar. Then, 1000ppm of H_2 was inserted at the chamber for 5 minutes to examine the response of the sensor to hydrogen and finally synthetic air was inserted into the chamber for 5 minutes in order to examine the sensor's recovery. This gas alteration inside the chamber was repeated 5 times (5 cycles - repeatability). The process above was repeated for measurements in a different operating temperature, starting from RT to T=400°C with an increasing step of 50°C.

In the analysis following, only the graph for the optimum operating temperature (T=350°C) that provides the best response of the sensor, is exhibited. The rest of the graphs are included in the *Appendix A: #743_ZnAlO - Hydrogen gas sensing*.

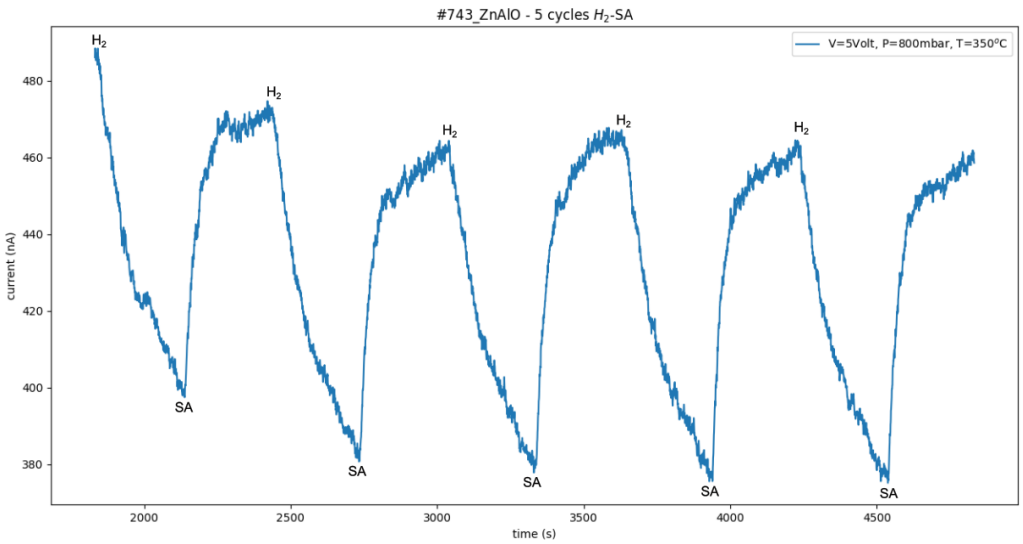

Figure 19: Current – time measurement at T=350°C in the presence of hydrogen

At T=350°C the sensor exhibited its best response and full recovery so we can calculate response / recovery times and the response (S) of the sensor:

The response time was calculated at the 90% of each peak alteration and its mean value is:

$\overline{T_{90}} = \frac{T_{90}^{(1)}+T_{90}^{(2)}+T_{90}^{(3)}+T_{90}^{(4)}+T_{90}^{(5)}}{5} \Rightarrow \overline{T_{90}} = 242\ sec$, best response time: 229 sec

Similarly, $\overline{T_{10}} = \frac{T_{10}^{(1)}+T_{10}^{(2)}+T_{10}^{(3)}+T_{10}^{(4)}+T_{10}^{(5)}}{5} \Rightarrow \overline{T_{10}} = 120\ sec$, best recovery time: 102 sec

The sensor's response at each cycle was calculated following equation (1), while the mean response value is equal to: $\bar{S} = 23.29$

Sensor: #743_ZnAlO			
Temperature (°C)	Sensitivity (%)	Response time T_{90} (best) [sec]	Recovery time T_{10} (best) [sec]
200	4.35	225 (180)	192 (108)
250	8.95	212 (182)	196 (159)
300	15.14	239 (226)	133 (126)
350	23.29	242 (229)	120 (102)
400	18.73	226 (210)	130 (78)

Table 7: Sensitivity-response, response / recovery time of the sensor for the different operating temperatures

By using the data from the Table 4, we can plot the response S of the sensor and the response / recovery times as function of the different operating temperatures:

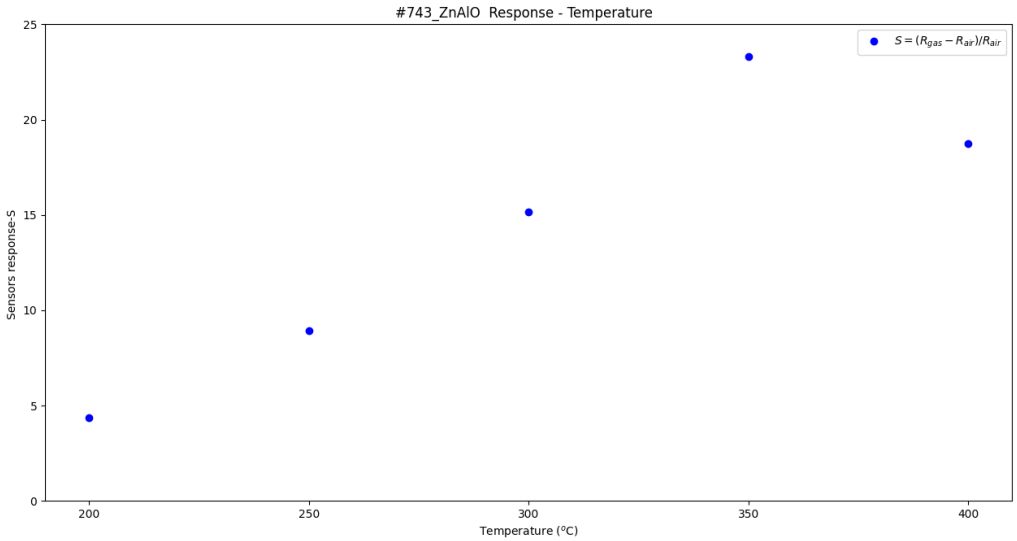

Figure 20: Sensor's response S for the different operating temperatures

In the operating temperature range of T=200°C - 400°C, it is clear that the sensor exhibits maximum response at T=350°C. Further increase or decrease of the temperature leads to lower response values.

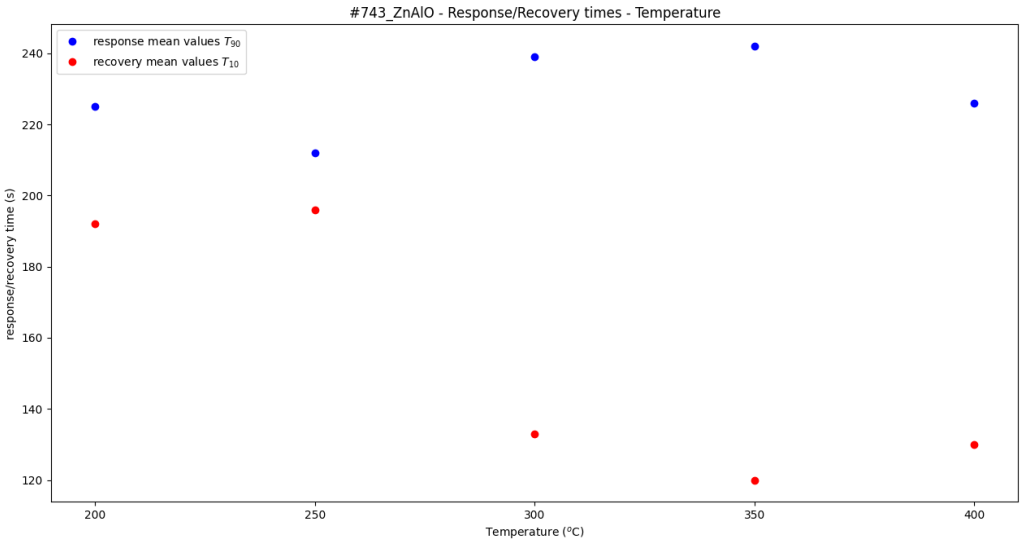

Figure 21: Response / recovery times for the different operating temperatures

The response time varied from 212 sec to 242 sec, while the recovery time exhibited a remarkable decrease from 192 sec to 120 sec at the optimal temperature.

At T=350°C, the sensors response to different hydrogen concentrations was examined in order to find the lower detection limit of hydrogen gas concentration that can be sensed. The dilution of the H_2 gas was achieved as hydrogen + synthetic air mixture.

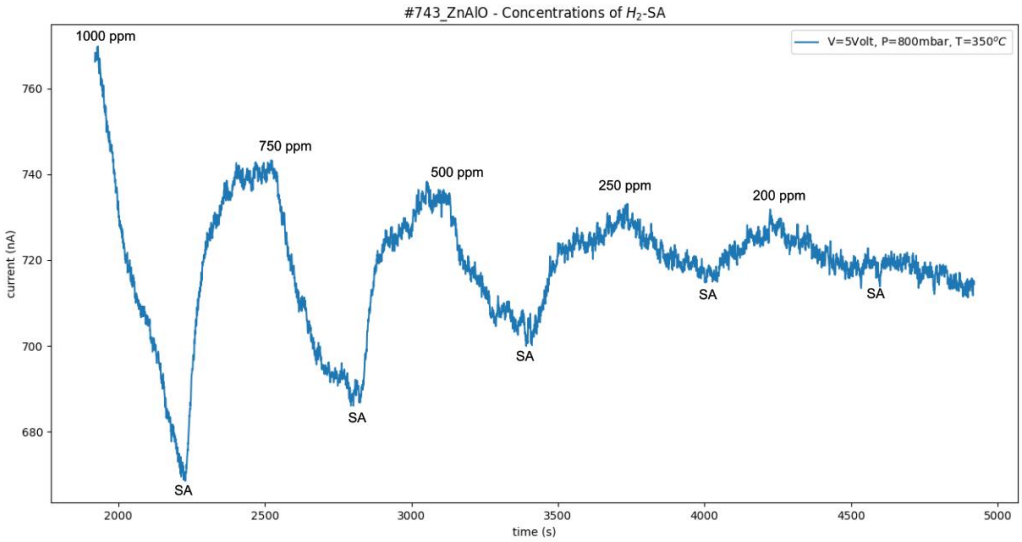

Figure 22: Current – time measurements at T=350°C in the presence of different hydrogen concentrations

H_2 concentrations	Sensitivity (%)	Response time T_{90} (sec)	Recovery time T_{10} (sec)
100% → 1000 ppm	15.19	253	122
75% → 750 ppm	8.11	165	192
50% → 500 ppm	5.4	140	236
25% → 250 ppm	2.43	238	157
20% → 200 ppm	2.38	115	134

Table 8: Sensitivity – Response of the sensor, response / recovery times towards different hydrogen concentrations

The response of the sensor takes its highest value at 1000 ppm hydrogen concentration. At lower hydrogen gas concentrations, we observe that the sensor finds difficulty in recovering to the initial state. Further decrease in the hydrogen concentration led to weakness in the sensing process.

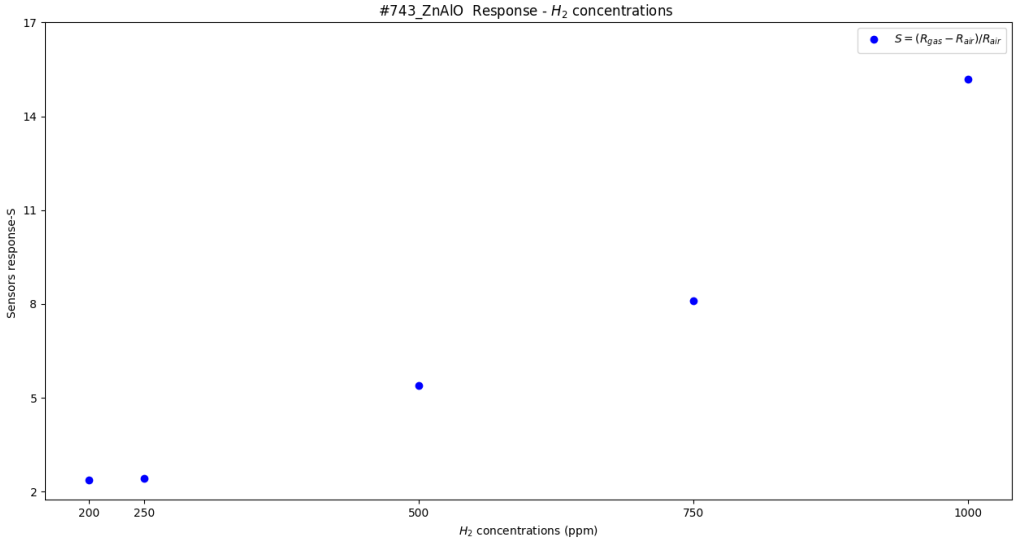

Figure 23: Sensor's response S for the different hydrogen gas concentrations

At low hydrogen concentration the response of the sensor exhibits linear dependence, while in total the response of the sensor follows exponential behavior.

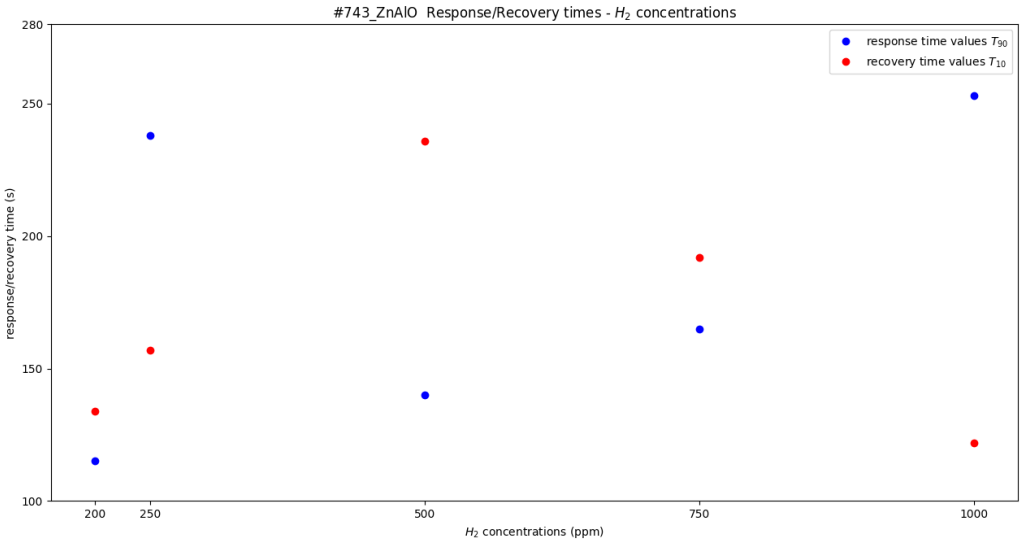

Figure 24: Response / recovery times for the different hydrogen concentrations

The response time varied from 115 sec to 253 sec at the maximum hydrogen concentration of 1000 ppm. The recovery time varies from 122 sec to 134 sec, exhibiting its maximum value for 500 ppm hydrogen concentration.

2.2 Methane sensing

The same experimental process was repeated in the case of methane gas. The applied bias was set to be V=5Volts. Then, synthetic air was inserted in the experimental chamber for 20 minutes to obtain a constant current baseline and finally the pressure was stabilized at 800 mbar. To examine the sensor's response to methane gas, pure methane was inserted into the chamber for 5 minutes, while afterwards synthetic air was inserted into the chamber for 5 minutes to examine the recovery of the sensor. The gas alteration was repeated 5 times (5 experimental cycles). Different operating temperatures were applied starting from RT to T=400° with an increasing step of 50°C.

In the analysis following, only the graph for the optimum operating temperature (T=400°C) that provides the best response of the sensor is exhibited. The rest of the graphs are included in the *Appendix A: #743_ZnAlO - Methane gas sensing*.

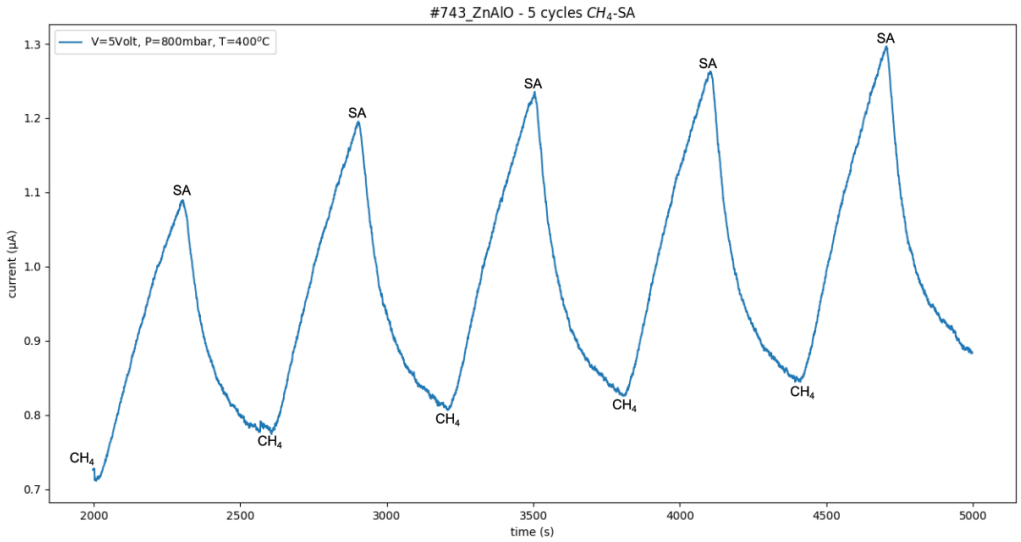

Figure 25: Current – time measurement at T=400°C in the presence of methane

At T=400°C the sensor exhibited its best response and satisfying recovery so we can calculate the response / recovery times and the response (S) of the sensor:

The response time was calculated at the 90% of each peak alteration and its mean value is:

$\overline{T_{90}} = \frac{T_{90}^{(1)}+T_{90}^{(2)}+T_{90}^{(3)}+T_{90}^{(4)}+T_{90}^{(5)}}{5} \Rightarrow \overline{T_{90}} = 268\,sec$, best response time: 261 sec

Similarly, $\overline{T_{10}} = \frac{T_{10}^{(1)}+T_{10}^{(2)}+T_{10}^{(3)}+T_{10}^{(4)}+T_{10}^{(5)}}{5} \Rightarrow \overline{T_{10}} = 185\,sec$, best recovery time: 163 sec

The sensor's response at each cycle was calculated following the equation (1) and the mean response value is equal to: $\bar{S} = 34.69$

Sensor: #743_ZnAlO			
Temperature (°C)	Sensitivity (%)	Response time T_{90} (best) [sec]	Recovery time T_{10} (best) [sec]
250	10.79	275 (254)	251 (232)
300	19.04	273 (266)	250 (231)
350	29.08	268 (257)	195 (162)
400	34.69	268 (261)	185 (163)

Table 9: Sensitivity – response, response / recovery times for the different operating temperatures

By using the data of Table 6, we can plot the response S of the sensor and the response / recovery times as function of the different operating temperatures:

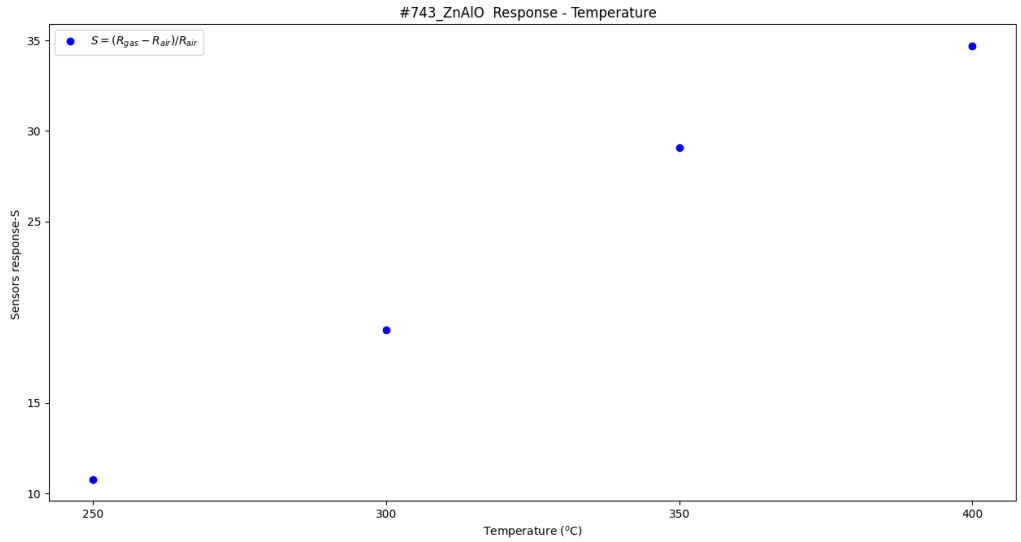

Figure 26: Sensor's response S for the different operating temperatures

It is clear that the response of the sensor exhibits linear increase as the temperature increases. At lower temperatures, the sensor exhibits response but no recovery. In particular, at T=150°C the response of the sensor was calculated to be S=6.25, while at T=200°C operating temperature the response was calculated to be S=9.51.

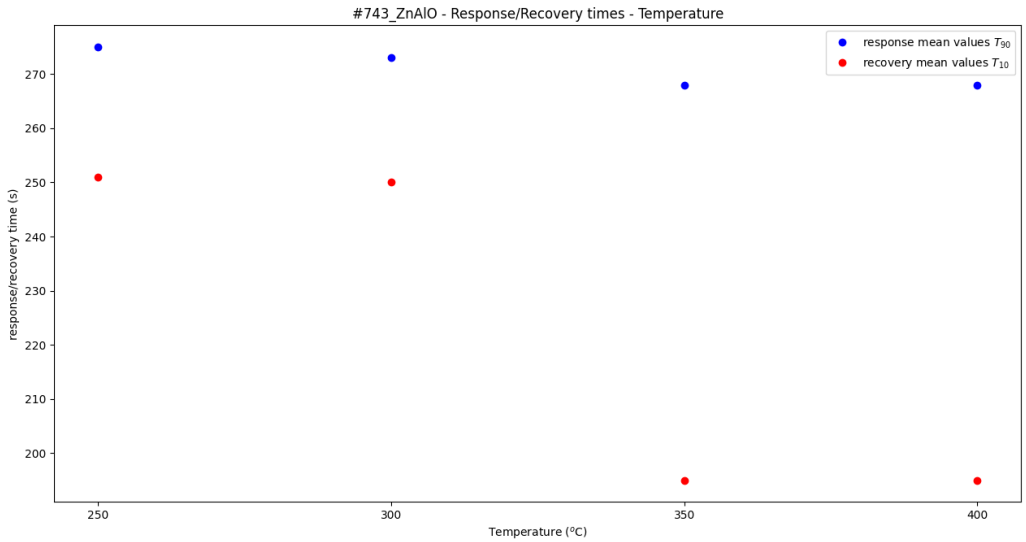

Figure 27: Response / recovery times for the different operating temperatures

The response time was quite stable, varying from 268 sec to 275 sec, while the recovery time of 185 sec at the optimal temperature, exhibits significant decrease in comparison to lower operating temperatures.

Furthermore, the response of the sensor was examined for different methane concentrations at T=400°C. The dilution in the pure methane gas was achieved by adding N_2 gas.

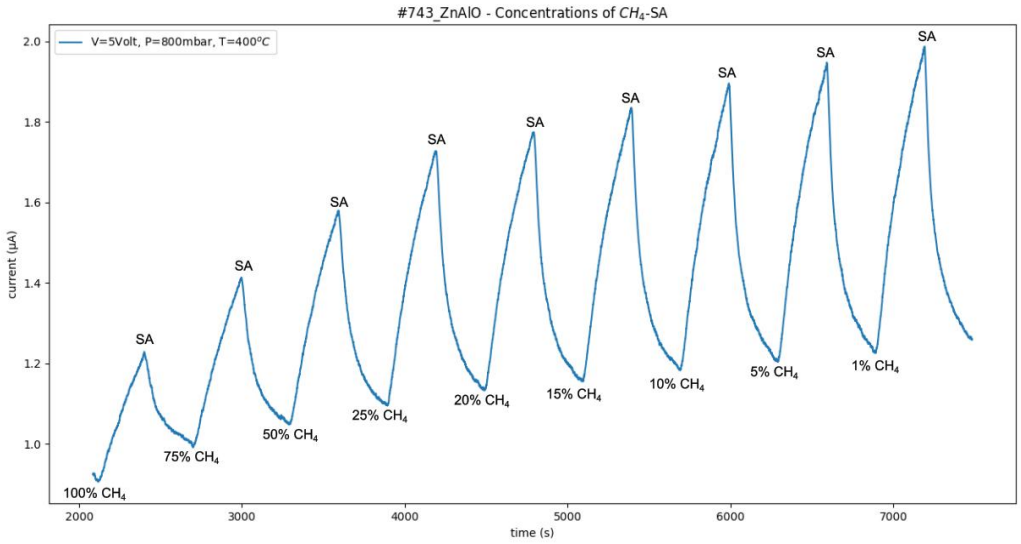

Figure 28: Current – time measurements at T=400°C in the presence of different methane concentrations

CH_4 concentrations	Sensitivity (%)	Response time T_{90} (sec)	Recovery time T_{10} (sec)
100%	25.74	279	263
75%	29.59	263	207
50%	33.58	265	186
25%	36.46	250	185
20%	36.13	249	159
15%	36.53	248	162
10%	37.01	227	191
5%	38.09	270	185
1%	37.56	254	114

Table 10: Sensitivity – response of the sensor, response / recovery times towards different methane concentrations

The pure 100% methane used in the experiments seems to lead the sensor in a saturation state because at lower methane concentrations the response of the sensor is higher. At methane concentrations between 1% and 25%, the response of the sensor remains constant. This methane concentration range is where it can be flammable, so this sensor is convenient for methane gas sensing.

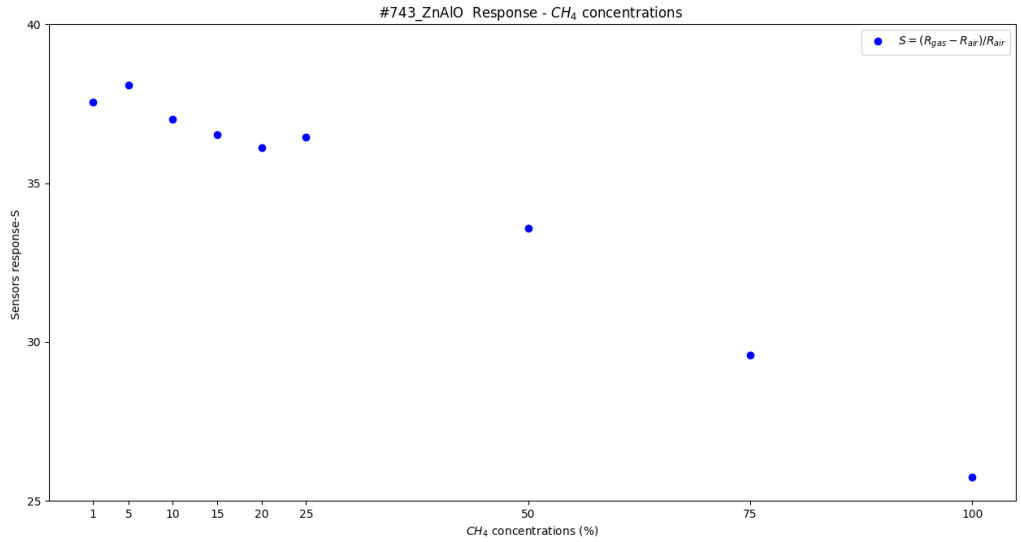

Figure 29: Sensor's response S for the different methane concentrations

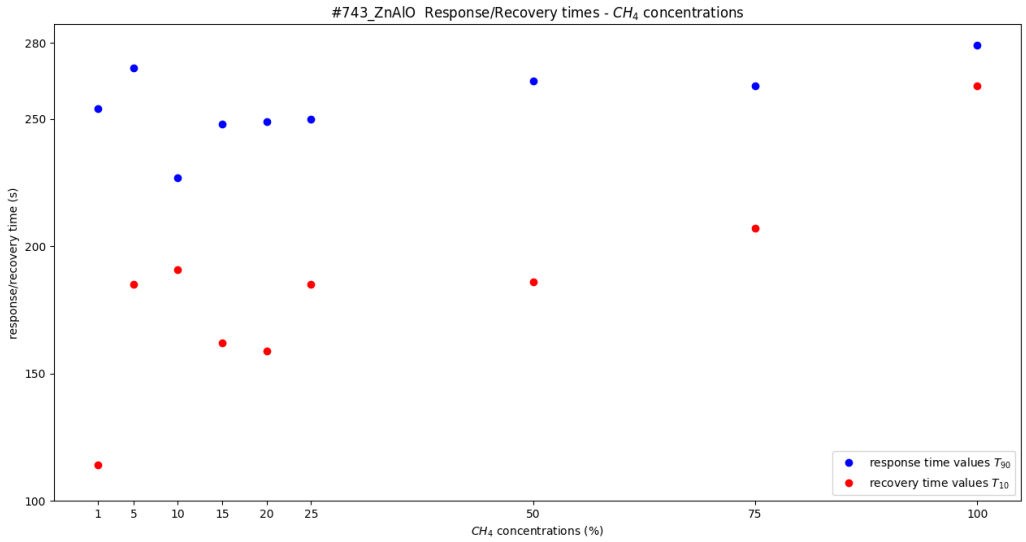

Figure 30: Response / recovery times for the different methane concentrations

The response time varies from 227 sec to 279 sec, while the response time varies from 114 sec to 263 sec, exhibiting its maximum value at pure methane gas and its minimum value at its lowest methane gas concentration tested.

3. Characterization of #745_ZnAlO – Structural, morphological and optical properties

In order to determine the structural, morphological and optical properties of the #745_ZnAlO sensing films, XRD, SEM, AFM, UV-vis spectroscopy techniques were utilized.

3.1 X-Ray diffraction analysis

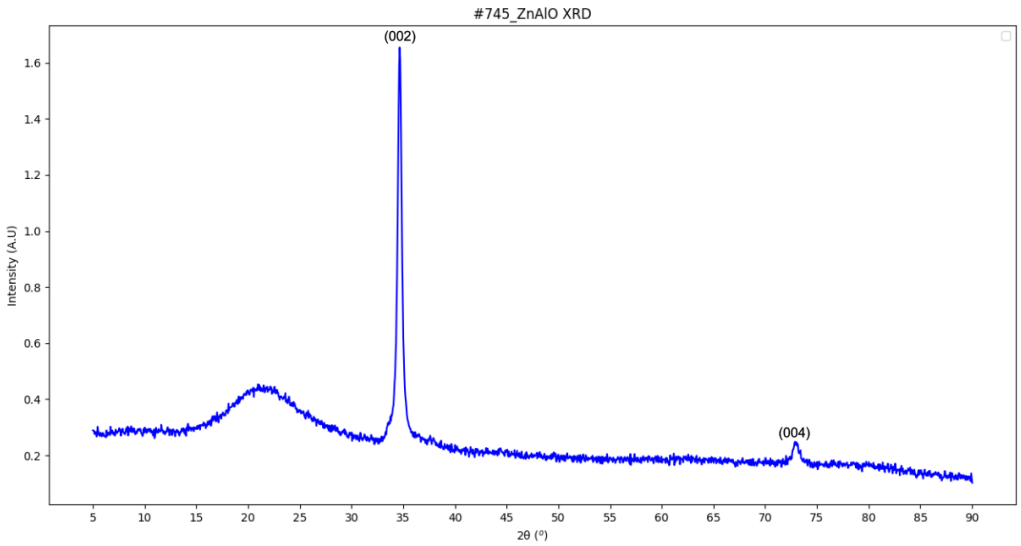

Figure 31: XRD pattern of #745_ZnAlO sensing film

Again, the XRD spectra were measured in the range of 5° - 90°, exhibiting the main peak of ZnAlO at $2\theta_1$=34.66° and a secondary peak at $2\theta_2$=72.98°.

The main peak θ_1 corresponds to the crystal plane with Miller indices (hkl)=(002), while the secondary peak θ_2 corresponds to the crystal plane with Miller indices (hkl)=(004).

Applying Gausian fitting around the main peak, we get the full width at half maximum (FWHM) of the peak, which is equal to $\beta=8.879*10^{-3}$ rad.

The crystallite size and the interplanar spacing of the sensing material can be calculated by using equations (13) and (14):

$$(13):\ D\ (nm) = \frac{K*\lambda}{\beta*cos\theta} \Rightarrow D = 16.358\ nm$$

$$(14):\ d_{hkl}(\text{Å}) = \frac{n*\lambda}{2*sin\theta} \Rightarrow d_{002} = 2.586\ \text{Å}$$

After calculating the interplanar spacing, the lattice parameters a, c for the hexagonal wurtzite ZnAlO structure can be calculated by using equation (15):

$$(15):\ \frac{1}{d^2_{(hkl)}} = \frac{4}{3} * \left(\frac{h^2 + h*k + k^2}{a^2}\right) + \frac{l^2}{c^2} \Rightarrow c^2 = 4 * d^2_{002} \Rightarrow c = 5.172\ \text{Å}$$

Making the assumption that the crystal structure remains the ideal wurtzite and there is low local symmetry distortion for the aluminum doped film, then a close calculation for the lattice parameter a can be made, resulting in a=3.167Å.

Finally, the lattice strain parameter ε_w can be calculated through the equation (16):

$$(16):\ \varepsilon_w = \frac{\beta * cot\theta}{4} \Rightarrow \varepsilon_w = 7.11 * 10^{-3}$$

The same analysis was held for the secondary peak, with the results quoted in the following summarizing table:

Peak 2θ	Crystallite size D (nm)	Interplanar spacing d_{hkl} (Å)	Lattice parameter c (Å)	Lattice parameter a (Å)	Lattice strain ε_w
$2\theta_1$=34.66°	16.358	(hkl)=(002) 2.586	5.172	3.167	$7.11*10^{-3}$
$2\theta_2$=72.98°	12.497	(hkl)=(004) 1.295	5.181	3.173	$4.66*10^{-3}$

Table 11: Structural parameters of #745_ZnAlO thin film

As well as the #743 developed sensor, the #745 displays its peaks in the same angles, corresponding to (002) and (004) crystalline planes. The highest peak linked to the (002) crystalline plane indicating that in the sample #745_ZnAlO, the crystal has strong preference in the c – axis orientation perpendicular to the substrate.

3.2 SEM

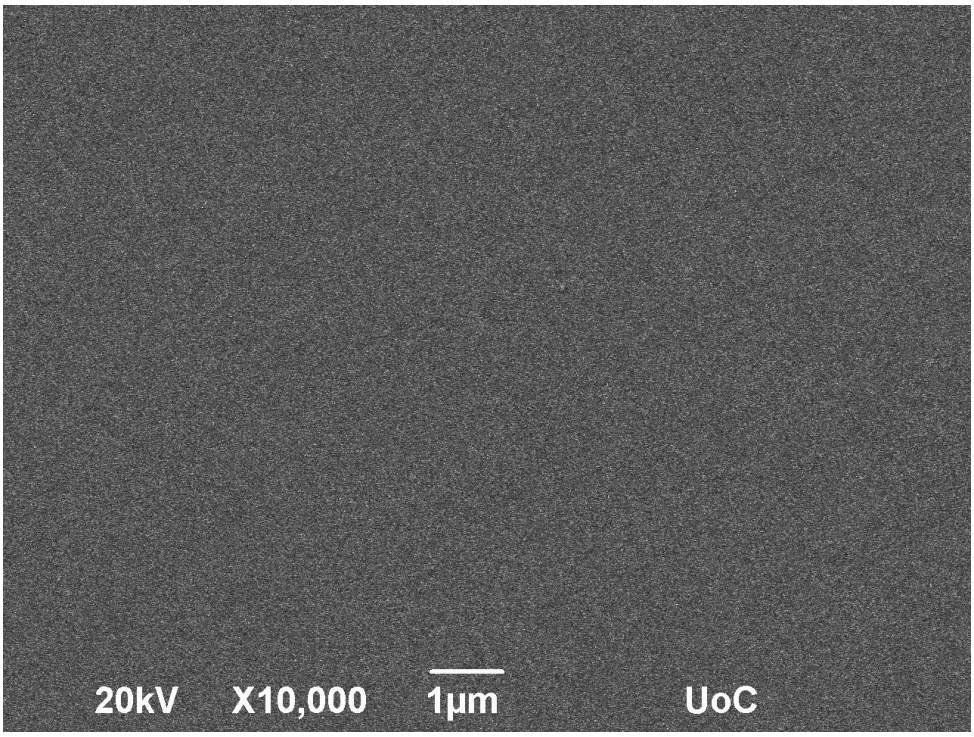

Figure 32: SEM micrograph of the #745_ZnAlO film

The film shows good uniformity and dense surface without visible holes or faulty zones on the film surface.

3.3 AFM

The roughness of the #745_ZnAlO sensing film was calculated through an AFM measurement. The average roughness value was found to be R_a=2.855nm, while the root mean square value was found to be R_s=3.848nm.

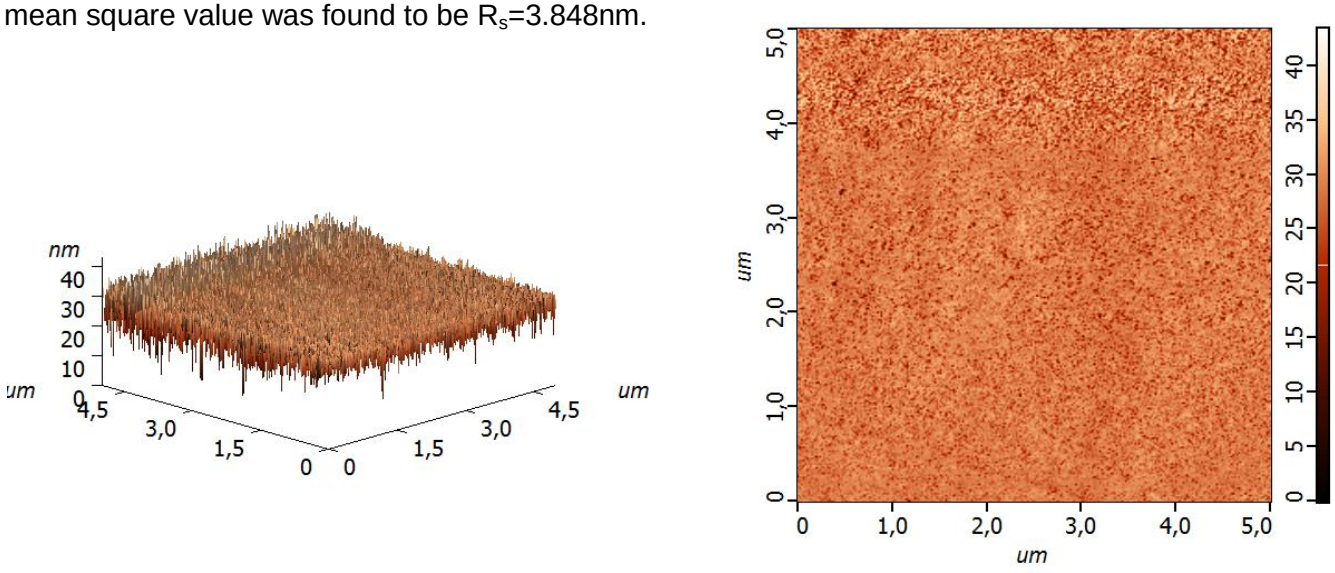

Figure 33: 3D and 2D AFM micrographs (4.5µm x 4.5µm) of the #745_ZnAlO film

3.4 UV-vis spectroscopy

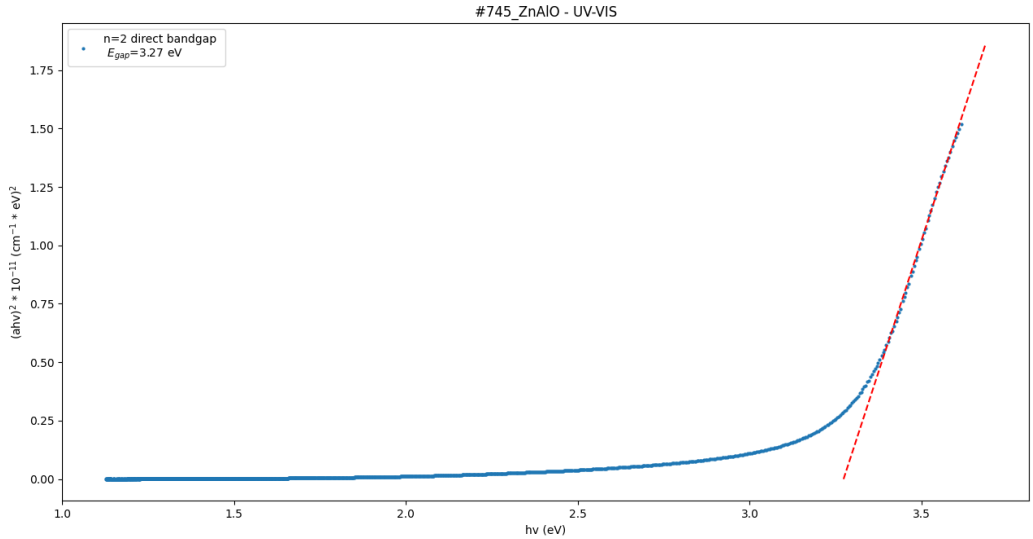

Figure 34: Tauc plot of #745_ZnAlO for the direct energy band gap case (n=2)

The energy gap was calculated from the linear part of the Tauc plot. It appears to be E_g= 3.27 eV for the direct band gap case.

3.5 I-V characteristics

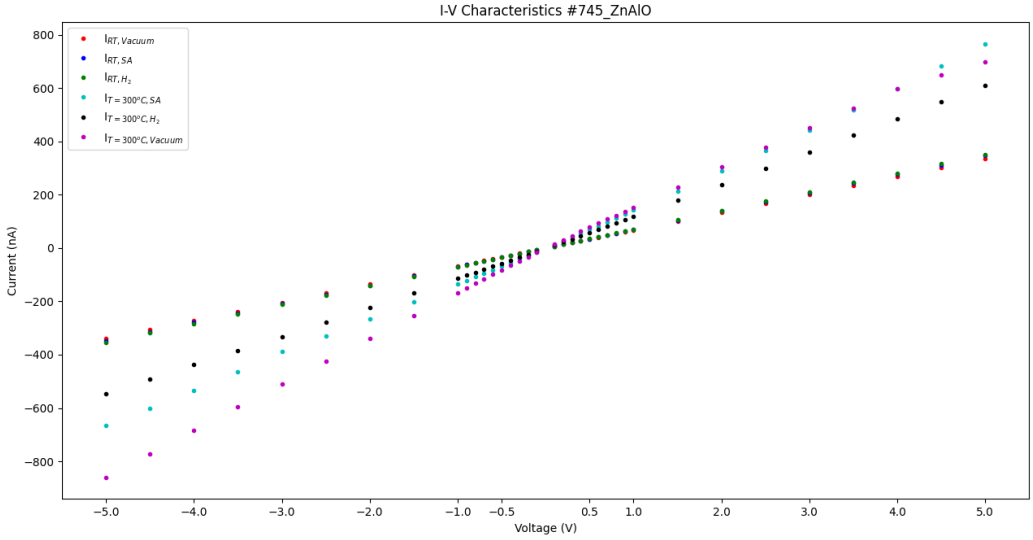

Figure 35: I-V measurements of #745_ZnAlO sensor operating in room temperature (RT) or at T=300°C under vacuum either in the presence of synthetic air or 1000ppm of hydrogen.

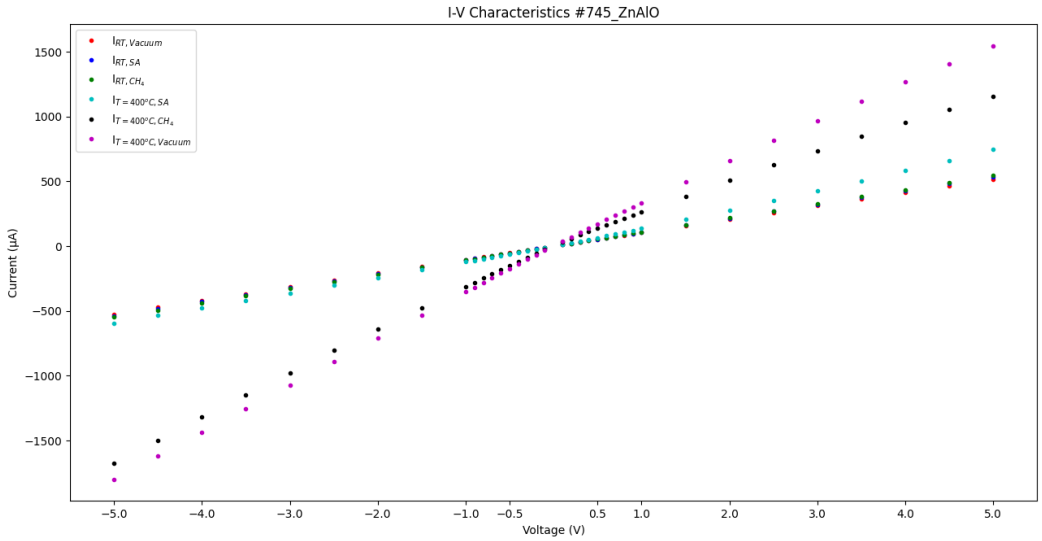

Figure 36: I-V measurements of #745_ZnAlO sensor operating in room temperature (RT) or at T=400°C under vacuum either in the presence of synthetic air or 100% methane.

For both hydrogen and methane gases, we observe linearity in the I-V characteristics around the applied bias of V=1Volt. That linearity indicates that we have an Ohmic junction.

4. #745_ZnAlO sensing results

#	Material	Thickness (d)	Sputtering deposition time	Ar	O_2	$I_{sputtering}$	$T_{substrate}$
745	ZnAlO (Heraeus-Metallic ZnAl2%)	68 nm	3 min	40% (6.4 sccm)	60% (9.6 sccm)	0.45A	RT

Table 12: Sputtering parameters used for #745_ZnAlO development

4.1 Hydrogen sensing

The developed sensor was tested against H_2 gas sensing. The applied bias was set to be V=1Volt. Then, synthetic air was inserted in the experimental chamber for 20 minutes to obtain a constant current baseline and finally the pressure was stabilized in 800 mbar. To examine the response of the sensor to hydrogen gas, 1000ppm of hydrogen gas were inserted into the chamber for 5 minutes, while afterwards synthetic air was inserted into the chamber for 5 minutes to examine the recovery of the sensor. This gas alteration was repeated 5 times (5 experimental cycles - repeatability). Also, different operating temperatures were applied starting from RT to T=400°C with an increasing step of 50°C.

In the analysis following, only the graph for the optimum operating temperature (T=300°C) that provides the best response of the sensor is exhibited. The rest of the graphs are included in the Appendix A: #745_ZnAlO - Hydrogen gas sensing.

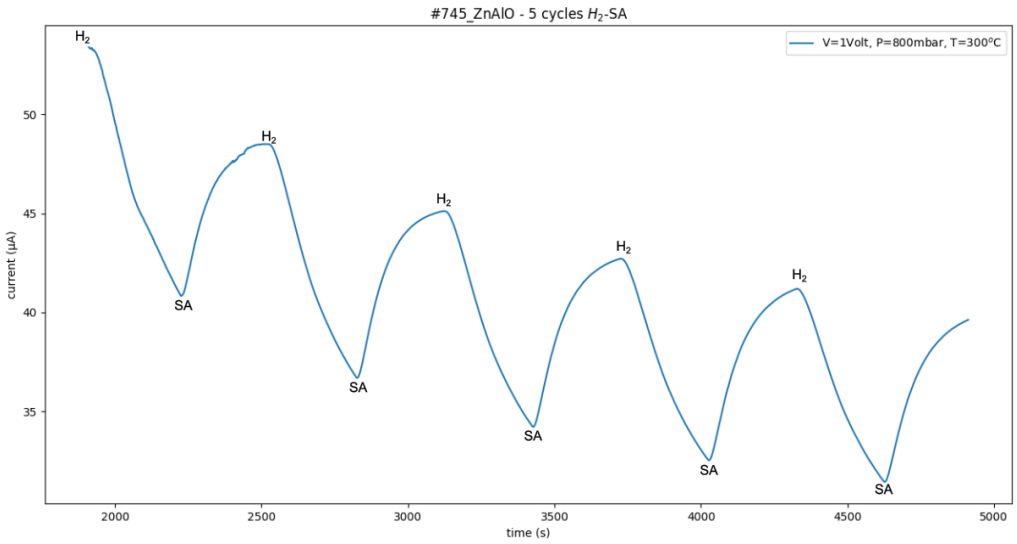

Figure 37: Current – time measurement at T=300°C in the presence of hydrogen

At T=300°C the sensor exhibited its best response and satisfying recovery so we can calculate the response / recovery times and the response (S) of the sensor:

The response time was calculated at the 90% of each peak alteration and its mean value is:

$\overline{T_{90}} = \frac{T_{90}^{(1)}+T_{90}^{(2)}+T_{90}^{(3)}+T_{90}^{(4)}+T_{90}^{(5)}}{5} \Rightarrow \overline{T_{90}} = 263\ sec$, best response time: 252 sec

Similarly, $\overline{T_{10}} = \frac{T_{10}^{(1)}+T_{10}^{(2)}+T_{10}^{(3)}+T_{10}^{(4)}+T_{10}^{(5)}}{5} \Rightarrow \overline{T_{10}} = 212\ sec$, best recovery time: 195 sec

The sensor's response at each cycle was calculated following equation (1) and the mean response value is equal to: $\bar{S} = 31.34$

Sensor: #745_ZnAlO			
Temperature (°C)	Sensitivity (%)	Response time T_{90} (best) [sec]	Recovery time T_{10} (best) [sec]
150	0.44	255 (230)	265 (239)
200	0.22	277 (267)	289 (273)
250	1.29	278 (265)	263 (250)
300	31.34	263 (252)	212 (195)
350	18.91	256 (246)	238 (227)
400	27.26	243 (229)	201 (193)

Table 13: Sensitivity – response, response / recovery times of the sensor for different operating temperature.

By using the data of table 10, we can plot the response S of the sensor and the response / recovery times as function of the different operating temperatures:

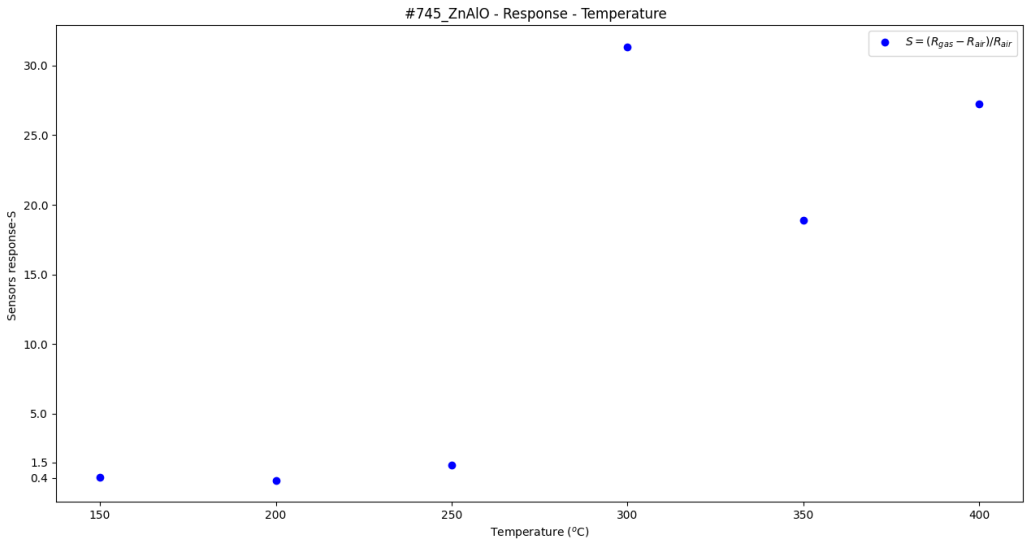

Figure 38: Sensor's response S for the different operating temperatures

In the operating temperature range of T=150°C - 400°C, it is clear that the sensor appears to have its maximum response at T=300°C. Further increase in operating temperature results

in lower response values, while for operating temperatures lower than T=250°C the sensor appears to struggle in hydrogen gas sensing.

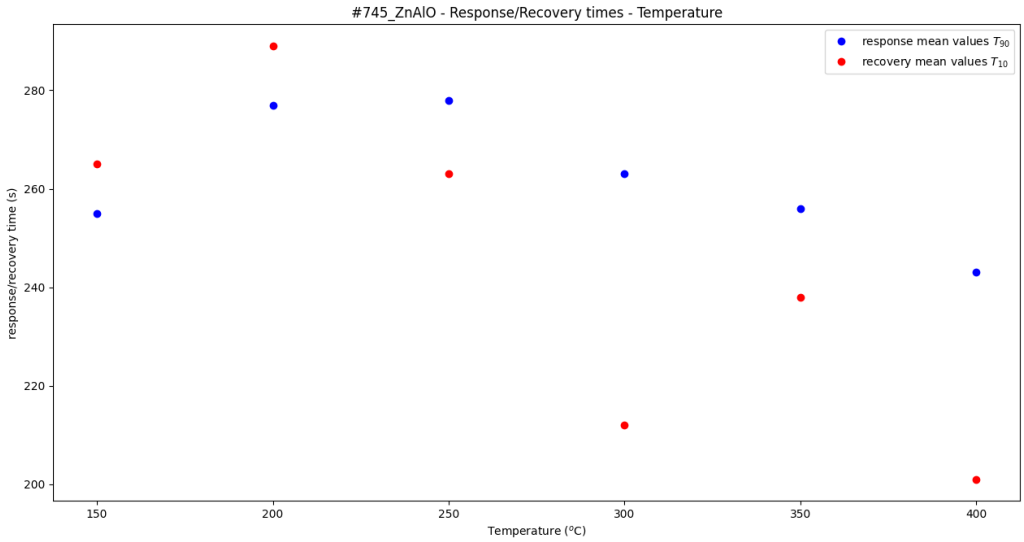

Figure 39: Response / recovery times of the sensor for the different operating temperatures

The response time varied from 243 sec to 278 sec, while the recovery time varied from 201 sec to 289 sec. The best response and recovery times were observed for the highest applied temperature (T=400°C).

At T=300°C, the sensor's response to different hydrogen concentrations was examined in order to find the lower detection limit of hydrogen gas concentration that can be sensed. The dilution of the H_2 gas was achieved as hydrogen + synthetic air mixture.

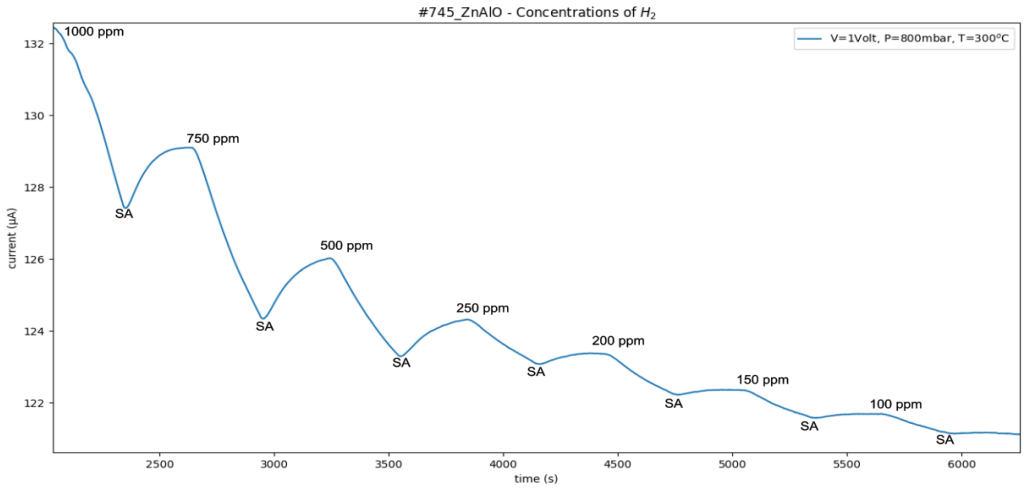

Figure 40: Current - time measurements at T=300°C in the presence of hydrogen gas concentrations

H_2 concentrations	Sensitivity (%)	Response time T_{90} (sec)	Recovery time T_{10} (sec)
100% → 1000 ppm	3.96	280	175
75% → 750 ppm	3.79	264	240
50% → 500 ppm	2.23	246	275
25% → 250 ppm	1.02	257	151
20% → 200 ppm	0.89	258	153
15% → 150 ppm	0.65	255	280
10% → 100 ppm	0.46	253	273

Table 14: Sensitivity – response of the sensor, response / recovery times towards different hydrogen concentrations

The response of the sensor takes its highest value at 1000 ppm hydrogen concentration. At lower hydrogen gas concentrations, we observe that the sensor finds difficulty in response and recovering to the initial state.

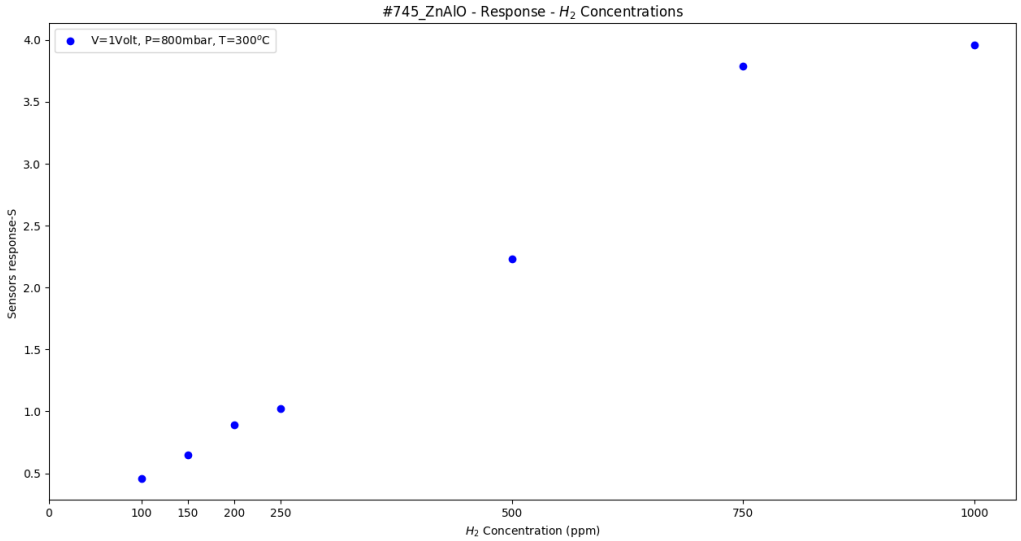

Figure 41: Sensor's response S for the different hydrogen gas concentrations

At low hydrogen concentration the response of the sensor exhibits linear dependence. After applying linear fitting we can find the detection limit (intersection of the fitting line with x-axis), which is found to be 4 ppm.

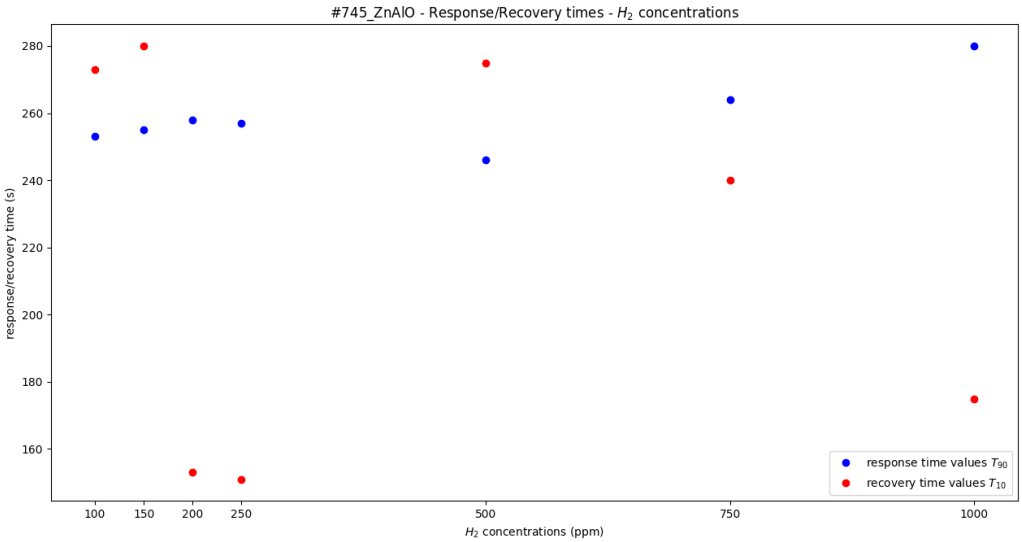

Figure 42: Response / recovery times for the different hydrogen gas concentrations

The response time varied from 246 sec to 280 sec, while the recovery time varied from 151 sec to 280 sec. At 1000 ppm hydrogen concentration the response time has its maximum value.

4.2 Methane sensing

The same experimental process was repeated in the case of methane gas. The applied bias was set to be V=1Volt. Then, synthetic air was inserted in the experimental chamber for 20 minutes to obtain a constant current baseline and finally the pressure was stabilized in 800 mbar. To examine the response of the sensor to methane gas, pure methane was inserted into the chamber for 5 minutes, while afterwards synthetic air was inserted into the chamber for 5 minutes to examine the recovery of the sensor. The gas alteration was repeated for 5 times (5 experimental cycles - repeatability) and different operating temperatures were applied starting from RT to T=400°C with an increasing step of 50°C.

In the analysis following, only the graph for the optimal operating temperature (T=400°C) that provides the best response of the sensor is exhibited. The rest of the graphs are included in the Appendix A: #745_ZnAlO - Methane gas sensing.

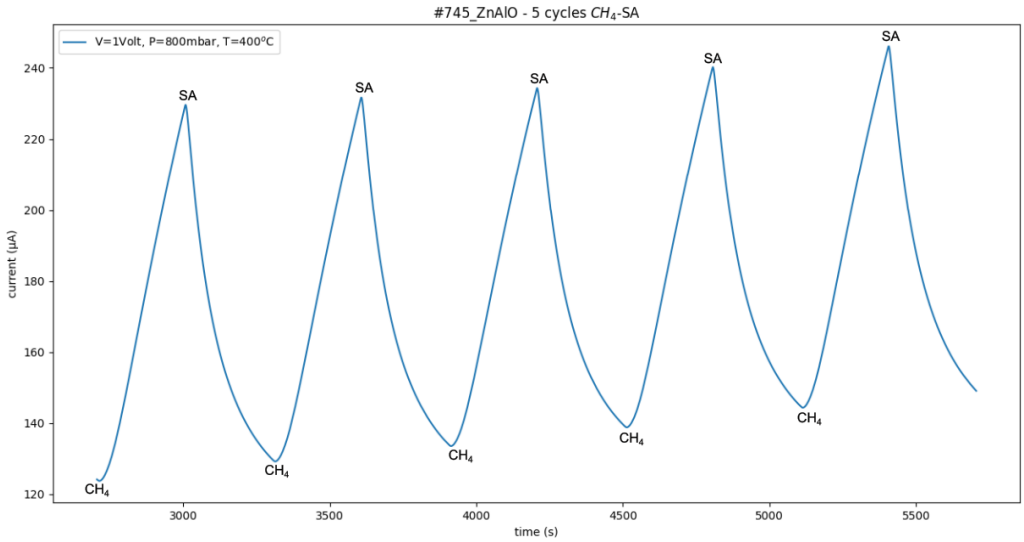

Figure 43: Current – time measurements at T=400°C in the presence of methane

At T=400°C the sensor exhibited its best response and full recovery so we can calculate the response / recovery times and the response (S) of the sensor:

The response time was calculated at the 90% of each peak alteration and its mean value is:

$\overline{T_{90}} = \frac{T_{90}^{(1)}+T_{90}^{(2)}+T_{90}^{(3)}+T_{90}^{(4)}+T_{90}^{(5)}}{5} \Rightarrow \overline{T_{90}} = 274\ sec$, best response time: 258 sec

Similarly, $\overline{T_{10}} = \frac{T_{10}^{(1)}+T_{10}^{(2)}+T_{10}^{(3)}+T_{10}^{(4)}+T_{10}^{(5)}}{5} \Rightarrow \overline{T_{10}} = 212\ sec$, best recovery time: 205 sec

The sensor's response at each cycle was calculated following the equation (1) and the mean response value is equal to: $\bar{S} = 43.23$

Sensor: #745_ZnAlO

Temperature (°C)	Sensitivity (%)	Response time T_{90} (best) [sec]	Recovery time T_{10} (best) [sec]
250	4.03	279 (270)	256 (240)
300	10.18	244 (232)	267 (251)
350	23.95	271 (264)	248 (238)
400	43.23	274 (258)	212 (205)

Table 15: Sensitivity – response, response / recovery times for the different operating temperatures

By using the data of Table 12, we can plot the response S of the sensor and the response / recovery times as function of the different operating temperatures:

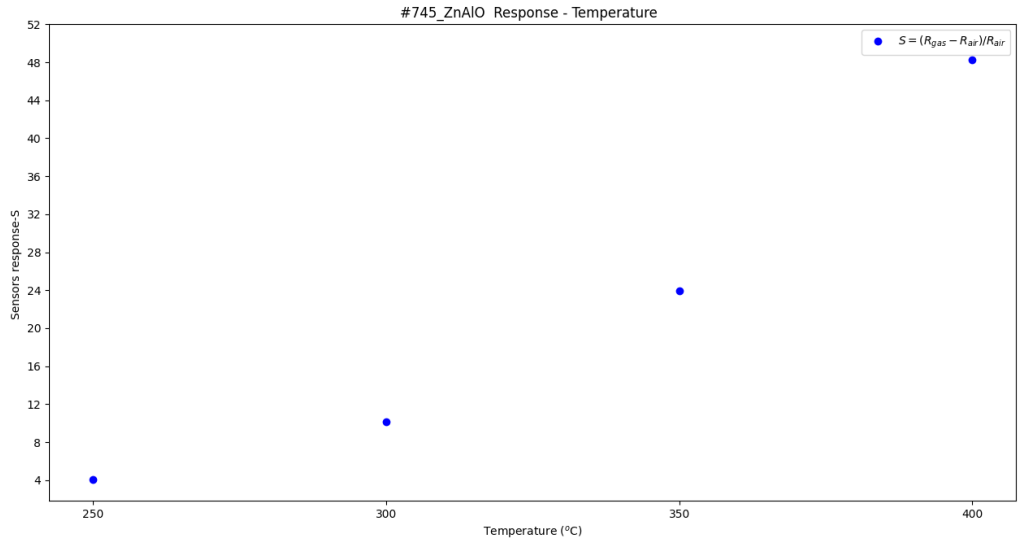

Figure 44: Sensor's response S for the different operating temperatures

In this case, the response of the sensor seems to exhibit an exponential increase as the operating temperature increases. At lower temperatures, the sensor does not exhibit response at all.

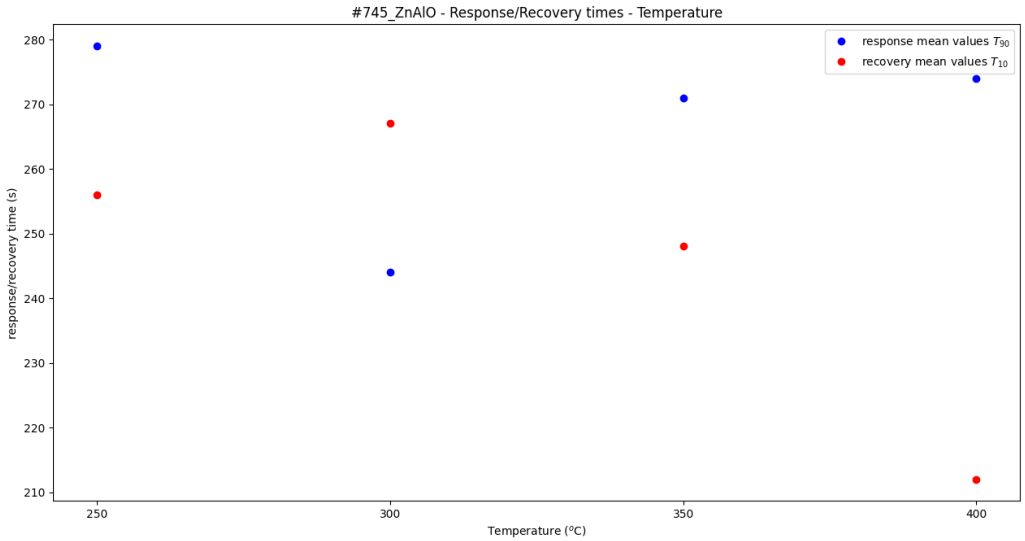

Figure 45: Response / recovery times of the sensor for the different operating temperatures

The response time values are quite slow, varying from 244 sec to 279 sec, while in the recovery process the sensor seems to perform faster varying from 212 sec to 267 sec. At the optimal operating temperature, the sensor has the fastest response time.

Furthermore, the response of the sensor was examined for different methane concentration at T=400°C. The dilution in the pure methane gas was achieved by adding N_2 gas.

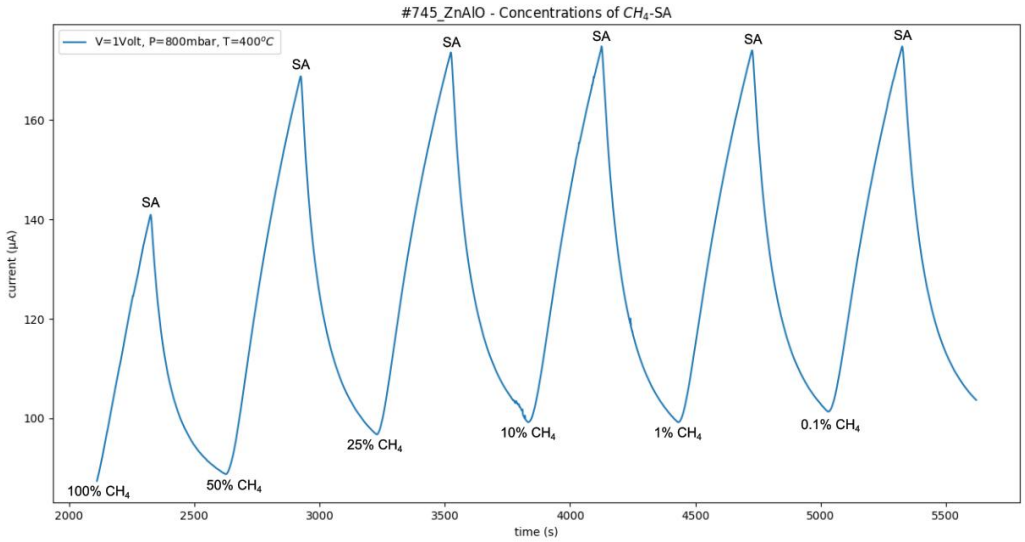

. **Figure 46:** Current – time measurements at T=400°C in the presence of different methane concentrations

CH_4 concentrations	Sensitivity (%)	Response time T_{90} (sec)	Recovery time T_{10} (sec)
100%	38.08	279	194
50%	43.38	272	199
25%	44.10	267	206
10%	42.99	266	202
1%	42.56	274	201
0.1%	41.40	269	204

Table 16: Sensitivity – response of the sensor, response / recovery for different methane concentrations

The pure 100% methane gas used in the repeatability experiments seems to lead the sensor in a saturation state, because at lower methane concentrations the response of the sensor is higher. At low methane concentrations the response of the sensor is higher than 40%. This sensor can be used for methane gas sensing because of his ability to react even at low methane concentrations.

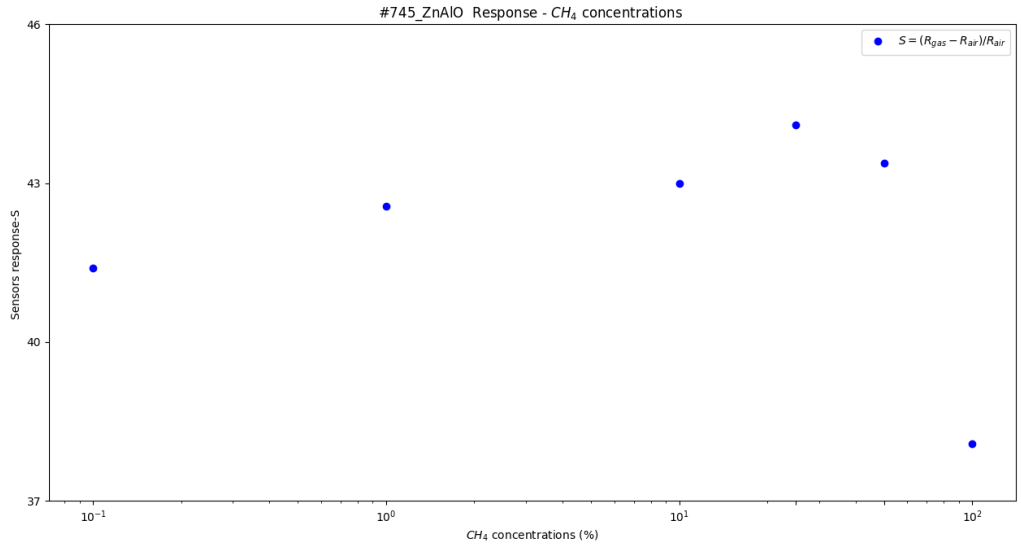

Figure 47: Sensor's response for the different methane gas concentrations

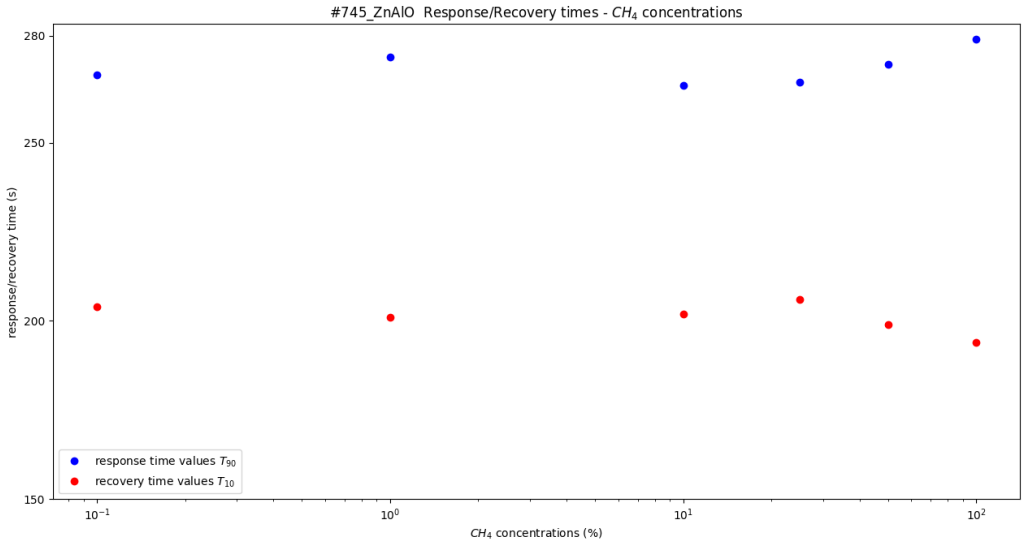

Figure 48: Response / recovery times of the sensor for the different methane concentrations

From the diagram above, we can see that both response and recovery times remain in the same values without any dependence on methane gas concentration.

b) $ZnAl_5O_x$ gas sensing results

5. Characterization of #532_$ZnAl_5O_x$ – Structural, morphological and optical properties

The structural, morphological and optical properties of #532_$ZnAl_5O_x$ sensing films were examined by using the XRD, SEM, AFM and UV-vis spectroscopy techniques.

5.1 X-Ray Diffraction analysis

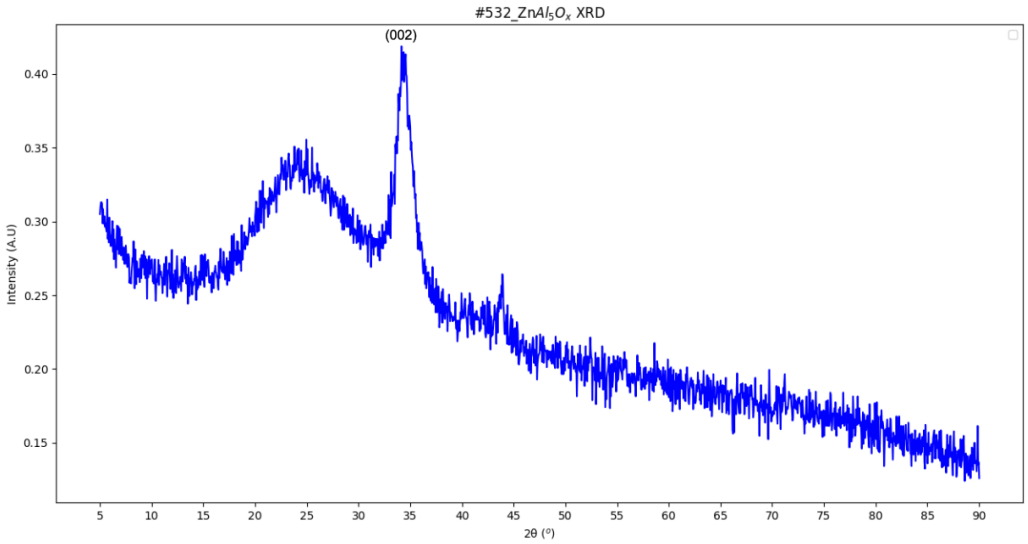

Figure 49: XRD pattern of #532_$ZnAl_5O_x$ sensing film

The XRD spectra were measured in the range of 5° - 90°, exhibiting its main peak at $2\theta_1$=34.36° corresponding to the crystal plane with Miller indices (hkl)=(002).

Applying Gaussian fitting around the main peak we can obtain the full width at half maximum (FWHM) of the peak, which is β=0.0266 rad.

Then, the crystallite size and the interplanar spacing of the sensing material can be calculated by using equations (13) and (14):

$$(13):\ D\ (nm) = \frac{K*\lambda}{\beta*cos\theta} \Rightarrow D = 5.456\ nm$$

$$(14):\ d_{hkl}(\text{Å}) = \frac{n*\lambda}{2*sin\theta} \Rightarrow d_{002} = 2.608\ \text{Å}$$

After calculating the interplanar spacing, the lattice parameters a,c for the hexagonal wurtzite $ZnAl_5O_x$ structure can be calculated by using the equation (15):

$$(15):\ \frac{1}{d^2_{(hkl)}} = \frac{4}{3} * \left(\frac{h^2 + h * k + k^2}{a^2}\right) + \frac{l^2}{c^2} \Rightarrow c^2 = 4 * d^2_{002} \Rightarrow c = 5.216\ \text{Å}$$

Making the assumption that the crystal structure remains the ideal wurtzite and there is low local symmetry distortion for the aluminum doped film, then a close calculation for the lattice parameter a can be made, resulting in a=3.194Å.

Finally, the lattice strain parameter ε_w can be calculated through the equation (16):

$$(16):\ \varepsilon_w = \frac{\beta * cot\theta}{4} \Rightarrow \varepsilon_w = 2.15 * 10^{-2}$$

A summarizing table for the obtained results following:

Peak 2θ	Crystallite size D (nm)	Interplanar spacing d_{hkl} (Å)	Lattice parameter c (Å)	Lattice parameter a (Å)	Lattice strain ε_w
$2\theta_1$=34.36°	5.456	(hkl)=(002) 2.608	5.216	3.194	$2.15*10^{-2}$

Table 17: Structural parameters of #532_$ZnAl_5O_x$

The #532 developed sensor exhibits its highest peak corresponding to the (002) crystalline plane, indicating that the crystal has strong preference in the c – axis orientation perpendicular to the substrate.

5.2 SEM

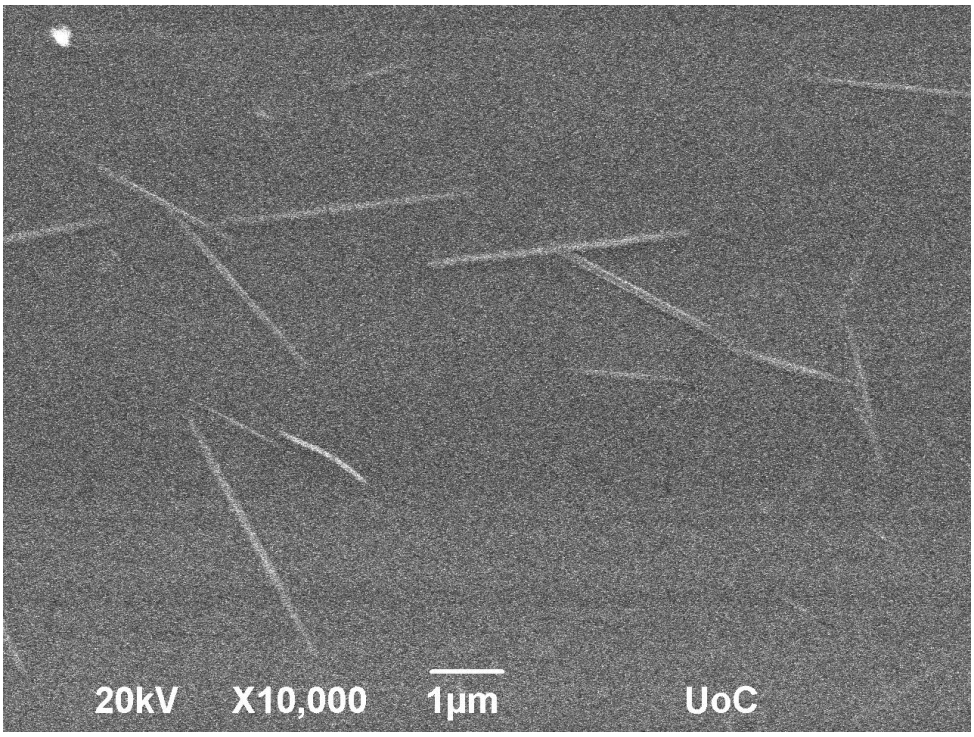

Figure 50: SEM micrograph of #532_$ZnAl_5O_x$ film

The film shows good uniformity and dense surface without visible holes on the film surface, but exhibits needle like morphology probably attributed to scratches on the film surface during the handling of the sample.

5.3 AFM

The roughness of the #532_$ZnAl_5O_x$ sensing film was calculated through an AFM measurement. The average roughness value was found to be R_a=0.637nm, while the root mean square value was found to be R_s=1.436nm.

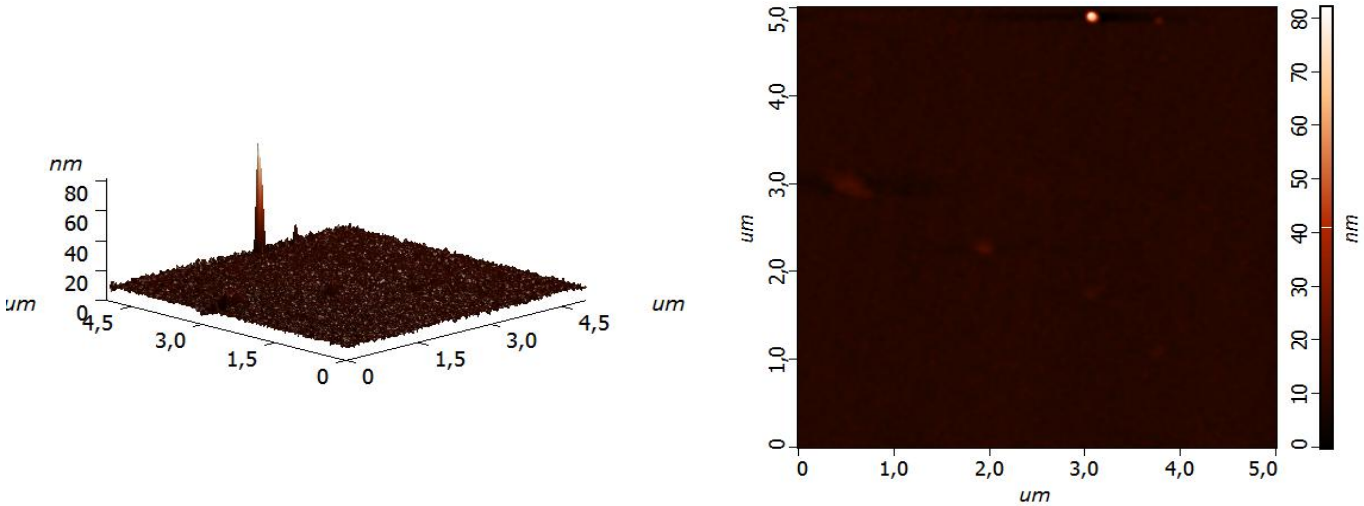

Figure 51: 3D and 2D AFM micrographs (4.5μm x 4.5μm) of the #532_$ZnAl_5O_x$ film

5.4 UV-vis spectroscopy

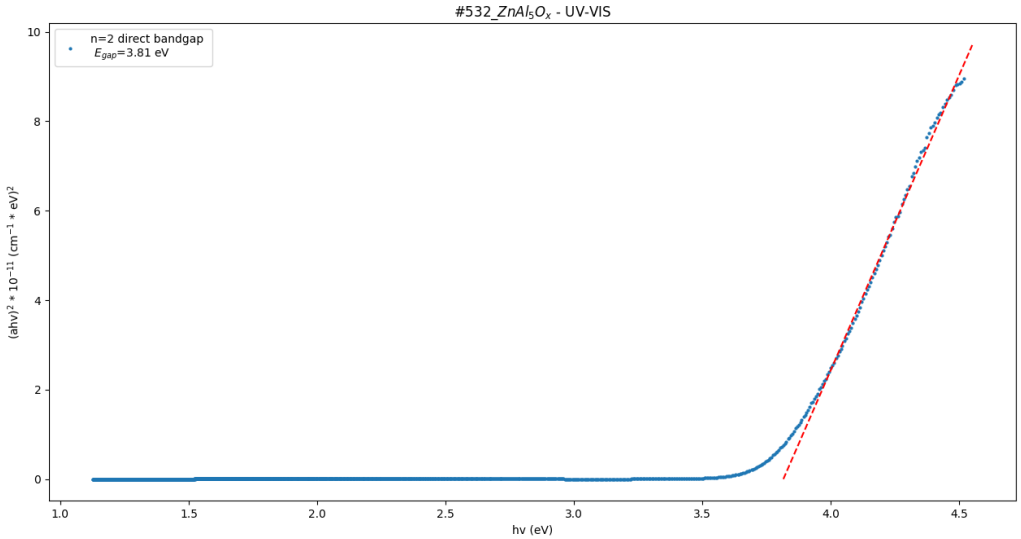

Figure 52: Tauc plot of #532_$ZnAl_5O_x$ for the direct energy band gap case (n=2)

The energy gap was calculated from the linear part of Tauc plot. It appears to be E_g=3.81 eV for the direct band gap case. The obtained energy gap value seems to be overestimated in comparison to the values mentioned in the bibliography.

5.5 I-V characteristics

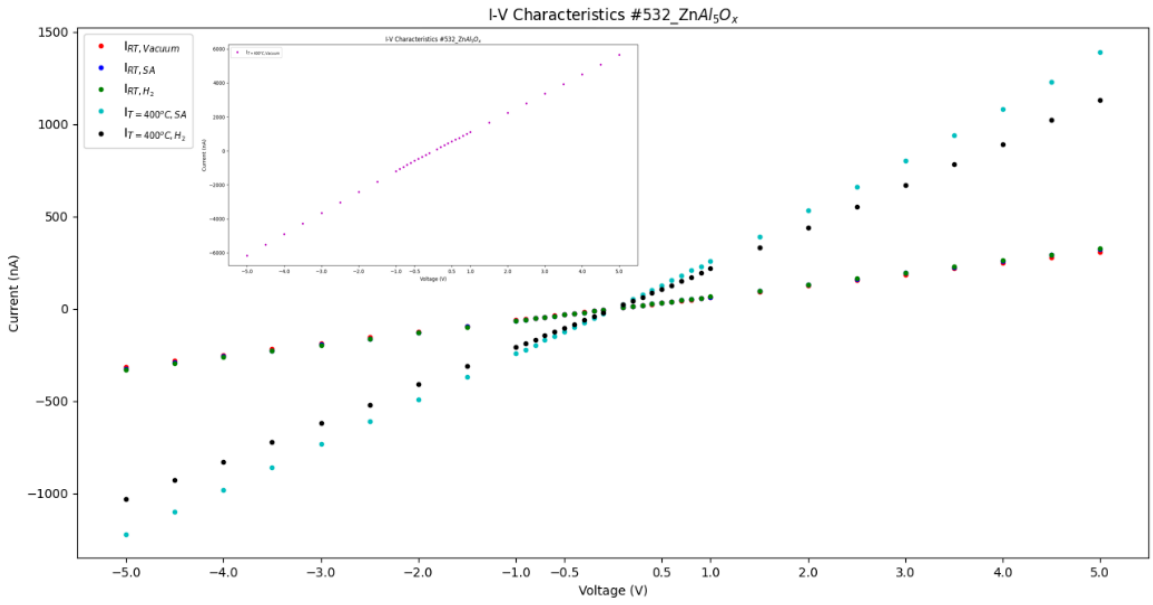

Figure 53: I-V measurements of #532_$ZnAl_5O_x$ sensor oparating in room temperature (RT) or at T=400°C under vacuum either in the presense of synthetic air or 1000 ppm hydrogen gas. In the inset, the I-V at T=400°C under vacuum is depicted.

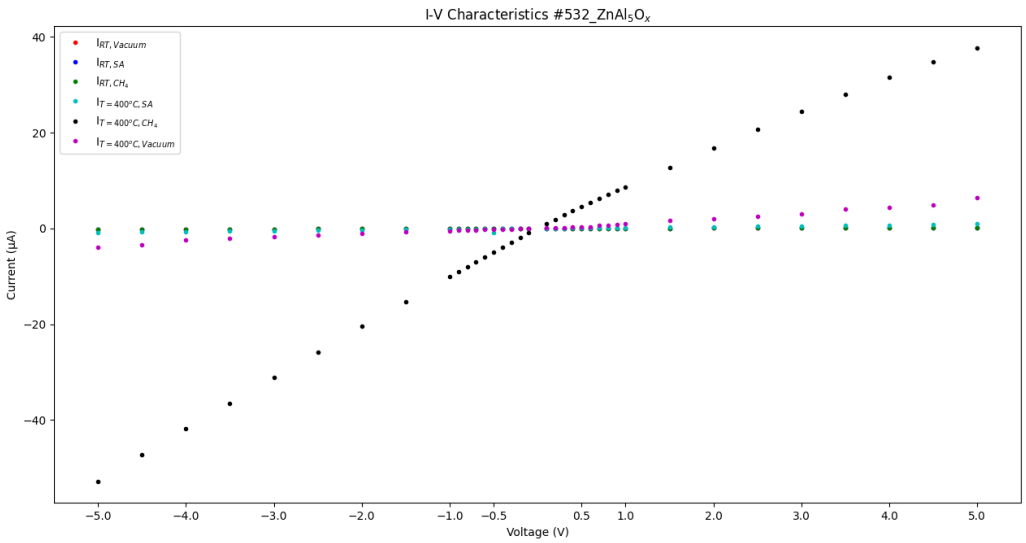

Figure 54: I-V measurements of #532_ $ZnAl_5O_x$ operating in room temperature (RT) or at T=400°C under vacumm either in the presense of synthetic air or 100% methane gas

In both hydrogen and methane gases, we observe linearity in the I-V characteristics around the applied bias of V=1Volt. That linearity indicates that we have an Ohmic junction.

6. #532_$ZnAl_5O_x$ sensing results

#	Material	Thickness (d)	Sputtering deposition time	Ar	O_2	$I_{sputtering}$	$T_{substrate}$
532	$ZnAl_5O_x$ (ZAO5 Hereaus)	101.4 nm	3min, 10 sec	100% (8sccm)	-	0.45A	RT

Table 18: Sputtering parameters used for #532_$ZnAl_5O_x$ development

6.1 Hydrogen sensing

The developed sensor was tested against H_2 gas sensing. The applied bias was set to be V=1Volt. Then, synthetic air was inserted in the experimental chamber for 20 minutes to obtain a constant current baseline and finally the pressure was stabilized in 800 mbar. To examine the response of the sensor to hydrogen gas, 1000 ppm of hydrogen gas were inserted into the chamber for 5 minutes, while afterwards synthetic air was inserted into the chamber for 5 minutes to examine the recovery of the sensor. This gas alteration was repeated for 5 times (5 experimental cycles – reapitability). Also, different operating temperatures were applied starting from RT to T=400°C with an increasing step of 50°C.

In the analysis following, only the graph for the optimum operating tempeature (T=350°C) that provides the best response of the sensor is exhibited. The rest of the graphs are included in the Appendix B: #532_ZnAl5Ox – Hydrogen gas sensing

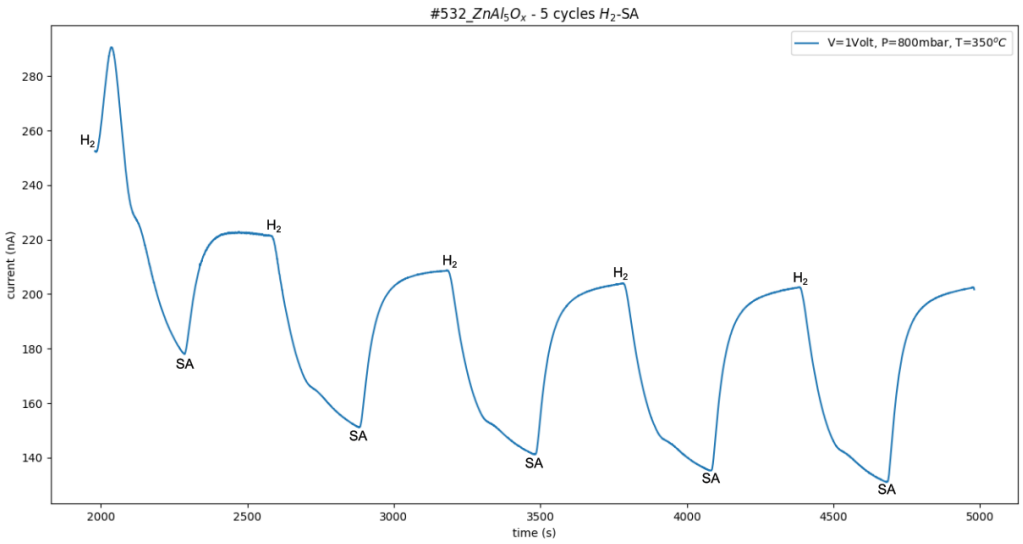

Figure 55: Current – time measurement at T=350°C in the presence of hydrogen

At T=350°C the sensor exhibited its best response and full recovery so we can calculate the response / recovery times and the response (S) of the sensor:

The response time was calculated at the 90% of each peak alteration and its mean value is:

$\overline{T_{90}} = \frac{T_{90}^{(1)}+T_{90}^{(2)}+T_{90}^{(3)}+T_{90}^{(4)}+T_{90}^{(5)}}{5} \Rightarrow \overline{T_{90}} = 218\ sec$, best response time: 192 sec

Similarly, $\overline{T_{10}} = \frac{T_{10}^{(1)}+T_{10}^{(2)}+T_{10}^{(3)}+T_{10}^{(4)}+T_{10}^{(5)}}{5} \Rightarrow \overline{T_{10}} = 120\ sec$, best recovery time: 95 sec

The sensor's response at each cycle was calculated following the equation (1) and the mean response value is equal to: $\bar{S} = 48.09$

Sensor: #532_ZnAl$_5$Ox			
Temperature (°C)	Sensitivity (%)	Response time T_{90} (best) [sec]	Recovery time T_{10} (best) [sec]
250	6.82	272 (253)	259 (254)
300	37.98	254 (243)	208 (205)
350	48.09	218 (192)	120 (95)
400	32.77	176 (139)	121 (105)

Table 19: Sensitivity – response, response / recovery times of the sensor for different operating temperatures

By using the data of the table 16, we can plot the response S of the sensor and the response / recovery times as function of the different operating temperatures:

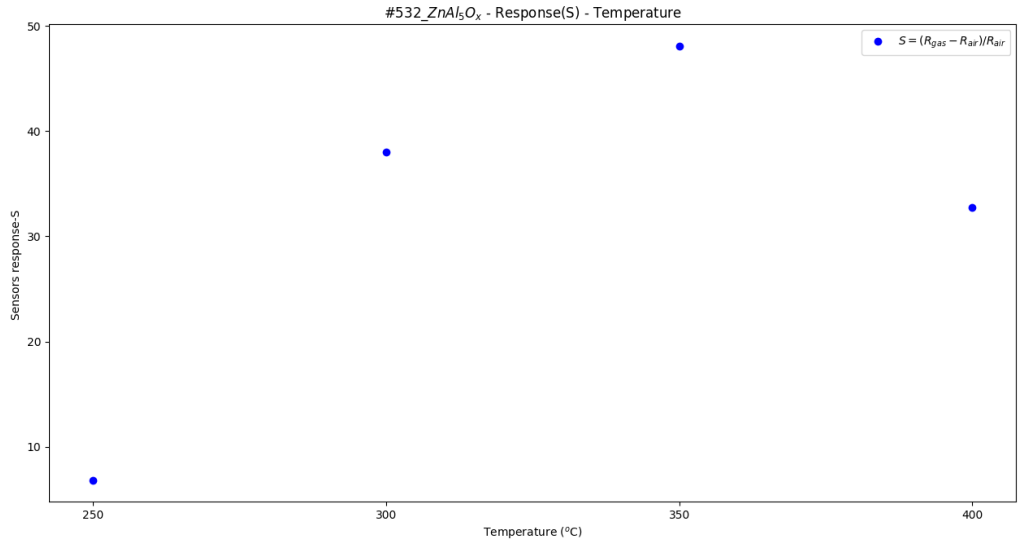

Figure 56: Sensor's response S for the different operating temperatures

In the operating temperature range of T=250°C - 400°C, it is clear that the sensor appears to have its maximum response at T=350°C. Lower or higher operating temperatures result in lower response values.

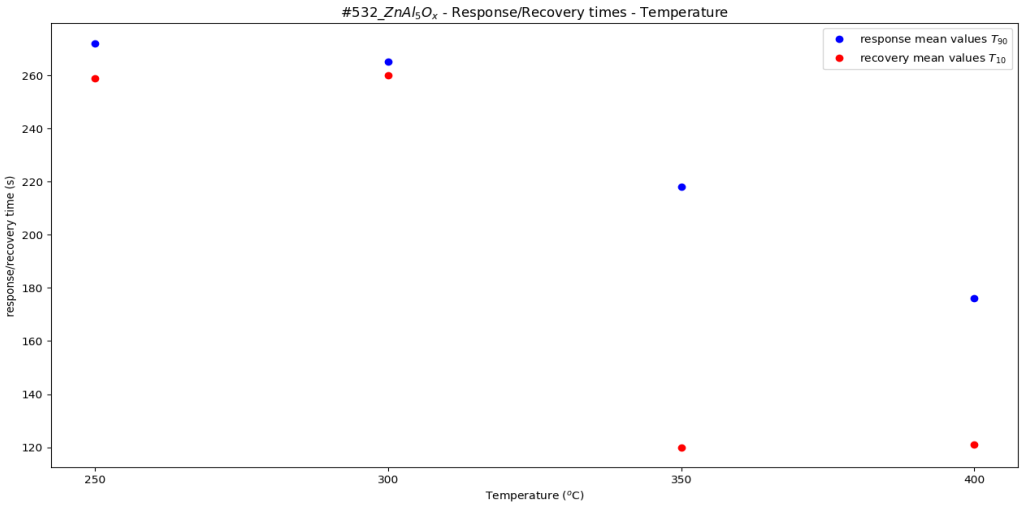

Figure 57: Response / recovery times of the sensor for the different operating temperatures

The response time varied from 176 sec to 272 sec, while the recovery time varied from 120 sec to 259 sec. Both response and recovery times decline with the temperature increasement.

At T=350°C, the response of the sensor was examined for different hydrogen concentrations in order to find the lower detection limit of hydrogen that can be sensed. The dilution of the hydrogen gas was achieved as hydrogen + synthetic air mixture.

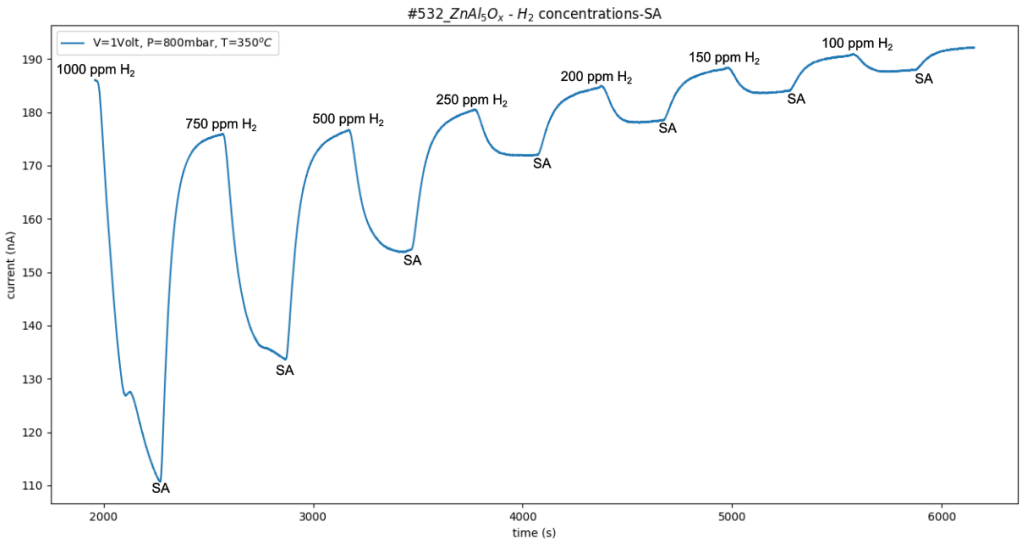

Figure 58: Current – time measurement at T=350°C in the presence of hydrogen gas concentrations

H_2 concentrations	Sensitivity (%)	Response time T_{90} (sec)	Recovery time T_{10} (sec)
100% →1000 ppm	68.07	225	122
75% → 750 ppm	31.15	152	141
50% → 500 ppm	14.46	137	159
25% → 250 ppm	4.67	115	180
20% → 200 ppm	3.73	101	219
15% → 150 ppm	2.45	98	191
10% → 100 ppm	1.64	99	171

Table 20: Sensitivity – Response of the sensor, response / recovery times towards different hydrogen gas concentrations

The response of the sensor takes its highest value at 1000 ppm of hydrogen concentration. For hydrogen gas lower than 250 ppm inserted the chamber, we observe that the sensor finds difficulty to respond.

From the table 17, we can plot the response of the sensor, the response and recovery times in fuction with the different hydrogen gas concentration.

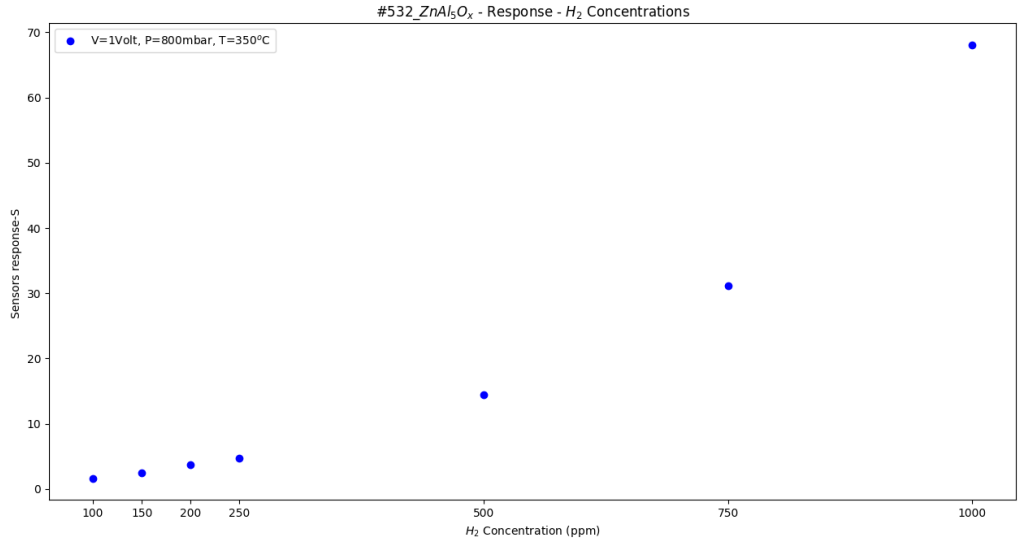

Figure 59: Sensor's response S for the different hydrogen gas concentration

At hydrogen concentration lower than 250 ppm, the response of the sensor exhibits linear dependance to concentration. After applying linear fitting we can find the detection limit (intersection of the fitting with the x-axis), which is found to be 25 ppm.

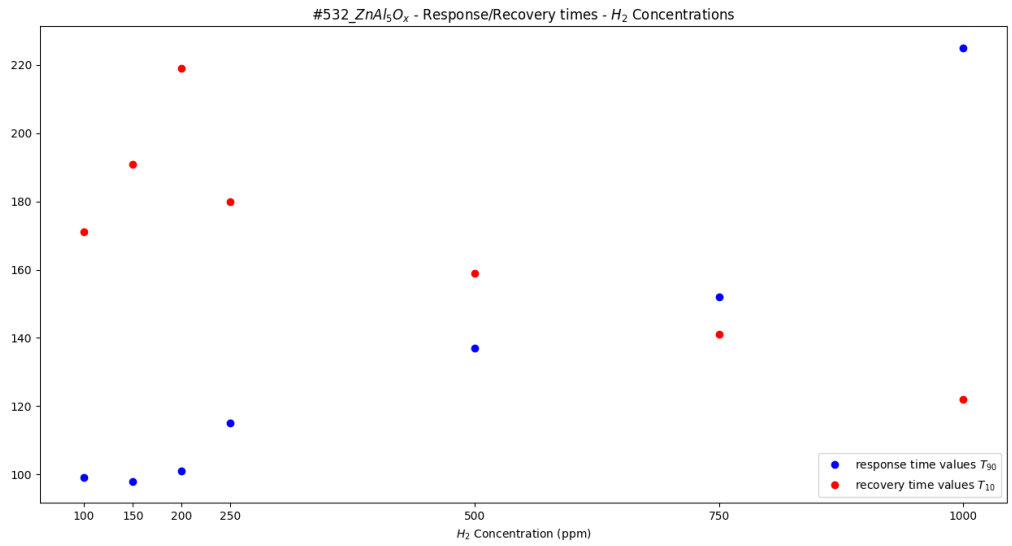

Figure 60: Response / Recovery times of the sensor for different hydrogen gas concentration

At low hydrogen concentrations we observe low response times, while at the highest hydrogen gas concentration, we observe the lowest recovery time.

6.2 Methane gas sensing

The same experimental process was repeated in the case of methane gas. The applied bias was set to be V=1Volt. Then, synthetic air was inserted in the experimental chamber for 20 minutes to obtain a constant current baseline and finally the pressure was stabilized in 800 mbar. To examine the response of the methane gas, pure methane was inserted into the chamber for 5 minutes, while afterwards synthetic air was inserted into the chamber for 5 minutes to examine the recovery of the sensor. The gas alteration was repeated for 5 times (5 experimental cycles – repeatability) and different operating temperatures were applied starting from RT to T=400°C with an increasing step of 50°C.

In the analysis following, only the graph for the optimal operating temperature (T=400°C) that provides the best response of the sensor is exhibited. The rest of the graphs are included in the Appendix B: #532_ZnAl5Ox – Methane gas sensing

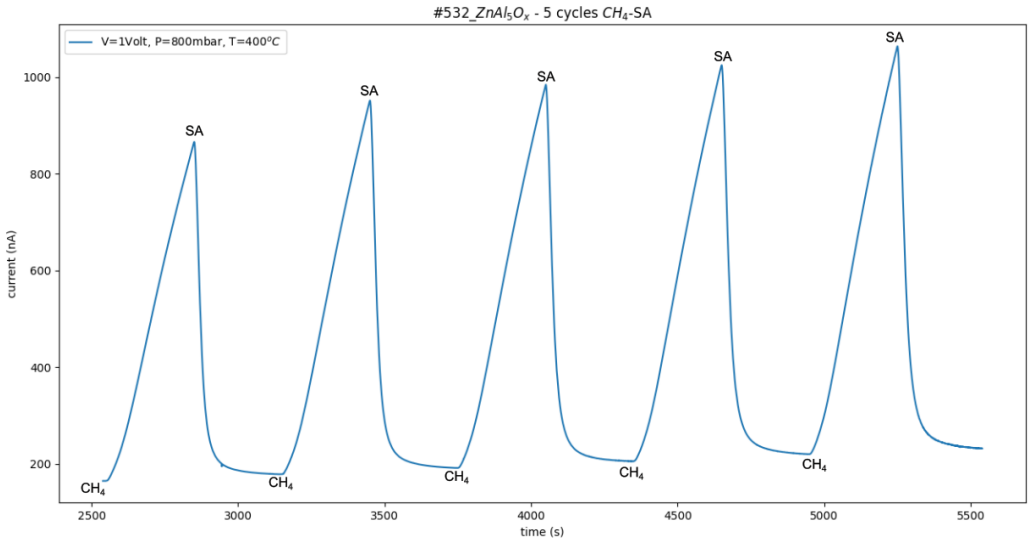

Figure 61: Current – time measurement at T=400°C in the presence of methane

At T=400°C the sensor exhibited its best response and full recovery so we can calculate the response / recovery times and the response (S) of the sensor:

The response time was calculated at the 90% of each peak alteration and its mean value is:

$\overline{T_{90}} = \frac{T_{90}^{(1)}+T_{90}^{(2)}+T_{90}^{(3)}+T_{90}^{(4)}+T_{90}^{(5)}}{5} \Rightarrow \overline{T_{90}} = 271\ sec$, best response time: 266 sec

Similarly, $\overline{T_{10}} = \frac{T_{10}^{(1)}+T_{10}^{(2)}+T_{10}^{(3)}+T_{10}^{(4)}+T_{10}^{(5)}}{5} \Rightarrow \overline{T_{10}} = 73\ sec$, best recovery time: 70 sec

The sensor's response at each cycle was calculated following the equation (1) and the mean response value is equal to: $\bar{S} = 80.05$

Sensor: #532_ZnAl$_5$Ox			
Temperature (°C)	Sensitivity (%)	Response time T_{90} (best) [sec]	Recovery time T_{10} (best) [sec]
200	6.8	283 (281)	265 (261)
250	27.11	265 (237)	244 (222)
300	48.52	263 (253)	138 (102)
350	54.35	281 (277)	180 (171)
400	80.05	271 (266)	73 (70)

Table 21: Sensitivity – response, response / recovery times of the sensor for different operating temperatures

By using the data of Table 16, we can plot the response S of the sensor and the response / recovery times as function of the different operating temperatures:

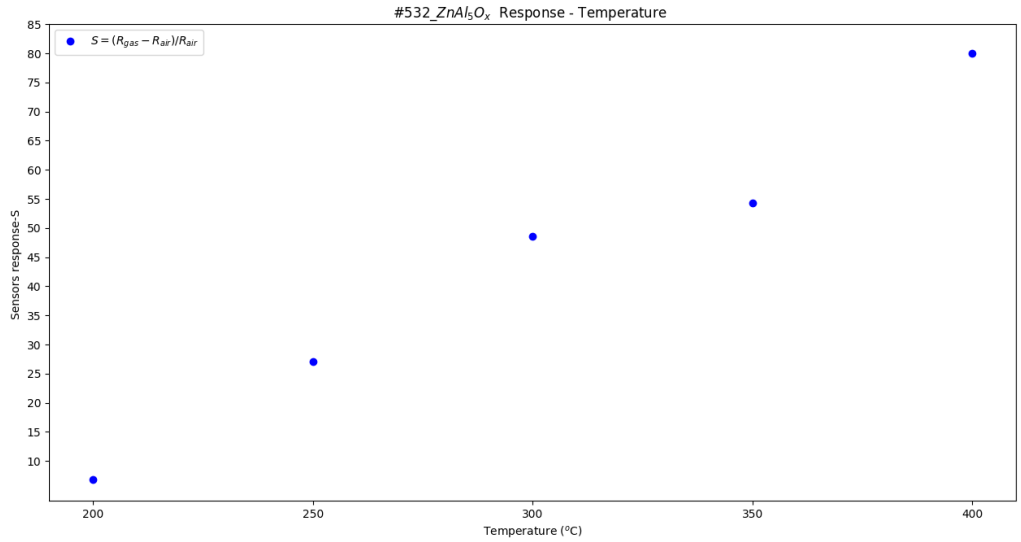

Figure 62: Response S of the sensor for different operating temperatures

The response of the sensor increases almost linearly with the temperature incensement. At lower temperatures, methane gas sensing by this sensor is weak and did not exhibit recovery in the initial state of each experimental cycle.

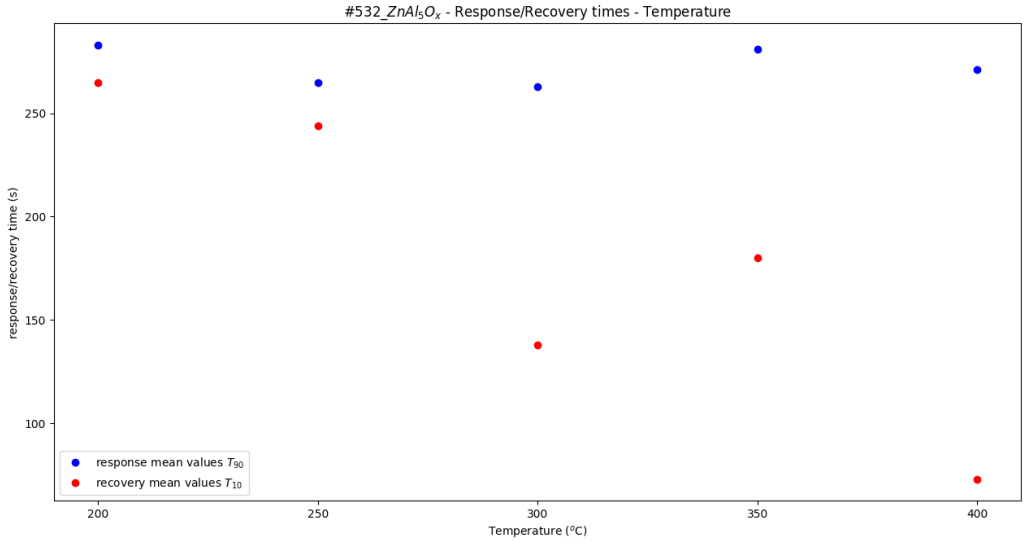

Figure 63: Response / recovery times of the sensor at different operating temperatures

The response time is quit slow, varies from 263 sec to 283 sec, while the recovery time varied from 73sec to 265 sec, exhibiting so fast response time at the optimal temperature of T=400°C.

Furthermore, the response of the sensor was examined for different methane concentrations at T=400°C. The dilution in the pure methane was achieved by adding N_2 gas.

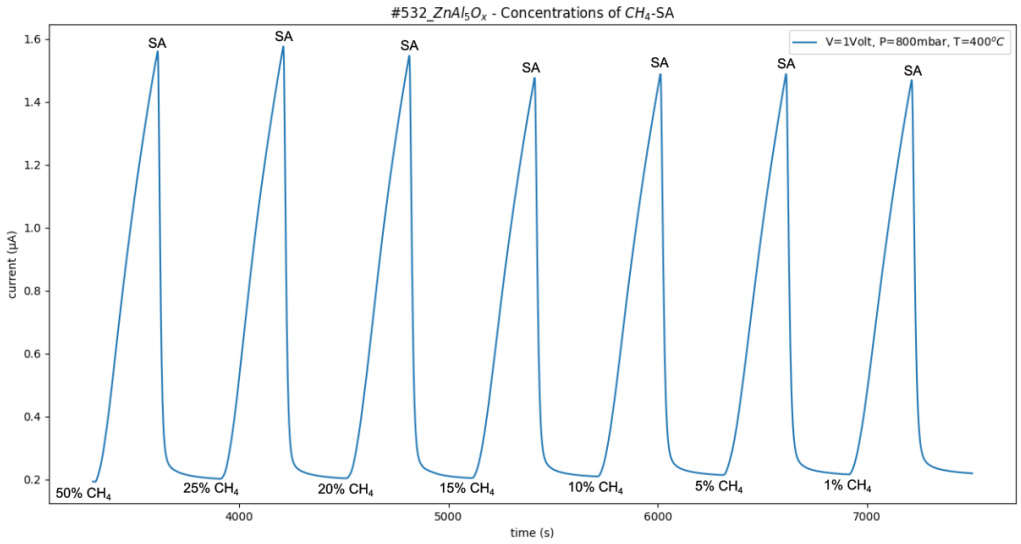

Figure 64: Current – time measurements at T=400°C in the presence of different methane concentrations

CH_4 concentrations	Sensitivity (%)	Response time T_{90} (sec)	Recovery time T_{10} (sec)
50%	87.38	270	38
25%	87.26	274	39
20%	86.84	276	42
15%	85.75	275	43
10%	85.91	271	44
5%	85.40	270	47
1%	84.90	278	49

Table 22: Sensitivity – response, response / recovery times of the sensor for the different methane concentrations

This sensor exhibits response higher than 85% and very quick recovery time, but lack in response quickness.

By using the data of Table 19, we produce the following diagrams of the response S and response / recovery times as function of the different methane concentrations.

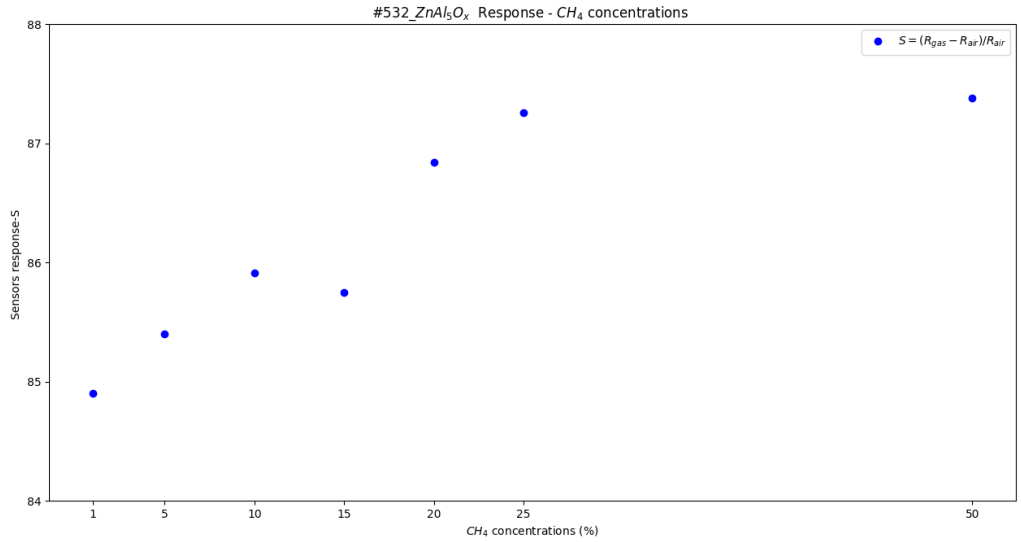

Figure 65: Sensor's response for the different methane concentrations

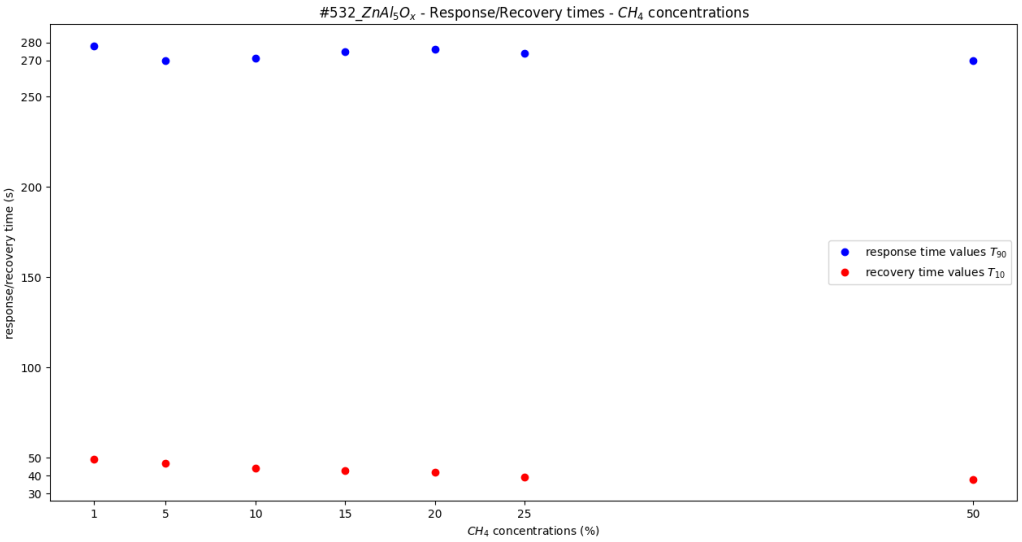

Figure 66: Response / recovery times for the different methane concentration

Even in low methane concentrations the response and recovery time of the sensor remain the same.

7. Characterization of #533_$ZnAl_5O_x$ – Structural, morphological and optical properties

The structural, morphological and optical properties of #533_$ZnAl_5O_x$ sensing films were examined by using the XRD, SEM, AFM and UV-vis spectroscopy techniques.

7.1 X-Ray Diffraction analysis

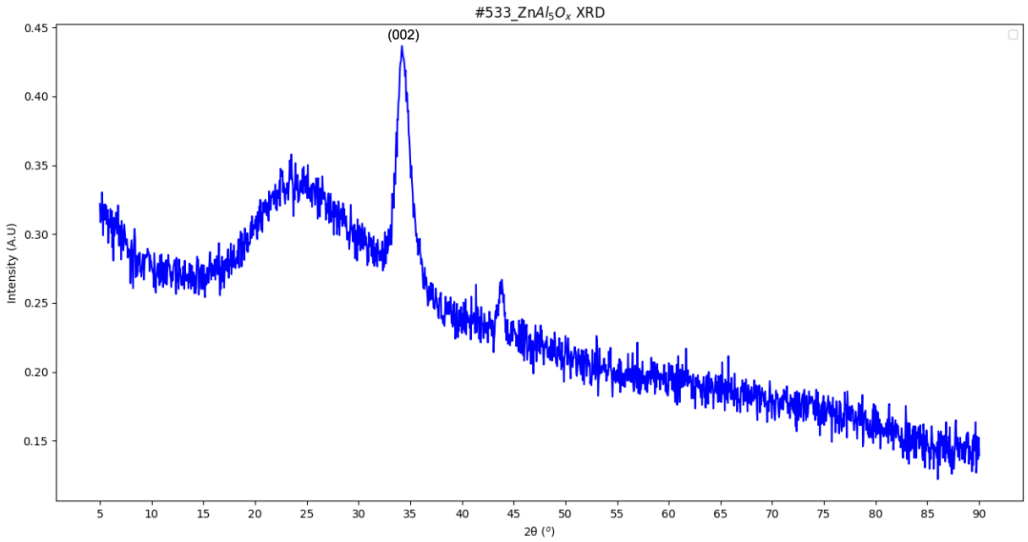

Figure 67: XRD pattern of #533_$ZnAl_5O_x$ sensing film

The XRD spectra were measured in the range of 5° - 90°, exhibiting the main peak at $2\theta_1$=34.30°.

The main peak θ_1 corresponds to the crystal plane with Miller indices (hkl)=(002). Applying Gaussian fitting around the main peak, we get the full width at half maximum (FWHM) of the peak, which is equal to β=0.027 rad.

The crystallite size and the interplanar spacing of the sensing material can be calculated by using equation (13) and (14):

$$(13):\ D\ (nm) = \frac{K * \lambda}{\beta * cos\theta} \Rightarrow D = 5.374\ nm$$

$$(14):\ d_{hkl}(\text{Å}) = \frac{n * \lambda}{2 * sin\theta} \Rightarrow d_{002} = 2.612\ \text{Å}$$

After calculating the interplanar spacing, the lattice parameters a,c for the hexagonal wurtzite $ZnAl_5O_x$ structure can be calculated by using equation (15):

$$(15):\ \frac{1}{d^2_{(hkl)}} = \frac{4}{3} * \left(\frac{h^2 + h*k + k^2}{a^2}\right) + \frac{l^2}{c^2} \Rightarrow c^2 = 4 * d^2_{002} \Rightarrow c = 5.225\ \text{Å}$$

Making the assumption that the crystal structure remains the ideal wurtzite and there is a low local symmetry distortion for the aluminum doped film, then a close calculation for the lattice parameter a can be made, resulting in a=3.199Å.

Finally, the lattice strain parameter ε_w can be calculated through the equation (16):

$$(16):\ \varepsilon_w = \frac{\beta * cot\theta}{4} \Rightarrow \varepsilon_w = 2.18 * 10^{-2}$$

A summarizing table for the obtained result follows:

Peak 2θ	Crystallite size D (nm)	Interplanar spacing d_{hkl} (Å)	Lattice parameter c (Å)	Lattice parameter a (Å)	Lattice strain ε_w
$2\theta_1$=34.30°	5.374	(hkl)=(002) 2.612	5.225	3.199	$2.18*10^{-2}$

Table 23: Structural parameters of #533_$ZnAl_5O_x$ thin film

The #532 developed sensor exhibits its highest peak corresponding to the (002) crystalline plane, indicating that the crystal has strong preference in the c – axis orientation perpendicular to the substrate.

7.2 SEM

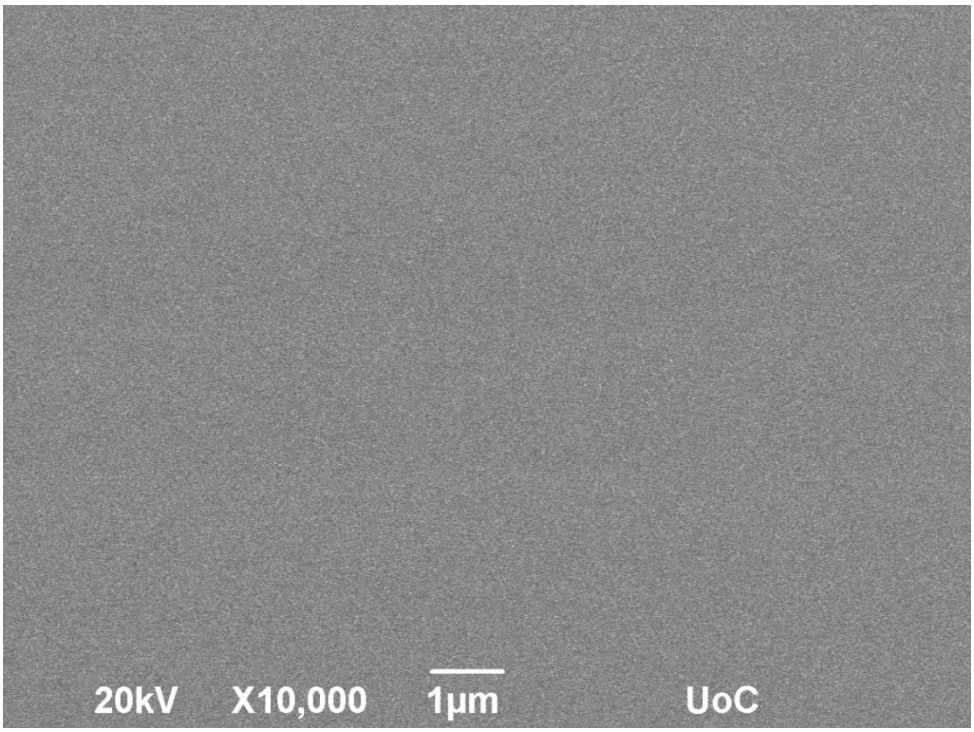

Figure 68: SEM micrograph of #533_$ZnAl_5O_x$ film

The film shows good uniformity and dense surface without visible holes or faulty zones on the film surface.

7.3 AFM

The roughness of the #533_$ZnAl_5O_x$ sensing film was calculated through an AFM measurement. The average roughness value was found to be R_a=16.538nm, while the root mean square value was found to be R_s=26.072nm.

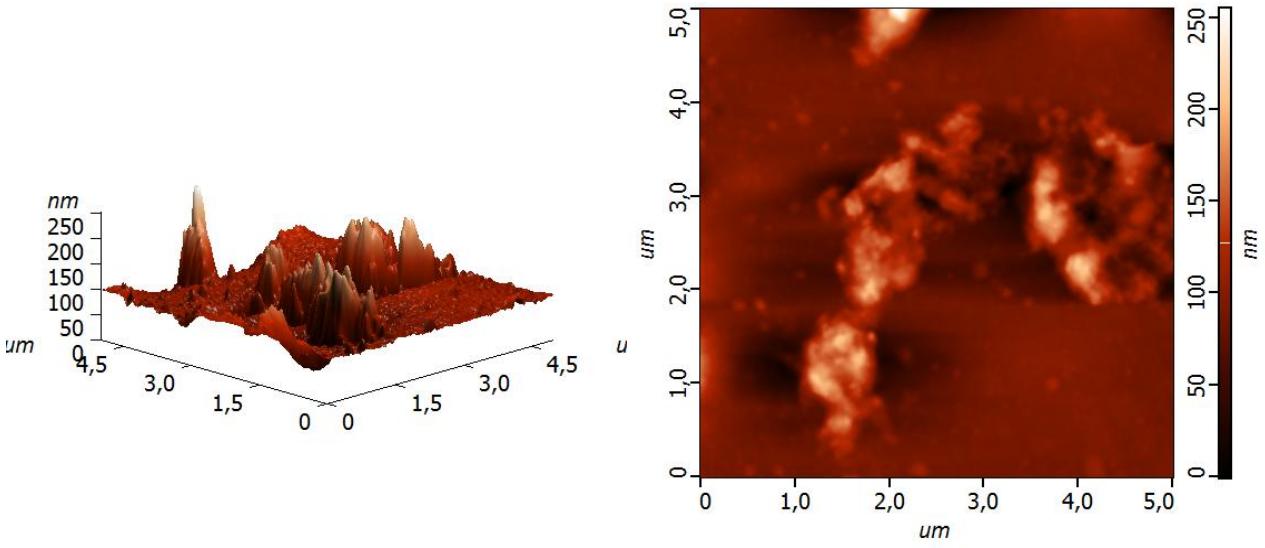

Figure 69: 3D and 2D AFM micrographs (4.5µm x 4.5µm) of the #533_$ZnAl_5O_x$ film

7.4 UV-vis spectroscopy

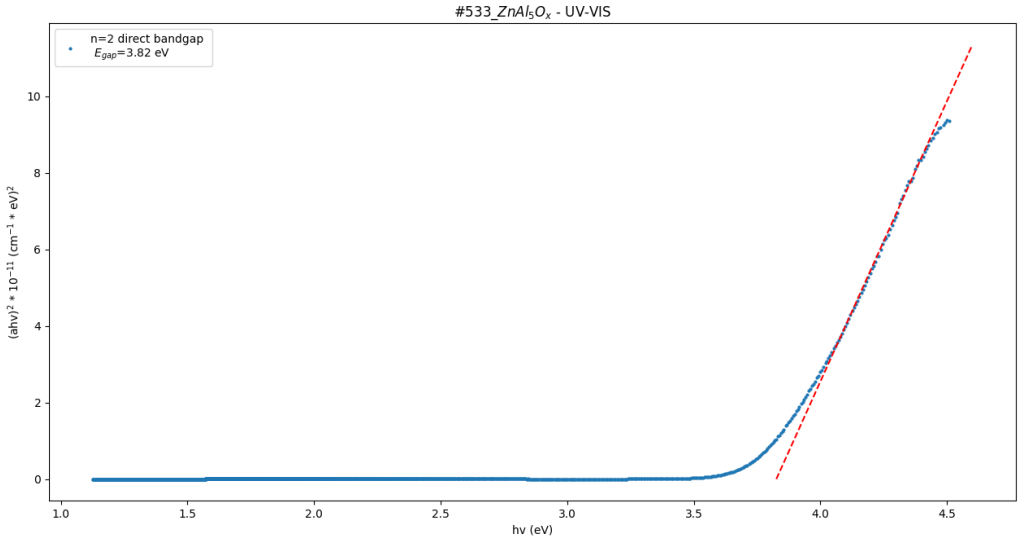

Figure 70: Tauc plot of #533_$ZnAl_5O_x$ for the direct energy band gap case (n=2)

The energy gap was calculated from the linear part of Tauc plot. It appears to be E_g=3.82 eV for the direct band gap case. The obtained energy gap value seems to be overestimated in comparison to the values mentioned in the bibliography.

7.5 I-V characteristics

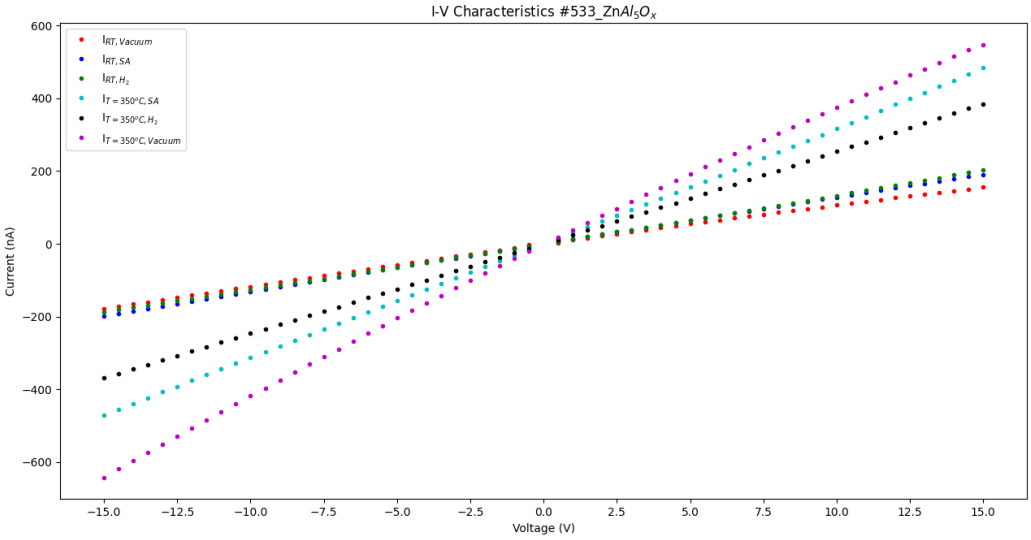

Figure 71: I-V measurements of #533_$ZnAl_5O_x$ sensor operating in room temperature (RT) or at T=350°C under vacuum either in the presence of synthetic air or 1000ppm of hydrogen

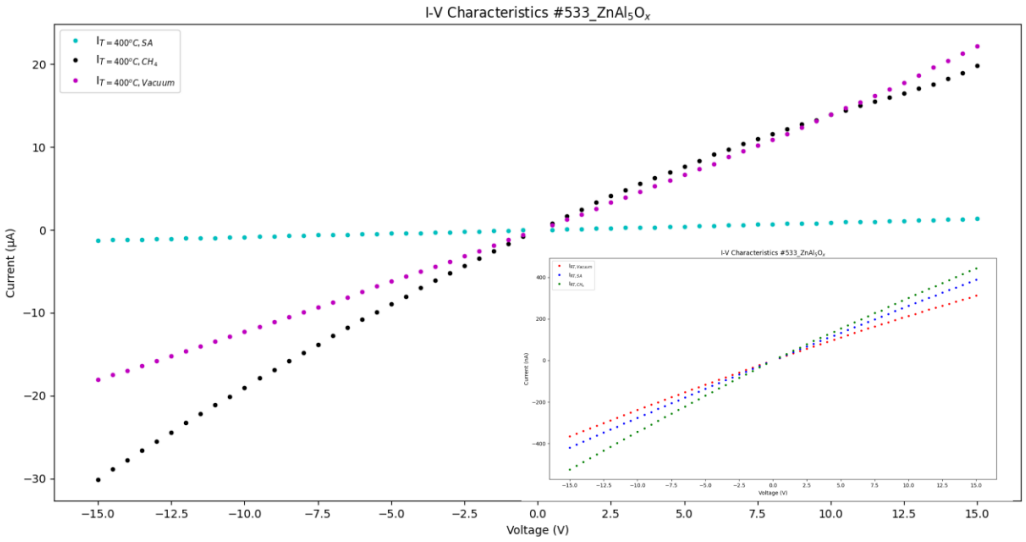

Figure 72: I-V measurements of #533_$ZnAl_5O_x$ sensor operating in room temperature (RT) or at T=400°C under vacuum either in the presence of synthetic air or 100% methane

In both hydrogen and methane gases, we observe linearity in the I-V characteristics around the applied bias of V=5Volts. That linearity indicates that we have an Ohmic junction.

8. #533_$ZnAl_5O_x$ sensing results

#	Material	Thickness (d)	Sputtering deposition time	Ar	O_2	$I_{sputtering}$	$T_{substrate}$
533	$ZnAl_5O_x$ (ZAO5 Heraeus)	101.3 nm	5min, 50 sec	100% (8sccm)	-	0.25A	RT

Table 24: Sputtering parameters used for #533_$ZnAl_5O_x$ development

8.1 Hydrogen sensing

The developed sensor was tested against H_2 gas sensing. The applied bias was set to be V=5Volts. Then, synthetic air was inserted in the experimental chamber for 20 minutes to obtain a constant current baseline and finally the pressure was stabilized in 800 mbar. To examine the response of the sensor to hydrogen gas, 1000 ppm of hydrogen gas were inserted into the chamber for 5 minutes, while afterwards synthetic air was inserted into the chamber for 5 minutes to examine the recovery of the sensor. This gas alteration was repeated for 5 times (5 experimental cycles – reapitability). Also, different operating temperatures were applied starting from RT to T=400°C with an increasing step of 50°C.

In the analysis following, only the graph for the optimum operating tempeature (T=350°C) that provides the best response of the sensor is exhibited. The rest of the graphs are included in the Appendix B: #533_ZnAl5Ox – Hydrogen gas sensing.

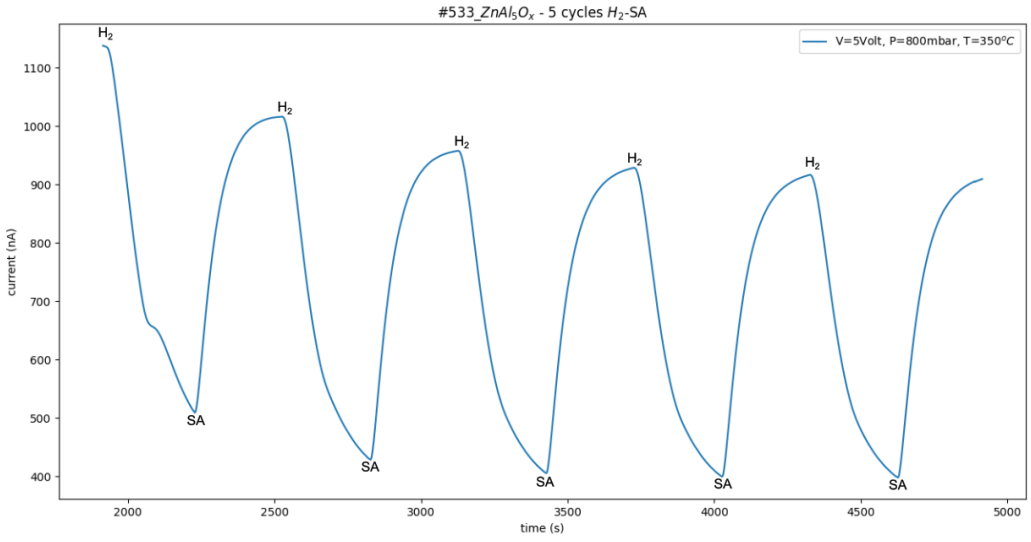

Figure 73: Current – time measurements at T=350°C in the presence of hydrogen

At T=350°C the sensor exhibited its best response and full recovery so we can calculate the response / recovery times and the response (S) of the sensor:

The response time was calculated at the 90% of each peak alteration and its mean value is:

$\overline{T_{90}} = \frac{T_{90}^{(1)}+T_{90}^{(2)}+T_{90}^{(3)}+T_{90}^{(4)}+T_{90}^{(5)}}{5} \Rightarrow \overline{T_{90}} = 216\ sec$, best response time: 193 sec

Similarly, $\overline{T_{10}} = \frac{T_{10}^{(1)}+T_{10}^{(2)}+T_{10}^{(3)}+T_{10}^{(4)}+T_{10}^{(5)}}{5} \Rightarrow \overline{T_{10}} = 171\ sec$, best recovery time: 164 sec

The sensor's response at each cycle was calculated following the equation (1) and the mean response value is equal to: $\bar{S} = 132.6$

Sensor: #533_$ZnAl_5Ox$			
Temperature (°C)	Sensitivity (%)	Response time T_{90} (best) [sec]	Recovery time T_{10} (best) [sec]
250	4.18	280 (275)	252 (232)
300	26.05	265 (246)	260 (258)
350	132.6	216 (193)	171 (164)
400	71.06	154 (108)	103 (92)

Table 25: Sensitivity – response, response / recovery times of the sensor for different operating temperatures

By using the data of the table 22, we can plot the response S of the sensor and the response / recovery times as function of the different operating temperatures:

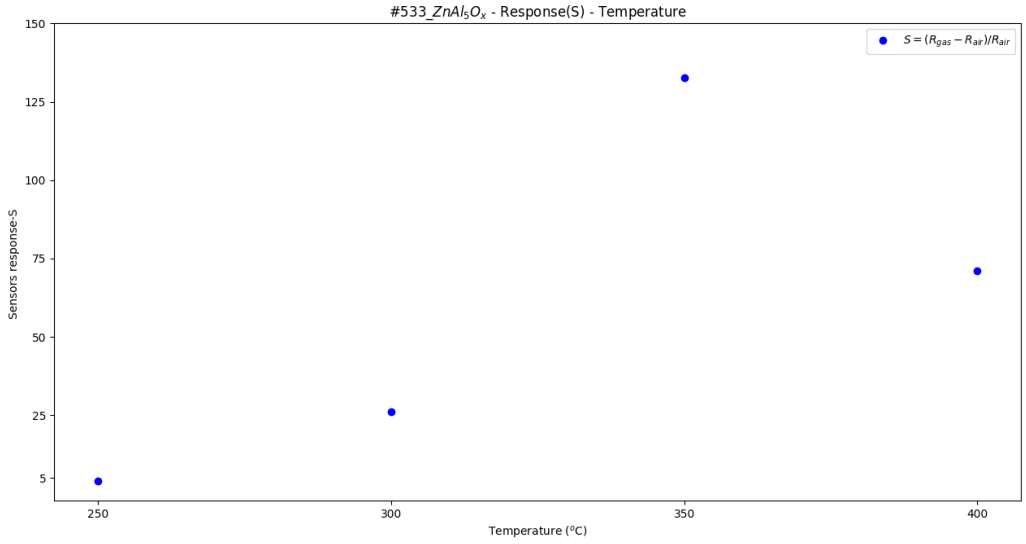

Figure 74: Sensor's response S for the different operating temperatures

In the operating temperature range of T=250°C – T=400°C, the sensor appears to have its maximum response at T=350°C. Lower or higher operating temperatures result in lower response values.

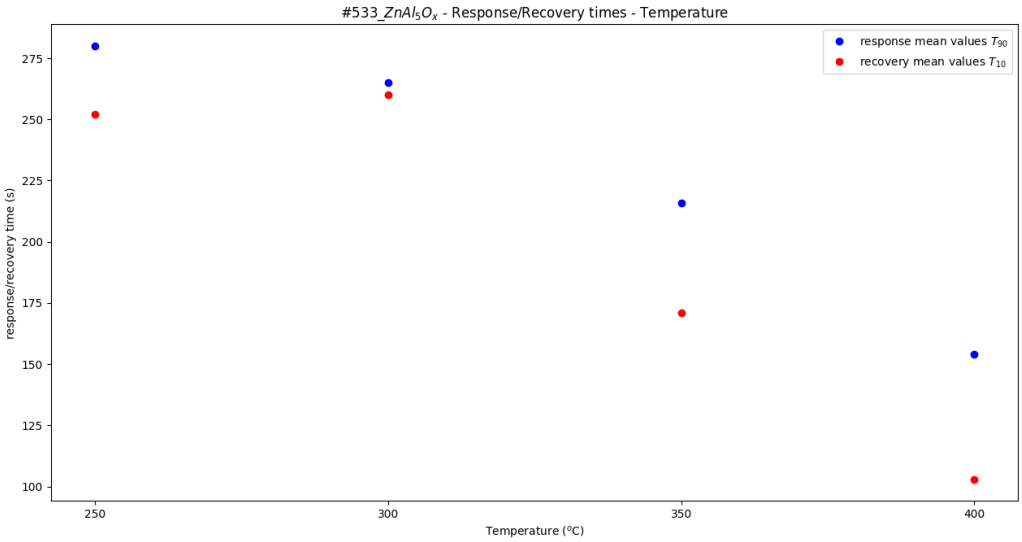

Figure 75: Response / recovery times of the sensor for the different operating temperatures

The response time varied from 154 sec to 280 sec, while the recovery time varied from 103 sec to 260 sec. Again, both response and recovery times decline with the temperature incensement.

At T=350°C, the response of the sensor was examined for different hydrogen concentrations in order to find the lower detection limit of hydrogen that can be sensed. The dilution of the hydrogen gas was achieved as hydrogen + synthetic air mixture.

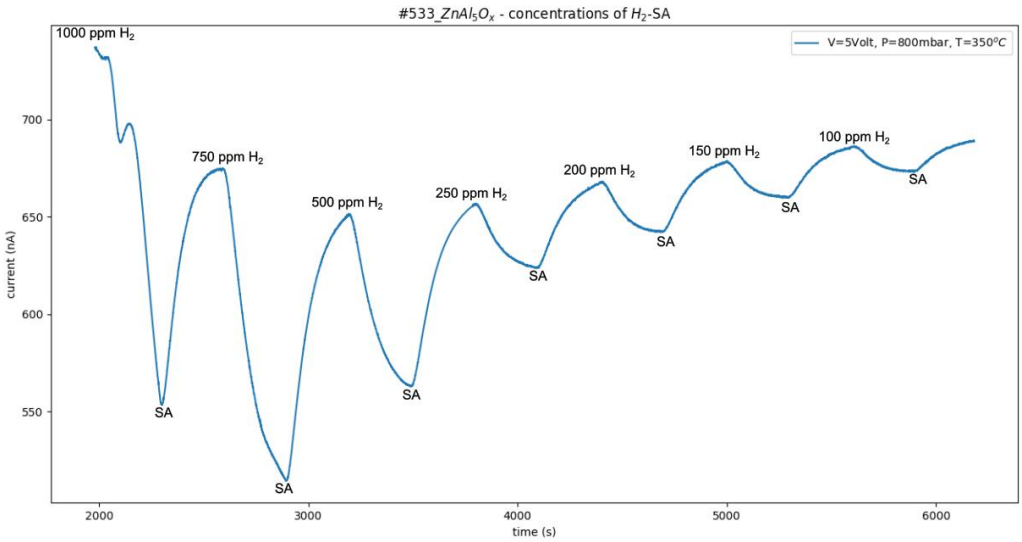

Figure 76: Current – time measurement at T=350°C in the presence of different hydrogen gas concentrations

H_2 concentrations	Sensitivity (%)	Response time T_{90} (sec)	Recovery time T_{10} (sec)
100% → 1000 ppm	32.77	283	193
75% →750 ppm	31.32	196	221
50% →500 ppm	15.16	222	213
25% →250 ppm	5.22	207	237
20% →200 ppm	3.91	188	231
15% →150 ppm	2.78	198	240
10% →100 ppm	1.81	158	208

Table 26: Sensitivity – response, response / recovery times of the sensor for the different hydrogen concentrations

The response of the sensor takes its highest value at 1000 ppm of hydrogen concentration. It must be mentioned that the sensor's response at 1000 ppm of hydrogen gas is lower in comparison to the equivalent response at the repeatability experiment.

From the table 23, we can plot the response of the sensor and the response and recovery times in function with the different hydrogen gas concentration.

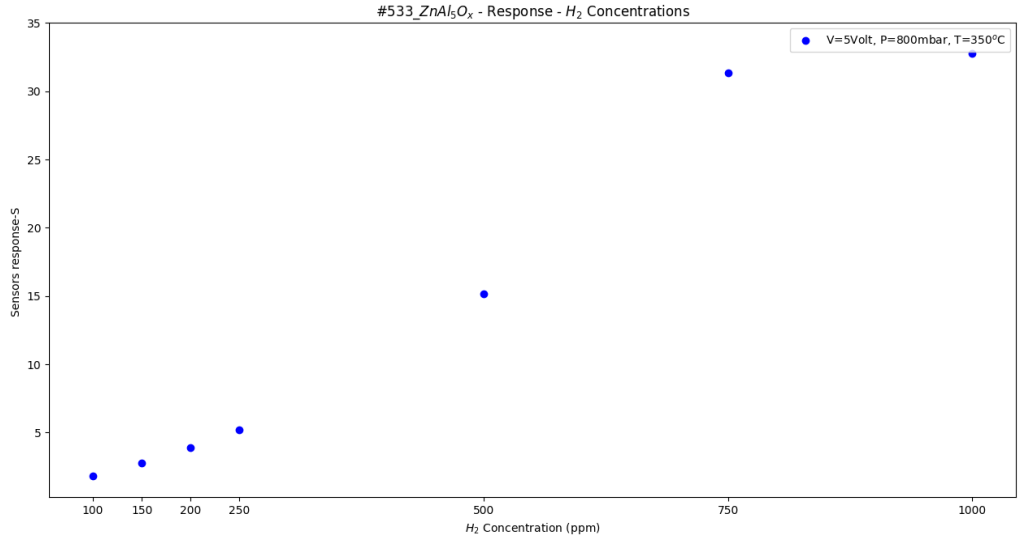

Figure 77: Sensor's response S for the different hydrogen gas concentrations

At hydrogen concentration lower than 250 ppm, the response of the sensor exhibits linear dependence to hydrogen gas concentration. After applying a linear fitting we can find the detection limit (intersection of fitting with the x – axis), which is found to be 25 ppm.

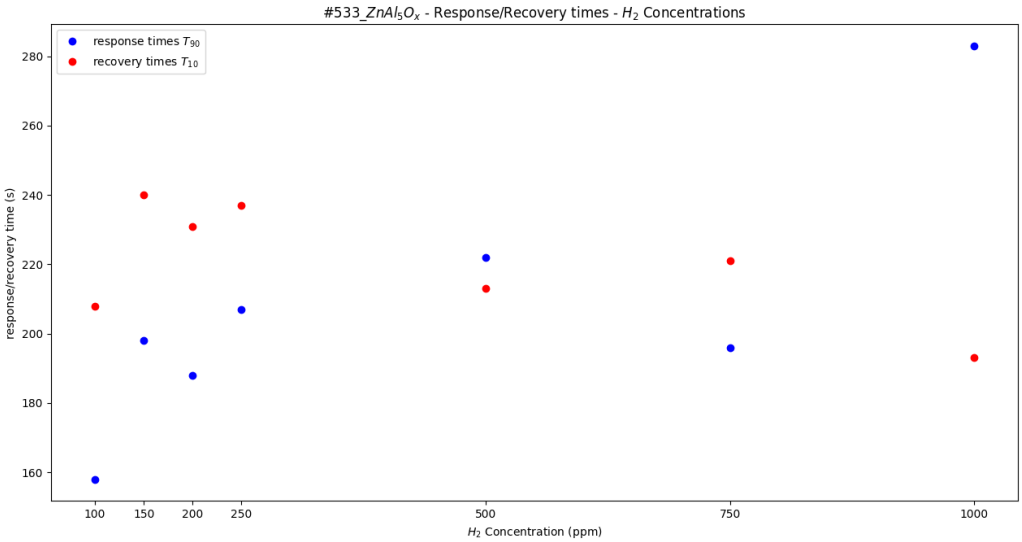

Figure 78: Response / recovery times of the sensor for the different hydrogen concentrations

The response time of the sensor exhibits its lowest value at the minimum sensed hydrogen concentration of 100 ppm and its lowest recovery time value at 1000 ppm of hydrogen.

8.2 Methane sensing

The same experimental process was repeated in the case of methane gas. The applied bias was set to be V=5Volts. Then, synthetic air was inserted in the experimental chamber for 20 minutes to obtain a constant current baseline and finally the pressure was stabilized in 800 mbar. To examine the response of the methane gas, pure methane was inserted into the chamber for 5 minutes, while afterwards synthetic air was inserted into the chamber for 5 minutes to examine the recovery of the sensor. The gas alteration was repeated for 5 times (5 experimental cycles – repeatability) and different operating temperatures were applied starting from RT to T=400°C with an increasing step of 50°C.

In the analysis following, only the graph for the optimal operating temperature (T=400°C) that provides the best response of the sensor is exhibited. The rest of the graphs are included in the Appendix B: #533_ZnAl5Ox – Methane gas sensing.

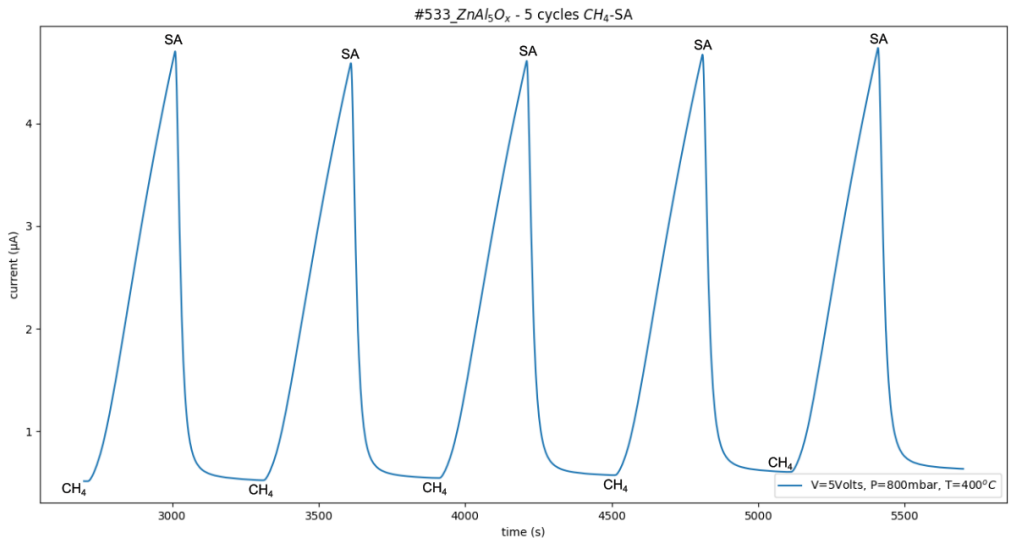

Figure 79: Current – time measurement at T=400°C in the presence of methane

At T=400°C the sensor exhibited its best response and full recovery so we can calculate the response / recovery times and the response (S) of the sensor:

The response time was calculated at the 90% of each peak alteration and its mean value is:

$\overline{T_{90}} = \frac{T_{90}^{(1)}+T_{90}^{(2)}+T_{90}^{(3)}+T_{90}^{(4)}+T_{90}^{(5)}}{5} \Rightarrow \overline{T_{90}} = 275\ sec$, best response time: 263 sec

Similarly, $\overline{T_{10}} = \frac{T_{10}^{(1)}+T_{10}^{(2)}+T_{10}^{(3)}+T_{10}^{(4)}+T_{10}^{(5)}}{5} \Rightarrow \overline{T_{10}} = 60\ sec$, best recovery time: 51 sec

The sensor's response at each cycle was calculated following the equation (1) and the mean response value is equal to: $\bar{S} = 88.06$

Sensor: #533_ZnAl$_5$Ox			
Temperature (°C)	Sensitivity (%)	Response time T_{90} (best) [sec]	Recovery time T_{10} (best) [sec]
150	12.81	271 (266)	221 (117)
200	18.00	265 (255)	246 (210)
250	28.33	266 (257)	214 (187)
300	28.27	276 (261)	249 (243)
350	62.65	273 (265)	165 (152)
400	88.06	275 (263)	60 (51)

Table 27: Sensitivity – response, response / recovery times of the sensor for different operating temperatures

By using the data of Table 24, we can plot the response S of the sensor and the response / recovery times as function of the different operating temperatures.

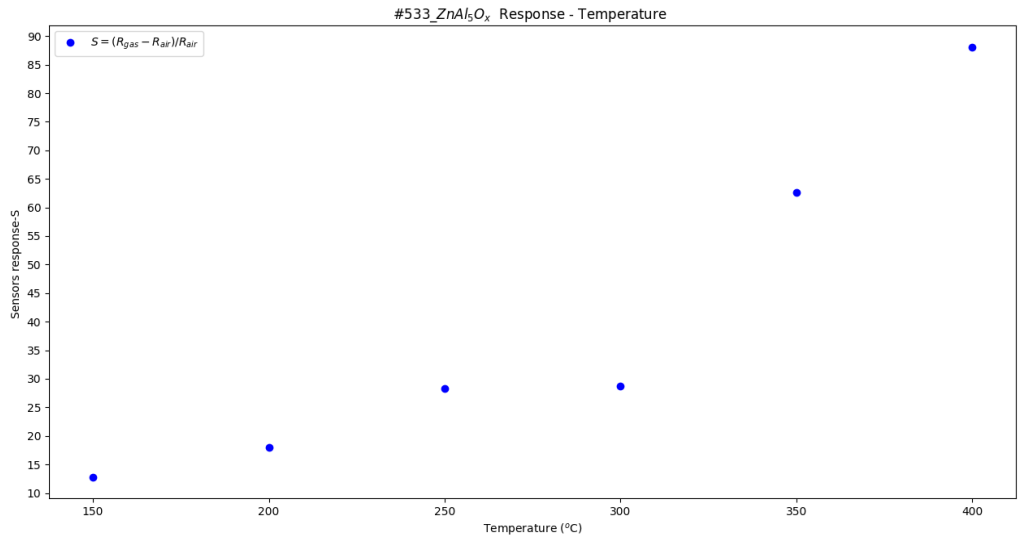

Figure 80: Sensor's response for different operating temperatures

The response of the sensor is gradually increased as the operating temperature gets increased too. At T=400°C the sensor performed better in the presence of methane gas, achieving the remarkable value of S=88.06%. At lower operating temperatures, the sensor struggled in methane gas sensing, exhibiting low current alterations and inability to recovery in the initial state.

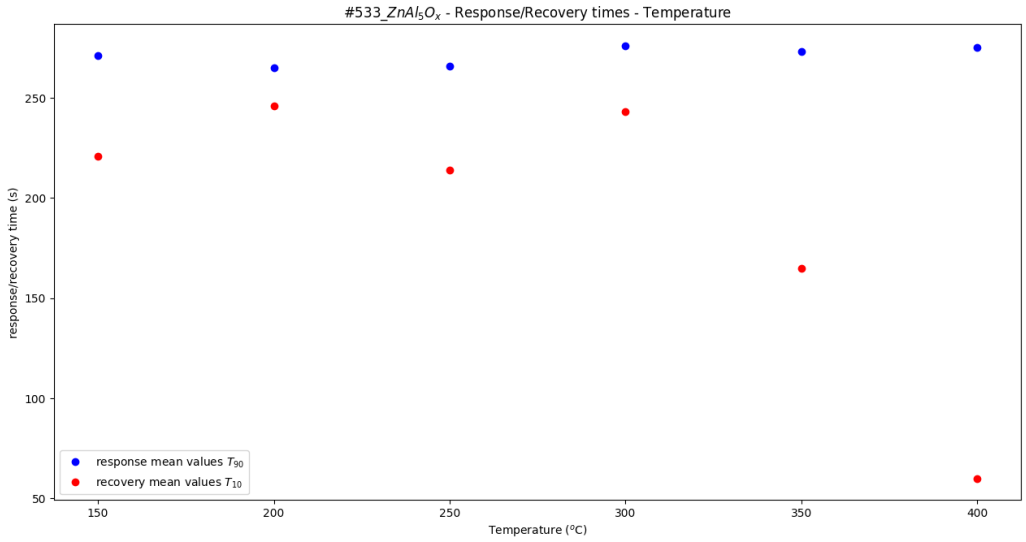

Figure 81: Response / recovery times of the sensor at different operating temperatures

The response times of the sensor are around 270 sec, while the recovery times of the sensor vary from 60 sec to 249 sec. At T=400°C, the sensor exhibits just a minute - the lowest recovery time.

Furthermore, the response of the sensor was examined for different methane concentrations at T=400°C. The dilution in the pure methane was achieved by adding N_2 gas.

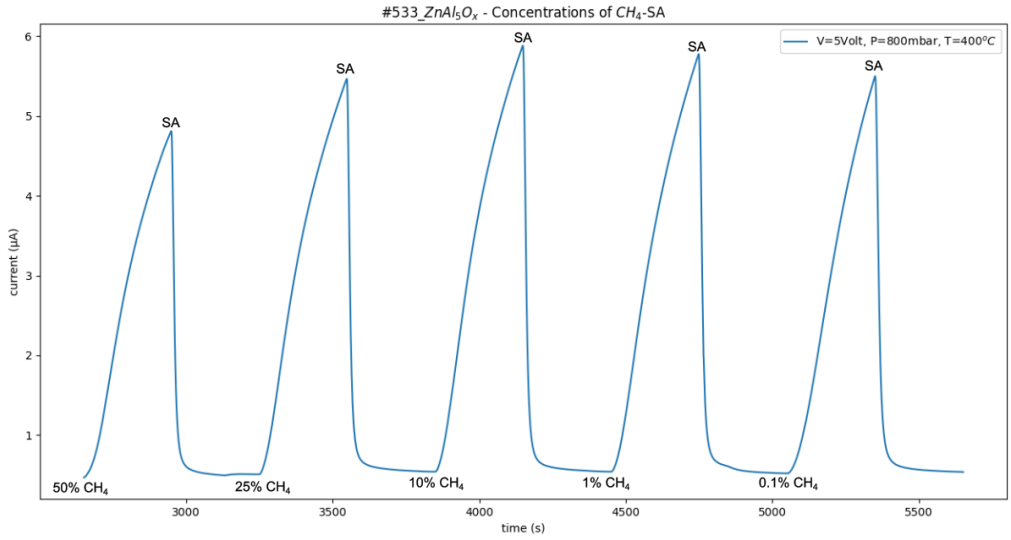

Figure 82: Current – time measurement at T=400°C in the presence of different methane concentrations

CH_4 concentrations	Sensitivity (%)	Response time T_{90} (sec)	Recovery time T_{10} (sec)
50%	89.99	257	25
25%	90.43	248	18
10%	90.93	253	47
1%	90.85	260	32
0.1%	90.23	270	18

Table 28: Sensitivity – response, response / recovery times of the sensor for the different methane concentrations

By using the data of Table 25, we can plot the response S of the sensor and the response / recovery times as function of the different methane concentrations:

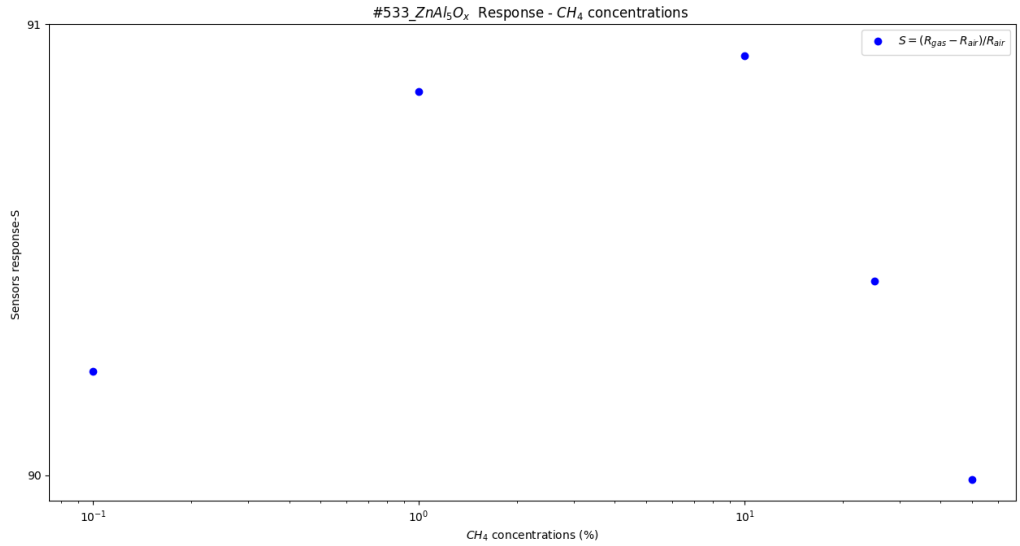

Figure 83: Sensor's response for the different methane concentrations

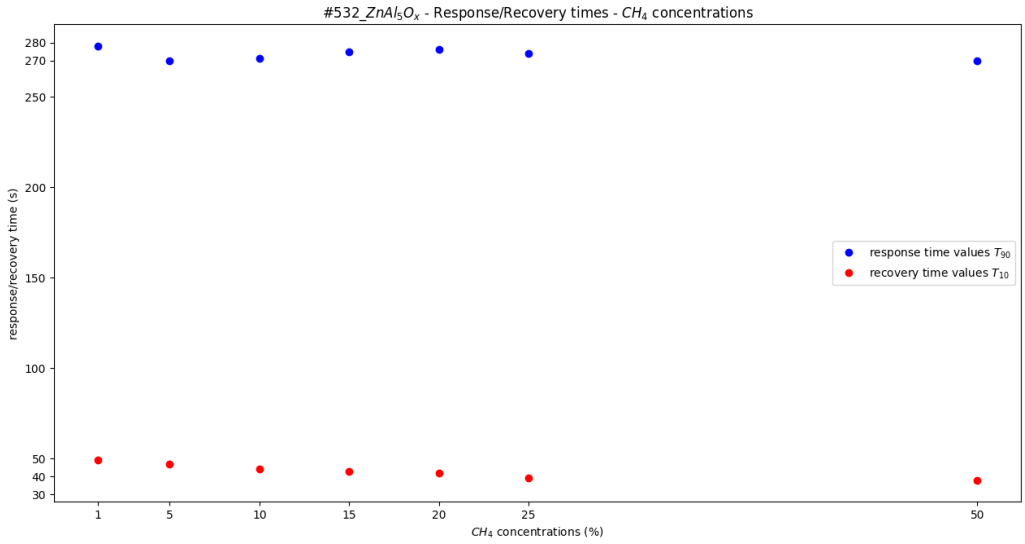

Figure 84: Response / recovery times for the different methane concentrations

This sensor exhibits a remarkable response ~90%, even in the low methane gas concentrations and fast recovery times at each experimental process.

9. Characterization of #534_$ZnAl_5O_x$ – Structural, morphological and optical properties

The structural, morphological and optical properties of #534_$ZnAl_5O_x$ sensing films were examined by using the XRD, SEM, AFM, UV-vis and EDS spectroscopy techniques.

9.1 X-Ray Diffraction analysis

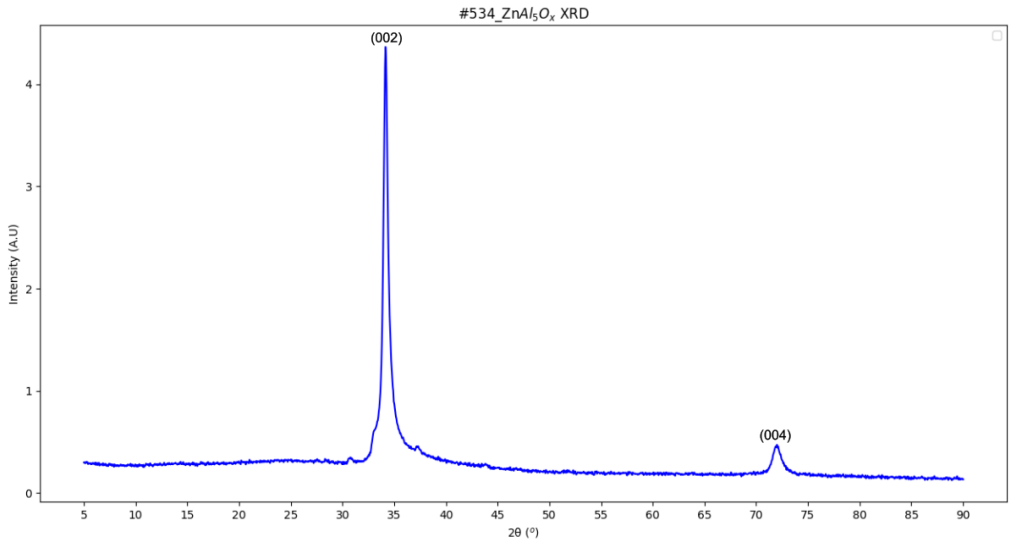

Figure 85: XRD pattern of #534_$ZnAl_5O_x$ sensing film

The XRD spectra were measured in the range of 5° - 90°, exhibiting its main peak at $2\theta_1$=34.19°, corresponding to the crystal plane with Miller indices (hkl)=(002) and a secondary peak at $2\theta_2$=72.02°, corresponding to the crystal plane with Miller indices (hkl)=(004).

Applying Gaussian fitting around the main peak we obtain the full width at half maximum (FWHM) of the peak, which is β=0.0113 rad.

Then, the crystallite size and the interplanar spacing of the sensing material can be calculated by using equations (13) and (14):

$$(13):\ D\ (nm) = \frac{K * \lambda}{\beta * cos\theta} \Rightarrow D = 12.837\ nm$$

$$(14):\ d_{hkl}(\text{Å}) = \frac{n * \lambda}{2 * sin\theta} \Rightarrow d_{002} = 2.620\ \text{Å}$$

After calculating the interplanar spacing, the lattice parameters a,c for the hexagonal wurtzite $ZnAl_5O_x$ structure can be calculated by using equation (15):

$$(15):\ \frac{1}{d^2_{(hkl)}} = \frac{4}{3} * \left(\frac{h^2 + h*k + k^2}{a^2}\right) + \frac{l^2}{c^2} \Rightarrow c^2 = 4 * d^2_{002} \Rightarrow c = 5.241\ \text{Å}$$

Making the assumption that the crystal structure remains the ideal wurtzite and there is low local symmetry distortion for the aluminum doped film, then a close calculation for the lattice parameter a can be made, resulting in a=3.209Å.

Finally, the lattice strain parameter ε_w can be calculated through the equation (16):

$$(16):\ \varepsilon_w = \frac{\beta * cot\theta}{4} \Rightarrow \varepsilon_w = 9.18 * 10^{-3}$$

The same analysis was held for the secondary peak, with the results quoted in the following summarizing table:

Peak 2θ	Crystallite size D (nm)	Interplanar spacing d_{hkl} (Å)	Lattice parameter c (Å)	Lattice parameter a (Å)	Lattice strain ε_w
$2\theta_1$=34.19°	12.837	(hkl)=(002) 2.620	5.241	3.209	$9.18*10^{-3}$
$2\theta_2$=72.02°	9.367	(hkl)=(004) 1.310	5.241	3.209	$6.29*10^{-3}$

Table 29: Structural parameters of #534_$ZnAl_5O_x$ thin film

As well as the #532, #533 developed sensors, the #534 displays its main peak in the same angle, corresponding to (002) crystalline plane. This sensing film is much thicker than the other two, exhibiting also the peak that corresponds to the (004) crystalline plane. Again, we observe that the crystal has strong preference in the c – axis orientation perpendicular to the substrate.

9.2 SEM

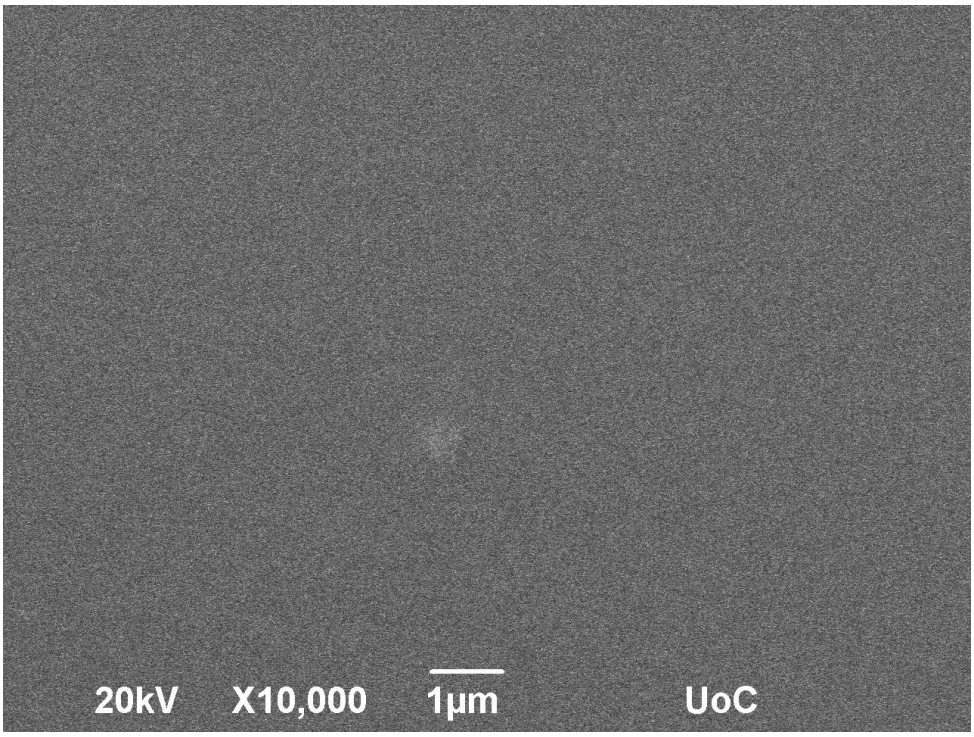

Figure 86: SEM micrograph of #534_$ZnAl_5O_x$ film

The film shows good uniformity and dense surface without visible holes or faulty zones on the film surface.

9.3 AFM

The roughness of the #534_$ZnAl_5O_x$ sensing film was calculated through an AFM measurement. The average roughness value was found to be R_a=0.676nm, while the root mean square value was found to be R_s=0.943nm.

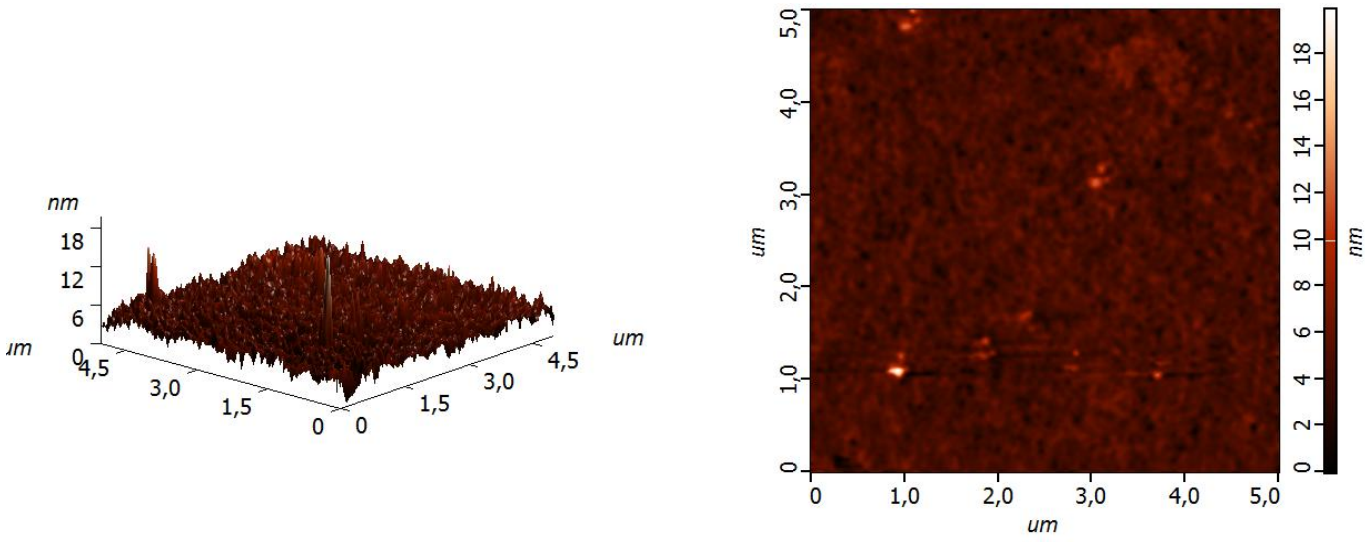

Figure 87: AFM micrographs (4.5µm x 4.5µm) of the #534_$ZnAl_5O_x$ film

9.4 UV-vis spectroscopy

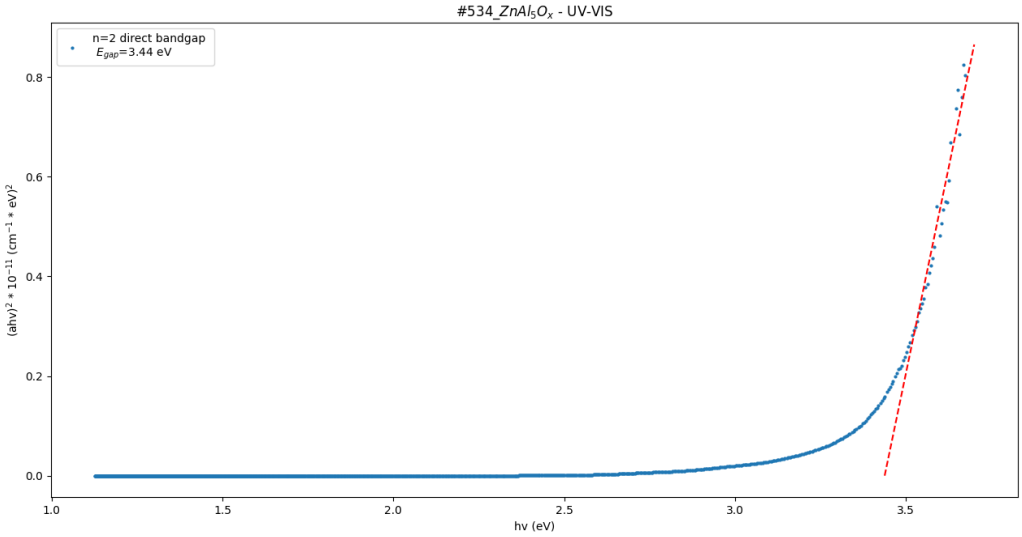

Figure 88: Tauc plot of #534_$ZnAl_5O_x$ for the direct energy band gap case (n=2)

The energy gap was calculated from the linear part of Tauc plot. It appears to be E_g=3.44 eV for the direct band gap case.

9.5 EDS analysis

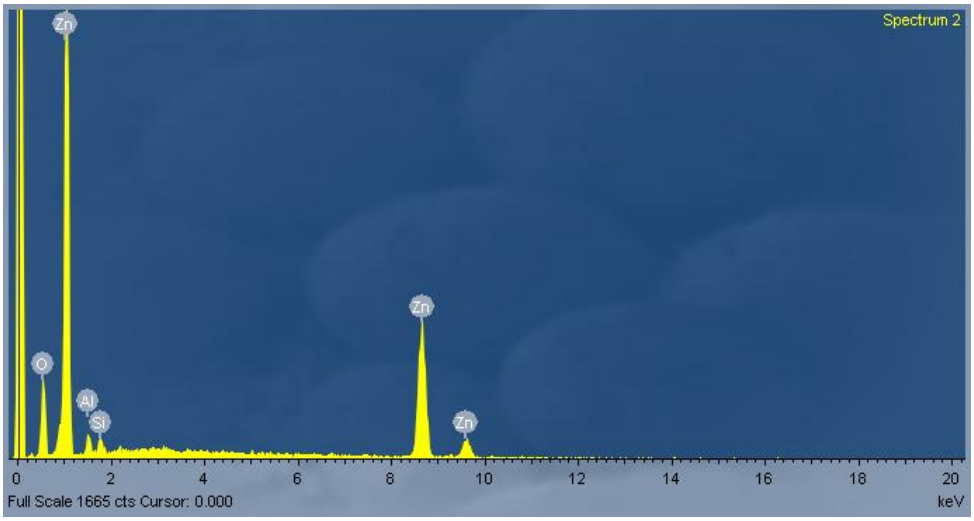

Element	Atomic%
O K	43.14
Al K	3.95
Si K	2.32
Zn K	50.60

Figure 89: Material identified in the #534_$ZnAl_5O_x$ film with EDS technique

From the EDS analysis, the elements of Oxygen:43.14%, Aluminum:3.95%, Zinc:50.60% and Silicon:2.32% were identified with the atomic ratio mentioned above. The atomic ratio of Zn:Al~12.81 indicates the existence of Aluminum as doping element in the ZnO pristine crystal structure. The Si peak is possibly attributed to the glass substrate, thus and the oxygen concentration is overestimated due to the glass substrate.

9.6 I-V characteristics

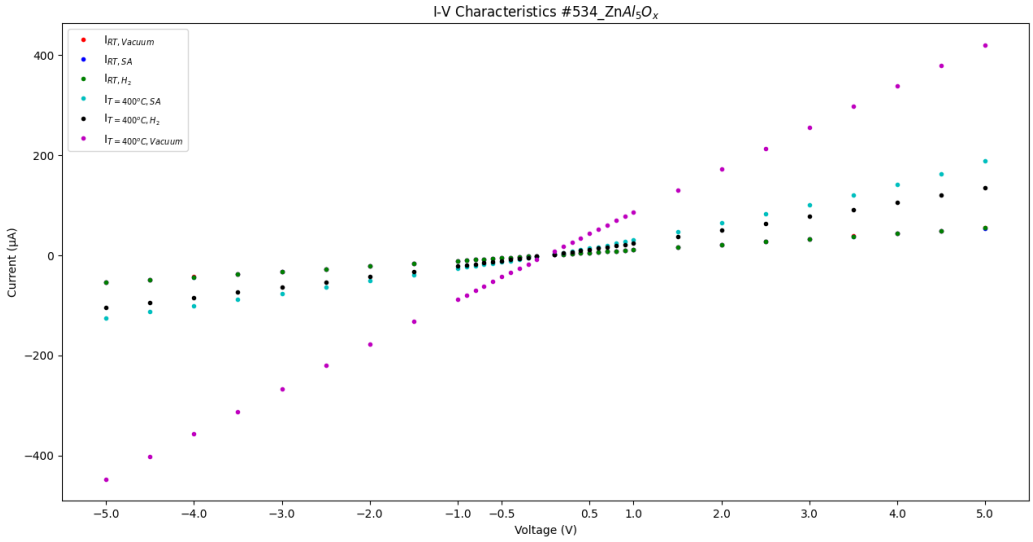

Figure 90: I-V measurements of #534_$ZnAl_5O_x$ sensor operating in room temperature (RT) or at T=400°C under vacuum either in the presence of synthetic air or 1000ppm of hydrogen.

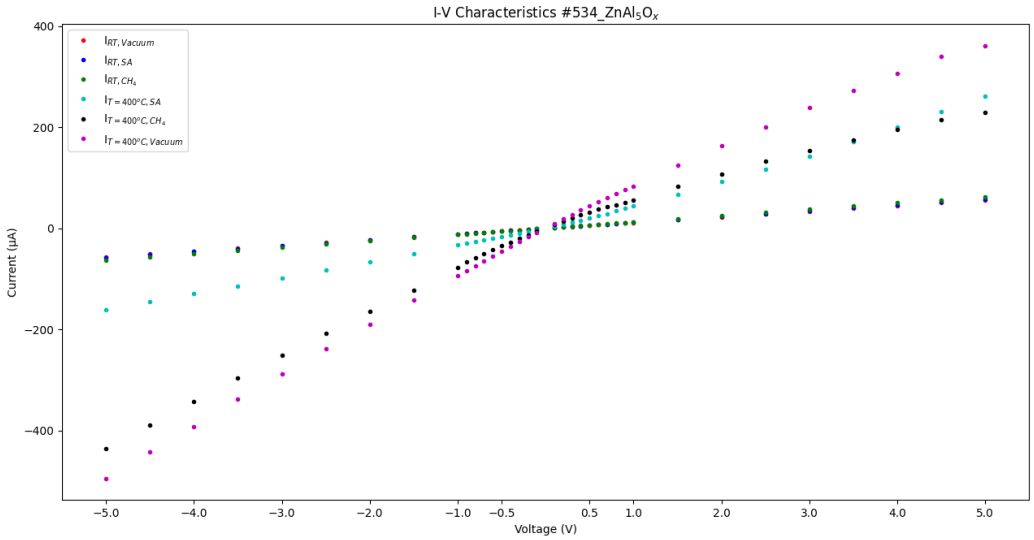

Figure 91: I-V measurements of #534_$ZnAl_5O_x$ sensor operating in room temperature (RT) or at T=400°C under vacuum either in the presence of synthetic air or 100% methane.

For both hydrogen and methane gases, we observe linearity in the I-V characteristics around the applied bias of V=1Volt. That linearity indicates that we have an Ohmic junction.

10. #534_$ZnAl_5O_x$ sensing results

#	Material	Thickness (d)	Sputtering deposition time	Ar	O_2	$I_{sputtering}$	$T_{substrate}$
534	$ZnAl_5O_x$ (ZAO5 Heraeus)	1.050 μm	25min, 30 sec	100% (8sccm)	-	0.45A	RT

Table 30: Sputtering parameters used for #534_$ZnAl_5O_x$ development

10.1 Hydrogen sensing

The developed sensor was tested against H_2 gas sensing. The applied bias was set to be V=1Volt. Then, synthetic air was inserted in the experimental chamber for 20 minutes to obtain a constant current baseline and finally the pressure was stabilized in 800 mbar. To examine the response of the sensor to hydrogen gas, 1000 ppm of hydrogen gas were inserted into the chamber for 5 minutes, while afterwards synthetic air was inserted into the chamber for 5 minutes to examine the recovery of the sensor. This gas alteration was repeated for 5 times (5 experimental cycles – reapitability). Also, different operating temperatures were applied starting from RT to T=400°C with an increasing step of 50°C.

In the analysis following, only the graph for the optimum operating tempeature (T=400°C) that provides the best response of the sensor is exhibited. The rest of the graphs are included in the Appendix B: #534_ ZnAl5Ox – Hydrogen gas sensing.

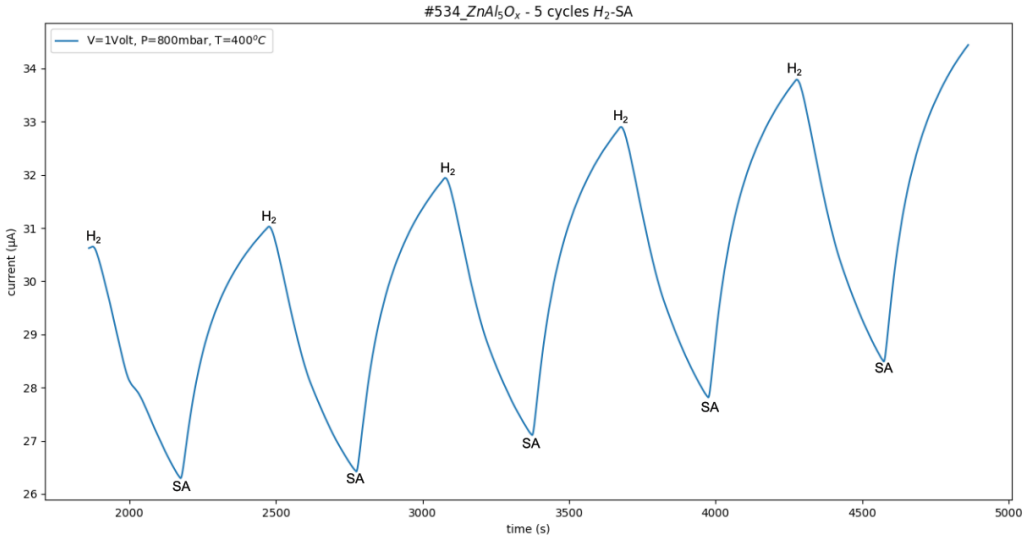

Figure 92: Current – time measurement at T=400°C in the presence of hydrogen

At T=400°C the sensor exhibited its best response and full recovery so we can calculate the response / recovery times and the response (S) of the sensor:

The response time was calculated at the 90% of each peak alteration and its mean value is:

$\overline{T_{90}} = \frac{T_{90}^{(1)}+T_{90}^{(2)}+T_{90}^{(3)}+T_{90}^{(4)}+T_{90}^{(5)}}{5} \Rightarrow \overline{T_{90}} = 252\ sec$, best response time: 248 sec

Similarly, $\overline{T_{10}} = \frac{T_{10}^{(1)}+T_{10}^{(2)}+T_{10}^{(3)}+T_{10}^{(4)}+T_{10}^{(5)}}{5} \Rightarrow \overline{T_{10}} = 230\ sec$, best recovery time: 218 sec

The sensor's response at each cycle was calculated following the equation (1) and the mean response value is equal to: $\bar{S} = 17.74$

Sensor: #534_$ZnAl_5Ox$			
Temperature (°C)	Sensitivity (%)	Response time T_{90} (best) [sec]	Recovery time T_{10} (best) [sec]
300	1.72	267 (259)	234(227)
350	6.72	262 (247)	229 (210)
400	17.74	252 (248)	230 (218)

Table 31: Sensitivity – response, response / recovery times of the sensor for different operating temperatures

By using the data of the table 28, we can plot the response S of the sensor and the response / recovery times as function of the different operating temperatures:

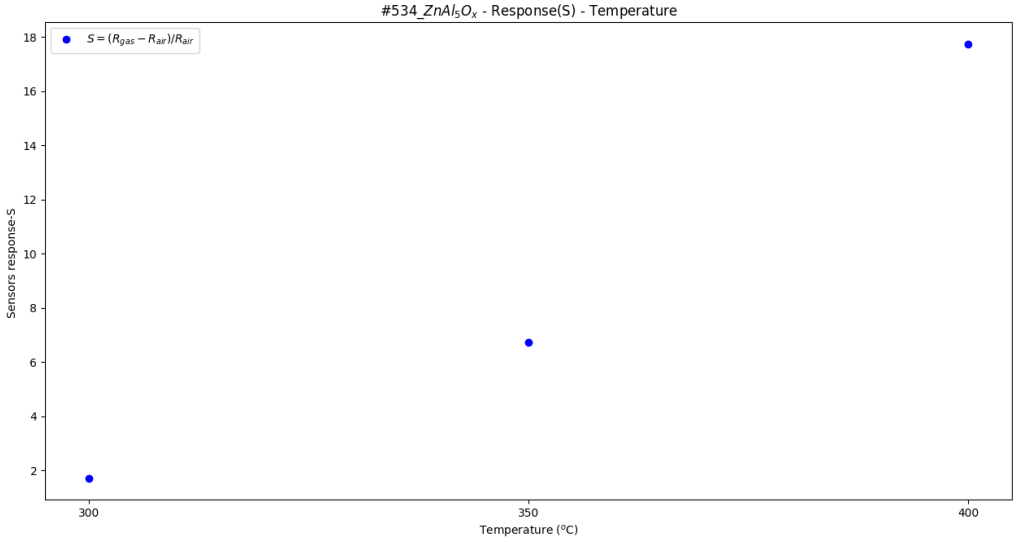

Figure 93: Sensor's response S for the different operating temperatures

This sensor was functional only in the high operating temperatures. At temperatures lower than T=300°C, the sensor did not exhibit response and recovery pattern at all.

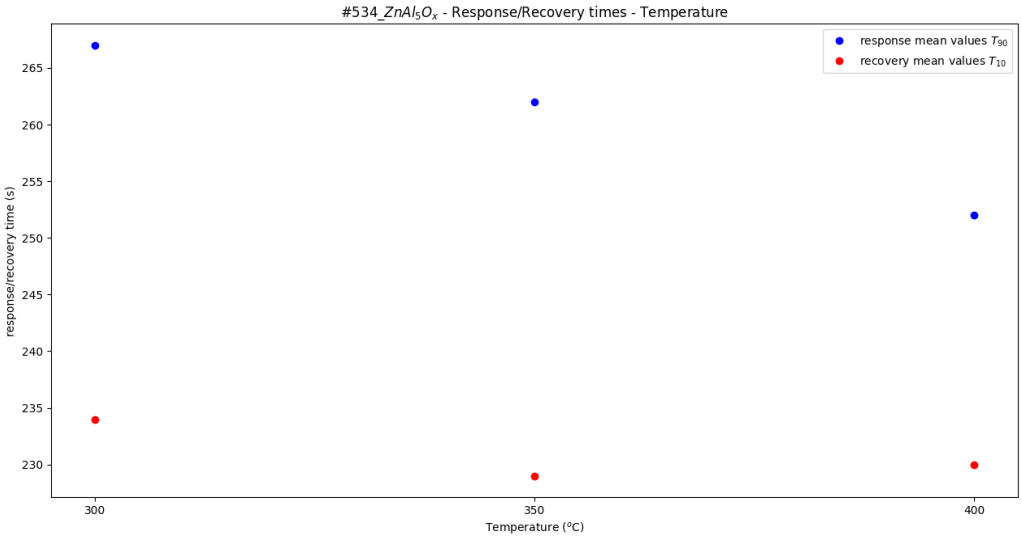

Figure 94: Response / recovery times of the sensor for the different operating temperatures

The response time varied from 267 sec to 252 sec, exhibiting a decline with the temperature increase, while the recovery time remained almost constant varying from 229 sec to 234 sec.

At T=400°C, the response of the sensor was examined for different hydrogen concentrations in order to find the lower detection limit of hydrogen that can be sensed. The dilution of the hydrogen gas was achieved as hydrogen + synthetic air mixture.

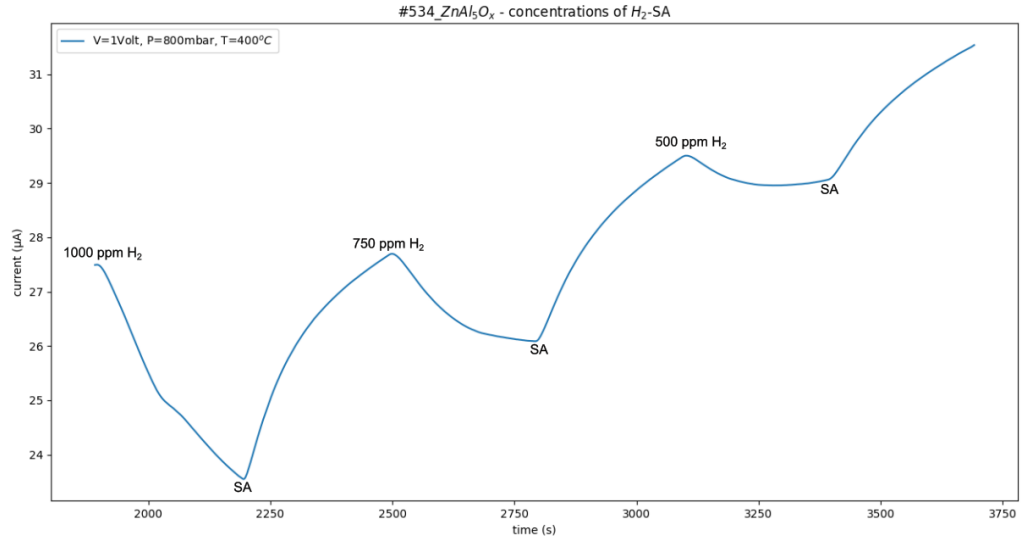

Figure 95: Current – time measurement at T=400°C in the presence of different hydrogen gas concentrations

Hydrogen concentrations	Sensitivity (%)	Response time T_{90} (sec)	Recovery time T_{10} (sec)
100% → 1000 ppm	16.56	249	234
75% → 750 ppm	6.34	189	249
50% → 500 ppm	1.56	88	252

Table 32: Sensitivity – response, response / recovery times of the sensor for the different hydrogen concentrations

From the data of the table 29, we can plot the response of the sensor and the response / recovery times in function with the different hydrogen gas concentration:

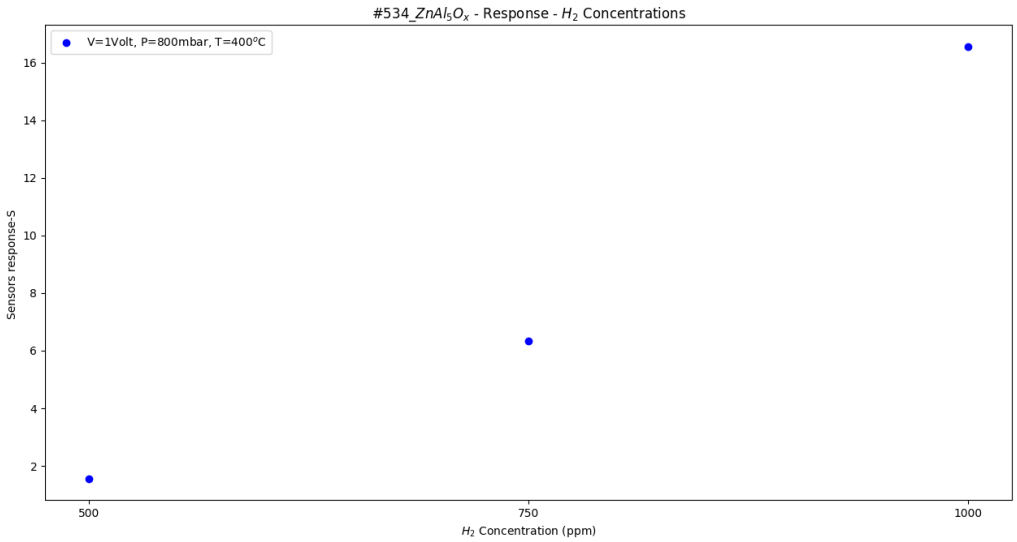

Figure 96: Sensor's response S for the different hydrogen gas concentrations

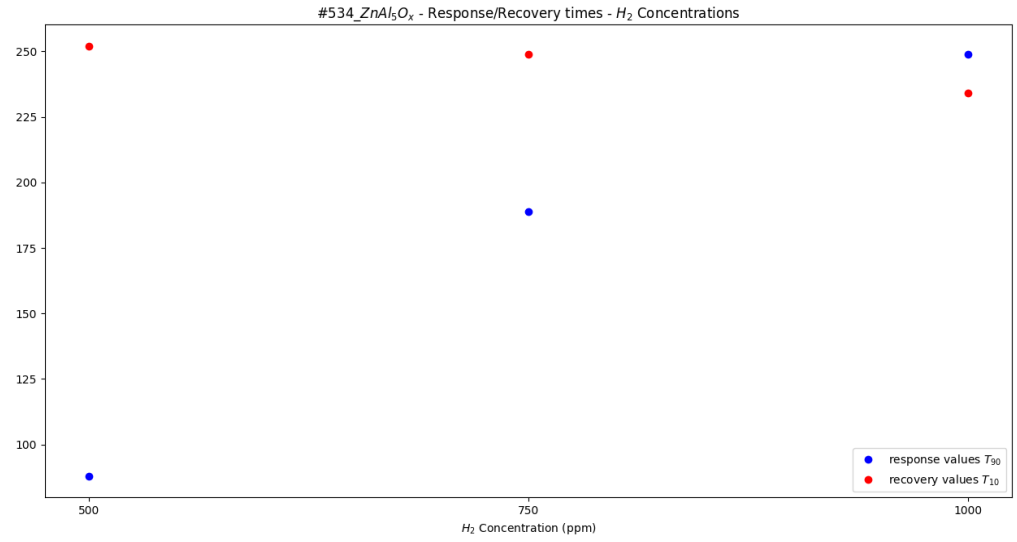

Figure 97: Response / recovery times of the sensor for the different hydrogen concentrations

The highest response of the sensor occurs at the maximum hydrogen concentration of 1000 ppm. The response time exhibited a remarkable decrease from 249 sec at 1000 ppm to 88 sec at 500 ppm, while the recovery time remained at the same level, varying from 234 sec to 252 sec.

10.2 Methane sensing

The same experimental process was repeated in the case of methane gas. The applied bias was set to be V=1Volt. Then, synthetic air was inserted in the experimental chamber for 20 minutes to obtain a constant current baseline and finally the pressure was stabilized in 800 mbar. To examine the response of the methane gas, pure methane was inserted into the chamber for 5 minutes, while afterwards synthetic air was inserted into the chamber for 5 minutes to examine the recovery of the sensor. The gas alteration was repeated for 5 times (5 experimental cycles – repeatability) and different operating temperatures were applied starting from RT to T=400°C with an increasing step of 50°C.

In the analysis following, only the graph for the optimal operating temperature (T=400°C) that provides the best response of the sensor is exhibited. The rest of the graphs are included in the Appendix B: #534_ZnAl5Ox – Methane gas sensing.

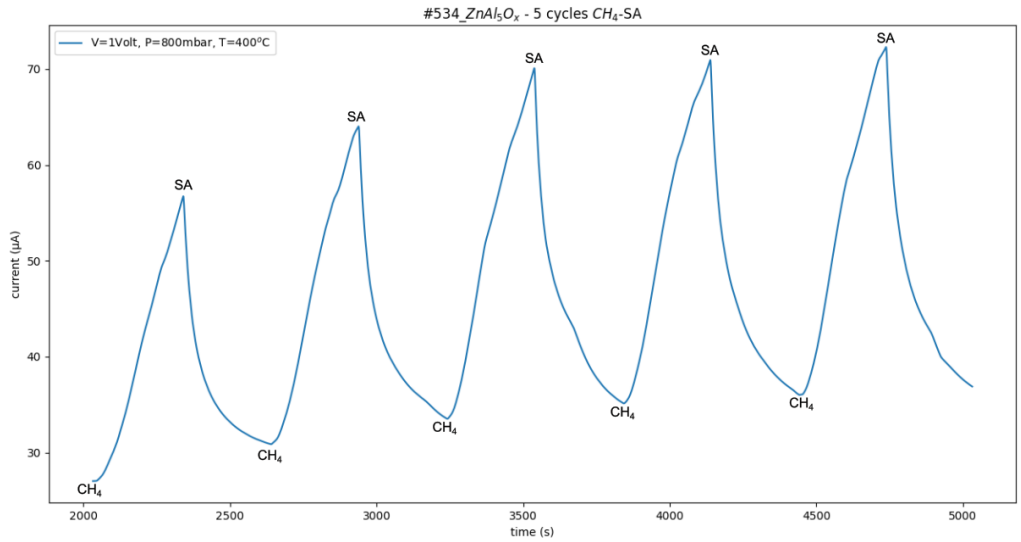

Figure 98: Current – time measurement at T=400°C in the presence of methane

At T=400°C the sensor exhibited its best response and full recovery so we can calculate the response / recovery times and the response (S) of the sensor:

The response time was calculated at the 90% of each peak alteration and its mean value is:

$\overline{T_{90}} = \frac{T_{90}^{(1)}+T_{90}^{(2)}+T_{90}^{(3)}+T_{90}^{(4)}+T_{90}^{(5)}}{5} \Rightarrow \overline{T_{90}} = 270\ sec$, best response time: 260 sec

Similarly, $\overline{T_{10}} = \frac{T_{10}^{(1)}+T_{10}^{(2)}+T_{10}^{(3)}+T_{10}^{(4)}+T_{10}^{(5)}}{5} \Rightarrow \overline{T_{10}} = 182\ sec$, best recovery time: 153 sec

The sensor's response at each cycle was calculated following the equation (1) and the mean response value is equal to: $\bar{S} = 51.11$

Sensor: #534_$ZnAl_5Ox$			
Temperature (°C)	Sensitivity (%)	Response time T_{90} (best) [sec]	Recovery time T_{10} (best) [sec]
250	5.46	274 (272)	224 (210)
300	7.17	274 (270)	231 (205)
350	23.08	269 (259)	231 (214)
400	51.11	270 (260)	182 (153)

Table 33: Sensitivity – response, response / recovery times of the sensor for different operating temperatures

By using the data of the table 30, we can plot the response of the sensor, the response and recovery times as function of the different operating temperatures:

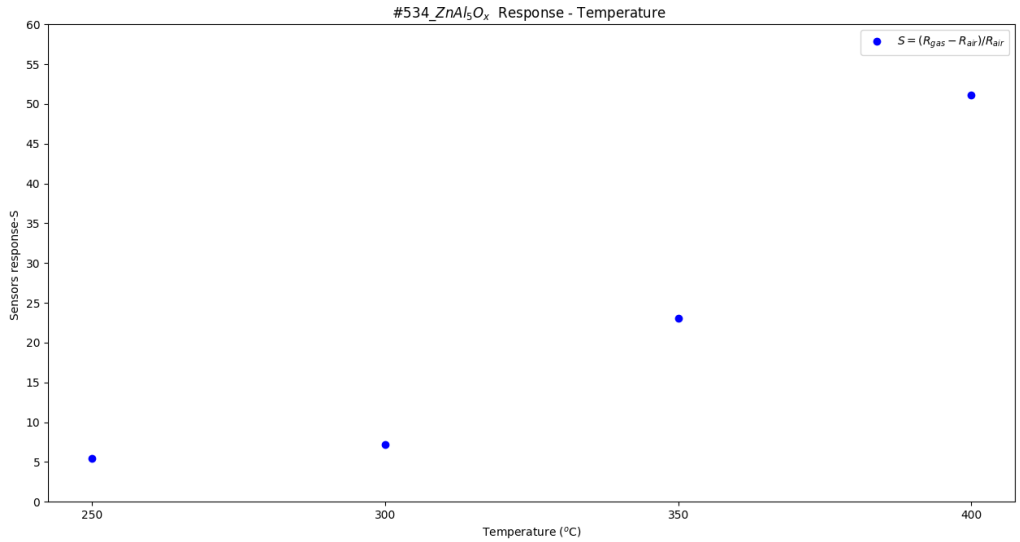

Figure 99: Sensor's response for the different operating temperature

At T=400°C the sensor exhibits its highest response S=51%. Decreasing the applied temperature, results in the decrease of the sensor's response.

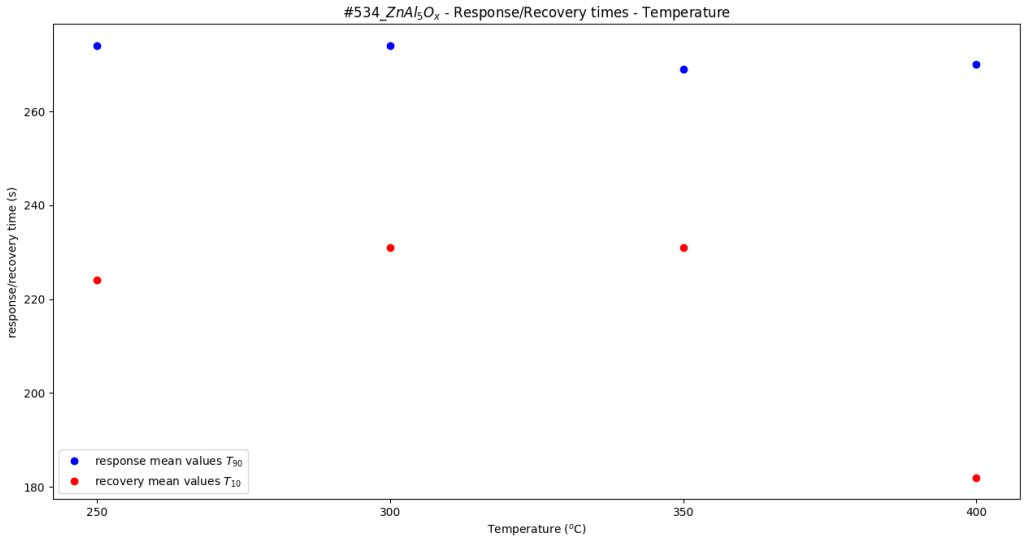

Figure 100: Response / recovery times of the sensor at different operating temperatures

The response times of the sensor are around 270 sec, while the recovery times vary from 182 sec and 231 sec.

Furthermore, the response of the sensor was examined for different methane concentrations at T=400°C. The dilution in the pure methane was achieved by adding N_2 gas.

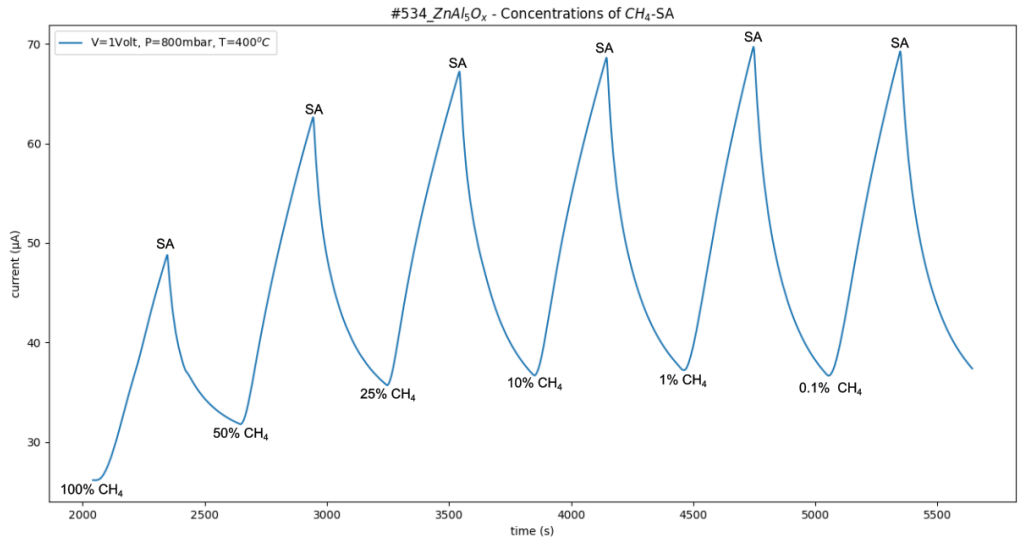

Figure 101: Current – time measurement at T=400°C in the presence of different methane concentrations

CH_4 concentrations	Sensitivity (%)	Response time T_{90} (sec)	Recovery time T_{10} (sec)
100%	45.92	276	189
50%	49.32	263	200
25%	46.51	259	210
10%	46.24	268	214
1%	46.37	268	208
0.1%	46.85	272	209

Table 34: Sensitivity – response, response / recovery times of the sensor for the different methane concentrations

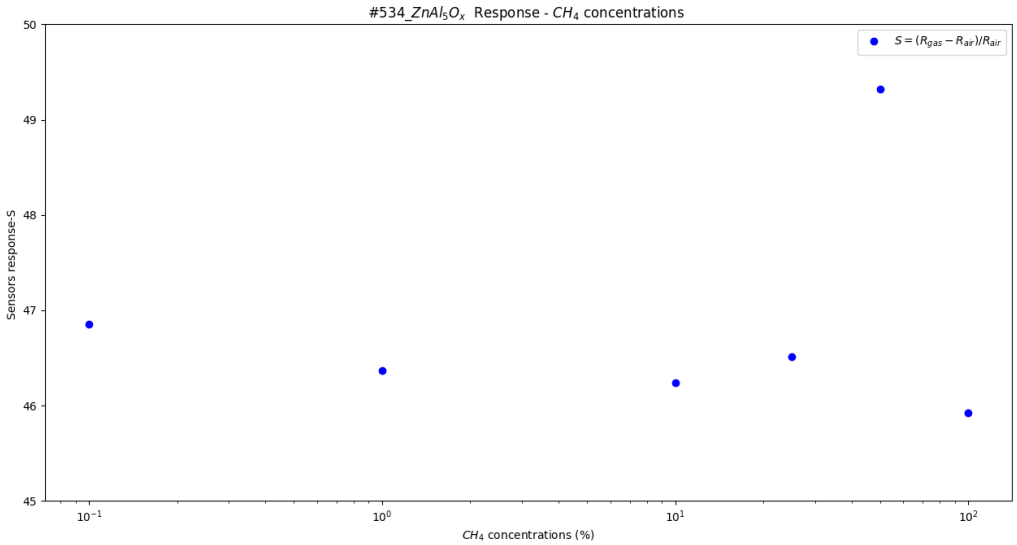

Figure 102: Sensor's response for the different methane concentrations

This sensor seems to reach a saturation state when pure methane is inserted to the experimental chamber. The response of the sensor is quite stable, varying from 45.92% to 49.32%.

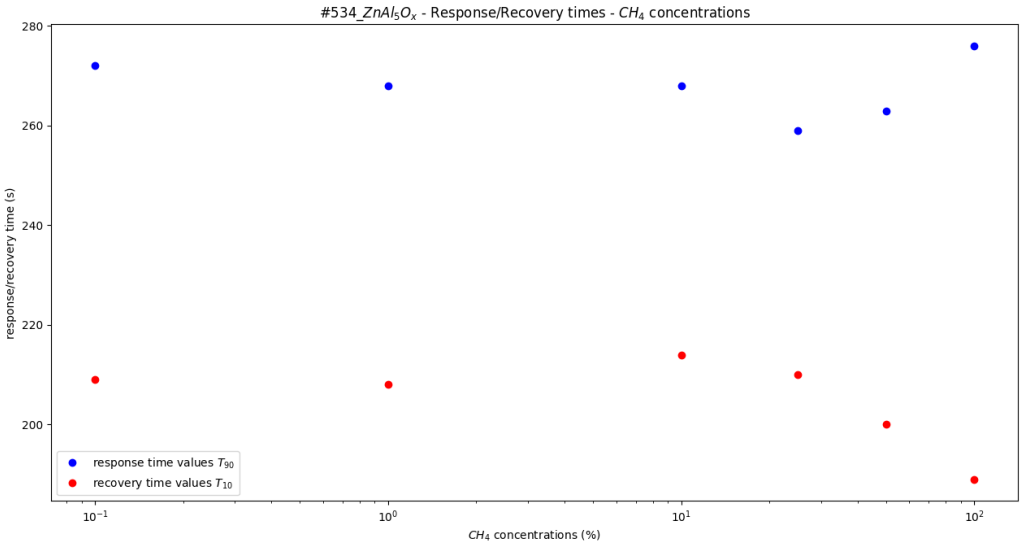

Figure 103: Response / recovery times of the sensor for different operating temperatures

The response time of the sensor remains around 270 sec, while the recovery time varies from 189 sec to 214 sec. The fastest recovery occurs in the case of the minimum methane gas concentration.

c) $ZnAlSiO_x$ gas sensors results

11. Characterization of #530_$ZnAlSiO_x$ – Structural, morphological and optical properties

In order to determine the morphological, structural and optical properties of the #530_$ZnAlSiO_x$ sensing films, XRD, SEM, AFM and UV-vis spectroscopy techniques were utilized.

11.1X-Ray Diffraction analysis

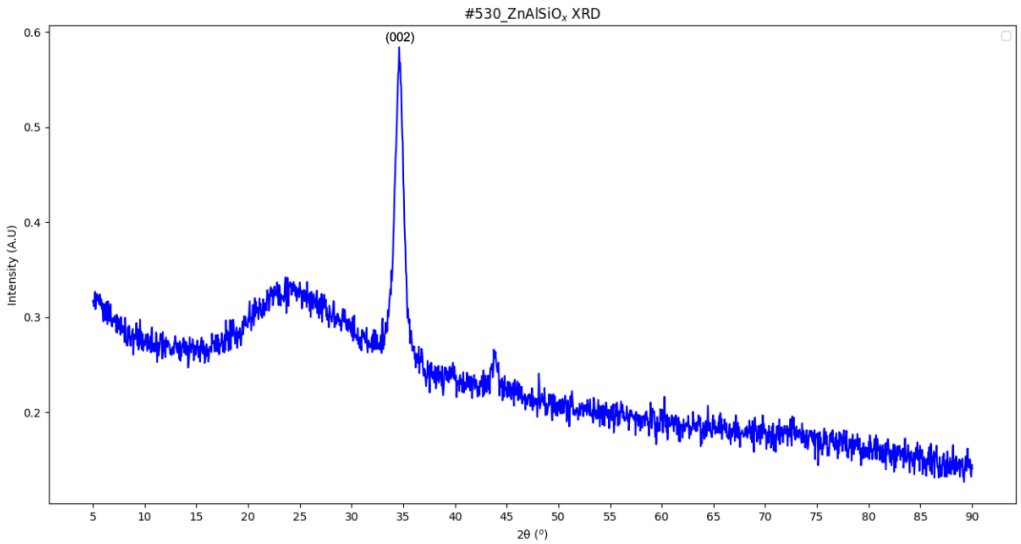

Figure 104: XRD pattern of #530_$ZnAlSiO_x$ sensing film

The XRD spectra were measured in the range of 5° - 90°, exhibiting the main peak of $ZnAlSiO_x$ at $2\theta_1$=34.61°.

According to bibliography, the main peak θ_1 corresponds to the crystal plane with Miller indices (hkl)=(002).

Applying Gaussian fitting around the main peak, we can obtain the full width at half maximum (FWHM) of the peak, which is β=0.0176 rad.

Then, the crystallite size and the interplanar spacing of the sensing material can be calculated by using the equations (13) and (14):

$$(13):\ D\ (nm) = \frac{K * \lambda}{\beta * cos\theta} \Rightarrow D = 8.252\ nm$$

$$(14):\ d_{hkl}(\text{Å}) = \frac{n * \lambda}{2 * sin\theta} \Rightarrow d_{002} = 2.590\ \text{Å}$$

After calculating the interplanar spacing, the lattice parameters a, c for the hexagonal wurtzite structure can be calculated by using equation (15):

$$(15):\ \frac{1}{d^2_{(hkl)}} = \frac{4}{3} * \left(\frac{h^2 + h * k + k^2}{a^2}\right) + \frac{l^2}{c^2} \Rightarrow c^2 = 4 * d^2_{002} \Rightarrow c = 5.179\ \text{Å}$$

Making the assumption that there is low local symmetry distortion for the co-doped with Aluminum and Silicon sensing film, then c/a ratio remains constant and a close calculation for the lattice parameter a can be made resulting in a=3.172Å.

Finally, the lattice strain parameter ε_w is calculated through the equation (16):

$$(16):\ \varepsilon_w = \frac{\beta * cot\theta}{4} \Rightarrow \varepsilon_w = 1.41 * 10^{-2}$$

A summarizing table for the obtained result follows:

Peak 2θ	Crystallite size D (nm)	Interplanar spacing d_{hkl} (Å)	Lattice parameter c (Å)	Lattice parameter a (Å)	Lattice strain ε_w
$2\theta_1$=34.61°	8.252	(hkl)=(002) 2.590	5.179	3.172	$1.41*10^{-2}$

Table 35: Structural parameters of #530_ZnAlSiO_x thin film

The #530 developed sensor exhibits its highest peak corresponding to the (002) crystalline plane, indicating that the crystal has strong preference in the c – axis orientation perpendicular to the substrate.

11.2 SEM

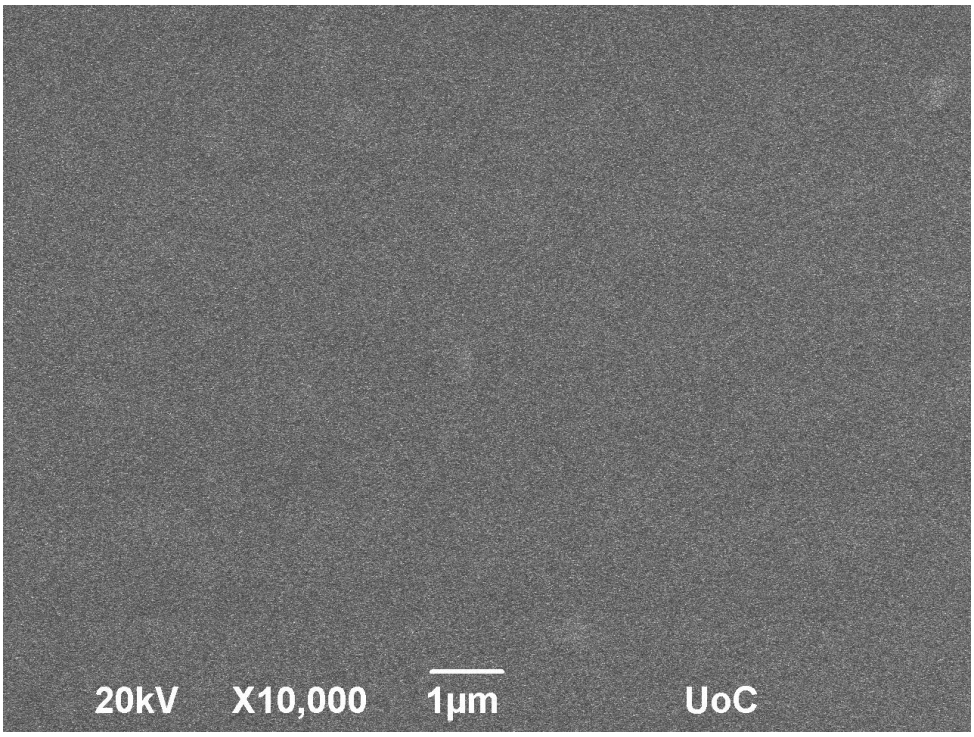

Figure 105: SEM micrograph of #530_ZnAlSiO$_x$ film

11.3 AFM

The roughness of the #530_ZnAlSiO$_x$ sensing film was calculated through an AFM measurement. The average roughness value was found to be R_a=2.433nm, while the root mean square value was found to be R_s=4.144nm.

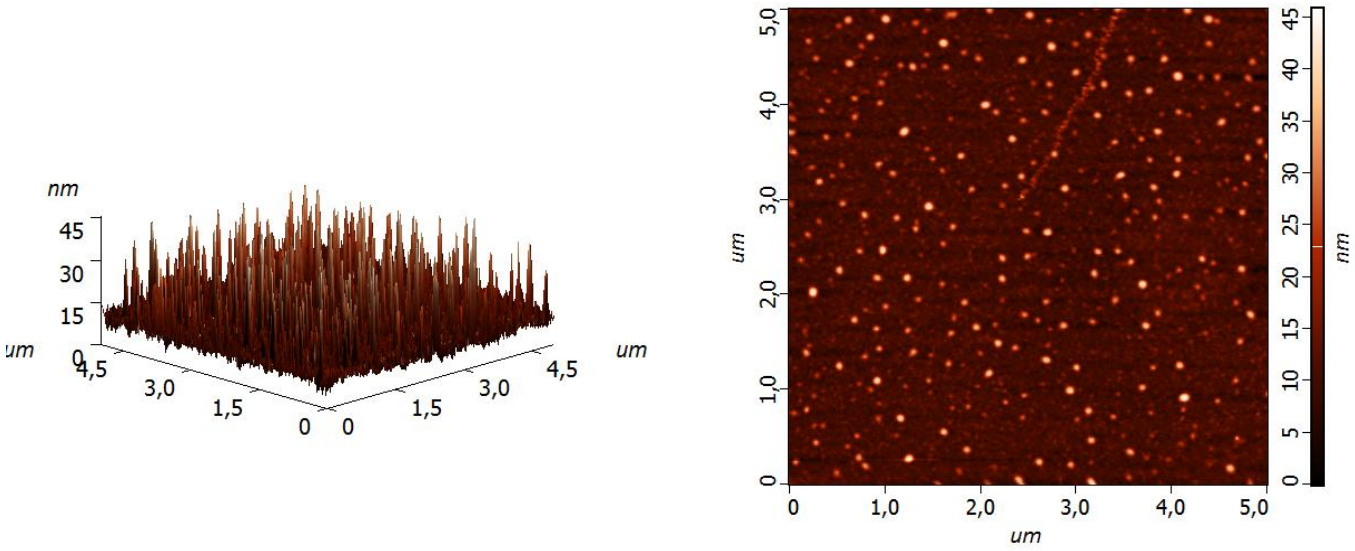

Figure 106: 3D and 2D AFM micrographs (4.5µm x 4.5µm) of the #530_ZnAlSiO$_x$ film

11.4 UV-vis spectroscopy

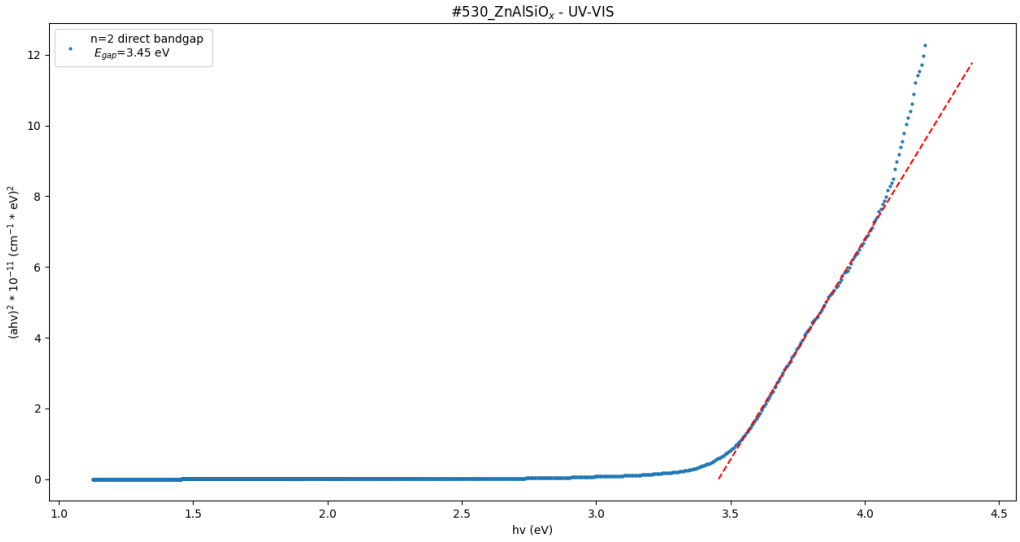

Figure 107: Tauc plot of #530_ZnAlSiO$_x$ for the direct energy band gap case (n=2)

The energy band gap was calculated from the linear part of Tauc plot. It appears to be E_g=3.45 Ev for the direct band gap case. The obtained energy gap value is in the energy gap value range that is mentioned in the bibliography.

11.5 I-V characteristics

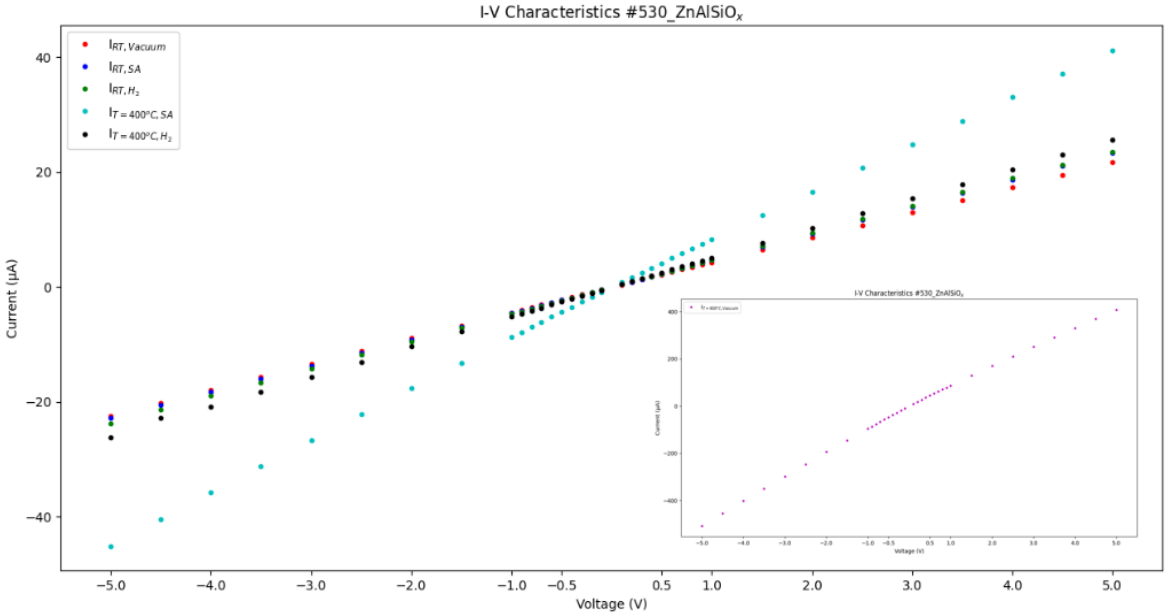

Figure 108: I-V measurements of #530_ZnAlSiO$_x$ sensor operating in room temperature (RT) or at T=400°C under vacuum either in the presence of synthetic air or 1000ppm of hydrogen. In the inset of the diagram, the case of vacuum at T=400°C is depicted.

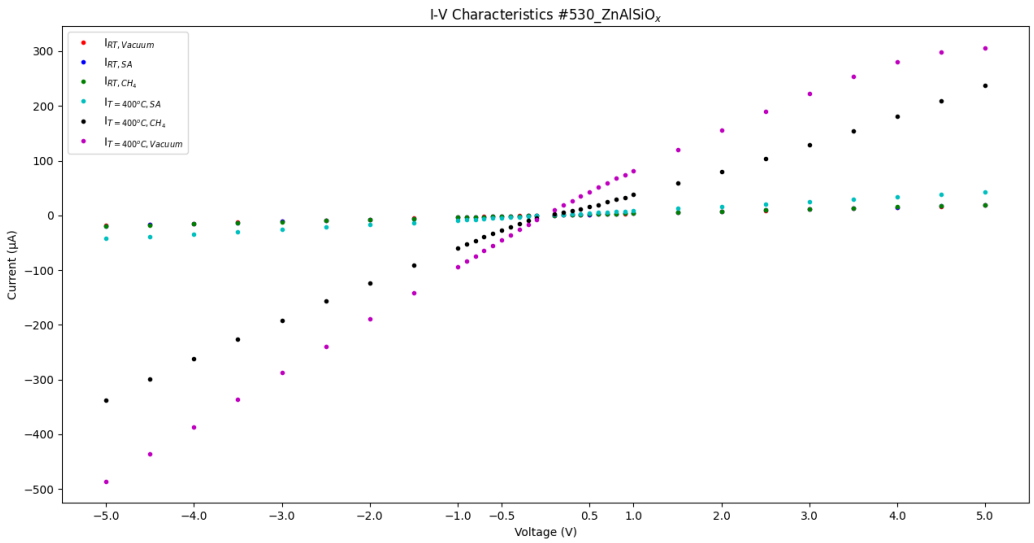

Figure 109: I-V measurements of #530_ZnAlSiO$_x$ sensor operating in room temperature (RT) or at T=400°C under vacuum either in the presence of synthetic air or 100% methane.

For both hydrogen and methane gases, we observe linearity in the I-V characteristics around the applied bias of V=1Volt. That linearity indicates that we have an Ohmic junction.

12. #530_ZnAlSiO$_x$ sensing results

#	Material	Thickness (d)	Sputtering deposition time	Ar	O_2	$I_{sputtering}$	$T_{substrate}$
530	ZnAlSiO$_x$ (ZAO2D Heraeus)	101.5 nm	6 min	100% (8sccm)	-	0.25A	RT

Table 36: Sputtering parameters used for #530_ZnAlSiO$_x$ development

12.1 Hydrogen sensing

The developed sensor was tested against H_2 gas sensing. The applied bias was set to be V=1Volt. Then, synthetic air was inserted in the experimental chamber for 20 minutes to obtain a constant current baseline and finally the pressure was stabilized in 800 mbar. To examine the response of the sensor to hydrogen gas, 1000 ppm of hydrogen gas were inserted into the chamber for 5 minutes, while afterwards synthetic air was inserted into the chamber for 5 minutes to examine the recovery of the sensor. This gas alteration was repeated for 5 times (5 experimental cycles – reapitability). Also, different operating temperatures were applied starting from RT to T=400°C with an increasing step of 50°C.

In the analysis following, only the graph for the optimum operating tempeature (T=400°C) that provides the best response of the sensor is exhibited. The rest of the graphs are included in the Appendix C: #530_ZnAlSiOx – Hydrogen gas sensing.

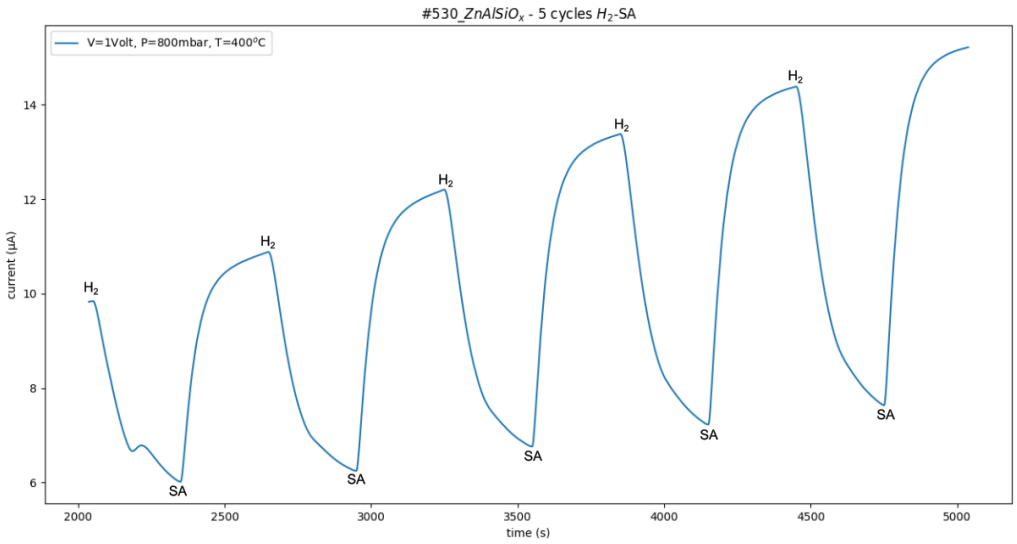

Figure 110: Current – time measurement at T=400°C in the presence of hydrogen

At T=400°C the sensor exhibited its best response and full recovery so we can calculate the response / recovery times and the response (S) of the sensor:

The response time was calculated at the 90% of each peak alteration and its mean value is:

$\overline{T_{90}} = \frac{T_{90}^{(1)}+T_{90}^{(2)}+T_{90}^{(3)}+T_{90}^{(4)}+T_{90}^{(5)}}{5} \Rightarrow \overline{T_{90}} = 210\ sec$, best response time: 196 sec

Similarly, $\overline{T_{10}} = \frac{T_{10}^{(1)}+T_{10}^{(2)}+T_{10}^{(3)}+T_{10}^{(4)}+T_{10}^{(5)}}{5} \Rightarrow \overline{T_{10}} = 145\ sec$, best recovery time: 134 sec

The sensor's response at each cycle was calculated following the equation (1) and the mean response value is equal to: $\bar{S} = 78.20$

Sensor: #530_ZnAlSiOx			
Temperature (°C)	Sensitivity (%)	Response time T_{90} (best) [sec]	Recovery time T_{10} (best) [sec]
250	2.24	274 (259)	261 (247)
300	13.37	279 (275)	249 (239)
350	64.03	251 (243)	220 (216)
400	78.2	210 (196)	145 (134)

Table 37: Sensitivity – response, response / recovery times of the sensor for the different operating temperatures

By using the data of Table 34, we can plot the response S of the sensor and the response / recovery times as function of the different operating temperatures:

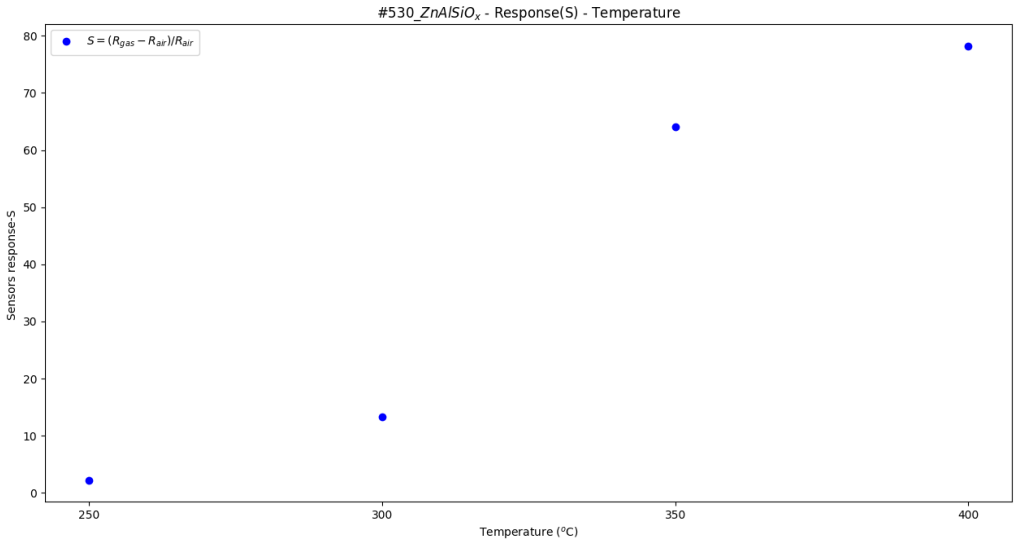

Figure 111: Sensor's response S for the different operating temperatures

In the operating temperature range of T=250°C – T=400°C, the sensor appears to have its maximum response at T=400°C. Lower operating temperatures result in lower response values.

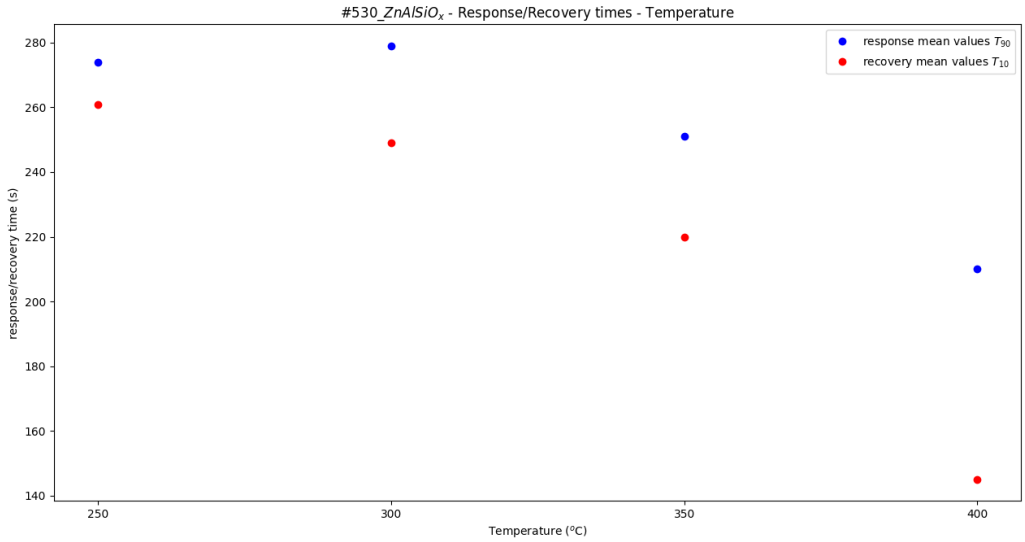

Figure 112: Response / recovery times of the sensor for the different operating temperatures

The response time varied from 279 sec to 210 sec, while the recovery time varied from 261 sec to 145 sec. Best response and recovery times obtained for the optimal operating temperature.

At T=400°C, the response of the sensor was examined for different hydrogen concentrations in order to find the lower detection limit of hydrogen that can be sensed. The dilution of the hydrogen was achieved as hydrogen + synthetic air mixture.

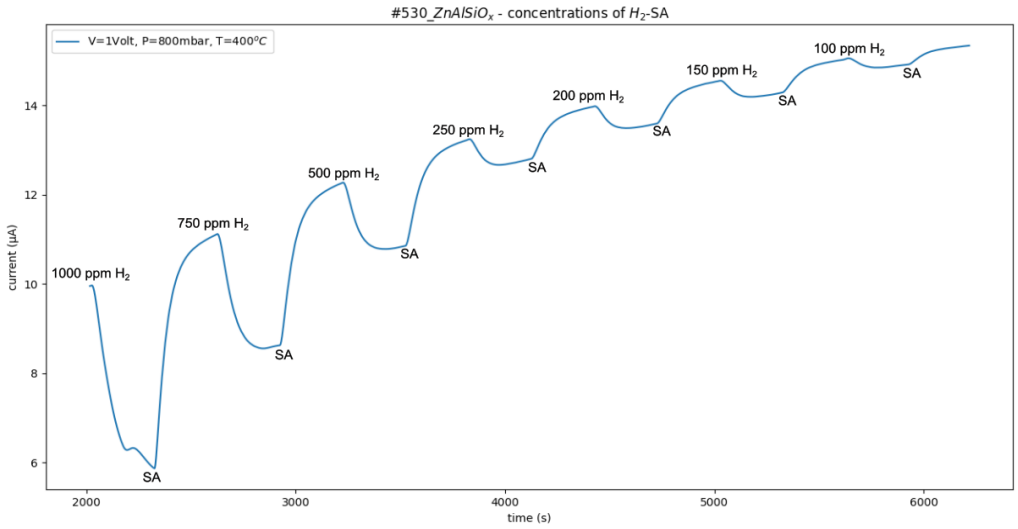

Figure 113: Current - time measurement in the presence of different hydrogen concentrations

Hydrogen concentrations	Sensitivity (%)	Response time T_{90} (sec)	Recovery time T_{10} (sec)
100% →1000 ppm	68.21	155	173
75% →750 ppm	28.21	133	179
50% →500 ppm	12.03	96	170
25% →250 ppm	3.18	80	213
20% →200 ppm	3.35	84	213
15% →150 ppm	2.62	78	201
10% →100 ppm	0.6	87	177

Table 38: Sensitivity – response, response / recovery times of the sensor for the different hydrogen concentrations

The response of the sensor takes its highest value at 1000 ppm of hydrogen concentration and declines rapidly with the decrease of hydrogen gas concentration.

From table 35, we can plot the response of the sensor and the response and recovery times in function with the different hydrogen gas concentration.

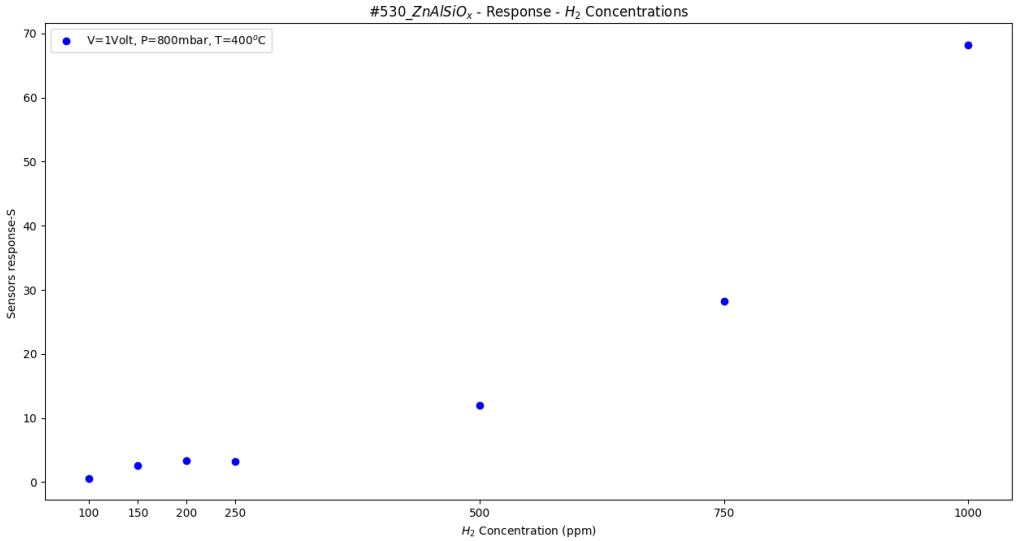

Figure 114: Sensor's response for the different hydrogen gas concentrations

At hydrogen concentration lower than 250 ppm, the response of the sensor exhibits linear dependence to hydrogen gas concentration. After applying a linear fitting we can find the detection limit (intersection of fitting with the x – axis), which is found to be 42 ppm.

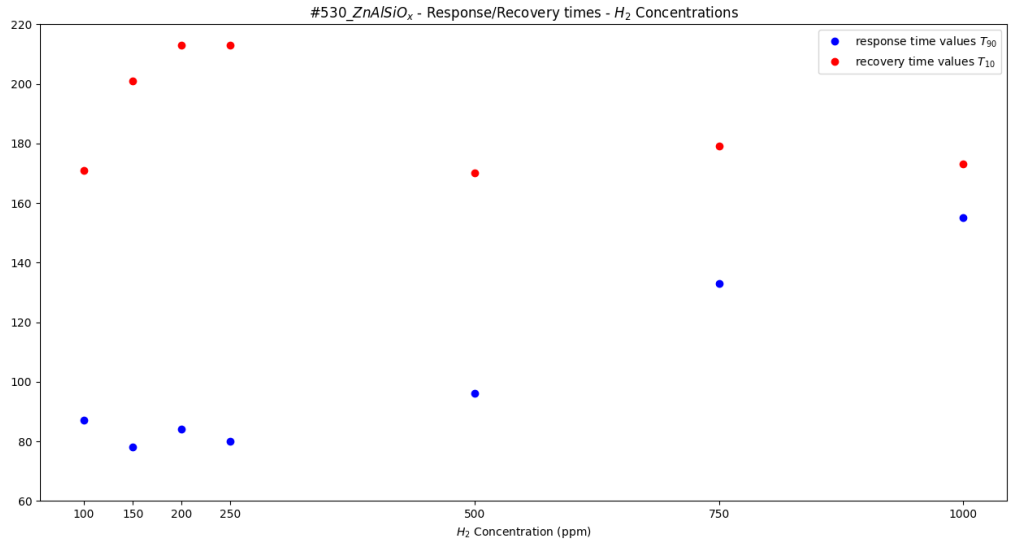

Figure 115: Response / recovery times of the sensor for the different hydrogen concentrations

The response time of the sensor exhibit its low value range at the low hydrogen gas concentration, while for recovery time the reversal behavior occurs.

12.2 Methane sensing

The same experimental process was repeated in the case of methane gas. The applied bias was set to be V=1Volt. Then, synthetic air was inserted in the experimental chamber for 20 minutes to obtain a constant current baseline and finally the pressure was stabilized in 800 mbar. To examine the response of the methane gas, pure methane was inserted into the chamber for 5 minutes, while afterwards synthetic air was inserted into the chamber for 5 minutes to examine the recovery of the sensor. The gas alteration was repeated for 5 times (5 experimental cycles – repeatability) and different operating temperatures were applied starting from RT to T=400°C with an increasing step of 50°C.

In the analysis following, only the graph for the optimal operating temperature (T=400°C) that provides the best response of the sensor is exhibited. The rest of the graphs are included in the Appendix C: #530_ZnAlSiOx – Methane gas sensing.

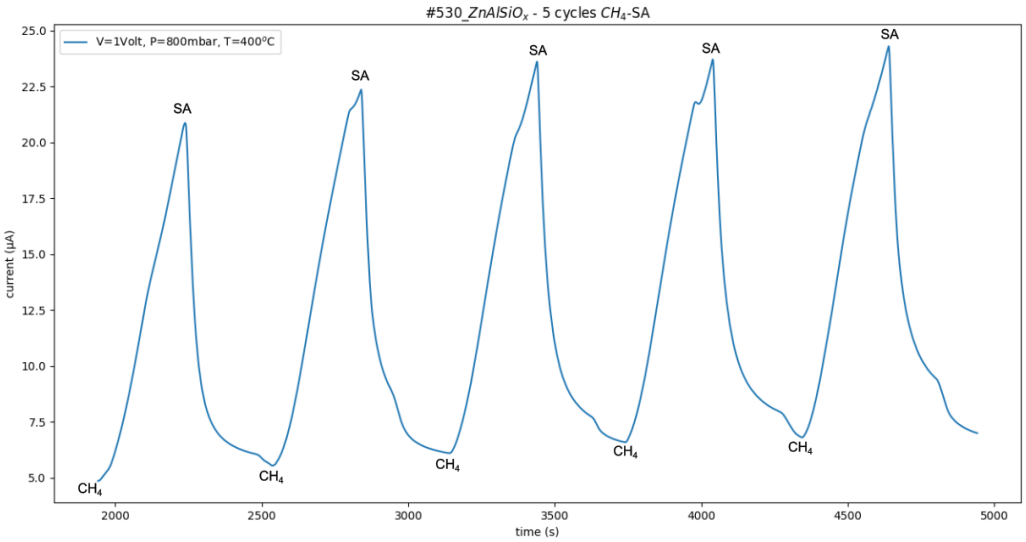

Figure 116: Current – time measurement at T=400°C in the presence of methane

At T=400°C the sensor exhibited its best response and full recovery so we can calculate the response / recovery times and the response (S) of the sensor:

The response time was calculated at the 90% of each peak alteration and its mean value is:

$\overline{T_{90}} = \frac{T_{90}^{(1)}+T_{90}^{(2)}+T_{90}^{(3)}+T_{90}^{(4)}+T_{90}^{(5)}}{5} \Rightarrow \overline{T_{90}} = 263\ sec$, best response time: 248 sec

Similarly, $\overline{T_{10}} = \frac{T_{10}^{(1)}+T_{10}^{(2)}+T_{10}^{(3)}+T_{10}^{(4)}+T_{10}^{(5)}}{5} \Rightarrow \overline{T_{10}} = 148\ sec$, best recovery time: 111 sec

The sensor's response at each cycle was calculated following the equation (1) and the mean response value is equal to: $\bar{S} = 73.79$

Sensor: #530_ZnAlSiOx			
Temperature (°C)	Sensitivity (%)	Response time T_{90} (best) [sec]	Recovery time T_{10} (best) [sec]
250	9.00	272 (258)	229 (191)
300	23.97	272 (256)	258 (241)
350	51.66	274 (270)	218 (205)
400	73.79	263 (248)	148 (111)

Table 39: Sensitivity – response, response / recovery times of the sensor for the different applied temperatures

By using the data of Table 36, we can plot the response S of the sensor and the response / recovery times as function of the different operating temperatures.

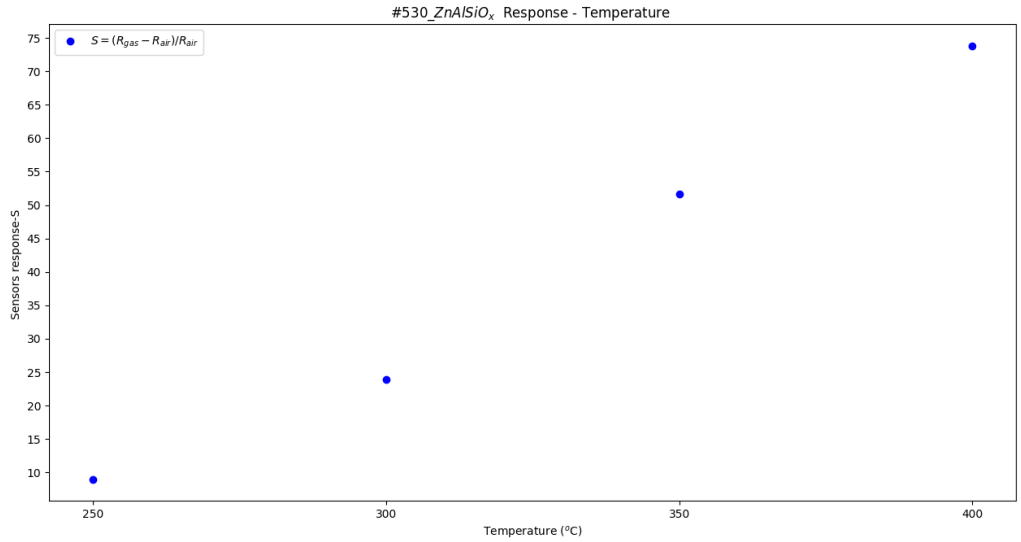

Figure 117: Sensor's response for the different operating temperatures

In this case, the sensor exhibits high response to methane gas that gradually increase with the rise of temperature.

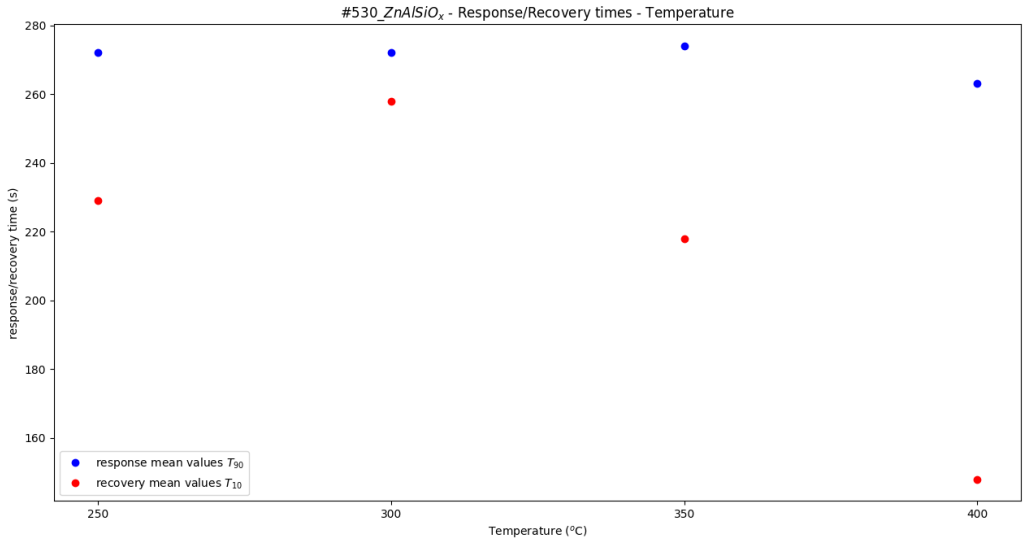

Figure 118: Response / recovery times of the sensor for the different operating temperatures

The response time remained constant at 272-274 sec until the operating temperature of T=350°C, noting down a small decrease at 263 sec for the optimal temperature. Regarding the recovery time, it drops from the value range of 218 sec – 258 sec at 111 sec in the case of the optimal operating temperature.

Furthermore, the response of the sensor was examined for different methane concentrations at T=400°C. The dilution in pure methane was achieved by adding N_2 gas.

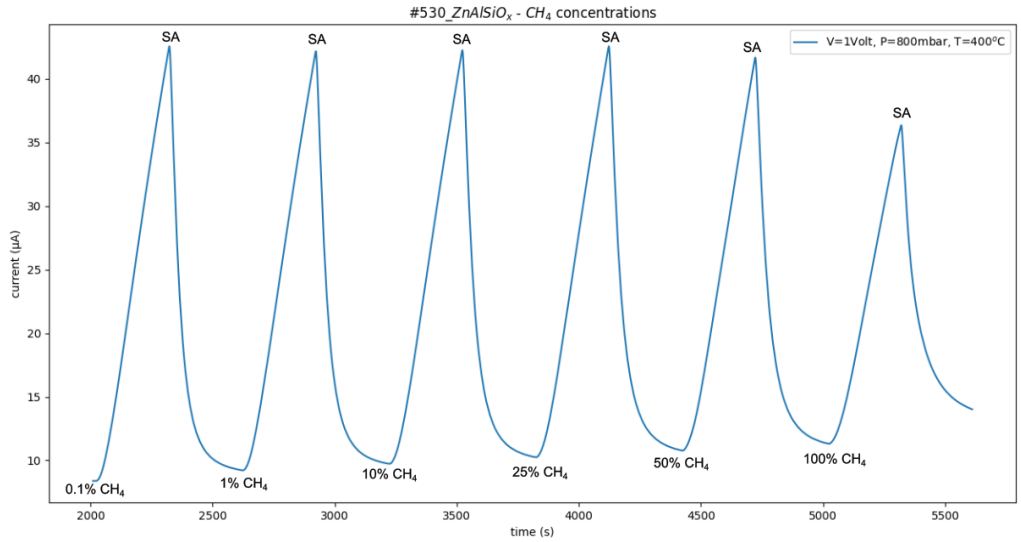

Figure 119: Current - time measurement in the presence of different methane concentrations

CH_4 concentrations	Sensitivity (%)	Response time T_{90} (sec)	Recovery time T_{10} (sec)
100%	68.86	274	157
50%	73.57	275	136
25%	76.05	272	140
10%	76.83	274	131
1%	77.8	272	124
0.1%	80.15	273	118

Table 40: Sensitivity – response, response / recovery times of the sensor for the different methane gas concentrations

By using the data of Table 37, we can plot the response S, the response and recovery times of the sensor as function of the different methane gas concentrations.

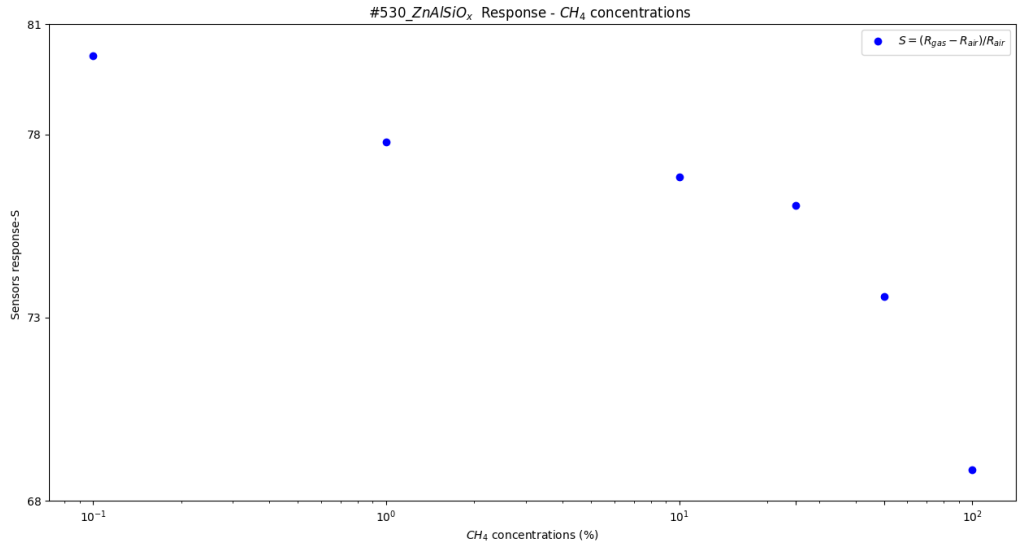

Figure 120: Sensor's response S in the presence of different methane concentrations

The sensor seems to reach a saturation state when pure methane is inserted in the chamber, resulting in the lowest calculated response. The highest response of the sensor occurs in the case of the most diluted methane gas inserted in the chamber.

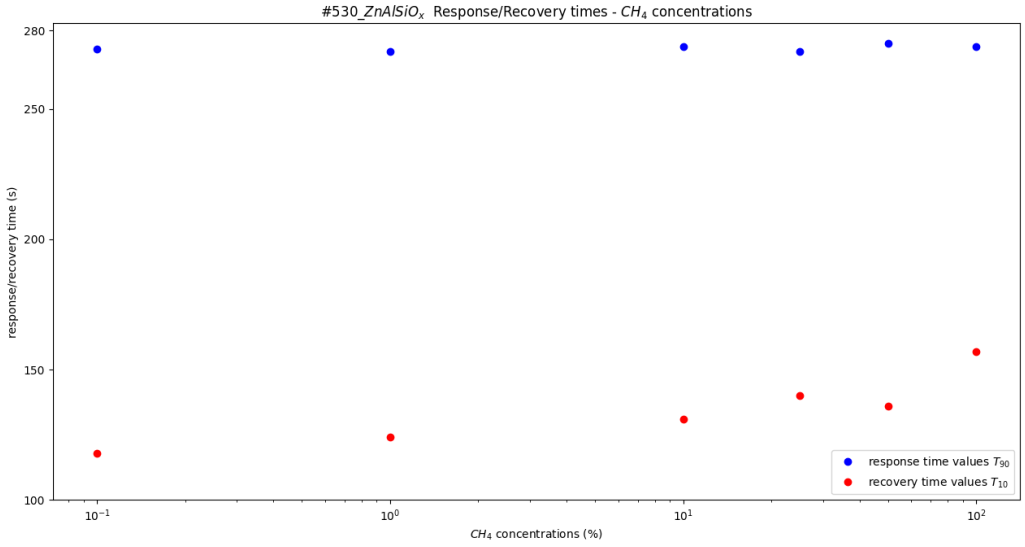

. **Figure 121:** Response / recovery times of the sensor for the different methane concentrations

The response time is stable at 272 sec – 275 sec, while the recovery time varies from 118 sec to 157 sec, increasing as the inserted methane gas is more pure.

13. Characterization of #524_ZnAlSiO$_x$ – Structural, morphological and optical properties

In order to determine the structural, morphological and optical properties of the #524_ZnAlSiO$_x$ sensing film, XRD, SEM, AFM and UV-vis spectroscopy techniques were utilized.

13.1 X-Ray Diffraction analysis

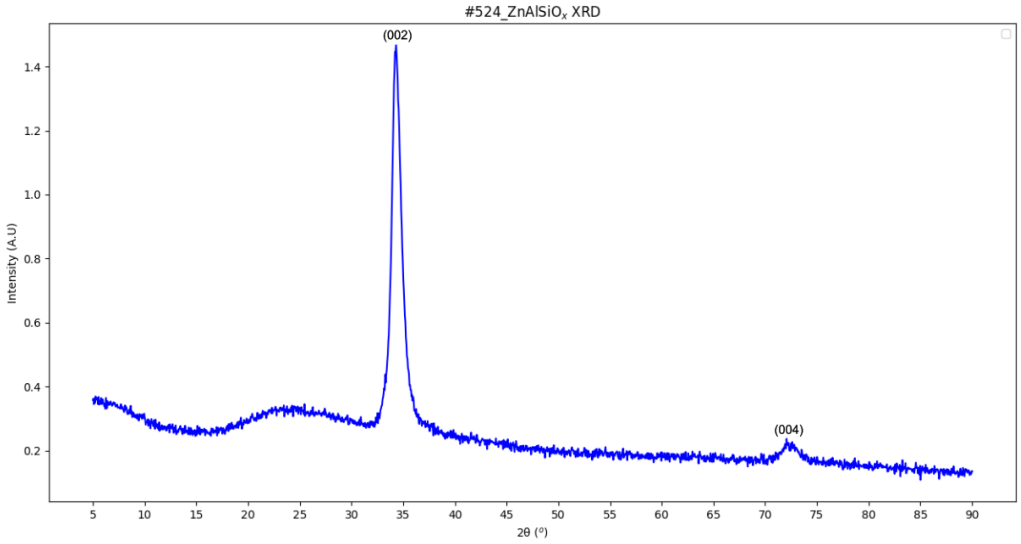

Figure 122: XRD pattern of #524_ZnAlSiO$_x$ sensing film

The XRD spectrum was measured in the range of 5° - 90°, exhibiting the main peak of ZnAlSiO$_x$ at $2\theta_1$=34.36° and a secondary peak at $2\theta_2$=72.38°, corresponding to the crystal planes with Miller indices (hkl)=(002) and (hkl)=(004) equivalently.

Applying Gaussian fitting around the main peak, we obtain the full width at half maximum (FWHM) of the peak, which is β=0.0202 rad.

Then, the crystallite size and the interplanar spacing of the sensing material can be calculated by using the equations (13) and (14):

$$(13):\ D\ (nm) = \frac{K * \lambda}{\beta * cos\theta} \Rightarrow D = 7.185\ nm$$

$$(14):\ d_{hkl}(\text{Å}) = \frac{n * \lambda}{2 * sin\theta} \Rightarrow d_{002} = 2.608\ \text{Å}$$

After calculating the interplanar spacing, the lattice parameters a, c for the hexagonal wurtzite structure can be calculated by using equation (15):

$$(15):\ \frac{1}{d^2_{(hkl)}} = \frac{4}{3} * \left(\frac{h^2 + h*k + k^2}{a^2}\right) + \frac{l^2}{c^2} \Rightarrow c^2 = 4 * d^2_{002} \Rightarrow c = 5.216\ \text{Å}$$

Making the assumption that there is low local symmetry distortion for the co-doped with Aluminum and Silicon sensing film, then c/a ratio remains constant and a close calculation for the lattice parameter a can be made resulting in a=3.194Å.

Finally, the lattice strain parameter ε_w is calculated through the equation (16):

$$(16):\ \varepsilon_w = \frac{\beta * cot\theta}{4} \Rightarrow \varepsilon_w = 1.63 * 10^{-2}$$

The same analysis was held for the secondary peak, with the results quoted in the following summarizing table:

Peak 2θ	Crystallite size D (nm)	Interplanar spacing d_{hkl} (Å)	Lattice parameter c (Å)	Lattice parameter a (Å)	Lattice strain ε_w
$2\theta_1$=34.36°	7.185	(hkl)=(002) 2.608	5.216	3.194	$1.63*10^{-2}$
$2\theta_2$=72.38°	5.206	(hkl)=(004) 1.305	5.218	3.196	$1.13*10^{-2}$

Table 41: Structural parameters of #524_ZnAlSiO_x thin film

The angles observed in the XRD spectrum correspond to the (002) and (004) crystalline planes, thus the crystal have strong preference in the c – axis orientation perpendicular to the substrate.

13.2 SEM

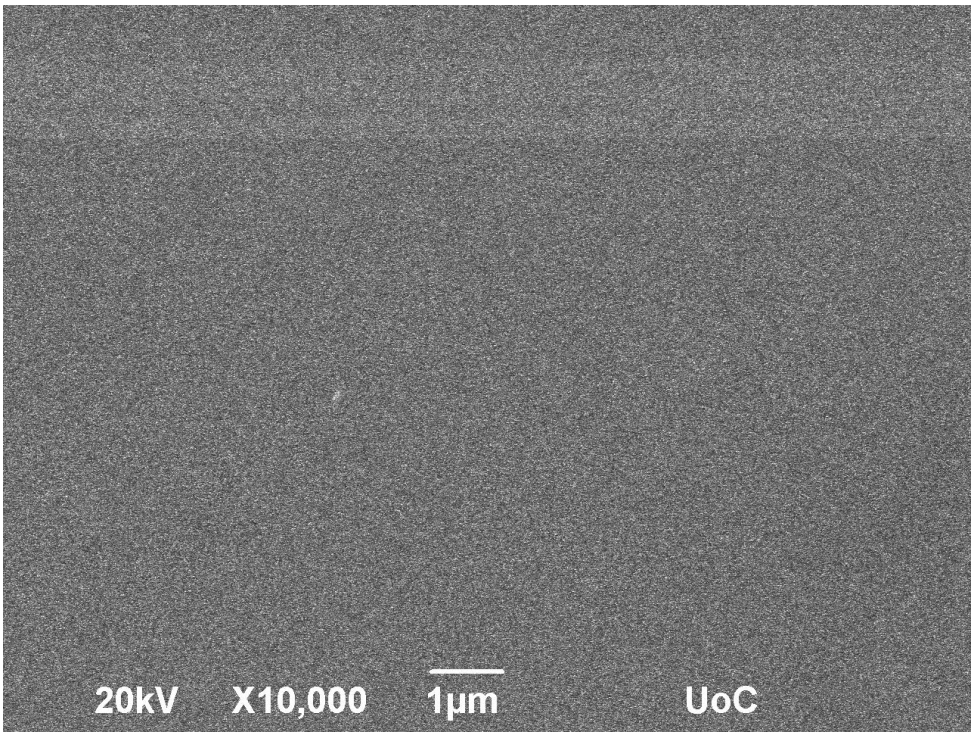

Figure 123: SEM micrograph of #524_ZnAlSiO$_x$ film

13.3 AFM

The roughness of the #524_ZnAlSiO$_x$ sensing film was calculated through an AFM measurement. The average roughness value was found to be R_a=2.380nm, while the root mean square value was found to be R_s=4.428nm.

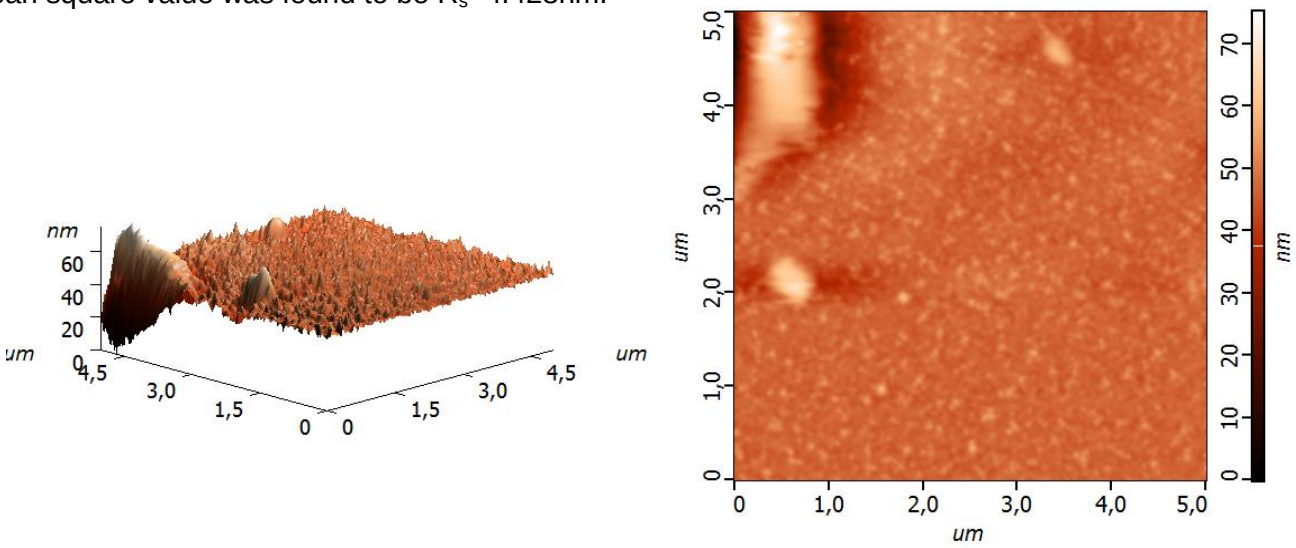

Figure 124: 3D and 2D AFM micrographs (4.5μm x 4.5μm) of the #524_ZnAlSiO$_x$ film

13.4 UV-vis spectroscopy

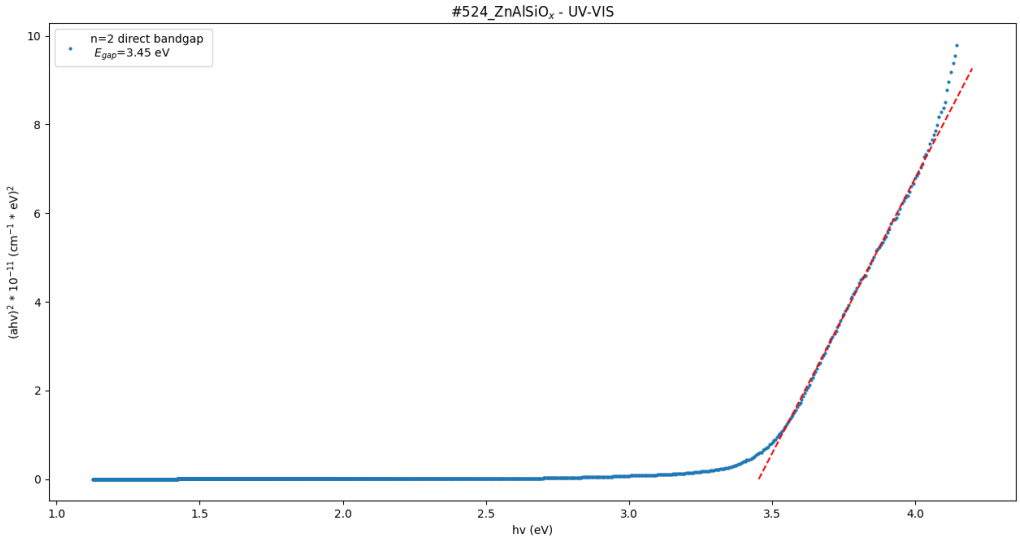

Figure 125: Tauc plot of #524_ZnAlSiO$_x$ for the direct energy band gap case (n=2)

The energy gap was calculated from the linear part of Tauc plot. It appears to be E_g=3.45 eV for the direct band gap case.

13.5 I-V characteristics

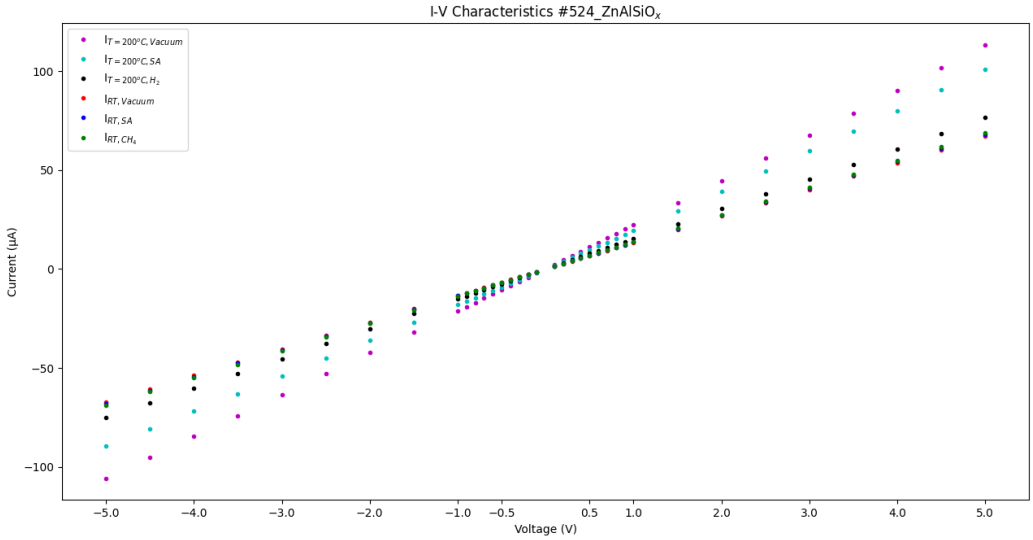

Figure 126: I-V measurement of #524_ZnAlSiO$_x$ sensor operating in room temperature (RT) or at T=200°C under vacuum either in the presence of synthetic air or at 1000 ppm hydrogen concentrations

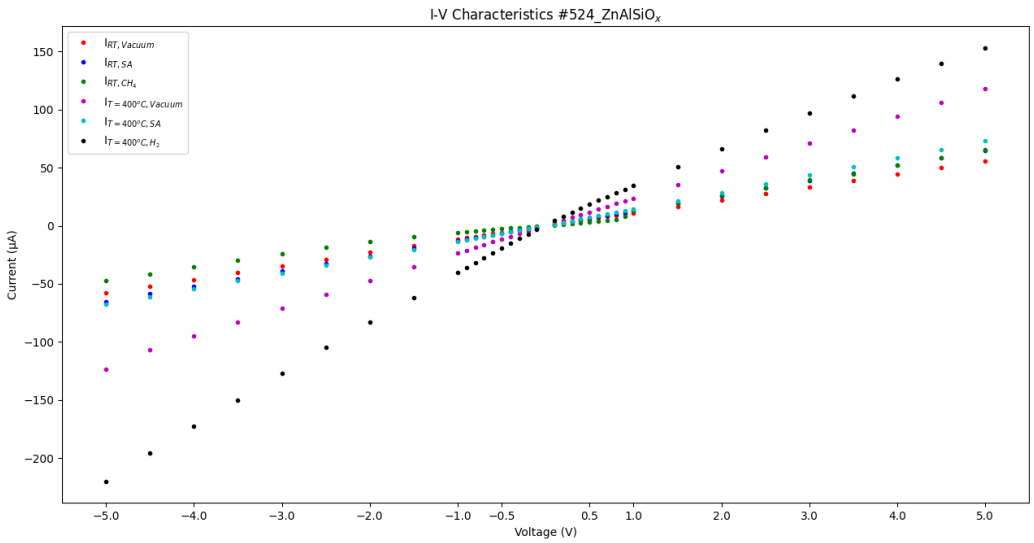

Figure 127: I-V measurements of #524_ZnAlSiO$_x$ sensor operating in room temperature (RT) or at T=400°C under vacuum either in the presence of synthetic air or methane gas

In both hydrogen and methane case, we observe linearity around the applied bias of V=1Volt. That linearity indicates that we have an Ohmic junction.

14. #524_ZnAlSiO$_x$ sensing results

#	Material	Thickness (d)	Sputtering deposition time	Ar	O_2	$I_{sputtering}$	$T_{substrate}$
524	ZnAlSiO$_x$ (ZAO2D Heraeus)	202.8 nm	6min, 50sec	100% (8sccm)	-	0.45A	RT

Table 42: Sputtering parameters used for #524_ZnAlSiO$_x$ development

14.1 Hydrogen sensing

The developed sensor was tested against H_2 gas sensing. The applied bias was set to be V=1Volt. Then, synthetic air was inserted in the experimental chamber for 20 minutes to obtain a constant current baseline and finally the pressure was stabilized in 800 mbar. To examine the response of the sensor to hydrogen gas, 1000 ppm of hydrogen gas were inserted into the chamber for 5 minutes, while afterwards synthetic air was inserted into the chamber for 5 minutes to examine the recovery of the sensor. This gas alteration was repeated for 5 times (5 experimental cycles – reapitability). Also, different operating temperatures were applied starting from RT to T=400°C with an increasing step of 50°C.

This sensor responded only at T=200°C. Further decrease or increase in the operating temperature led to weakness in response and recovery in the presence of hydrogen and synthetic air.

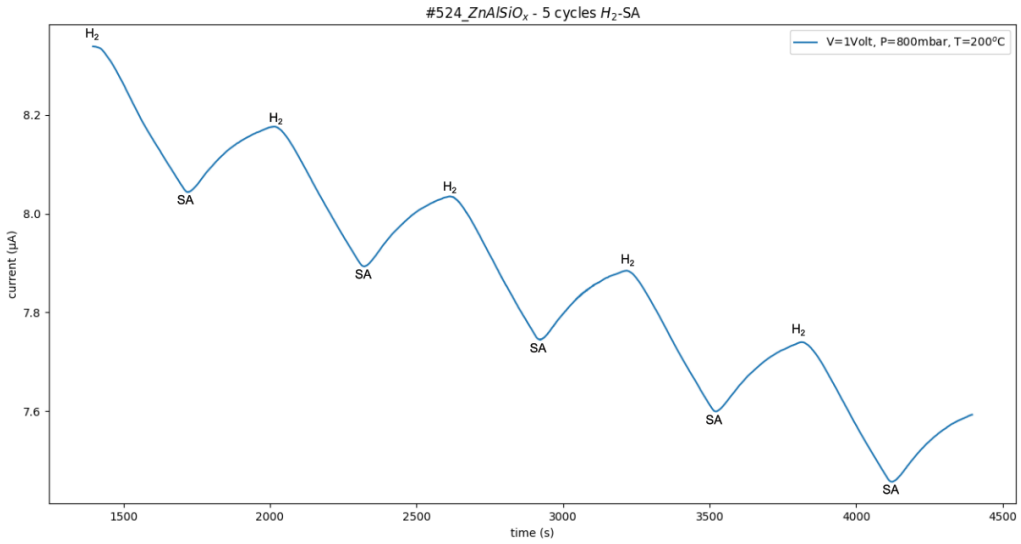

Figure 128: Current – time measurement at T=200°C in the presence of hydrogen

At T=200°C the sensor exhibited its best response and full recovery so we can calculate the response / recovery times and the response (S) of the sensor:

The response time was calculated at the 90% of each peak alteration and its mean value is:

$\overline{T_{90}} = \frac{T_{90}^{(1)}+T_{90}^{(2)}+T_{90}^{(3)}+T_{90}^{(4)}+T_{90}^{(5)}}{5} \Rightarrow \overline{T_{90}} = 276\,sec$, best response time: 272 sec

Similarly, $\overline{T_{10}} = \frac{T_{10}^{(1)}+T_{10}^{(2)}+T_{10}^{(3)}+T_{10}^{(4)}+T_{10}^{(5)}}{5} \Rightarrow \overline{T_{10}} = 260\,sec$, best recovery time: 249 sec

The sensor's response at each cycle was calculated following the equation (1) and the mean response value is equal to: $\bar{S} = 3.70$

At T=200°C, the response of the sensor was examined for hydrogen concentrations in order to find the lower detection limit of hydrogen that can be sensed. The dilution of the hydrogen gas was achieved as hydrogen + synthetic air mixture.

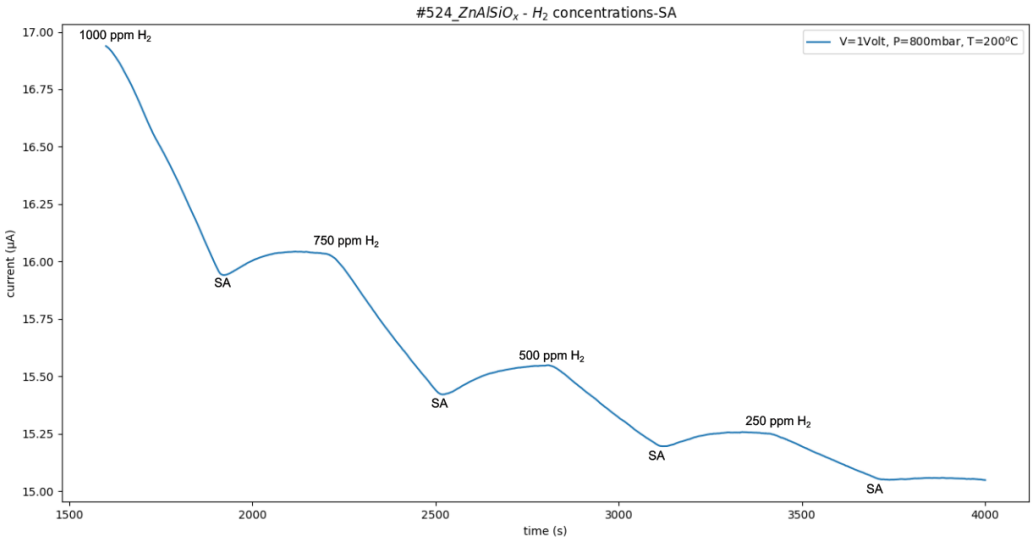

Figure 129: Current – time measurement in the presence of different hydrogen concentration

Hydrogen concentrations	Sensitivity (%)	Response time T_{90} (sec)	Recovery time T_{10} (sec)
100% →1000 ppm	5.92	278	279
75% →750 ppm	3.93	271	272
50% →500 ppm	2.36	258	254
25% →250 ppm	1.31	246	246

Table 43: Sensitivity – response, response / recovery times of the sensor for the different hydrogen concentrations

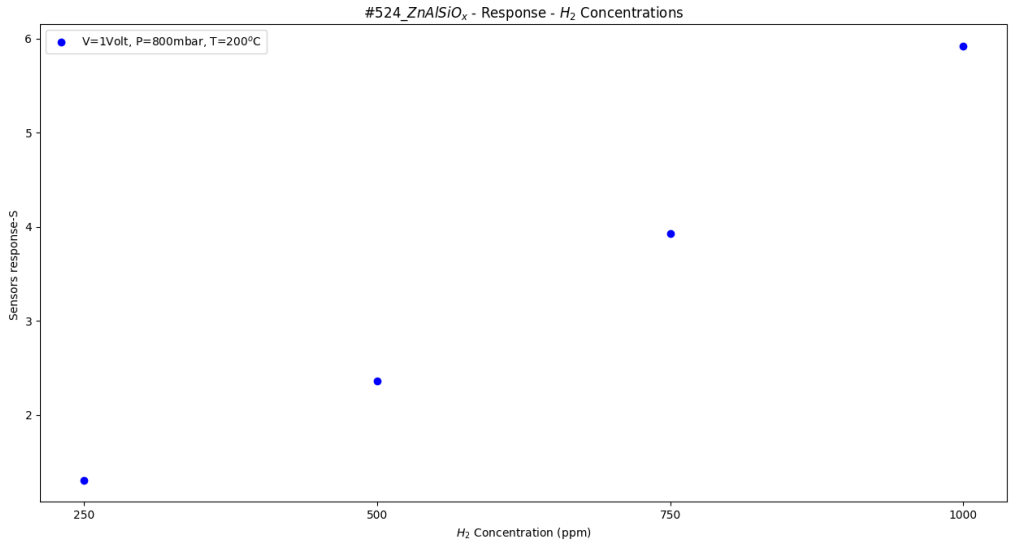

Figure 130: Sensor's response for the different hydrogen concentrations

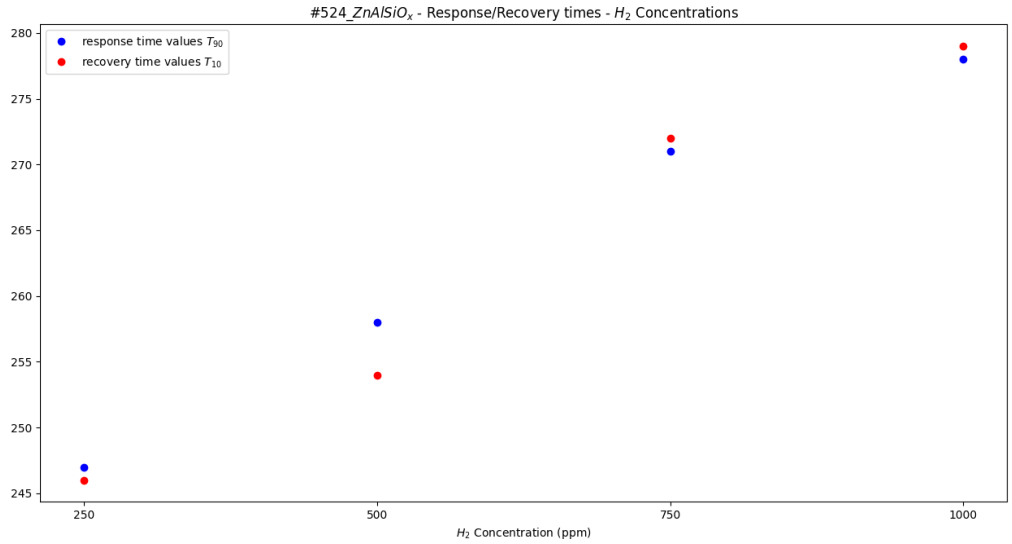

Figure 131: Response and recovery times of the sensor for the different hydrogen concentrations

At each hydrogen gas concentration, the response time matches the recovery time.

14.2 Methane sensing

The same experimental process was repeated in the case of methane gas. The applied bias was set to be V=1Volt. Then, synthetic air was inserted in the experimental chamber for 20 minutes to obtain a constant current baseline and finally the pressure was stabilized in 800 mbar. To examine the response of the methane gas, pure methane was inserted into the chamber for 5 minutes, while afterwards synthetic air was inserted into the chamber for 5 minutes to examine the recovery of the sensor. The gas alteration was repeated for 5 times (5 experimental cycles – repeatability) and different operating temperatures were applied starting from RT to T=400°C with an increasing step of 50°C.

In the analysis following, only the graph for the optimal operating temperature (T=400°C) that provides the best response of the sensor is exhibited. The rest of the graphs are included in the 13Appendix C: #524_ZnAlSiOx – Methane gas sensing.

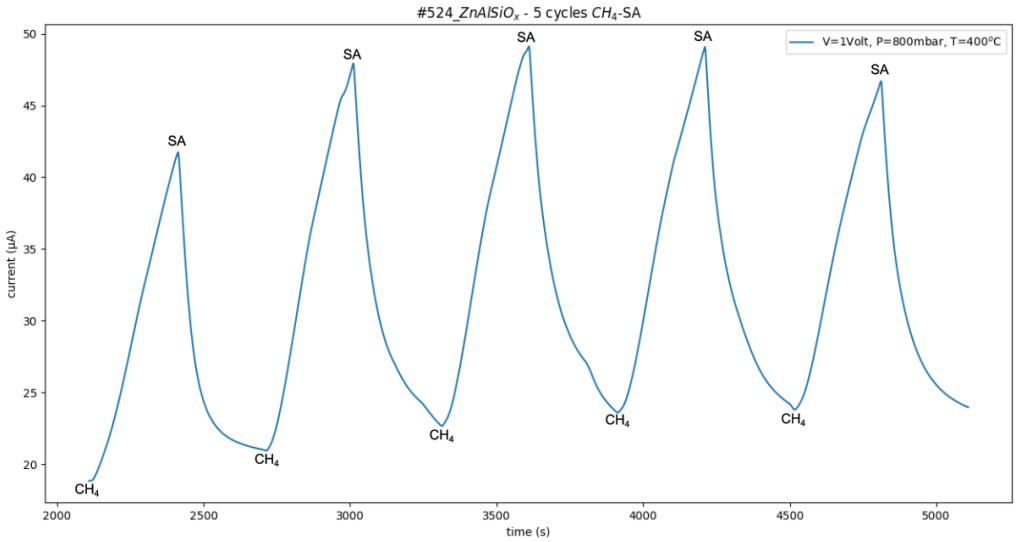

Figure 132: Current – time measurement at T=400°C in the presence of methane

At T=400°C the sensor exhibited its best response and full recovery so we can calculate the response / recovery times and the response (S) of the sensor:

The response time was calculated at the 90% of each peak alteration and its mean value is:

$\overline{T_{90}} = \frac{T_{90}^{(1)}+T_{90}^{(2)}+T_{90}^{(3)}+T_{90}^{(4)}+T_{90}^{(5)}}{5} \Rightarrow \overline{T_{90}} = 267\ sec$, best response time: 259 sec

Similarly, $\overline{T_{10}} = \frac{T_{10}^{(1)}+T_{10}^{(2)}+T_{10}^{(3)}+T_{10}^{(4)}+T_{10}^{(5)}}{5} \Rightarrow \overline{T_{10}} = 171\ sec$, best recovery time: 119 sec

The sensor's response at each cycle was calculated following the equation (1) and the mean response value is equal to: $\bar{S} = 52.88$

Sensor: #524_ZnAlSiOx			
Temperature (°C)	Sensitivity (%)	Response time T_{90} (best) [sec]	Recovery time T_{10} (best) [sec]
300	13.41	271 (262)	228 (221)
350	21.68	269 (260)	222 (194)
400	52.88	267 (259)	171 (119)

Table 44: Sensitivity – response, response / recovery times of the sensor for different operating temperatures

By using the data of Table 40, we can plot the response of the sensor, the response and recovery times as function of the different operating temperatures:

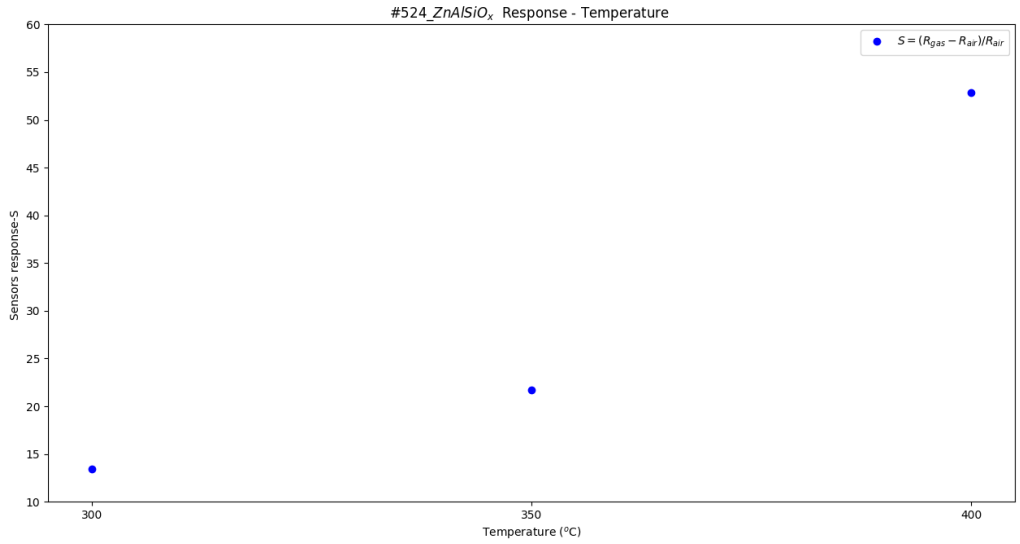

Figure 133: Sensor's response for the different operating temperatures

At T=400°C the sensor exhibits its highest response S=52.88%. Lower applied temperature results in the decrease of the sensor's response.

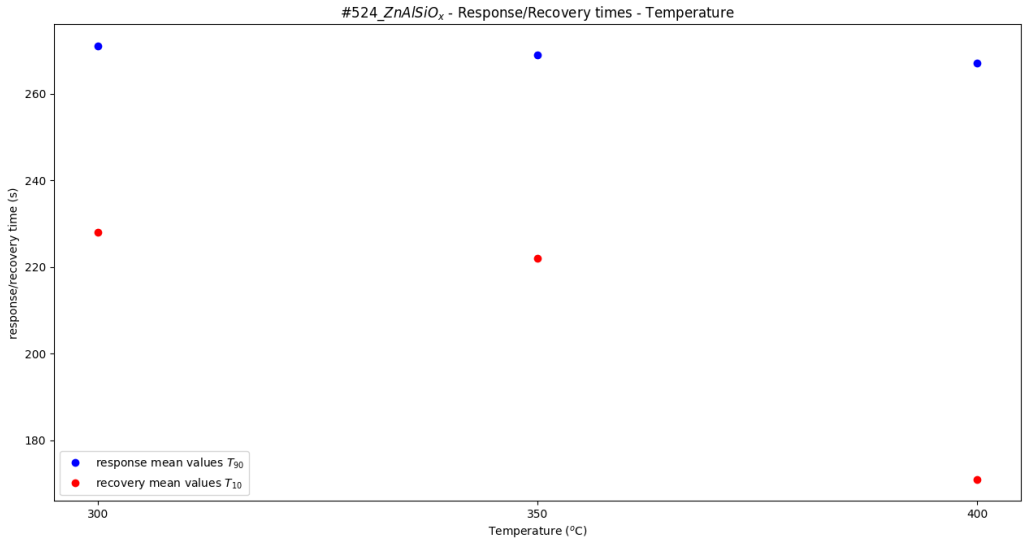

Figure 134: Response / recovery times of the sensor at different operating temperatures

The response time of the sensor is around 270 sec, while the recovery time varied from 228 sec to 171 sec. The lowest recovery time occurs in the case of the optimal temperature.

Furthermore, the response of the sensor was examined for different methane concentrations at T=400°C. The dilution in the pure methane was achieved by adding N_2 gas.

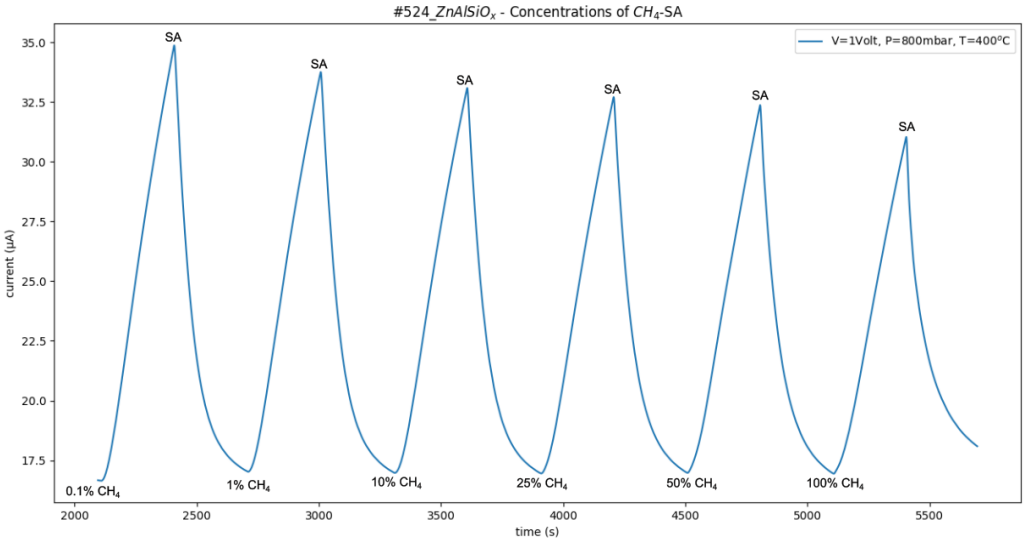

Figure 135: Current – time measurement at T=400°C in the presence of different methane concentration

CH4 concentrations	Sensitivity (%)	Response time T_{90} (sec)	Recovery time T_{10} (sec)
100%	45.05	273	189
50%	47.25	272	162
25%	47.85	281	174
10%	48.64	274	175
1%	49.09	272	170
0.1%	51.96	268	167

Table 45: Sensitivity – response, response / recovery times of the sensor for the different methane concentrations

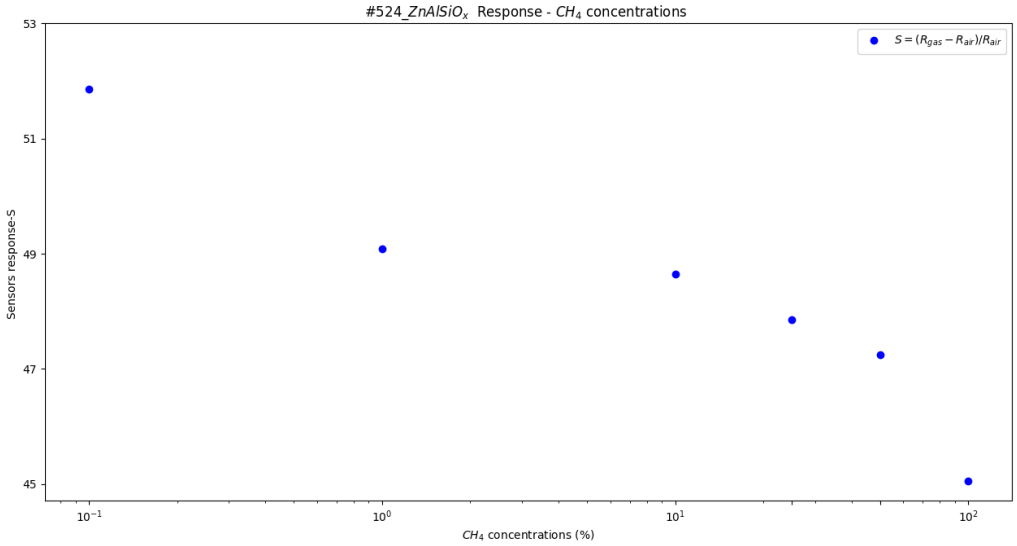

Figure 136: Sensor's response of the sensor for the different methane concentrations

The response of the sensor exhibits its highest value for the lowest methane concentration inserted inside the experimental chamber. When pure methane is inserted to the chamber, there is lower current change of the sensor, showing that the sensor reaches fast in a saturation state.

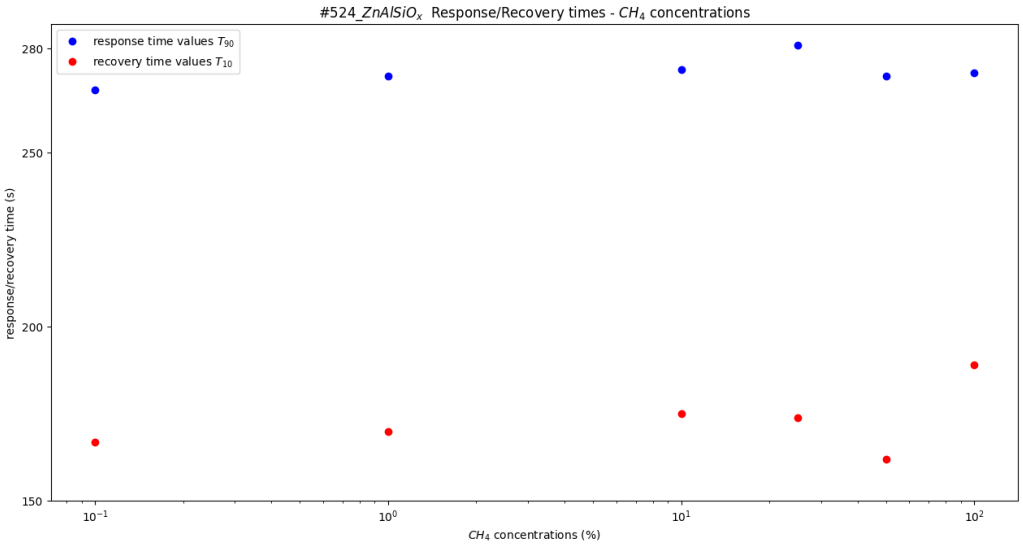

Figure 137: Response / recovery times of the sensor for the different methane concentration

The response time varied from 268 sec to 281 sec, while the recovery time varied from 162 sec to 189 sec, indicating its stable performance even at low methane gas concentrations.

15. Characterization of #525_ZnAlSiO$_x$ – Structural, morphological and optical properties

In order to determine the structural, morphological and optical properties of the #525_ZnAlSiO$_x$ sensing film, XRD, SEM, AFM and UV-vis spectroscopy techniques were utilized. The purity of the synthesized sensing films was examined through EDS spectroscopy.

15.1 X-Ray Diffraction analysis

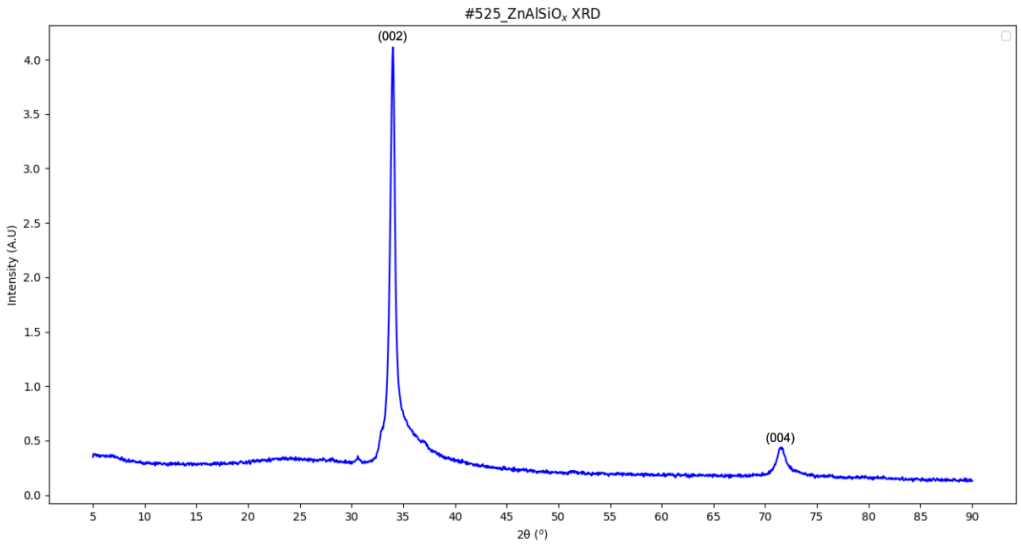

Figure 138: XRD pattern of #525_ZnAlSiO$_x$ sensing film

The XRD spectrum was measured in the range of 5° - 90°, exhibiting the main peak of ZnAlSiO$_x$ at $2\theta_1$=33.98° and a secondary peak at $2\theta_2$=71.57°, corresponding to the crystal planes with Miller indices (hkl)=(002) and (hkl)=(004) equivalently.

Applying Gaussian fitting around the main peak, we obtain the full width at half maximum (FWHM) of the peak, which is β=0.0107 rad.

Then, the crystallite size and the interplanar spacing of the sensing material can be calculated by using the equations (13) and (14):

$$(13):\ D\ (nm) = \frac{K * \lambda}{\beta * cos\theta} \Rightarrow D = 13.550\ nm$$

$$(14):\ d_{hkl}(\text{Å}) = \frac{n * \lambda}{2 * sin\theta} \Rightarrow d_{002} = 2.636\ \text{Å}$$

After calculating the interplanar spacing, the lattice parameters a, c for the hexagonal wurtzite structure can be calculated by using equation (15):

$$(15):\ \frac{1}{d^2_{(hkl)}} = \frac{4}{3} * \left(\frac{h^2 + h*k + k^2}{a^2}\right) + \frac{l^2}{c^2} \Rightarrow c^2 = 4 * d^2_{002} \Rightarrow c = 5.272\ \text{Å}$$

Making the assumption that there is low local symmetry distortion for the co-doped with Aluminum and Silicon sensing film, then c/a ratio remains constant and a close calculation for the lattice parameter a can be made resulting in a=3.229Å.

Finally, the lattice strain parameter ε_w is calculated through the equation (16):

$$(16):\ \varepsilon_w = \frac{\beta * cot\theta}{4} \Rightarrow \varepsilon_w = 8.75 * 10^{-3}$$

The same analysis was held for the secondary peak, with the results quoted in the following summarizing table:

Peak 2θ	Crystallite size D (nm)	Interplanar spacing d_{hkl} (Å)	Lattice parameter c (Å)	Lattice parameter a (Å)	Lattice strain ε_w
$2\theta_1$=33.98°	13.550	(hkl)=(002) 2.636	5.272	3.229	$8.75*10^{-3}$
$2\theta_2$=71.57°	9.602	(hkl)=(004) 1.317	5.269	3.227	$6.17*10^{-3}$

Table 46: Structural parameters of #525_ZnAlSiO_x thin film

Likewise with #524 film, the angles observed in the XRD spectrum correspond to the (002) and (004) crystalline planes, thus the crystal have strong preference in the c – axis orientation perpendicular to the substrate.

15.2 SEM

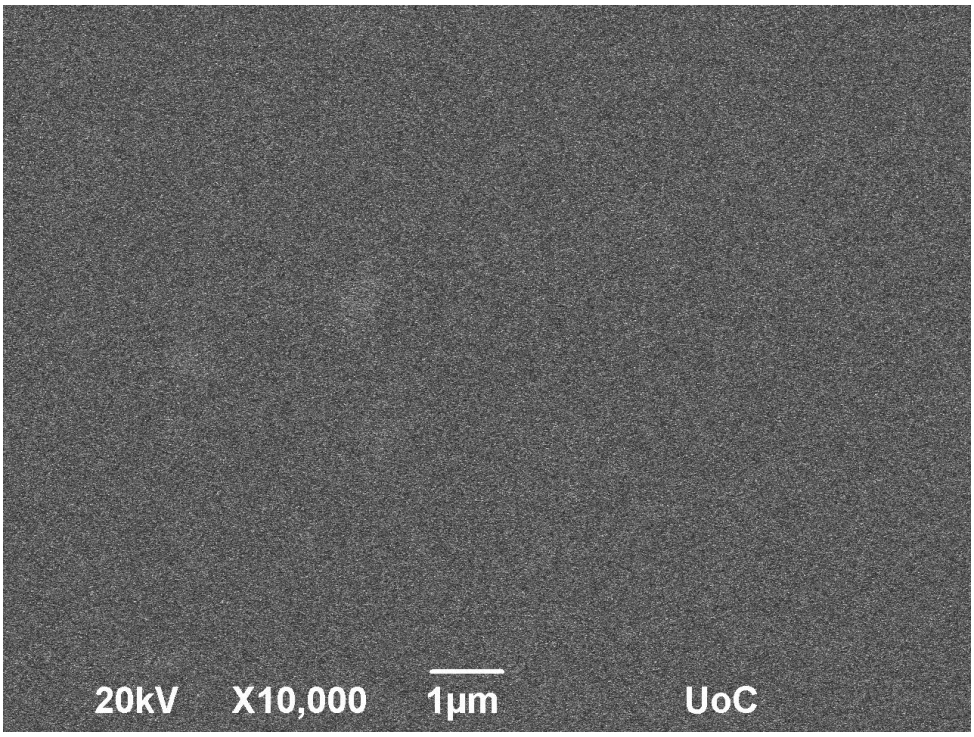

Figure 139: SEM micrograph of the #525_ZnAlSiO$_x$ film

15.3 AFM

The roughness of the #525_ZnAlSiO$_x$ sensing film was calculated through an AFM measurement. The average roughness value was found to be R_a=1.876nm, while the root mean square value was found to be R_s=2.691nm.

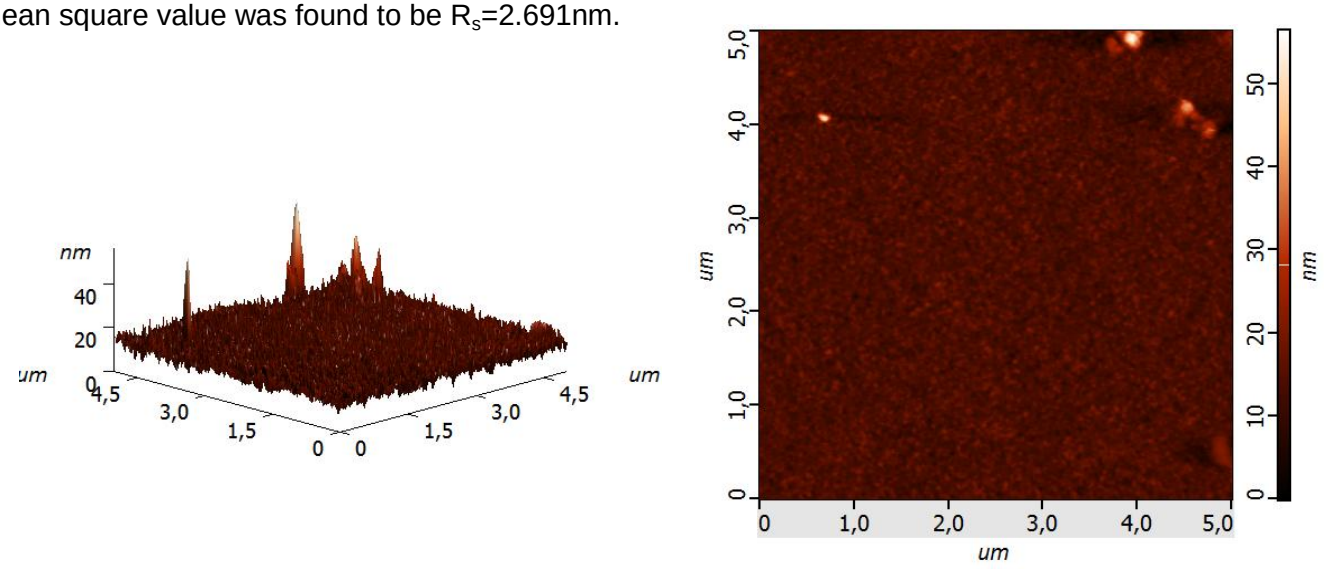

Figure 140: 3D and 2D AFM micrographs (4.5μm x 4.5μm) of the #525_ZnAlSiO$_x$ film

15.4 UV-vis spectroscopy

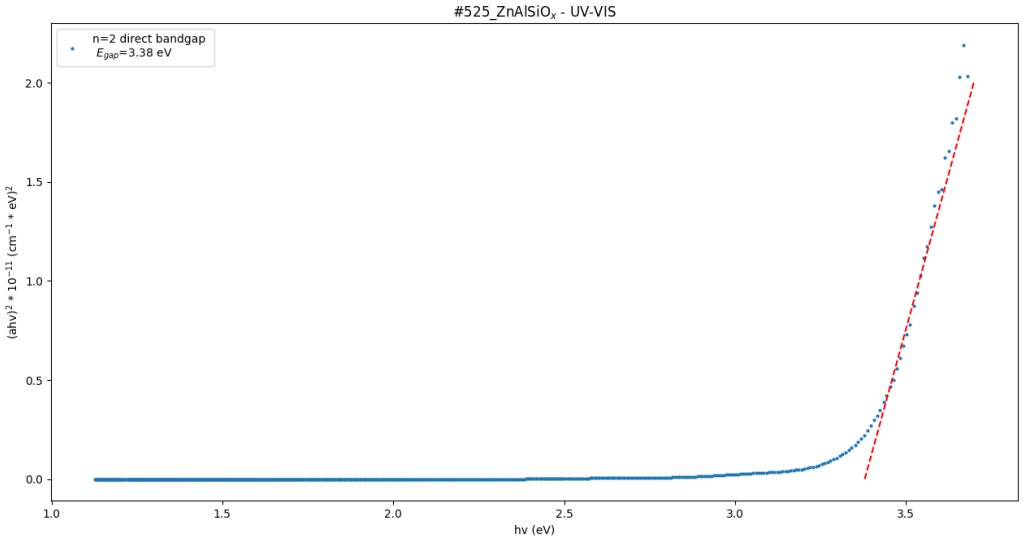

Figure 141: Tauc plot of #525_ZnAlSiO$_x$ for the direct energy band gap case (n=2)

The energy band gap was calculated from the linear part of Tauc plot. It appears to be E_g=3.38 eV for the direct band gap case. The obtained energy gap value is in the energy gap value range that is mentioned in the bibliography.

15.5 EDS analysis

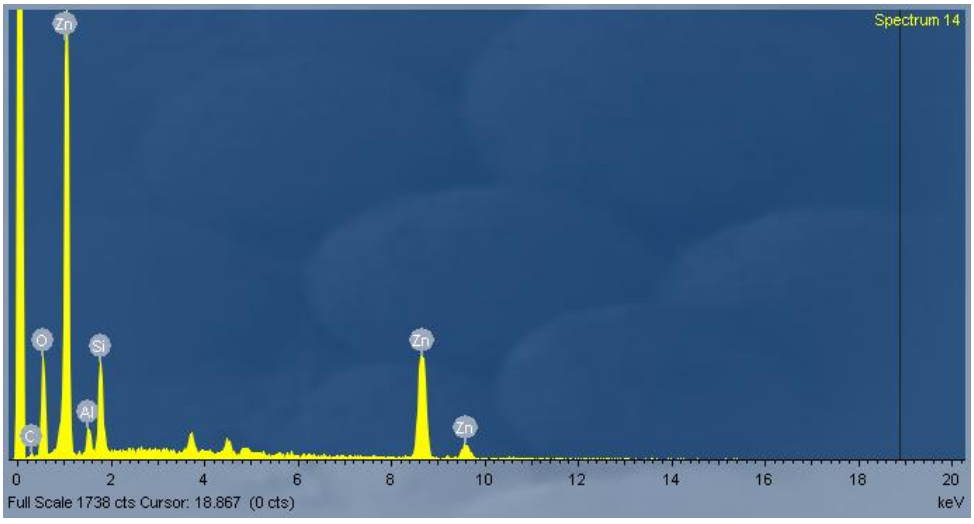

Element	Atomic%
C K	13.08
O K	42.97
Al K	3.31
Si K	9.50
Zn K	31.15

Figure 142: Material identified in the #525_ZnAlSiO$_X$ film with EDS technique

From the EDS analysis, the elements of Oxygen:42.97%, Aluminum:3.31%, Silicon:9.50%, Zinc:31.15% and Carbon:13.08% were identified with the atomic ratio mentioned above. The atomic ratio of Zn:Al~9.41 and Zn:Si~3.28 indicates the existence of

Aluminum and Silicon as doping elements in the crystal structure. In comparison to the EDS of #534_$ZnAl_5O_x$ the amount of Silicon existence is increased, indicating that Si peak can be attributed not only to the glass substrate but to Si element as doping. The existence of Carbon could possibly be related with the existence of dust upon the sensing film.

15.6 I-V characteristics

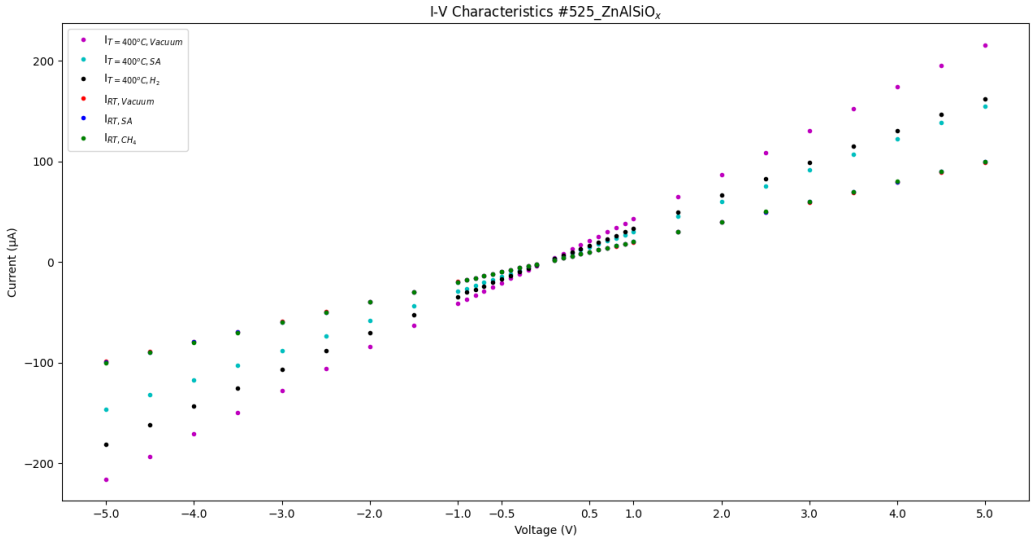

Figure 143: I-V measurement of #525_$ZnAlSiO_X$ sensor operating in room temperature (RT) or at T=400°C under vacuum either in the presence of synthetic air or pure methane gas.

Around the operating applied bias of V=1Volt, there is linearity in the diagram above, which means that we have an Ohmic junction.

16. #525_ZnAlSiO$_x$ sensing results

#	Material	Thickness (d)	Sputtering deposition time	Ar	O_2	$I_{sputtering}$	$T_{substrate}$
525	ZnAlSiO$_x$ (ZAO2D Heraeus)	503.6 nm	12min, 10sec	100% (8sccm)	-	0.45A	RT

Table 47: Sputtering parameters used for #525_ZnAlSiO$_x$ development

16.1 Hydrogen sensing

The developed sensor was tested against H_2 gas sensing following the same experimental process that is explained in the sections above. Although, this specific sensor did not exhibit response to hydrogen gas at all the operating temperature range. Thus, #525 sensor is ineligible for hydrogen gas sensing operation.

16.2 Methane sensing

The same experimental process was repeated in the case of methane gas. The applied bias was set to be V=1Volt. Then, synthetic air was inserted in the experimental chamber for 20 minutes to obtain a constant current baseline and finally the pressure was stabilized in 800 mbar. To examine the response of the methane gas, pure methane was inserted into the chamber for 5 minutes, while afterwards synthetic air was inserted into the chamber for 5 minutes to examine the recovery of the sensor. The gas alteration was repeated for 5 times (5 experimental cycles – repeatability) and different operating temperatures were applied starting from RT to T=400°C with an increasing step of 50°C.

In the analysis following, only the graph for the optimal operating temperature (T=400°C) that provides the best response of the sensor is exhibited. The rest of the graphs are included in the Appendix C: #525_ZnAlSiOx – Methane gas sensing.

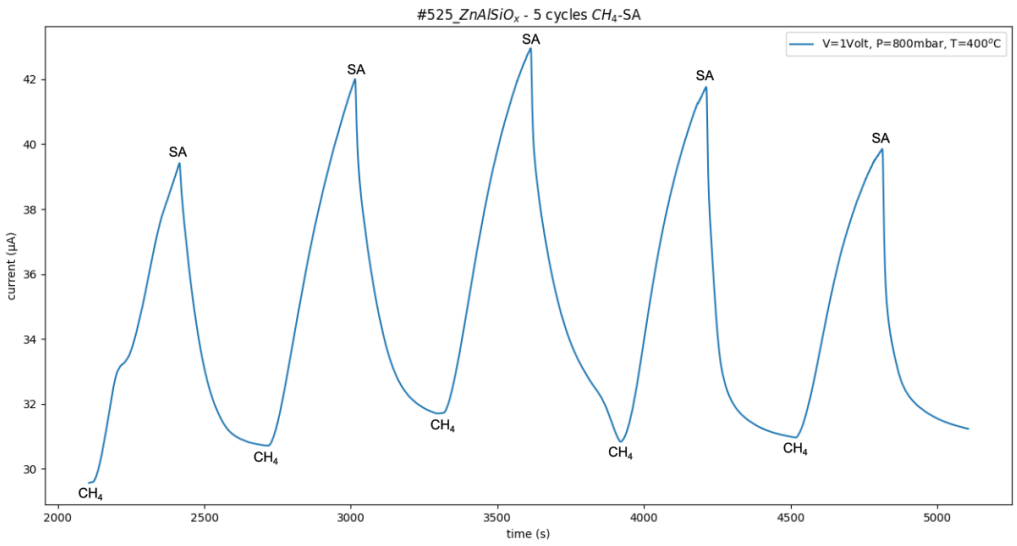

Figure 144: Current – time measurement at T=400°C in the presence of methane gas

At T=400°C the sensor exhibited its best response and full recovery so we can calculate the response / recovery times and the response (S) of the sensor:

The response time was calculated at the 90% of each peak alteration and its mean value is:

$\overline{T_{90}} = \frac{T_{90}^{(1)}+T_{90}^{(2)}+T_{90}^{(3)}+T_{90}^{(4)}+T_{90}^{(5)}}{5} \Rightarrow \overline{T_{90}} = 255\ sec$, best response time: 246 sec

Similarly, $\overline{T_{10}} = \frac{T_{10}^{(1)}+T_{10}^{(2)}+T_{10}^{(3)}+T_{10}^{(4)}+T_{10}^{(5)}}{5} \Rightarrow \overline{T_{10}} = 151\ sec$, best recovery time: 95 sec

The sensor's response at each cycle was calculated following the equation (1) and the mean response value is equal to: $\bar{S} = 25.23$

Sensor: #525_ZnAlSiOx			
Temperature (°C)	Sensitivity (%)	Response time T_{90} (best) [sec]	Recovery time T_{10} (best) [sec]
300	3.54	279 (278)	244 (238)
350	8.87	262 (259)	179 (170)
400	25.23	255 (246)	151 (95)

Table 48: Sensitivity – response, response / recovery times of the sensor for the different applied temperatures

By using the data of Table 44, we can plot the response S of the sensor and the response / recovery times as function of the different operating temperatures:

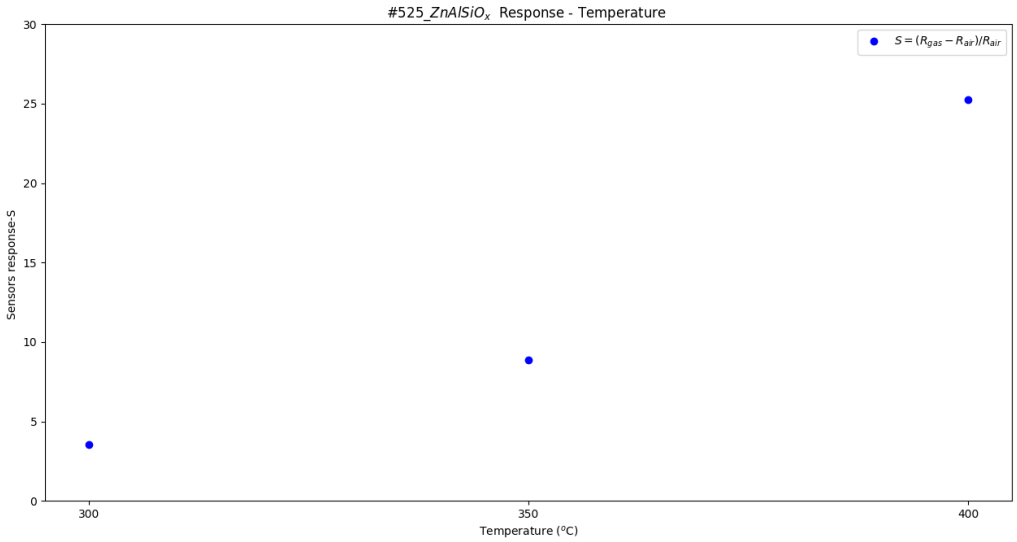

Figure 145: Sensor's response for the different operating temperatures

The sensor exhibits medium response to methane gas that gradually increase with the rise of temperature.

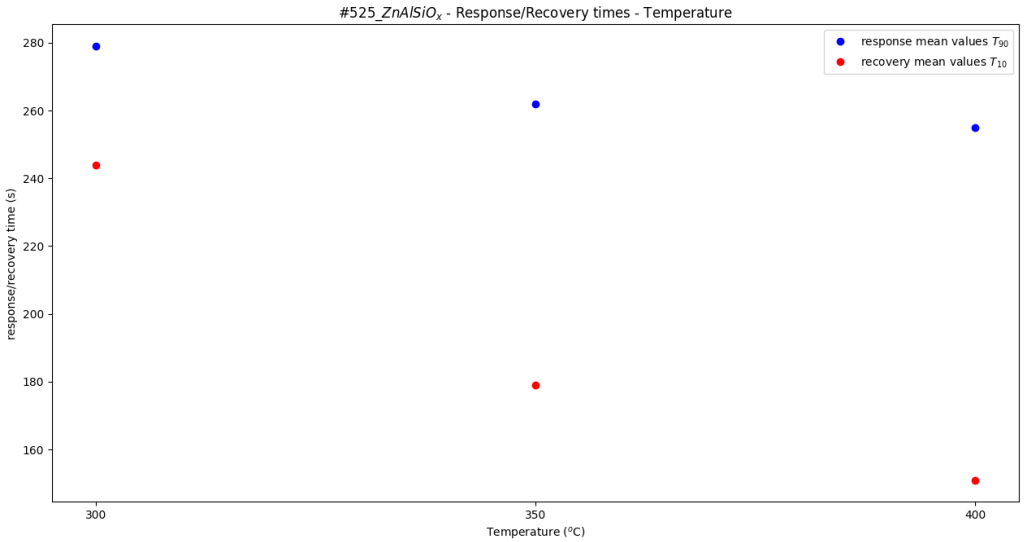

Figure 146: Response / recovery times of the sensor for the different operating temperatures

Both response and recovery times are reducing, while the operating temperature increases.

Furthermore, the response of the sensor was examined for different methane concentrations at T=400°C.The dilution in pure methane was achieved by adding N_2 gas.

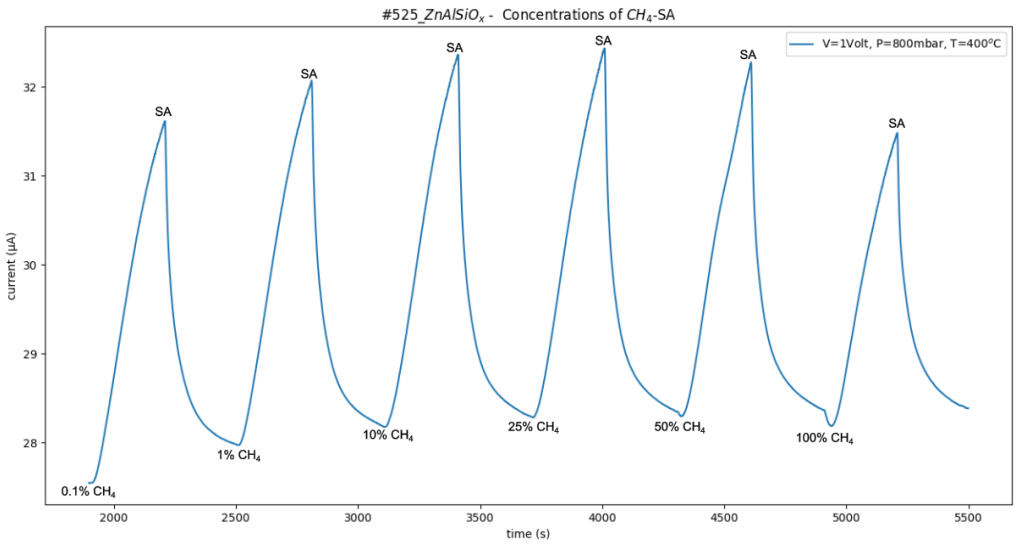

Figure 147: Current – time measurement at T=400°C in the presence of different methane concentrations

CH_4 concentrations	Sensitivity (%)	Response time T_{90} (sec)	Recovery time T_{10} (sec)
100%	10.37	268	151
50%	12.33	275	138
25%	12.73	266	134
10%	12.91	263	130
1%	12.71	258	147
0.1%	12.84	257	142

Table 49: Sensitivity – response, response / recovery times of the sensor for the different methane concentrations

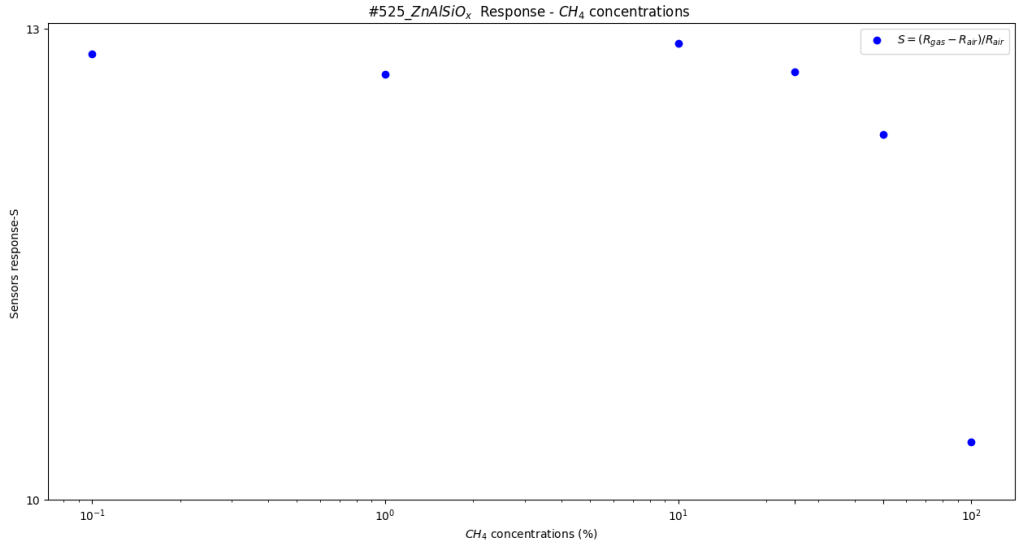

Figure 148: Sensor's response at different methane concentration

The response of the sensor exhibits its highest value for the lowest methane concentration inserted inside the experimental chamber. When pure methane is inserted to the chamber, there is lower current change of the sensor, showing that the sensor reaches fast in a saturation state.

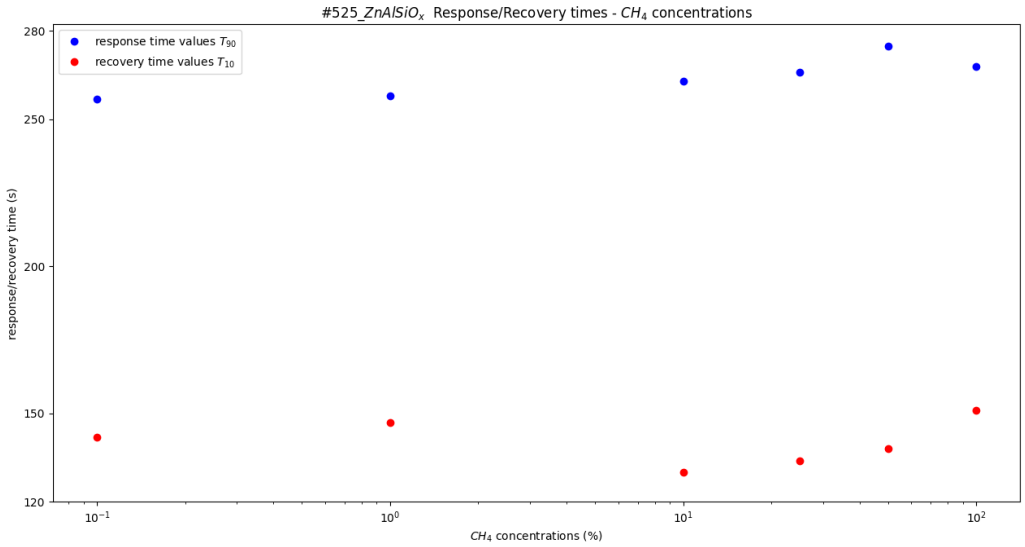

Figure 149: Response / recovery times of the sensor for the different methane concentrations

The response time varied from 268 sec to 281 sec, while the recovery time varied from 130 sec to 151 sec. Also, the response and recovery time values did not differentiate so much with the methane dilution.

Chapter IV – Conclusions

At this master thesis, conductometric gas sensors were developed by DC sputtering technique using three different target materials ZnAl2%, $ZnAl_5O_x$ and $ZnAlSiO_x$. The thickness of the developed films was in the range of 68 nm – 1.05 μm, which is highly dependent on the sputtering duration time and the applied current during the sputtering procedure. All the films were structurally, morphologically and optically characterized with the XRD, SEM, AFM and UV-vis spectroscopy. From the analysis above, all the sensing films exhibited strong preference of crystal growth in the c – axis orientation perpendicular to the substrate, due to the existence of the main peak at 2θ~34° which corresponds to the (002) crystalline plane and the existence of a secondary peak at 2θ~72° which corresponds to the (004) crystalline plane and it clearly appeared on thicker films. These two peaks in the XRD spectrum are characteristic peaks of the hexagonal wurtzite ZnO structure. From the SEM images it was made clear that each film shows good uniformity and dense surface without visible holes or faulty zones on the film surface. Also, the roughness of the surface was studied through AFM measurements, resulting in average roughness range of 0.25 nm -2.85 nm, except from the #533_$ZnAl_5O_x$ thin film that was the most rough (16.54nm). The calculation of the energy bandgap of each sensor was extracted by the linear part of the Tauc plot for the direct bandgap case, which occurs in the ZnO material. Doping Aluminum, or co-doping Aluminum and Silicon on the ZnO lattice make the films more transparent and result in widening the energy bandgap values from 3.27eV to 3.82 eV. From the I-V measurements at RT or at the optimal operating temperature under vacuum or in the presence of hydrogen and methane gas, there was linear dependence between the measured current and the applied bias, indicating the Ohmic behavior for the material resistance. Finally, EDS analysis was conducted in order to identify the purity of all the synthesized films, but trustworthy results were obtained for the thick films. In the case of thin films, high peaks of Silicon appeared in the EDS spectra corrupting the analysis, leading to false results.

The sensors were tested against hydrogen and methane gas sensing in a wide operating temperature range, from RT to T=400°C. The applied bias was low, either 1Volt or 5Volts. In the case of hydrogen gas, there is a variety in the optimal operating temperature, the majority of them around T=300°C-400°C. In the case of methane gas, all the maximum responses were obtained at T=400°C. Furthermore, the response of each sensor was examined for different hydrogen and methane concentrations in order to find the minimum gas concentration that can be sensed.

A short discussion of the sensing results follows:

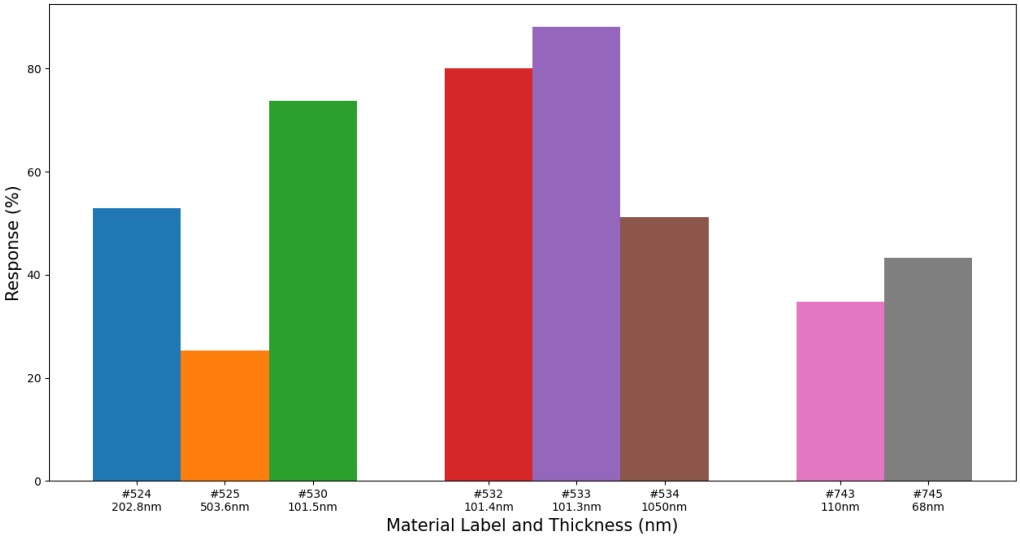

Figure 150: Summary of the sensor's response to methane gas for the different material categorization

From the diagram above, useful information can be extracted correlating the sensor's response at repeatability experiments with the film thickness. In each material category, the highest response of the sensor is attributed to the thinner film. Among the developed sensors with $ZnAlSiO_x$ as sensing film, the #530 exhibited response S=73.79%. The highest response of the sensor is observed for those with the stoichiometricaly more Aluminum in the sensing film, the #533 exhibited response S=88.06%. The developed thin films with stoichiometricaly less Aluminum exhibited relatively lower response at methane gas, noting response S=43.23%.

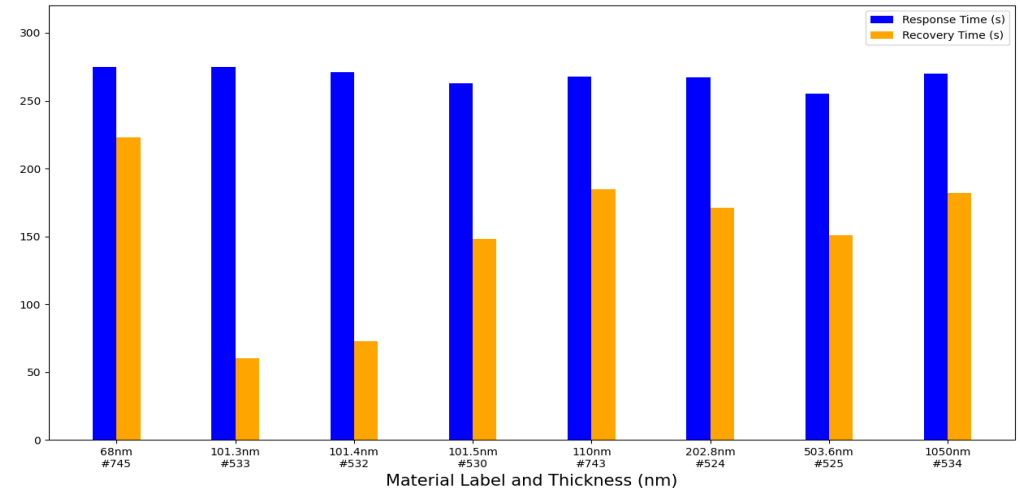

Figure 151: Summary of the response and recovery times at methane gas sensing in terms of increasing film thickness

In methane gas sensing all sensors exhibit a response time of more than four minutes, while the recovery time differs depending on the material and the film thickness. The average response time of the sensors is around three minutes, while the #533_$ZnAl_5O_x$ stands out with just a one minute recovery time.

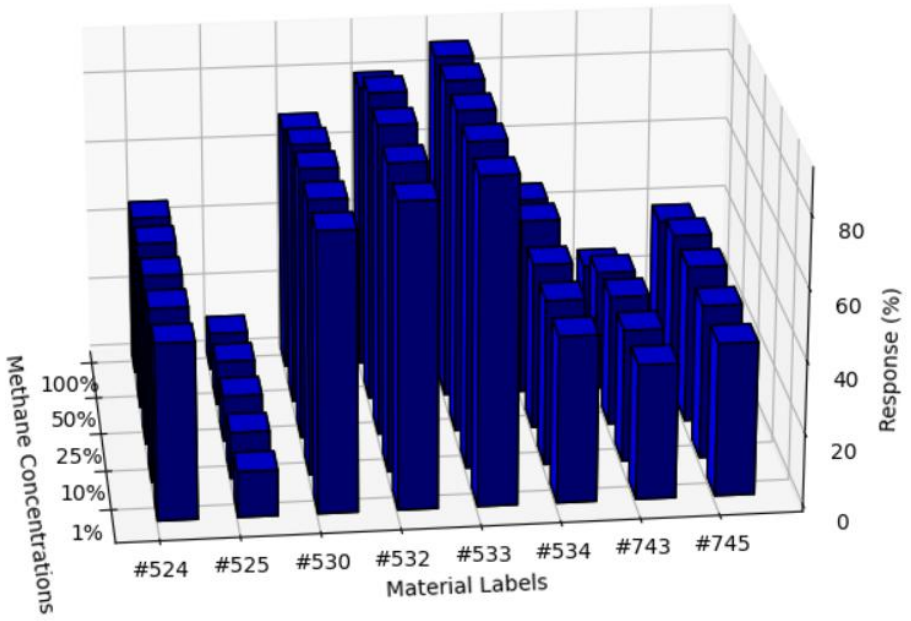

Figure 152: Summary of the sensor's response to different methane gas concentrations

All the developed gas sensors displayed reliable performance coupled with remarkable stability at methane gas sensing, even at the low concentrations and low input voltage. The best response was again obtained by the #533_$ZnAl_5O_x$ gas sensor. Their remarkable performance and cost-effectiveness make them suitable for various methane gas sensing applications.

Following the above discussion for methane results, the sensor was also examined in the presence of hydrogen gas. It must be mentioned that the response of the sensor exhibits behavior contrary to that expected. In our case, the developed materials ZnAlO, $ZnAl_5O_x$, $ZnAlSiO_x$ are n-type because dopants of Aluminum and Silicon replace Zinc atoms in the crystal lattice, providing more free electrons in the lattice of the material. Also, hydrogen gas is referred in the bibliography as a reducing gas, thus it should interact in a similar way with methane which is also a reducing gas. In literature, the hydrogen sensing mechanism of sensors based on a metal oxide semiconductor with the respective adsorption process of oxygen and its reaction with hydrogen, resulting in generating conduction band electrons according to the following reaction: $H_2 + \frac{1}{2}\, O_{2\,(ads)} \rightarrow H_2O + e^-$

Thus, in the presence of hydrogen the current should increase, but at all the conducted measurements a decline in the current magnitude was observed, without any dependence on the sensing material or on the applied temperature. This unexpected behavior to hydrogen gas sensing at all the operating temperature range (RT – T=400°C) indicates that it's not related on the oxygen species in the material surface. A possible explanation to this abnormal behavior to hydrogen sensing, could be that hydrogen decompose on the material surface, creating hydride compounds according to the following reaction: $H_2 + 2e^- \rightleftharpoons 2H^-$ Although, further investigation on theoretical level is essential and more specified methods must be used in order to obtain knowledge of the sensing mechanism that takes place in these sensors. For instance, in situ XPS measurements could recognize and visualize the interaction between the sensing material and the hydrogen gas.

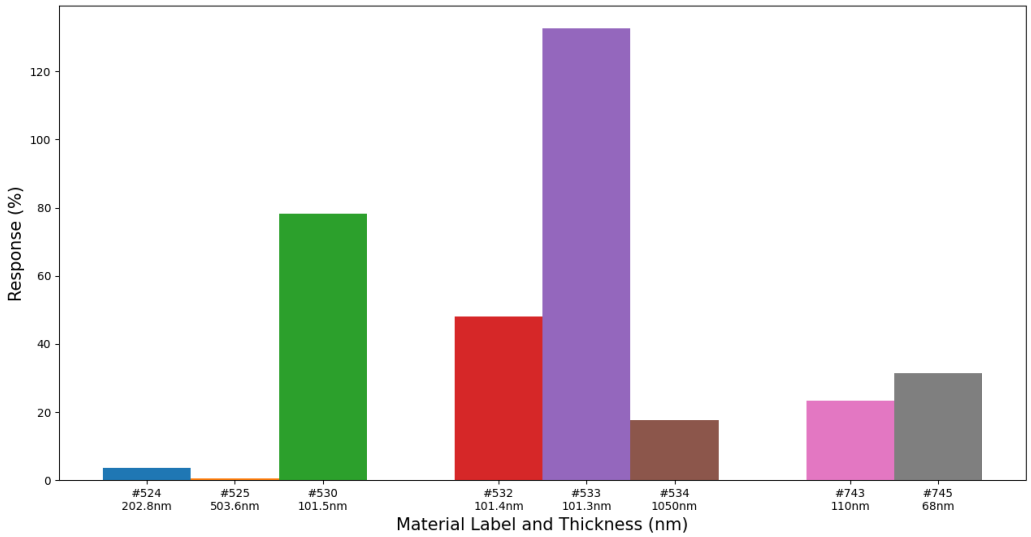

Figure 153: Summary of the sensor's response to hydrogen gas for the different material categorization

In accordance with the previous results for methane gas, the response of the sensors in the repeatability experiments of hydrogen gas sensing is higher for the thinner films at each material category. The #533_$ZnAl_5O_x$ developed sensor performed excellent response S=132.6% at hydrogen gas sensing, followed by the #530_$ZnAlSiO_x$ sensor that exhibited response S=78.2%. The developed $ZnAlSiO_x$ sensing films with higher thickness did not exhibit satisfying response at all. Although the #532_$ZnAl_5O_x$ and #533_$ZnAl_5O_x$ have the same film thickness, their response to hydrogen gas differs a lot. The only parameter that changes during the film development procedure was the applied current (#532 $\rightarrow$ $I_{sputtering}$ = 0.45A, #533 $\rightarrow$ $I_{sputtering}$ = 0.25A). Lower applied current, leads to slower deposition rate of material in the glass substrate, resulting in better performance for hydrogen gas sensing. The sensors with ZnAlO sensing material exhibited relatively good response S=23-31%.

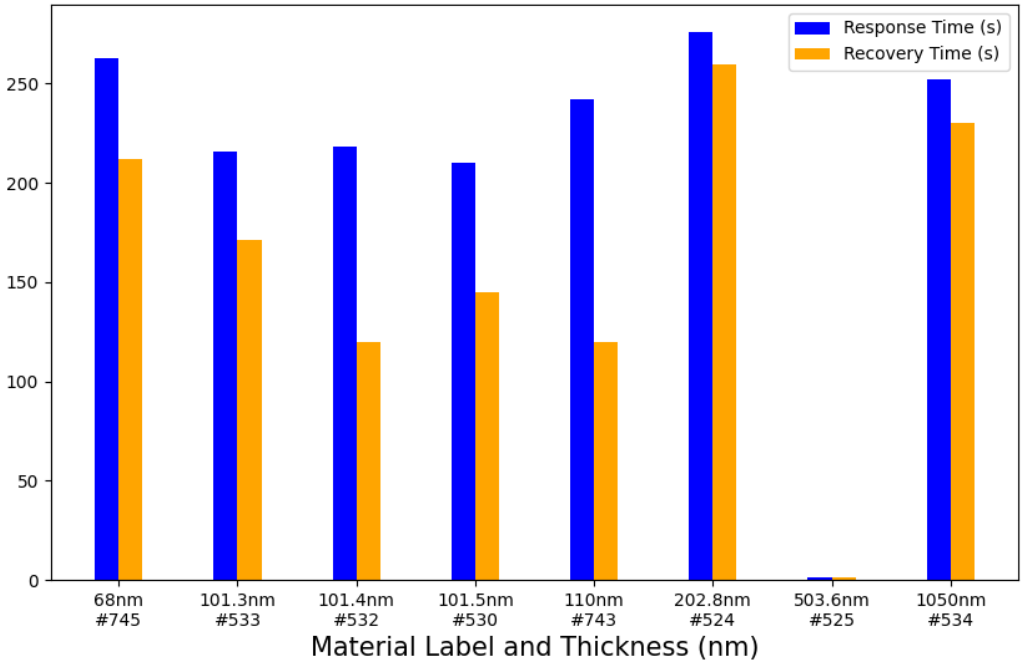

Figure 154: Summary of the response and recovery times at hydrogen gas sensing in regard with the increasing film thickness

In hydrogen gas sensing all the sensors exhibit response time about four minutes, while the recovery time differentiates and depend on the film thickness. For the sensing film thickness around 100 nm, the gas sensors tend to return on their initial state faster.

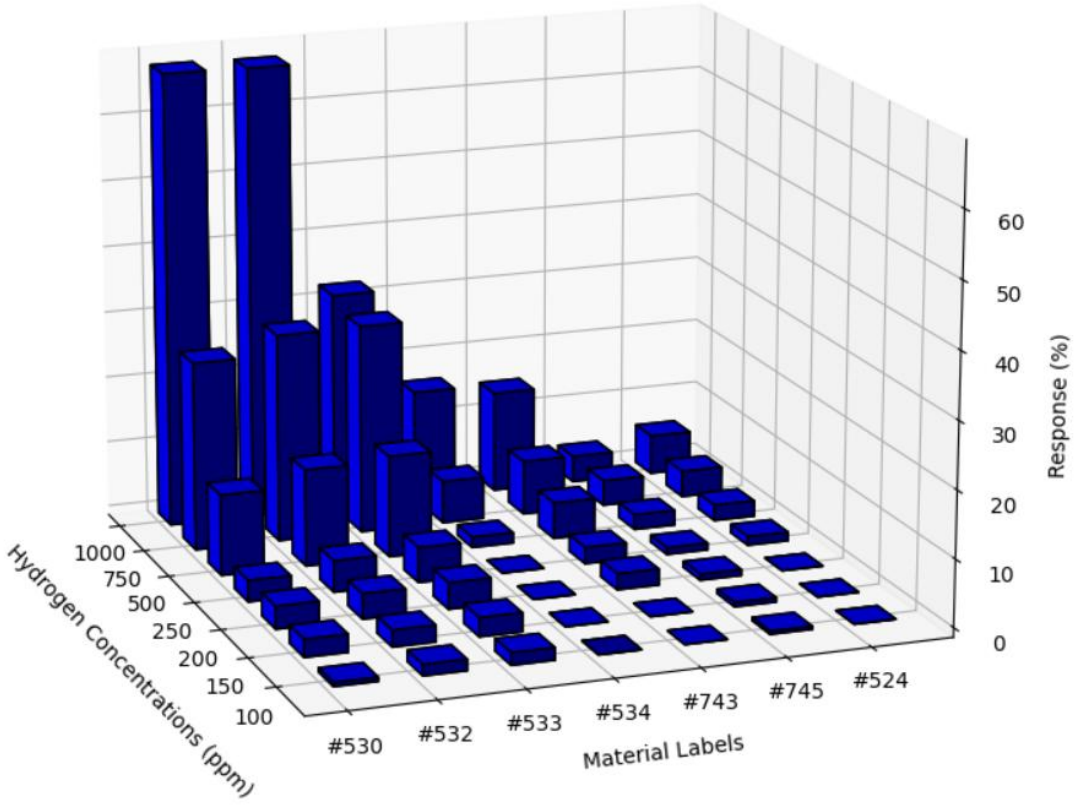

Figure 155: Summary of the sensor's response to different hydrogen gas concentrations

The response of the sensors at hydrogen gas concentrations is quite unstable, even at 1000 ppm of hydrogen gas, obtaining lower sensing response for the #533 and #745 sensors. These two sensor probably require more experimental cycles at the maximum hydrogen concentration in order to reach their high response potential, thus their response was an underperform result. When low hydrogen gas concentration is inserted in the experimental chamber, all sensors struggle in the sensing process, displaying huge decline in the response of the sensors. When the hydrogen gas concentration gets lower than 100 ppm, all sensors show weakness to respond.

Except from the #524, all developed sensors exhibited reliable performance and stability at hydrogen gas sensing. Their cost-effectiveness makes them suitable for various hydrogen gas sensing applications. Additional research and experiments must be conducted in order to improve the hydrogen gas sensing performance of the sensors even at the low concentration range.

Chapter V – Figure Appendixes

1. Appendix A: #743_ZnAlO - Hydrogen gas sensing

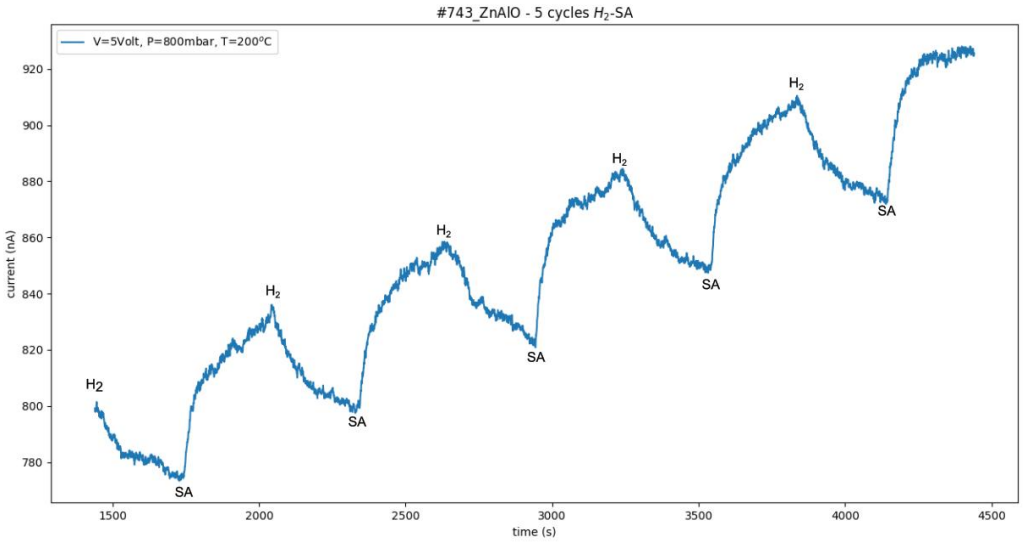

Figure A1.1: Current – time measurement at T=200°C in the presence of hydrogen

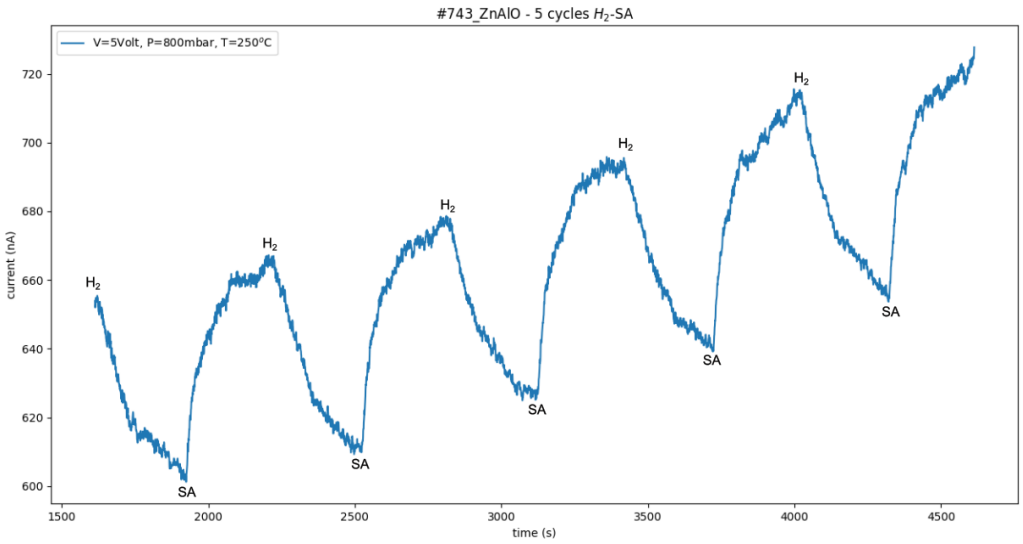

Figure A1.2: Current – time measurement at T=250°C in the presence of hydrogen

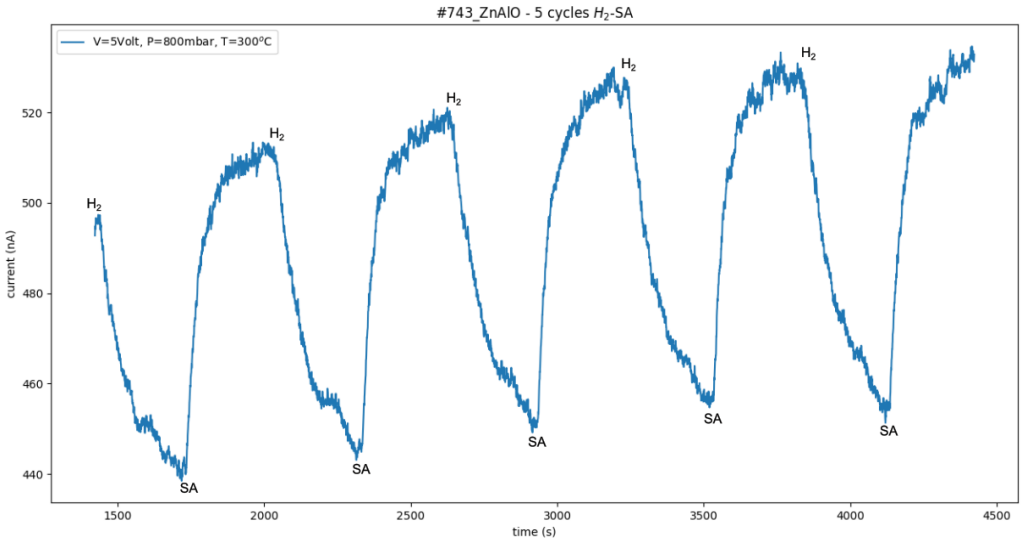

Figure A1.3: Current – time measurement at T=300°C in the presence of hydrogen

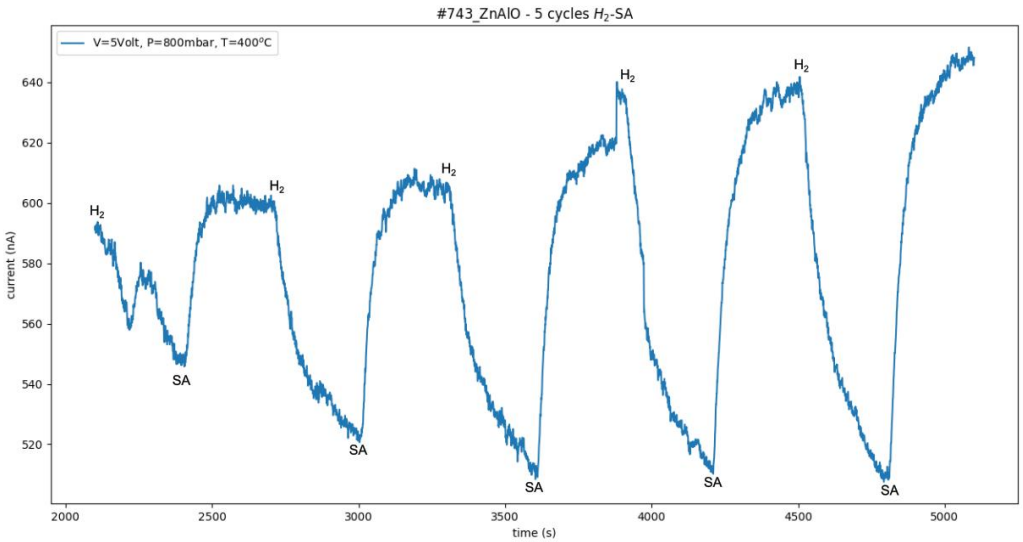

Figure A1.4: Current – time measurement at T=400°C in the presence of hydrogen

2. Appendix A: #743_ZnAlO - Methane gas sensing

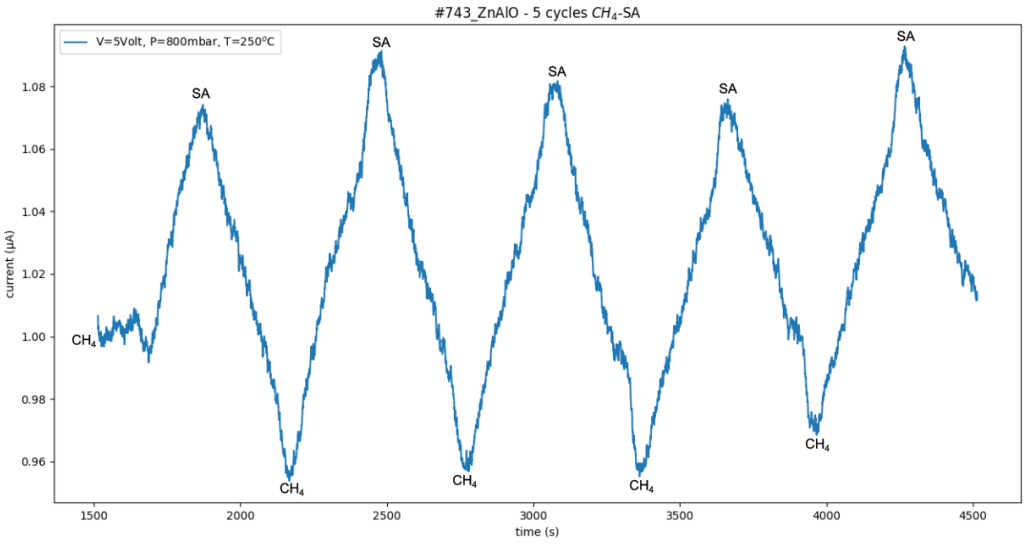

Figure A2.1: Current – time measurement at T=250°C in the presence of methane

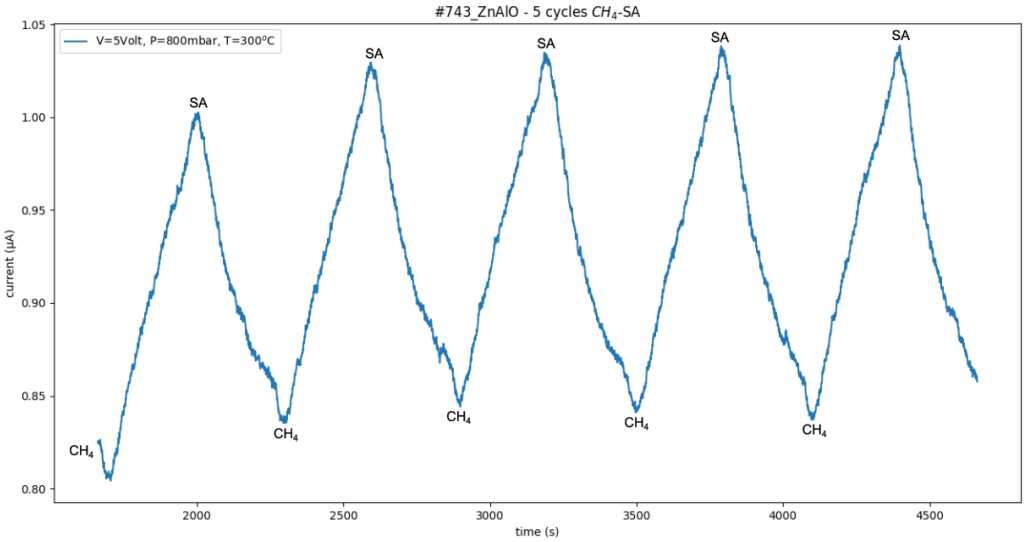

Figure A2.2: Current – time measurement at T=300°C in the presence of methane

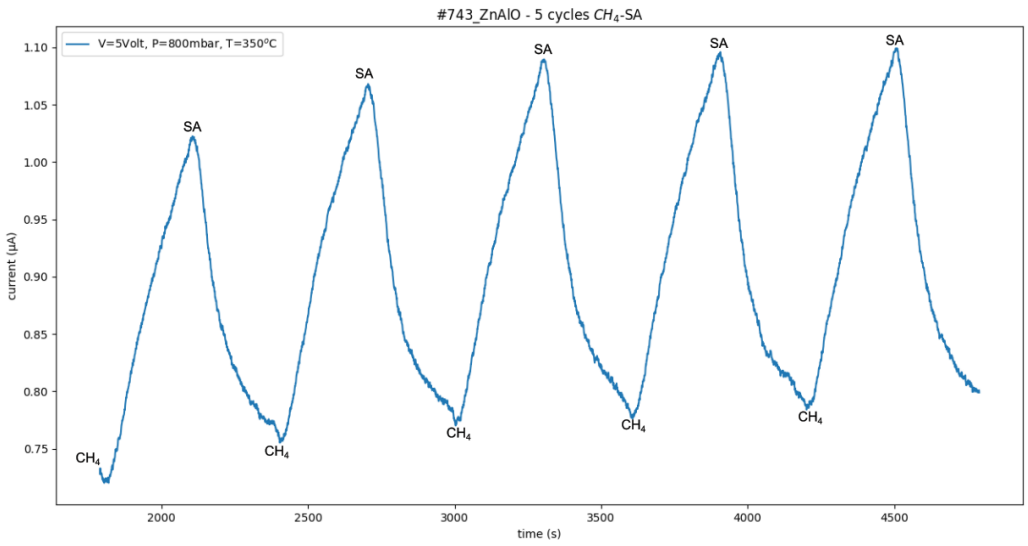

Figure A2.3: Current – time measurement at T=350°C in the presence of methane

3. Appendix A: #745_ZnAlO - Hydrogen gas sensing

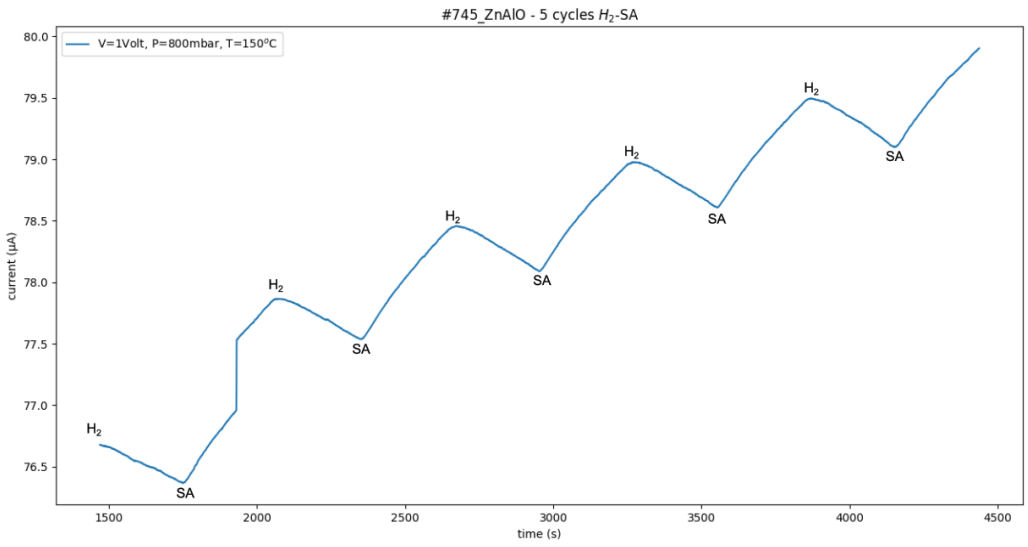

Figure A3.1: Current – time measurement at T=150°C in the presence of hydrogen

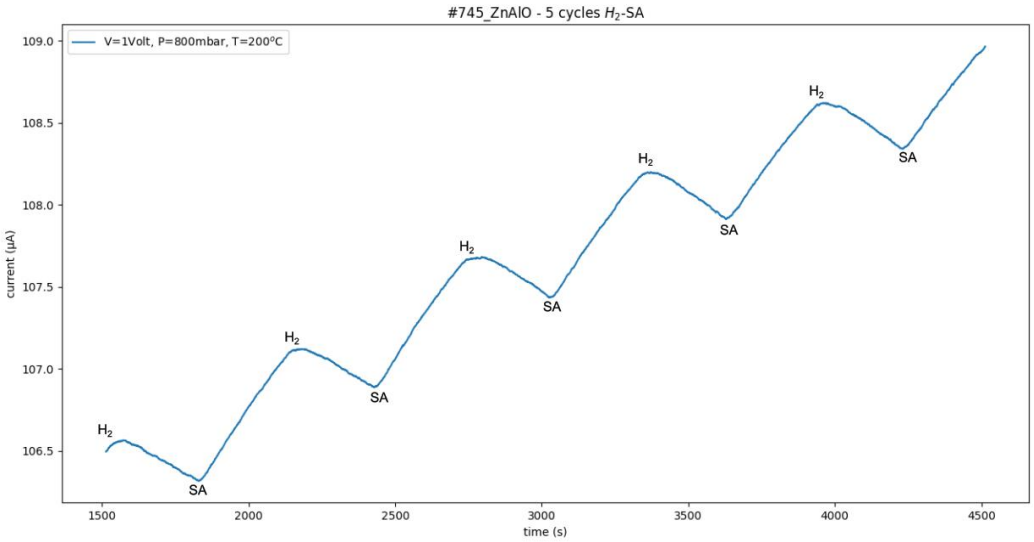

Figure A3.2: Current – time measurement at T=200°C in the presence of hydrogen

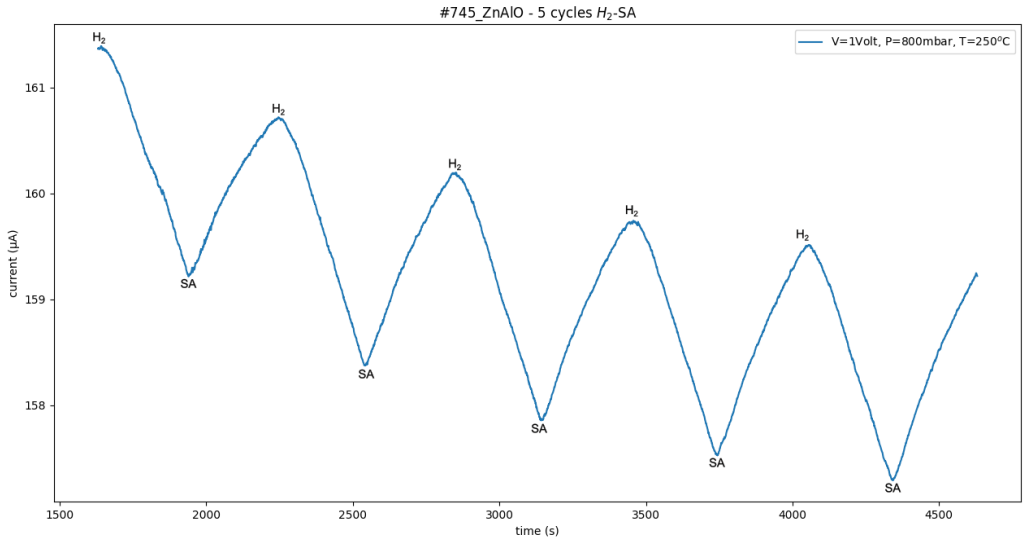

Figure A3.3: Current – time measurement at T=250°C in the presence of hydrogen

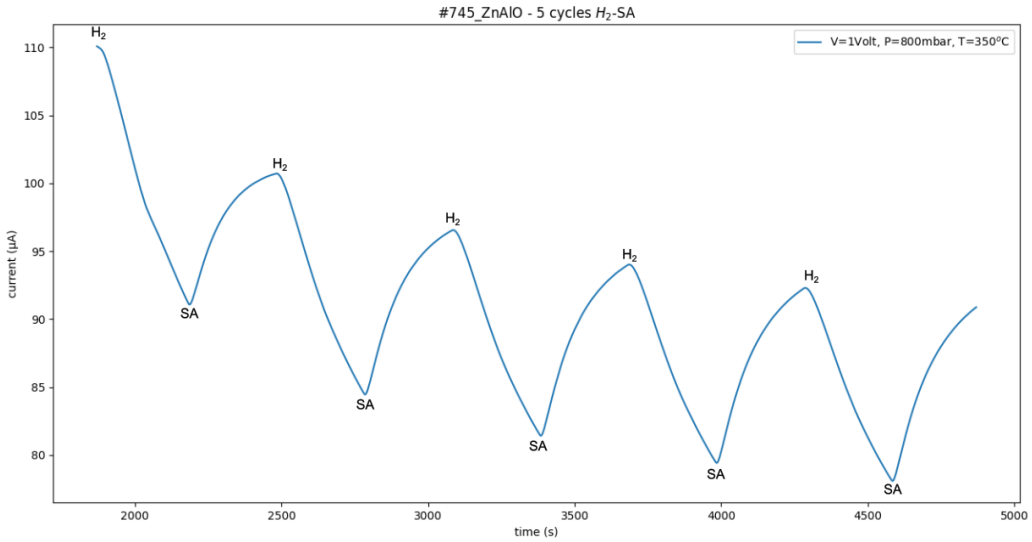

Figure A3.4: Current – time measurement at T=350°C in the presence of hydrogen

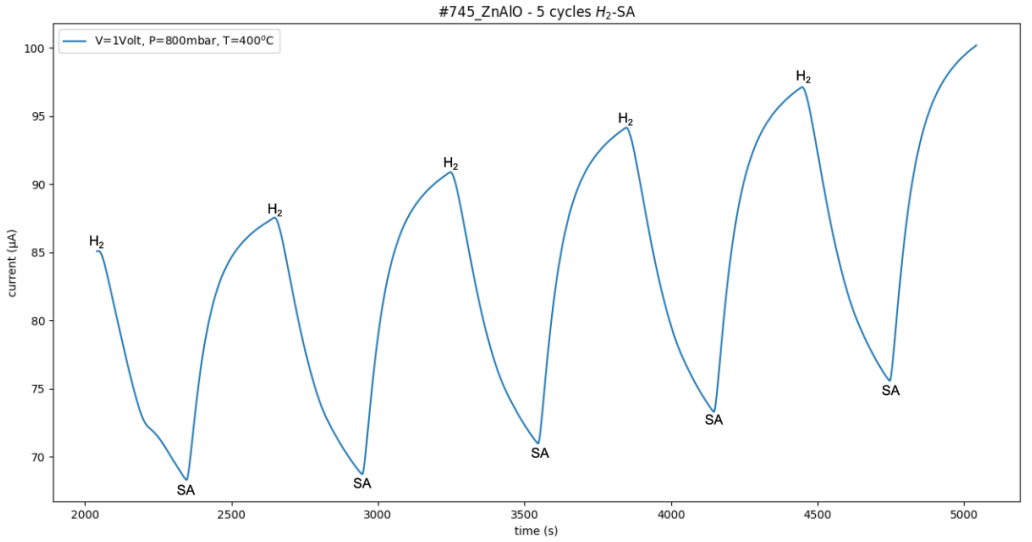

Figure A3.5: Current – time measurement at T=400°C in the presence of hydrogen

4. Appendix A: #745_ZnAlO - Methane gas sensing

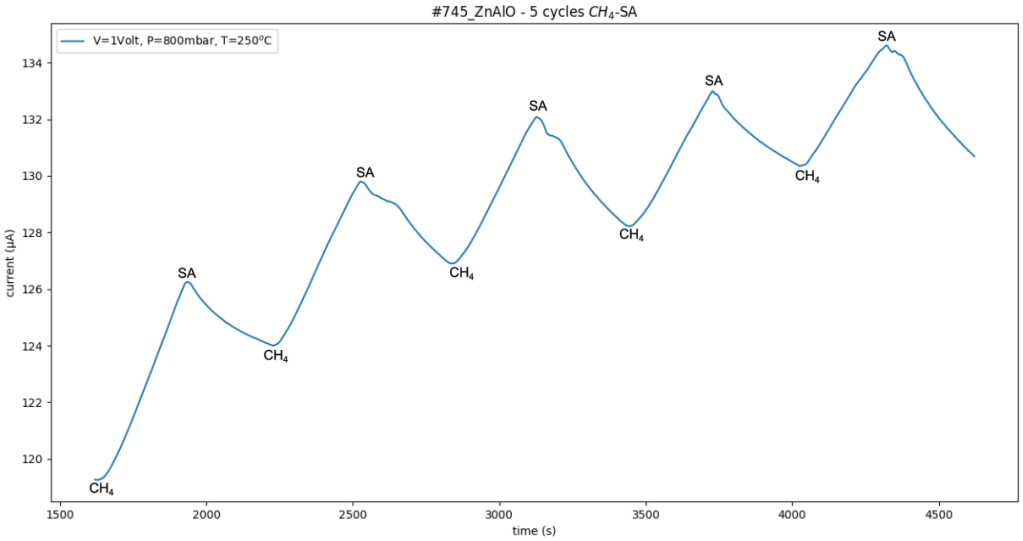

Figure A4.1: Current – time measurement at T=250°C in the presence of methane

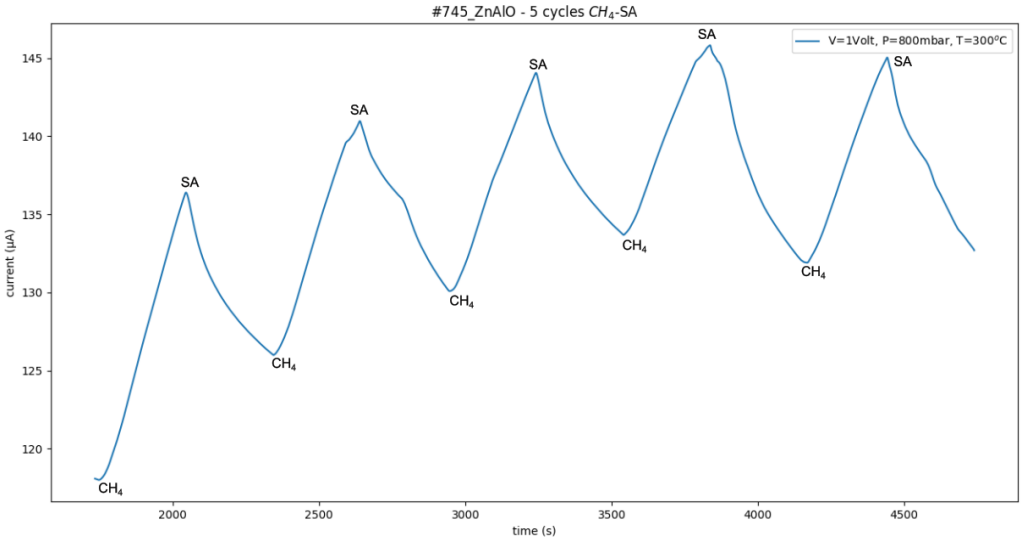

Figure A4.2: Current – time measurement at T=300°C in the presence of methane

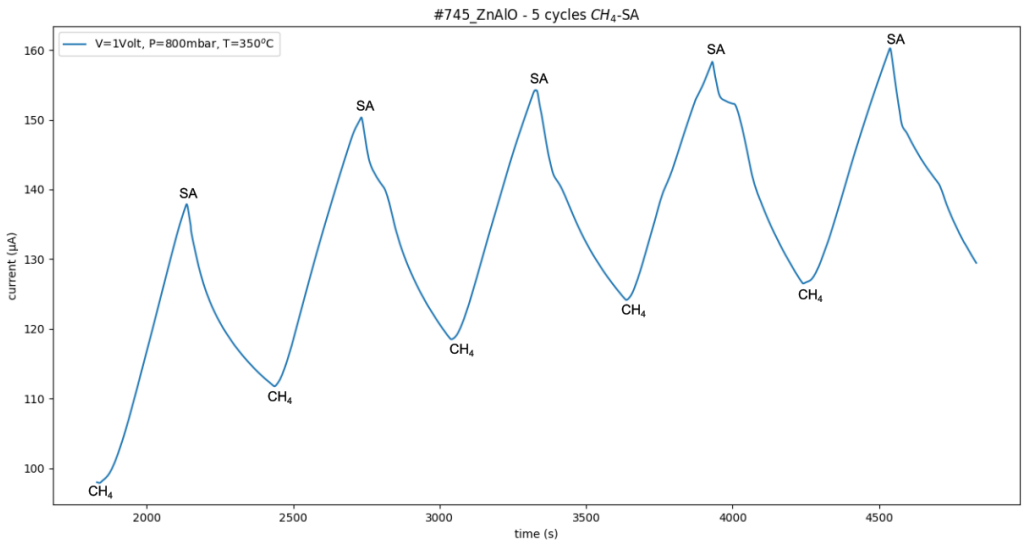

Figure A4.3: Current – time measurement at T=350°C in the presence of methane

5. Appendix B: #532_$ZnAl_5O_x$ – Hydrogen gas sensing

Figure B5.1: Current – time measurement at T=250°C in the presence of hydrogen

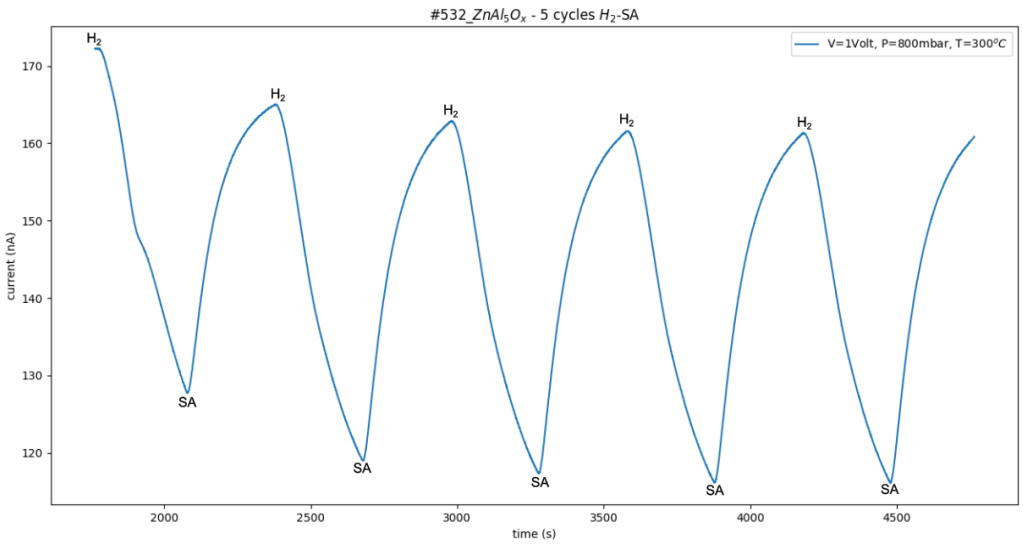

Figure B5.2: Current – time measurement at T=300°C in the presence of hydrogen

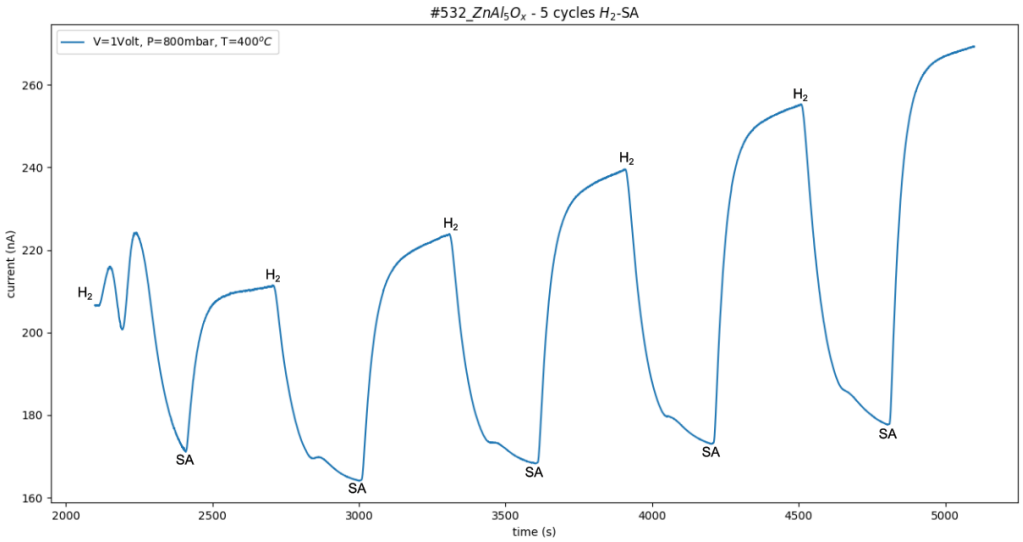

Figure B5.3: Current – time measurement at T=400°C in the presence of hydrogen

6. Appendix B: #532_$ZnAl_5O_x$ – Methane gas sensing

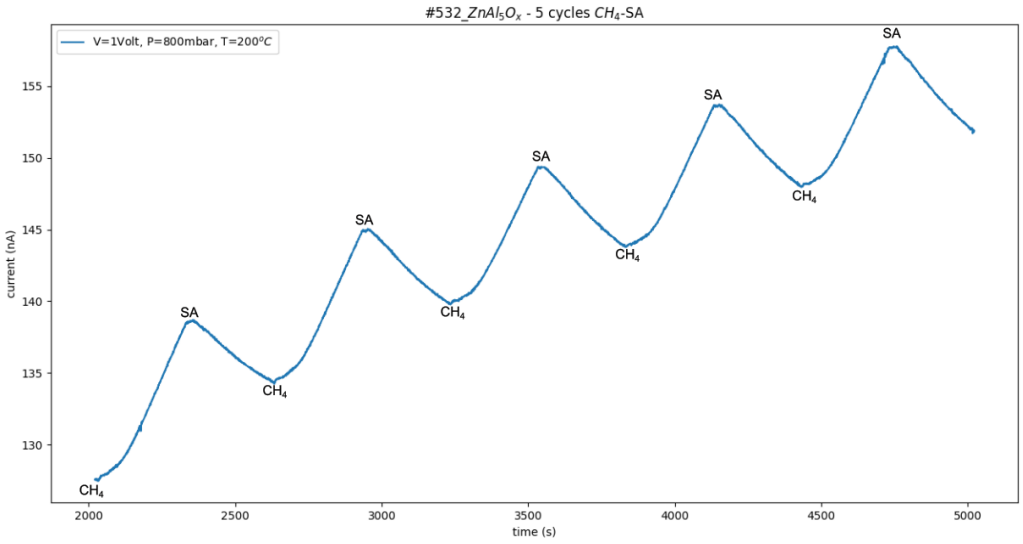

Figure B6.1: Current – time measurement at T=200°C in the presence of methane

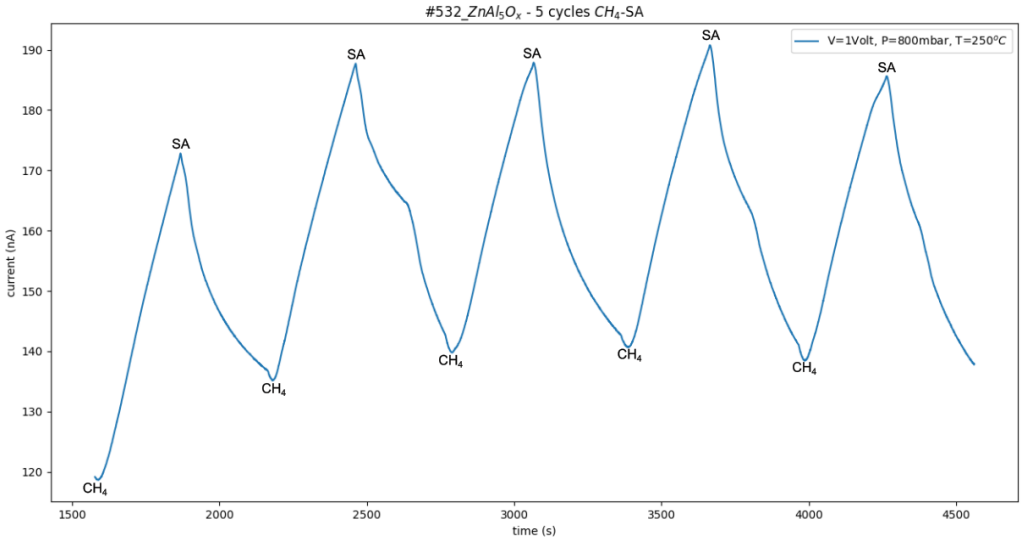

Figure B6.2: Current – time measurement at T=250°C in the presence of methane

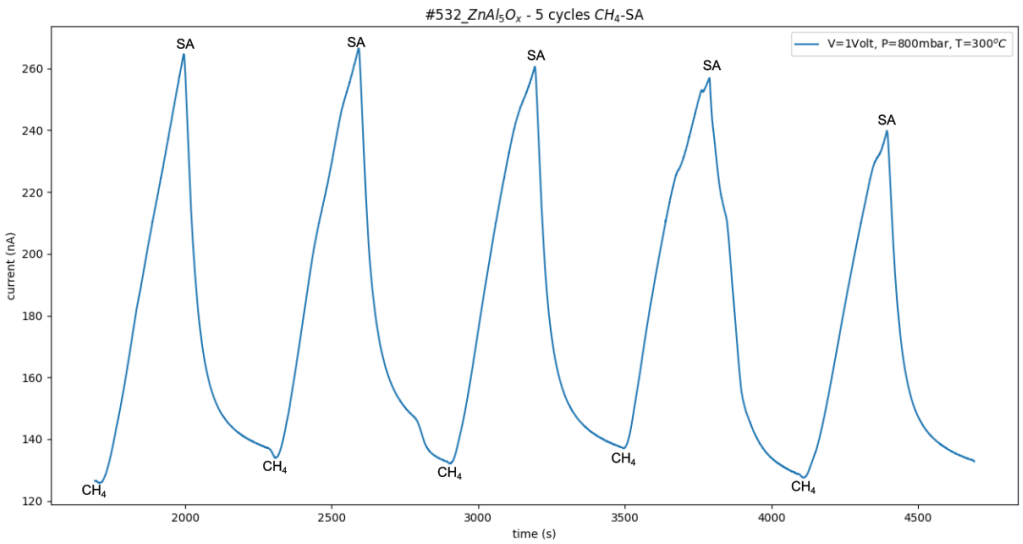

Figure B6.3: Current – time measurement at T=300°C in the presence of methane

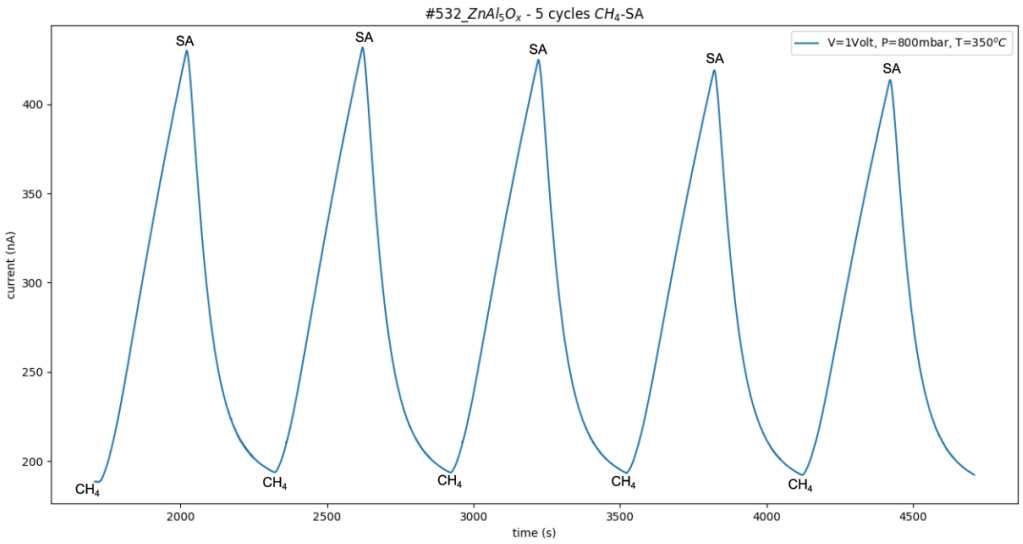

Figure B6.4: Current – time measurement at T=350°C in the presence of methane

7. Appendix B: #533_$ZnAl_5O_x$ – Hydrogen gas sensing

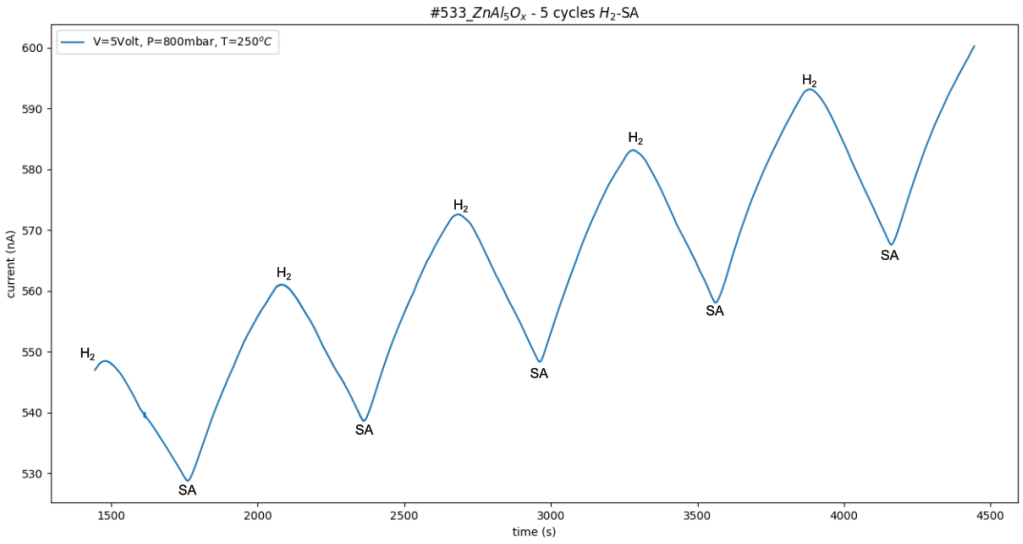

Figure B7.1: Current – time measurement at T=250°C in the presence of hydrogen

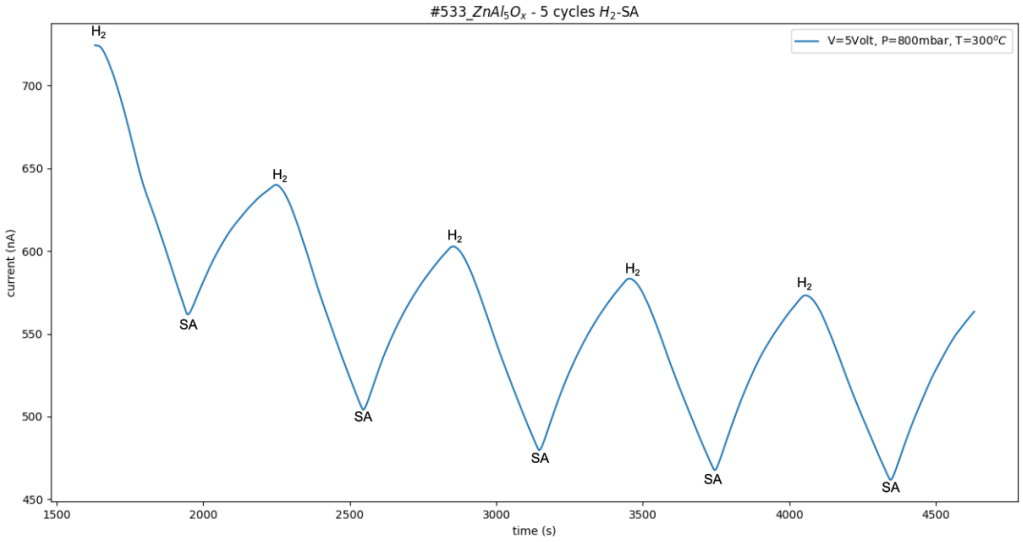

Figure B7.2: Current – time measurement at T=300°C in the presence of hydrogen

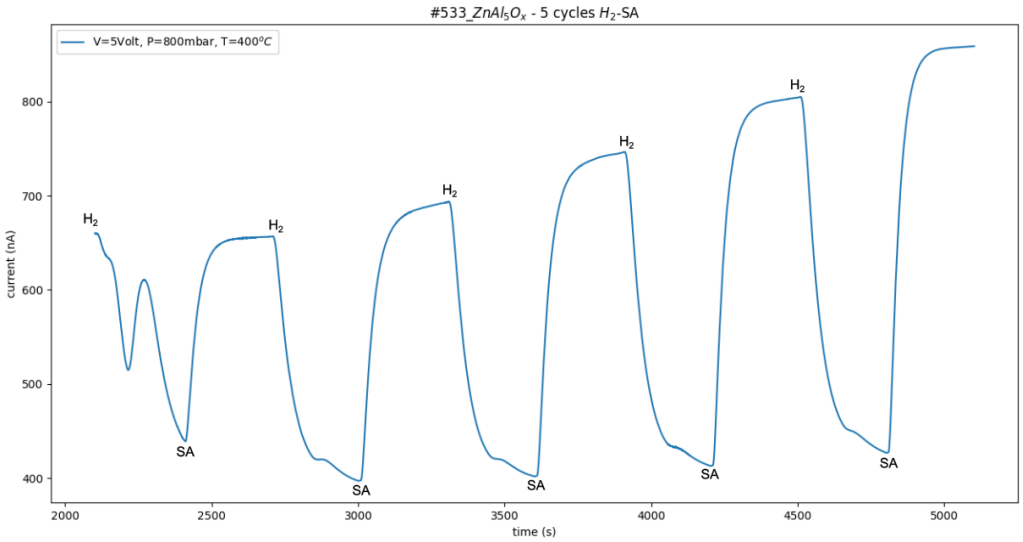

Figure B7.3: Current – time measurement at T=400°C in the presence of hydrogen

8. Appendix B: #533_ZnAl$_5$O$_x$ – Methane gas sensing

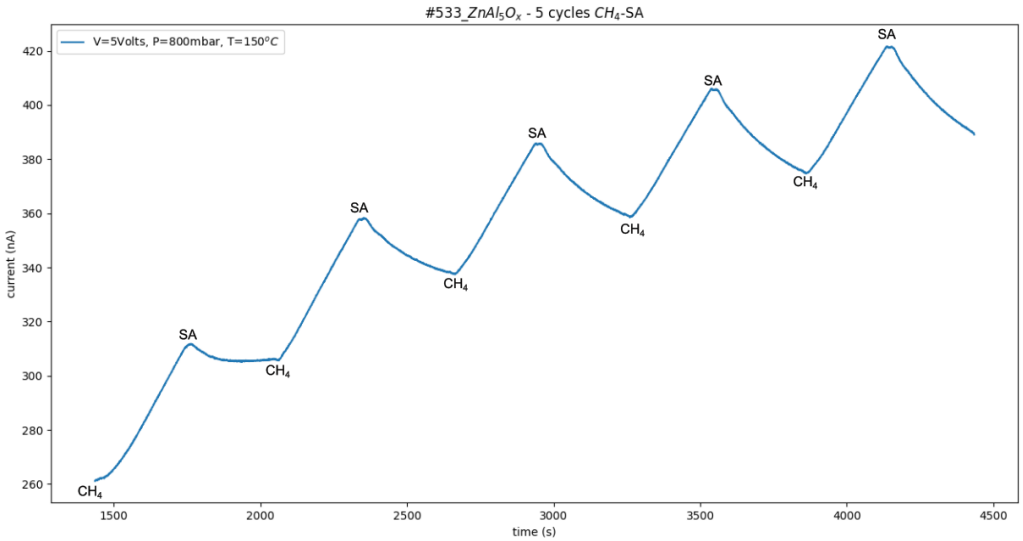

Figure B8.1: Current – time measurement at T=150°C in the presence of methane

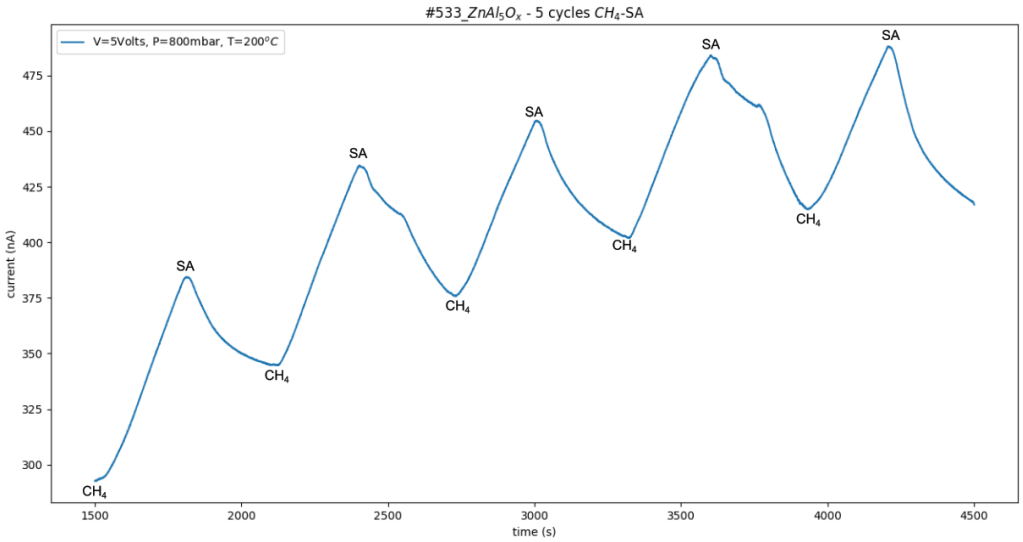

Figure B8.2: Current – time measurement at T=200°C in the presence of methane

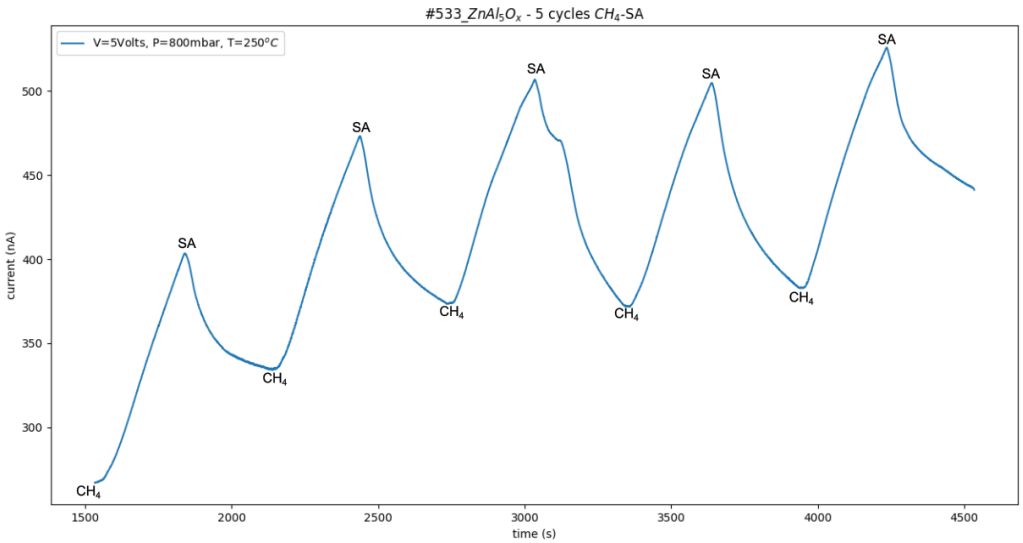

Figure B8.3: Current – time measurement at T=250°C in the presence of methane

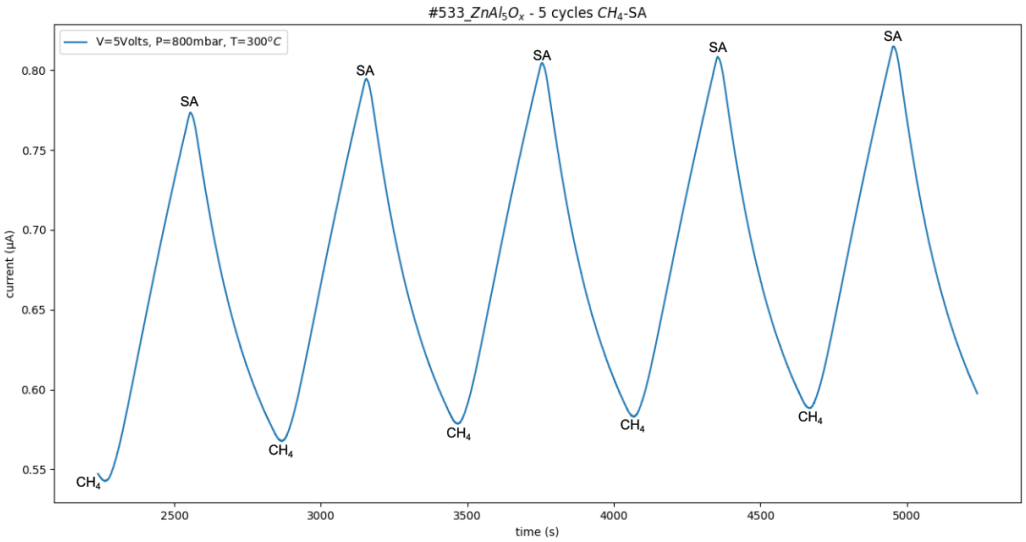

Figure B8.4: Current – time measurement at T=300°C in the presence of methane

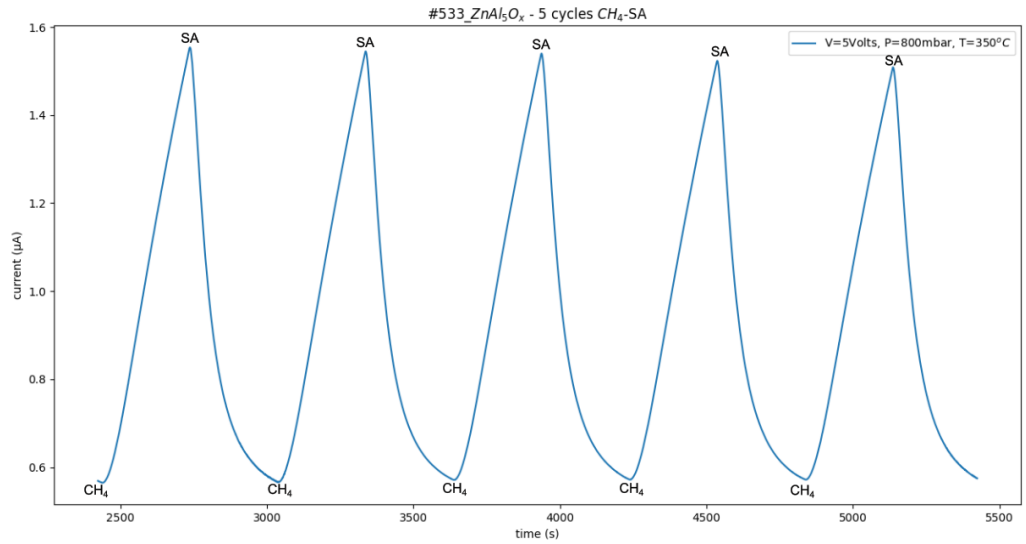

Figure B8.5: Current – time measurement at T=350°C in the presence of methane

9. Appendix B: #534_ $ZnAl_5O_x$ – Hydrogen gas sensing

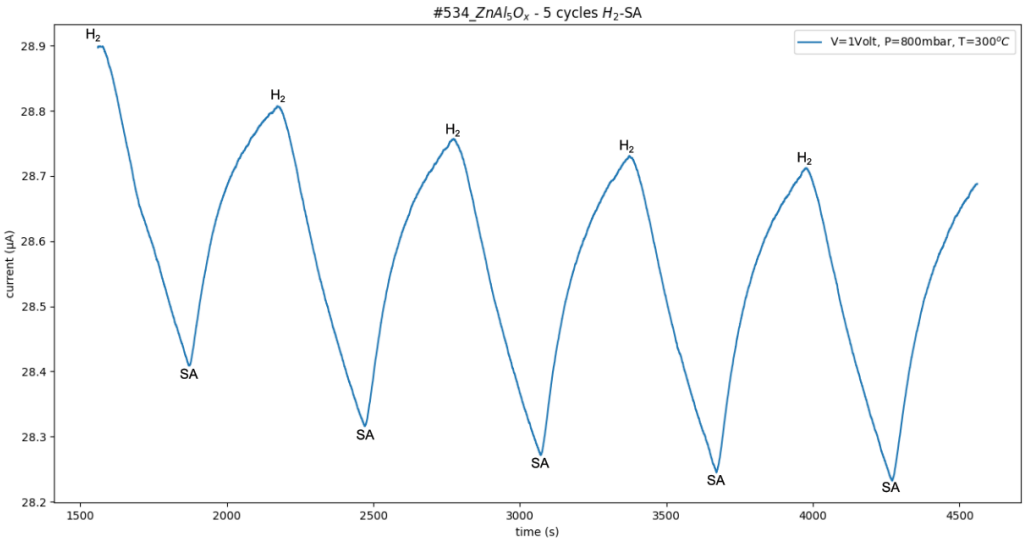

Figure B9.1: Current – time measurement at T=300°C in the presence of hydrogen

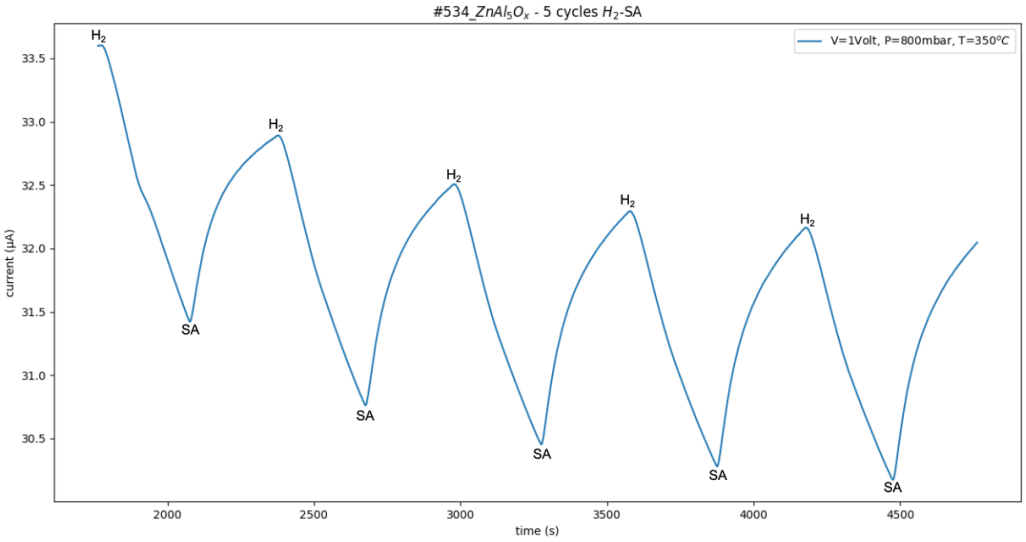

Figure B9.2: Current – time measurement at T=350°C in the presence of hydrogen

10. Appendix B: #534_$ZnAl_5O_x$ – Methane gas sensing

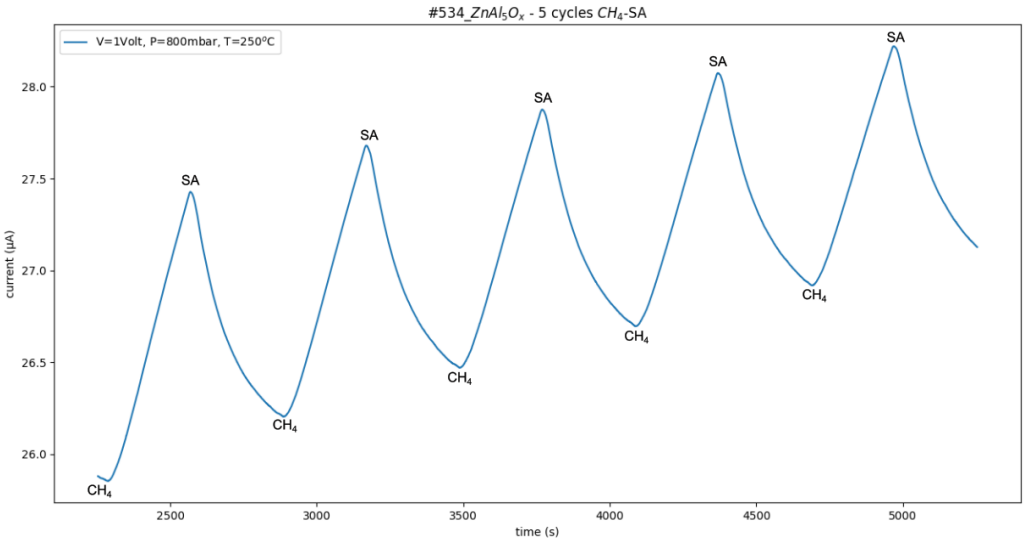

Figure B10.1: Current – time measurement at T=250°C in the presence of methane

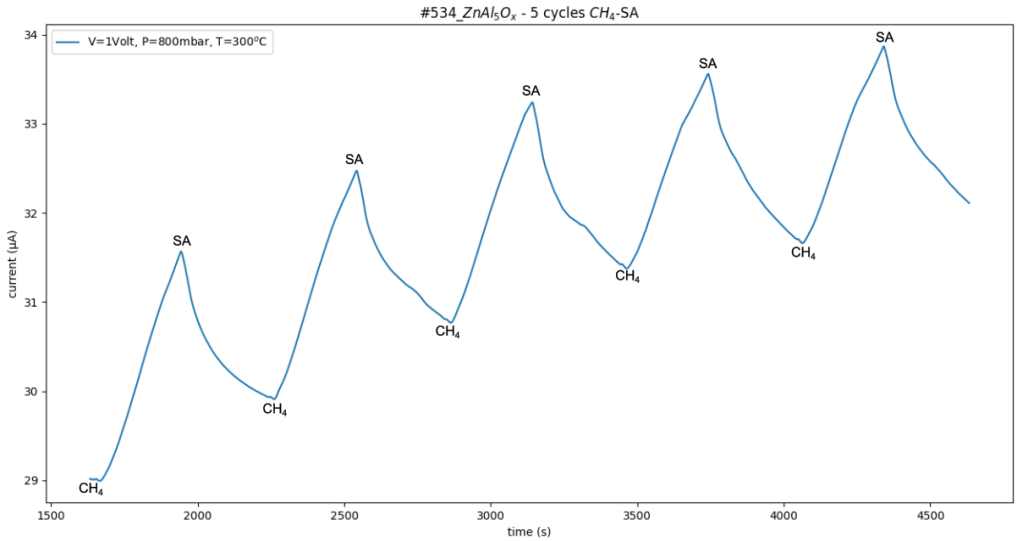

Figure B10.2: Current – time measurement at T=300°C in the presence of methane

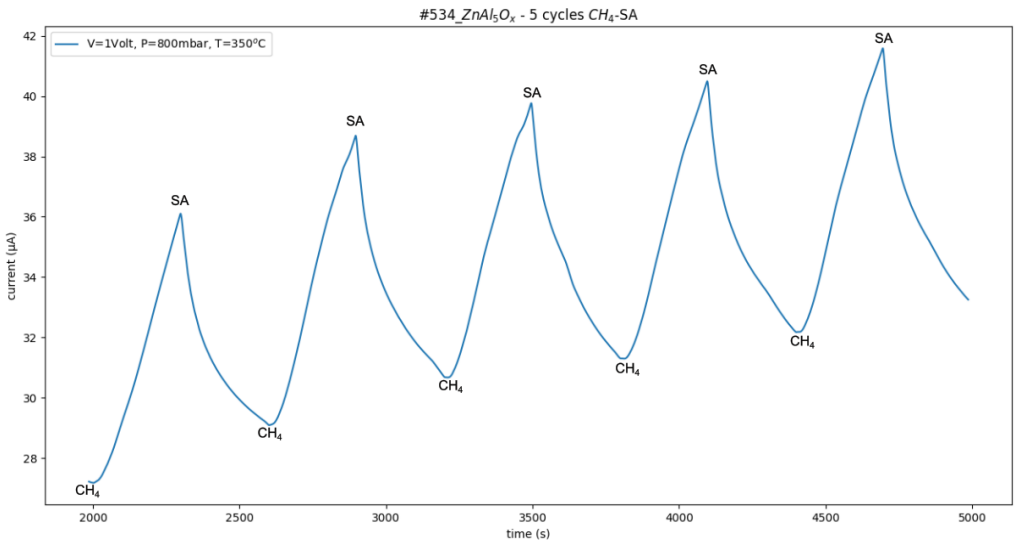

Figure B10.3: Current – time measurement at T=350°C in the presence of methane

11. Appendix C: #530_ZnAlSiO$_x$ – Hydrogen gas sensing

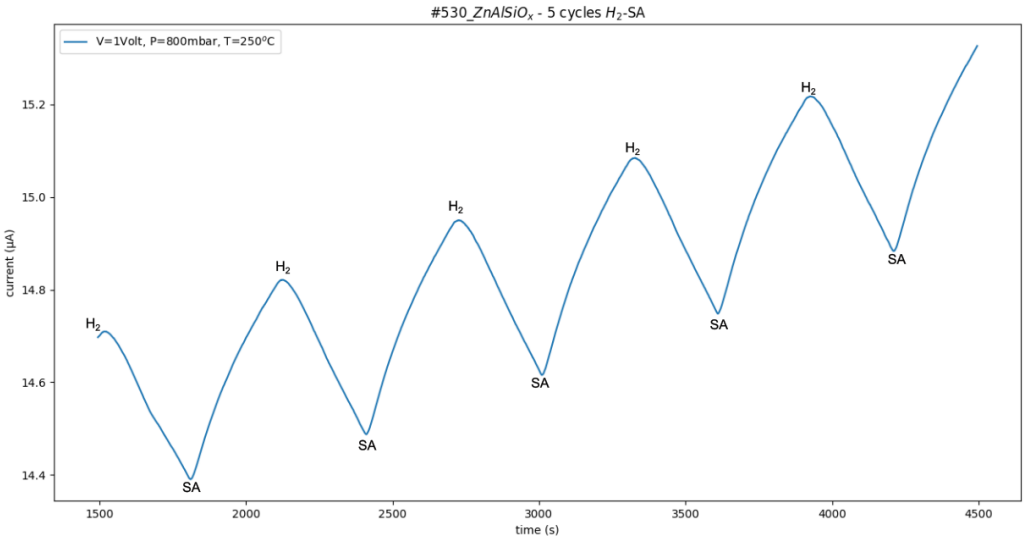

Figure C11.1: Current – time measurement at T=250°C, in the presence of hydrogen

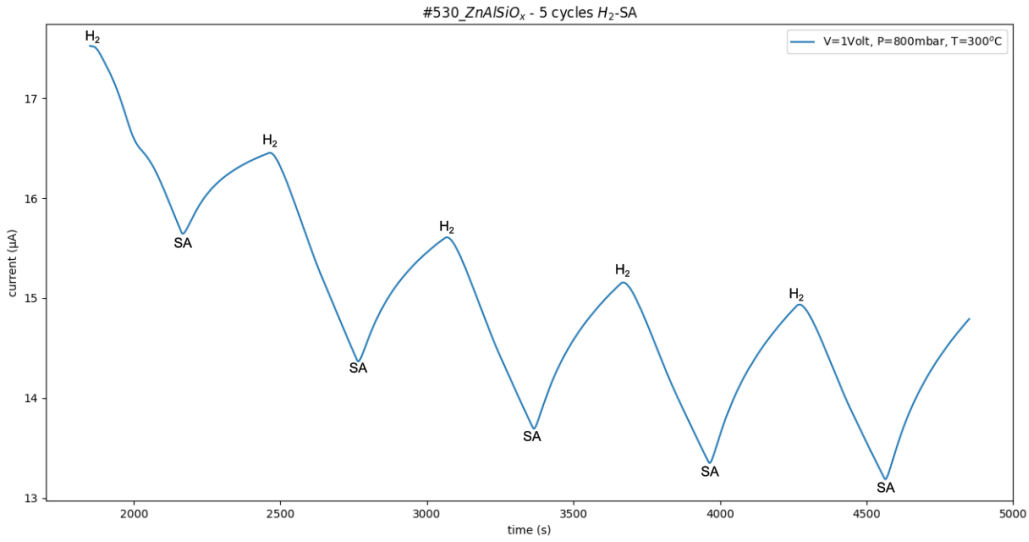

Figure C11.2: Current – time measurement at T=300°C, in the presence of hydrogen

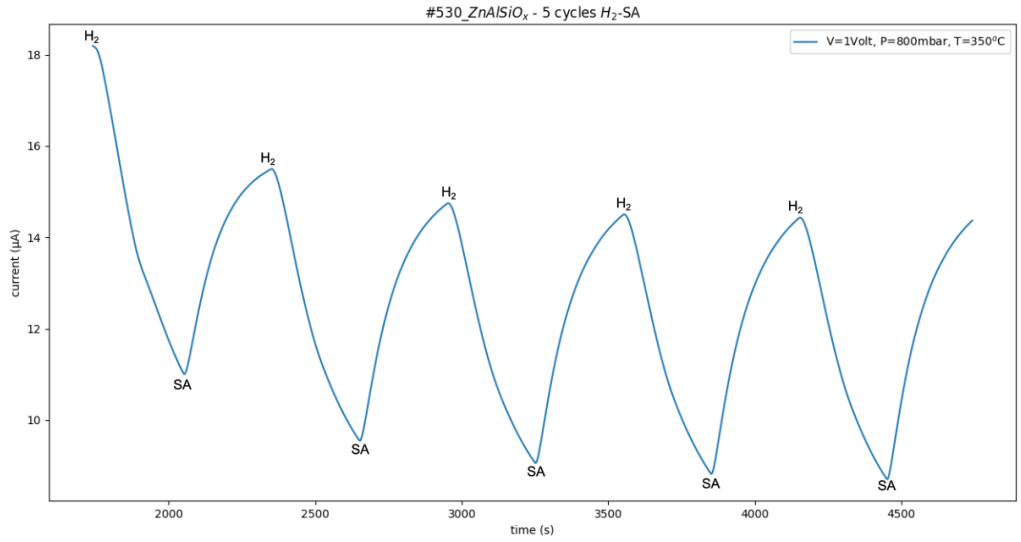

Figure C11.3: Current – time measurement at T=350°C, in the presence of hydrogen

12. Appendix C: #530_ZnAlSiO$_x$ – Methane gas sensing

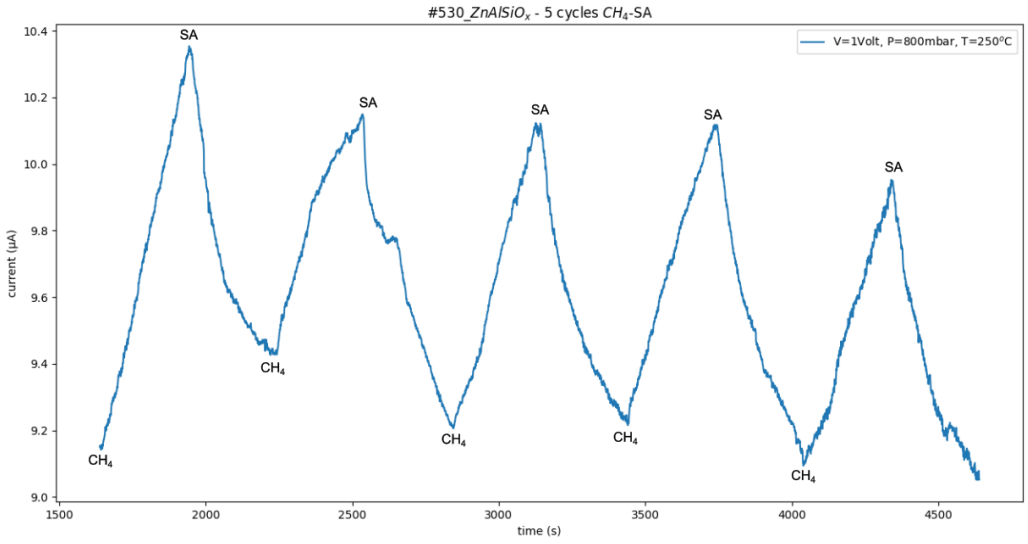

Figure C12.1: Current – time measurement at T=250°C, in the presence of methane

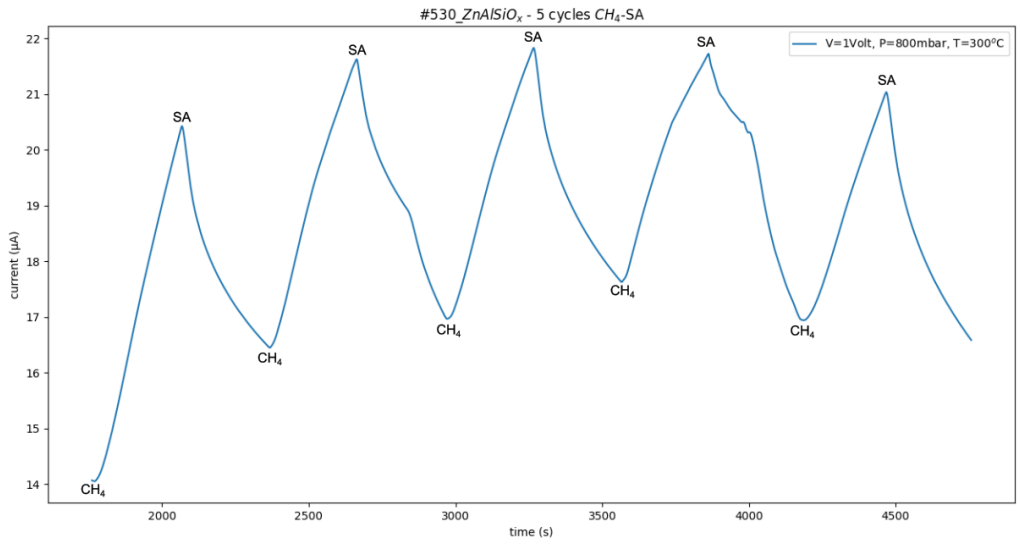

Figure C12.2: Current – time measurement at T=300°C, in the presence of methane

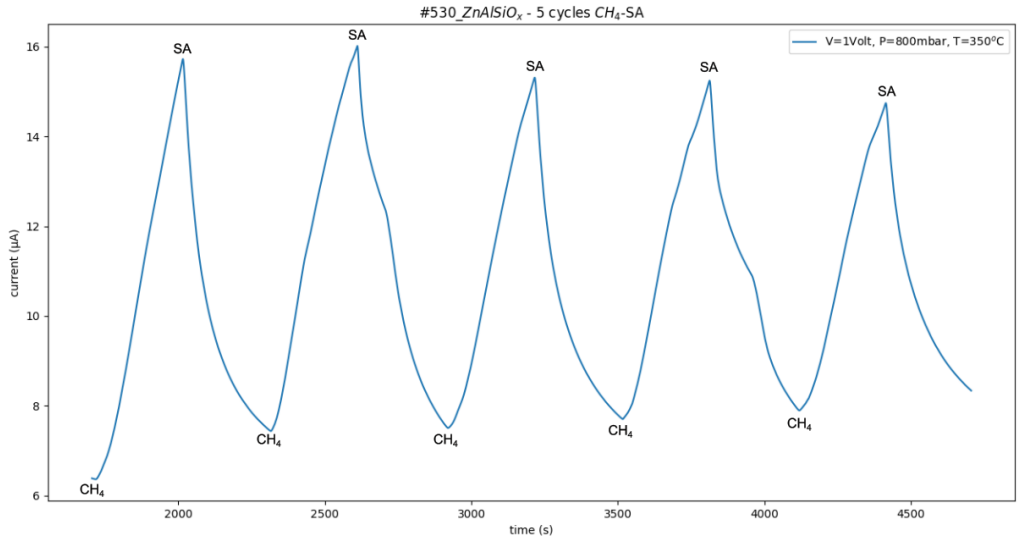

Figure C12.3: Current – time measurement at T=350°C, in the presence of methane

13. Appendix C: #524_ZnAlSiO$_x$ – Methane gas sensing

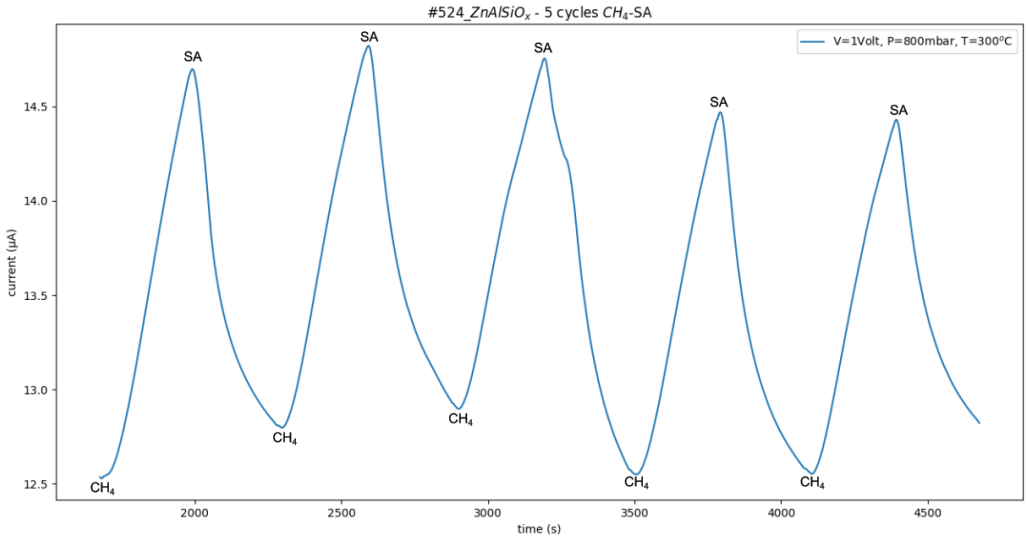

Figure C13.1: Current – time measurement at T=300°C, in the presence of methane

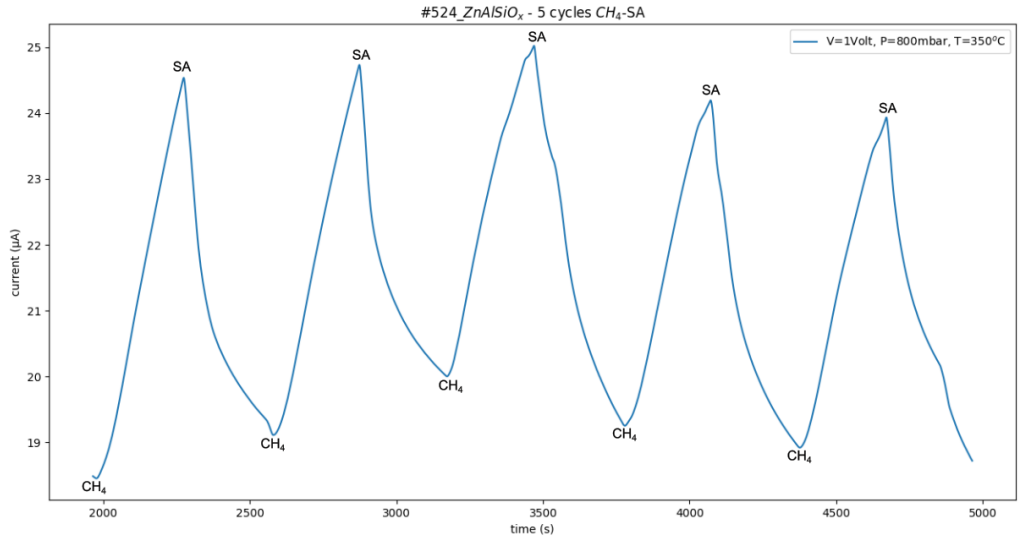

Figure C13.2: Current – time measurement at T=350°C, in the presence of methane

14. Appendix C: #525_ZnAlSiO$_x$ – Methane gas sensing

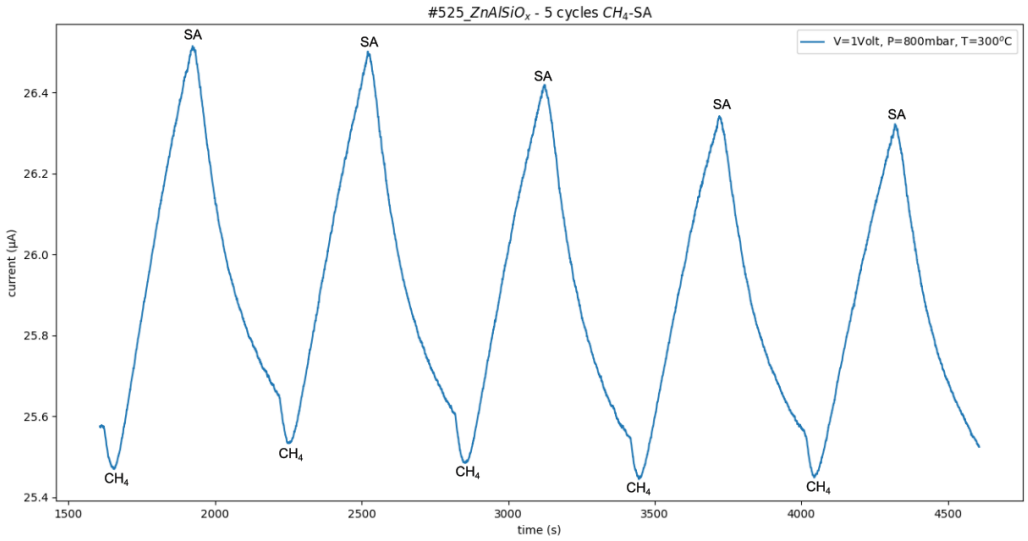

Figure C14.1: Current – time measurement at T=300°C, in the presence of methane

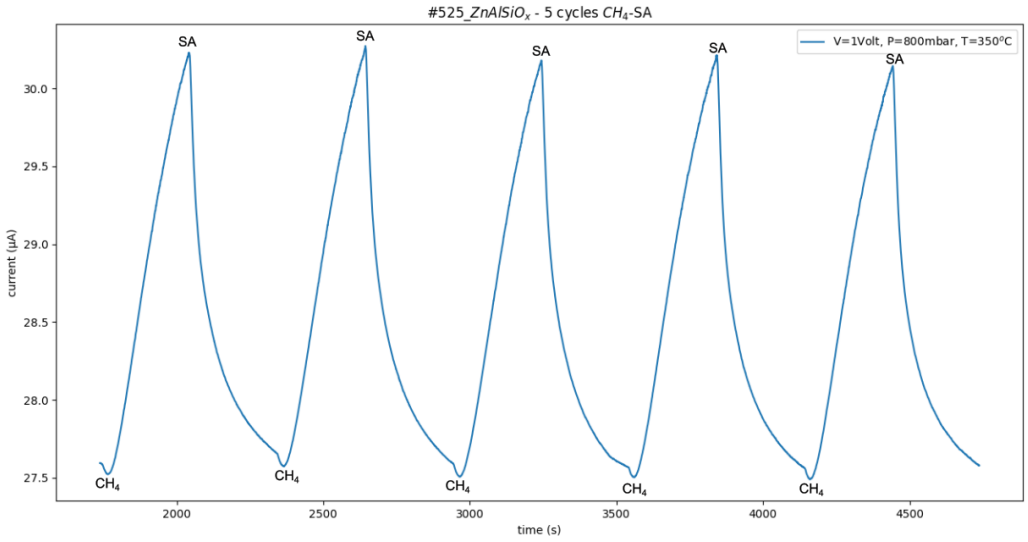

Figure C14.2: Current – time measurement at T=350°C, in the presence of methane

Chapter VI - References

[1] https://www.who.int/health-topics/air-pollution

[2] Yiwen Li (2023) “Wearable Gas Sensor Based on Reticular Antimony-Doped SnO_2/ PANI Nanocomposite Realizing Intelligent Detection of Ammonia within a Wide Range of Humidity” doi.org/10.1021/acssensors.4c00325

[3] Alejandro Santos-Betancourt (2024) “ZnO Decorated Graphene-Based NFC Tag for Personal NO_2 Exposure Monitoring during a Workday” doi.org/10.3390/s24051431

[4] Fan-Jian Meng (2023) “Metal Oxide Heterostructures for Improving Gas Sensing Properties: A Review” doi.org/10.3390/ma16010263

[5] Chengxiang Wang (2010) “Metal Oxide Gas Sensors: Sensitivity and Influencing Factors” doi: 10.3390/s100302088

[6] Sourav Deb (2024) “Review on development of metal-oxide and 2-D material based gas sensors under light-activation” doi.org/10.1016/j.cossms.2024.101160

[7] Hyo-Joong Kim (2014) “Highly sensitive and selective gas sensors using p-type oxide semiconductors: Overview” doi.org/10.1016/j.snb.2013.11.005

[8] Navpreet Kaur (2020) “One-Dimensional Nanostructured Oxide Chemiresistive Sensors” doi.org/10.1021/acs.langmuir.0c00701

[9] Mehran Dadkhah (2022) “Green Synthesis of Metal Oxides Semiconductors for Gas Sensing Applications” doi.org/10.3390/s22134669

[10] Choopun S. (2012) “Metal-Oxide Nanowires for Gas Sensors” doi:10.5772/54385

[11] Ni'matul Azizah (2020) “Influence of Al doping on the crystal structure, optical properties, and photodetecting performance of ZnO film” doi.org/10.1016/j.pnsc.2020.01.006

[12] Sung Min Kim (2019) “High-Performance, Transparent Thin Film Hydrogen Gas Sensor Using 2D Electron Gas at Interface of Oxide Thin Film Heterostructure Grown by Atomic Layer Deposition” doi.org/10.1002/adfm.201807760

[13] Wei Jian Tan (2022) “Enhanced Mitigation of Fire and Explosion Risks due to Hydrogen Leakage Using Targeted Nitrogen Nozzle Spray Approach” doi.org/10.1021/acs.chas.1c00096

[14] Maria Vesna Nikolic (2020) “Semiconductor Gas Sensors: Materials, Technology, Design, and Application” doi:10.3390/s20226694

[15] Dongzhi Zhang (2015) “Facile fabrication of ZnO nanocrystalline-modified graphene hybrid nanocomposite toward methane gas sensing application” doi: 10.1007/s10854-015-3165-2

[16] DC Magnetron sputtering image at page 15: https://vaccoat.com/blog/pulsed-dc-magnetron-sputtering/

[17] C. Klingshirn (2007) “ZnO: Material, Physics and Applications” doi.org/10.1002/cphc.200700002

[18] Anees A. Ansari (2022) “Current progress in organic–inorganic hetero-nano-interfaces based electrochemical biosensors for health care monitoring” doi.org/10.1016/j.ccr.2021.214282
[19] Kurugundla Gopi Krishna (2023) “Zinc oxide based gas sensors and their derivatives: a critical review” doi.org/10.1039/D2TC04690C
[20] Hao Sun (2023) “A ZnO Gas Sensor with an Abnormal Response to Hydrogen” doi.org/10.3390/en16155847
[21] J. Sahu (2023) “Electrochemical and electronic structure properties of high performance supercapacitor based on Nd-doped ZnO nanoparticles” doi.org/10.1016/j.est.2022.106499
[22] Ayse Nur Eroglu (2024) “Patterned ZnO nanorods/indium sulfide based self-powered photoelectrochemical photodetectors” doi.org/10.1016/j.optmat.2023.114763
[23] Darlington C. Ashiegbu (2023) “Improved photocatalytic activity of ZnO-[10%]BiOI and ZnO-[10%]WO_3 heterostructure in the destruction of 2-chlorobiphenyl” doi.org/10.1039/d2va00222a
[24] Haolin Li (2022) “Plasmon-enhanced photocatalytic properties of Au/ZnO nanowires” https://doi.org/10.1016/j.apsusc.2022.152539
[25] Anees A. Ansari (2021) “Organic-inorganic upconversion nanoparticles hybrid in dye-sensitized solar cells” https://doi.org/10.1016/j.ccr.2021.213805
[26] Yanjun Liu (2024) “Flowe-shaped S-scheme CdS-ZnO nanorods heterojunction assisted with SPR of low-content Au for accelerating photocatalytic hydrogen production” https://doi.org/10.1016/j.ijhydene.2024.01.180
[27] U. Ozgur (2005) “A Comprehensive Review of ZnO Materials and Devices” DOI:10.1063/1.1992666
[28] N. Rajeswari Yogamalar (2011) “Absorption-emission study of hydrothermally grown Al:ZnO nanostructures” doi.org/10.1016/j.jallcom.2011.06.012
[29] J. Tauc (1972) “States in the gap” doi.org/10.1016/0022-3093(72)90194-9
[30] Anees A. Ansari (2024) “ZnO nanostructures – Future frontiers in photcatalysis, solar cells, sensing, supercapacitors, fingerpring technologies, toxicity and clinical diagnostics” doi.org/10.1016/j.ccr.2024.215942
[31] Sonal Singhal (2012) “Cu-doped ZnO nanoparticles: Synthesis, structural and electrical properties” doi.org/10.1016/j.physb.2012.01.103
[32] Fan Zhou (2020) “Electrodeposition of gold nanoparticles of ZnO nanorods for improved performance of enzymatic glucose sensors” doi.org/10.1016/j.mssp.2019.104708
[33] A. Lotin (2010) “Epitaxial growth and properties of $Mg_xZn_{1-x}O$ films produced by pulsed laser deposition” doi:10.1134/S106378261002020X
[34] Said Benramache (2013) “Study on the correlation between crystallite size and optical energy gap of doped ZnO thin film” Journal Of Nanostructure in Chemistry